SINGLE-DISH INTENSITY MAPPING WITH THE QUIJOTE MFI AND GBT

A thesis submitted to the University of Manchester
for the degree of Doctor of Philosophy
in the Faculty of Engineering and Physical Sciences

2016

Stuart Harper
Department of Physics & Astronomy

Contents

Word count 59081

List of Tables

List of Figures

The University of Manchester

ABSTRACT OF THESIS submitted by Stuart Harper
for the degree of Doctor of Philosophy and entitled
"Single-Dish Intensity Mapping with the QUIJOTE MFI and GBT"
January 13, 2016

Today, there are only a limited number of surveys of the sky at 1 to 20 GHz. These frequencies lie below the all-sky surveys of *WMAP* and *Planck*, but are critical in constraining the spectral slope of Galactic synchrotron emission. Knowledge of the large-scale spectral morphology of Galactic synchrotron emission is critical in the understanding of the interstellar medium and the weak signal from the polarised cosmic microwave background. Recently, ground based observations from S-PASS, C-BASS and the QUIJOTE Multifrequency Instrument (MFI) have been populating these missing frequencies.

This thesis presents the first QUIJOTE MFI maps of the Northern sky in total intensity at 11, 13, 17 and 19 GHz, and the first single-dish mapping observations of Lynds dark cloud, LDN 1622 at 5 and 13.7 GHz. The observations from both instruments are used to probe the nature of spinning dust emission on degree and arcminute scales within the Galaxy.

A full data reduction and calibration pipeline for QUIJOTE MFI time-ordered-data is described. The absolute flux density scale uncertainty of the MFI data is between 2 and 3 per cent. The pipeline characterises key properties of the MFI, such as the RFI sources, beams, bandpasses, *1/f* noise and more.

A key part of the pipeline was the development of an `MPI` ready Destriping mapmaker and a maximum-likelihood map-maker. The map-making code can be applied to a range of different single-dish instruments and is used to reduce both the QUIJOTE MFI wide-survey maps of the Northern sky, and the GBT arcminute resolution raster observations of LDN 1622. A detailed discussion is given on the simulations used to test the integrity of the map-making implementation.

Parametric model fitting to the SEDs of four spinning dust emission regions is performed. The MFI wide-survey maps are used in conjunction with existing multifrequency 1 degree survey data. The addition of MFI maps is used to confirm the previously tentative spinning dust emission source LDN 1582/84. The mean peak frequency of spinning dust emission over the four spinning dust sources is found to be $\langle \nu_{\rm sp} \rangle = 27.2 \pm 0.7$ GHz, and the mean ratio of the peak spinning dust brightness over the dust optical depth is $\langle A_{\rm sp}/\tau_{250} \rangle = 1.24 \pm 0.18 \times 10^4$ Jy/τ_{250}.

Spectral index maps are derived from the MFI wide-survey data in combination with 408 MHz and *WMAP* 23 GHz data. These maps are used to further quantify the ubiquity of spinning dust emission throughout the Galaxy. The results show that the median flux density spectral index within the inner Galactic disk for $|b| < 2^\circ$ is 0.24 ± 0.07. This implies that at 23 GHz, spinning dust emission contributes 25 ± 5 per cent of the total integrated emission within the inner disk of the Galaxy.

Declaration

No portion of the work referred to in the thesis has been submitted in support of an application for another degree or qualification of this or any other university or other institute of learning.

Copyright Statement

i. The author of this thesis (including any appendices and/or schedules to this thesis) owns certain copyright or related rights in it (the "Copyright") and s/he has given The University of Manchester certain rights to use such Copyright, including for administrative purposes.

ii. Copies of this thesis, either in full or in extracts and whether in hard or electronic copy, may be made **only** in accordance with the Copyright, Designs and Patents Act 1988 (as amended) and regulations issued under it or, where appropriate, in accordance with licensing agreements which the University has from time to time. This page must form part of any such copies made.

iii. The ownership of certain Copyright, patents, designs, trade marks and other intellectual property (the "Intellectual Property") and any reproductions of copyright works in the thesis, for example graphs and tables ("Reproductions"), which may be described in this thesis, may not be owned by the author and may be owned by third parties. Such Intellectual Property and Reproductions cannot and must not be made available for use without the prior written permission of the owner(s) of the relevant Intellectual Property and/or Reproductions.

iv. Further information on the conditions under which disclosure, publication and commercialisation of this thesis, the Copyright and any Intellectual Property and/or Reproductions described in it may take place is available in the University IP Policy (see http://documents.manchester.ac.uk/DocuInfo.aspx?DocID=487), in any relevant Thesis restriction declarations deposited in the University Library, The University Library's regulations (see http://www.manchester.ac.uk/library/aboutus/regulations) and in The University's Policy on Presentation of Theses.

Acknowledgements

I would like to thank my supervisor, Professor Clive Dickinson for all his support and guidance throughout my PhD. I would like to thank Dr. Robert Watson for his advice and assistance, and the rest of the QUIJOTE collaboration. I would also like to thank the numerous other people who have supported me in various over the past several years. I would finally like to thank the Science and Technology Funding Council (STFC) for their sponsorship.

Thanks is also given to my thesis examiners Prof. Jo Dunkley and Dr. Rene Breton for taking the time to provide extremely useful feedback and comments on the work in this thesis.

Chapter 1

Introduction

"Stuff traces stuff."

de Oliveira-Costa et al. (2008b) *A model of diffuse Galactic radio emission from 10 MHz to 100 GHz.*

Over fifty years ago, Erickson (1957) postulated that the rapid rotation of interstellar grains with intrinsic electric or magnetic dipoles could be the source of a yet undetected emission mechanism. In 1996, correlations between dust and radio emission measured by the *Cosmic Background Explorer* (*COBE*) (Kogut et al., 1996) suggested that the current model of Galactic emission was incomplete. Numerous hypotheses were proposed to explain this *anomalous microwave emission* (AME) (Leitch et al., 1997; Bennett et al., 2003) but none withstood the mounting scientific scrutiny of subsequent observations, except for Erickson's *spinning dust*. This thesis will address the implications of this recently discovered emission from the Galaxy. To better place spinning dust within the context of Galactic emission as a whole, an understanding of each mechanism and the history of radio astronomy is necessary.

1.1 A Brief History of Radio Astronomy

From as early as the nineteenth century it has been known that objects such as the Sun do not just emit optical light as perceived by the human eye, but emit light across the entire electro-magnetic spectrum. The first measurements of celestial radio emission came many decades later when a Bell radio-engineer, Karl G. Jansky, recorded the emission originating from a single location in the local sky. The results of this

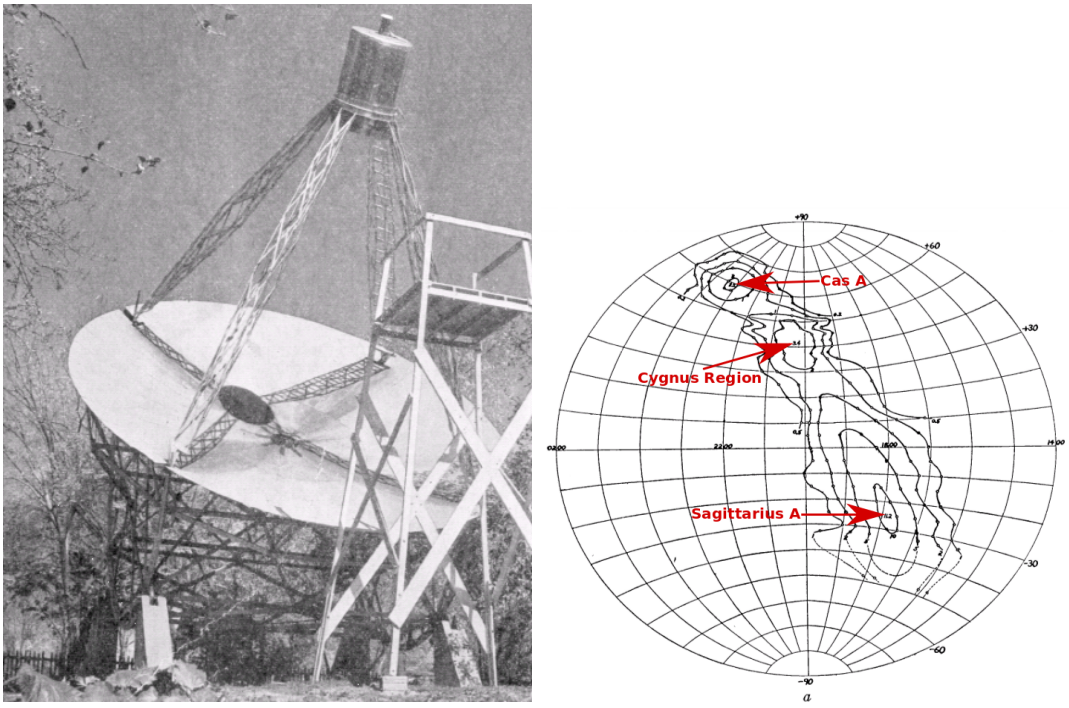

Figure 1.1: *Left:* The alt-azimuth mounted radio telescope used by Reber to produce a map (*right*) of the radio emission of the Milky Way in the Western hemisphere with annotations of several key features Galactic features at 160 MHz. Figures from Reber (1944).

observation revealed a correlation between both the recorded antenna voltage with the diurnal cycle and the plane of the Milky Way (Jansky, 1933). It was not until World War II that the first maps of the radio sky were generated using a ≈ 10 m diameter altitude-azimuth mounted telescope (Reber, 1944). Figure 1.1 shows Reber's telescope alongside his 160 MHz map of the Galaxy. Even in this very early map key features are clearly visible such as the supernova remnant Cassiopeia A and the Cygnus region, which includes the Cygnus A galaxy.

Today, radio astronomy has become a tool used alongside all other fields of astronomy, from infrared to gamma rays, as a way of probing the intricate connections between all wavelengths of light emitted by celestial objects. Radio astronomy gives insight into compact objects such as pulsars (Hewish et al., 1968) and masers (Weaver et al., 1965), and can be used to study the emission from galaxies in the early universe (Thrall et al., 2007). Radio astronomy can provide unique information on the largest structures within the Galaxy and the Universe as a whole, the latter being the focus of this thesis.

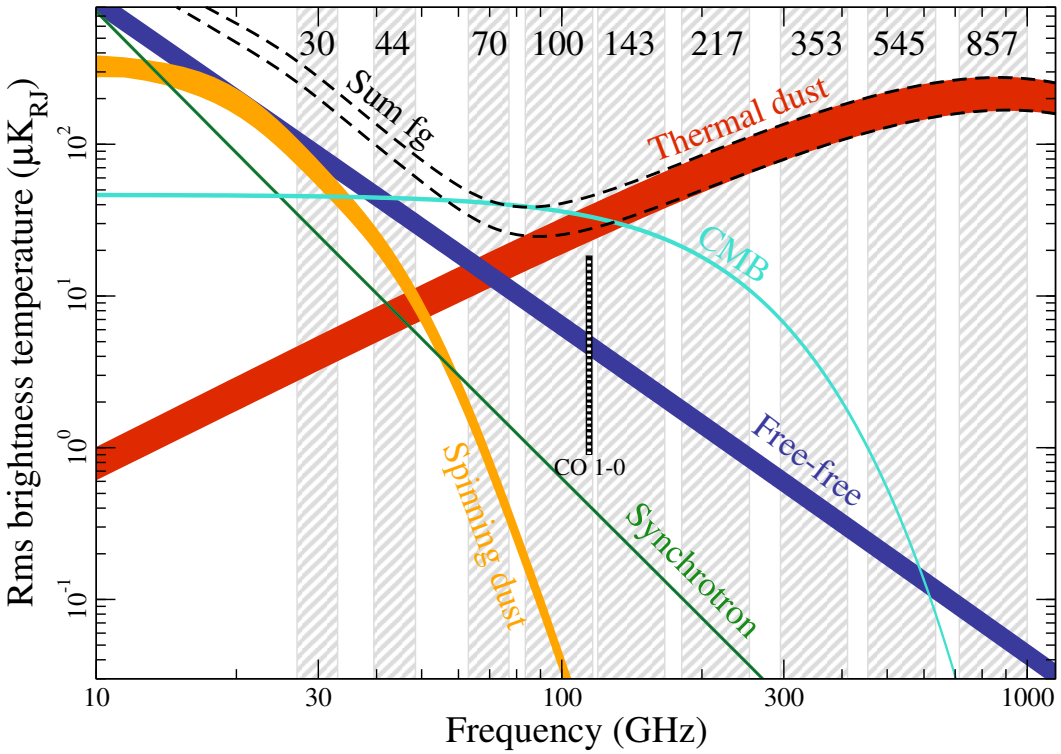

Figure 1.2: Brightness of Galactic foreground emissions as a function of frequency in total intensity at an angular resolution of 1 degree. The thickness of each line represents the emission measured using a mask covering 81 and 93 % of the sky (Planck Collaboration et al., 2015a).

1.2 Microwave Continuum Emission

Investigations into microwave continuum emission between 1 and 100 GHz provide an insight into the astrophysical mechanisms of free-free, synchrotron, thermal dust, and spinning dust emissions, and also into the structures of the *cosmic microwave background* (CMB)(Burke and Graham-Smith, 1996; Rohlfs and Wilson, 2004). Figure 1.2 shows the integrated spectral energy density of the Milky Way and the complexity of the interactions between the five microwave continuum emissions derived from the latest *Planck* results (Planck Collaboration et al., 2015a). One of the main drivers behind observing at microwave frequencies is to study the anisotropic structures of the CMB. However, a detailed understanding of the Galactic emission that lies in the foreground of the CMB is vital and is especially poignant at the present time due to the misidentification of polarised Galactic dust emission as a polarised CMB B-mode signal (BICEP2/Keck and Planck Collaborations et al., 2015a).

The following five subsections summarise the physical description of each microwave continuum emission and the resulting observable integrated spectrum.

1.2.1 The Cosmic Microwave Background

The CMB was discovered at a frequency of 4.08 GHz by Penzias and Wilson (1965). Initially, the CMB was considered by Penzias and Wilson to be an isotropic residual noise contribution of unknown origin. Soon after it was found that the temperature of this noise contribution matched the temperature of the CMB as predicted by a team at Princeton University (Dicke et al., 1965). The CMB is the remnant of the surface of last scattering, formed 300000 years after the Big Bang and corresponds to a black-body with a temperature of $T_{\rm CMB} = 2.7260 \pm 0.0013\,{\rm K}$ (Fixsen, 2009).

The first measurements of deviations in the CMB temperature, referred to as anisotropies, were first measured in the unpolarised CMB emission by the *COBE* satellite to be $\Delta T/T \approx 10^{-5}\,{\rm K}$ (Smoot et al., 1992). The CMB, along with Type Ia supernovae (e.g., Hicken et al., 2009; Betoule et al., 2014), galaxy clustering (e.g., Rozo et al., 2010) and gravitational weak lensing (e.g., Suyu et al., 2010), make up the suite of cosmological probes available to test cosmological models of the Universe. The CMB was crucial in the development of modern ΛCDM cosmology as it can constrain key cosmological parameters such as the balance between baryonic matter, dark matter and dark energy and models of inflation (Komatsu et al., 2011; Hinshaw et al., 2013; Planck Collaboration et al., 2014e).

The two key observables associated with the CMB are the temperature and linear polarised angular power spectra. The angular power spectrum defines the sky as a surface function that is composed of sums of spherical harmonics that describe different angular scales. Angular power spectra were originally devised for analysing the distribution of radio-sources (Yu and Peebles, 1969; Peebles and Hauser, 1974). The anisotropy of the CMB at the position θ and ϕ can be defined as,

$$\frac{\Delta T(\theta,\phi)}{T} = \sum_{\ell=0}^{\infty} \sum_{m=-\ell}^{+\ell} a_{\ell,m} Y_{\ell,m}(\theta,\phi), \tag{1.1}$$

where $Y_{\ell,m}(\theta,\phi)$ are the spherical harmonic functions and $a_{\ell,m}$ are the associated amplitudes. Equation 1.1 can be thought of as a 2D Fourier transform, where the $Y_{\ell,m}(\theta,\phi)$ terms replace the equivalent cosine and sine terms. As in the Fourier transform,

$Y_{\ell,m}(\theta,\phi)$ functions are all orthogonal, such that,

$$\int_{4\pi} Y_{\ell,m}(\theta,\phi)Y^*_{\ell',m'}(\theta,\phi)\mathrm{d}\Omega = \begin{cases} 1, & \text{if } \ell=\ell',\ m=m' \\ 0, & \text{otherwise} \end{cases} \tag{1.2}$$

where $Y^*_{\ell',m'}(\theta,\phi)$ is the conjugate of $Y_{\ell',m'}(\theta,\phi)$ and the integration is over the whole sky. Therefore, multiplying Equation 1.1 by the conjugate of $Y_{\ell,m}(\theta,\phi)$ and integrating, gives the required amplitudes as,

$$a_{\ell,m} = \int_{4\pi} \Delta T(\theta,\phi)Y^*_{\ell,m}(\theta,\phi)\mathrm{d}\Omega. \tag{1.3}$$

The angular power spectrum terms can then be derived from the amplitudes as the mean sum of squares $C_\ell = \langle|a_{\ell,m}|^2\rangle$, where each C_ℓ term has $2\ell+1$ associated amplitudes. The above method can be used to derive the CMB temperature power spectrum for an observation of the full sky, assuming the fluctuations are Gaussian.

Figure 1.3 shows the current best measurements of the temperature power spectrum from the latest *Planck* analysis (Planck Collaboration et al., 2015e). The multipole moments, ℓ, in the figure can be approximately related to the degree angular scales θ on the sky by $\theta \approx \ell/180^\circ$. This means that the small multipole moments in Figure 1.3 refer to the largest angular scales and vice versa for the largest multipole moments. The smallest scales in Figure 1.3 are supplemented by higher resolution observations by the Atacama Cosmology Telescope (ACT: Das et al., 2014) and the South Pole Telescope (SPT: Story et al., 2015).

The polarisation CMB signal can be analysed using the method above but when measuring a polarisation signal the orientation must also be considered. Typically, linearly polarised emission is decomposed into orthogonal states as described by the Stokes parameters Q and U. Stokes parameters are coordinate dependent but when measuring the intrinsic polarisation properties of the CMB, a coordinate independent definition is preferred. Therefore cosmologists have defined an orthogonal set of polarisation components known as curl-free E-modes and divergence-free B-modes (e.g., Zaldarriaga and Seljak, 1997). Figure 1.4 shows a set of CMB power spectra simulated using the `CAMB` software (Lewis and Challinor, 2011). The yellow line shows the temperature power-spectrum, while the blue and red lines show the CMB E-mode and B-mode spectra respectively. These simulated power-spectra show that both polarised spectra are typically several orders of magnitude below the temperature spectrum and

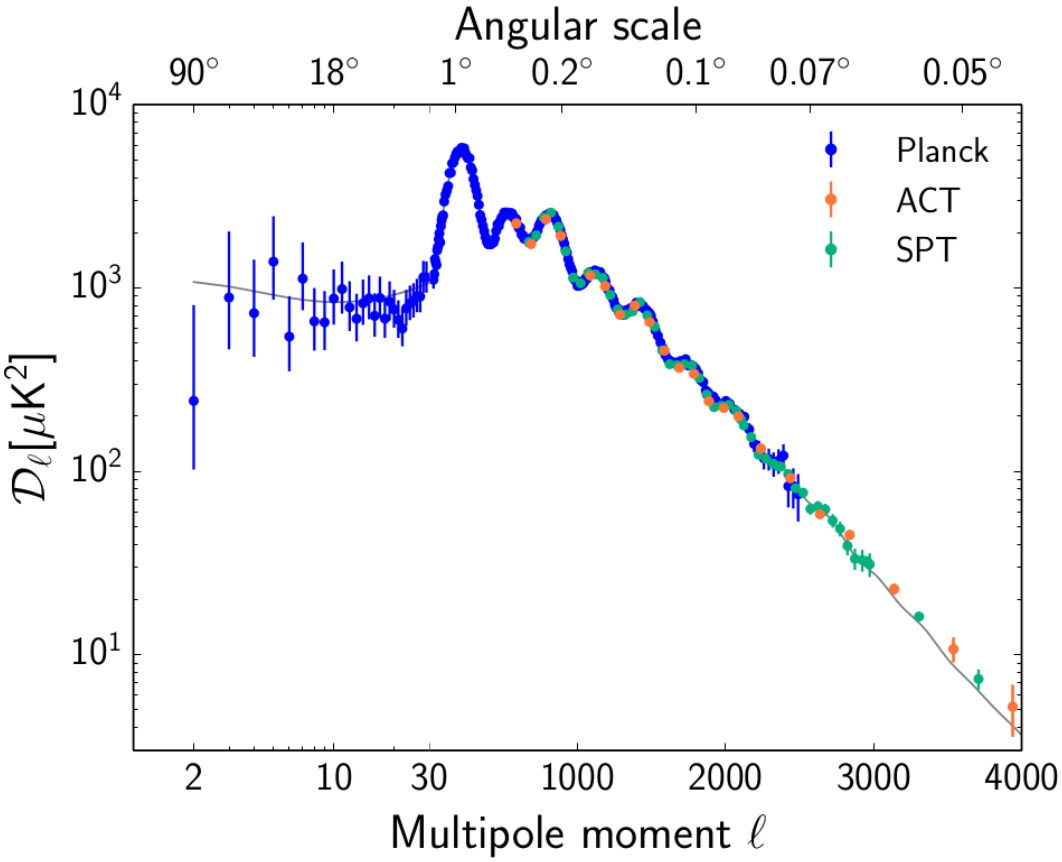

Figure 1.3: Observed temperature anisotropy angular power spectrum as found in the latest *Planck* release (Planck Collaboration et al., 2015e). Uncertainties increase at $\ell < 30$ due to cosmic variance. High resolution ground based observatories such as ACT and SPT provide constraints on the angular power spectrum for $\ell > 1000$.

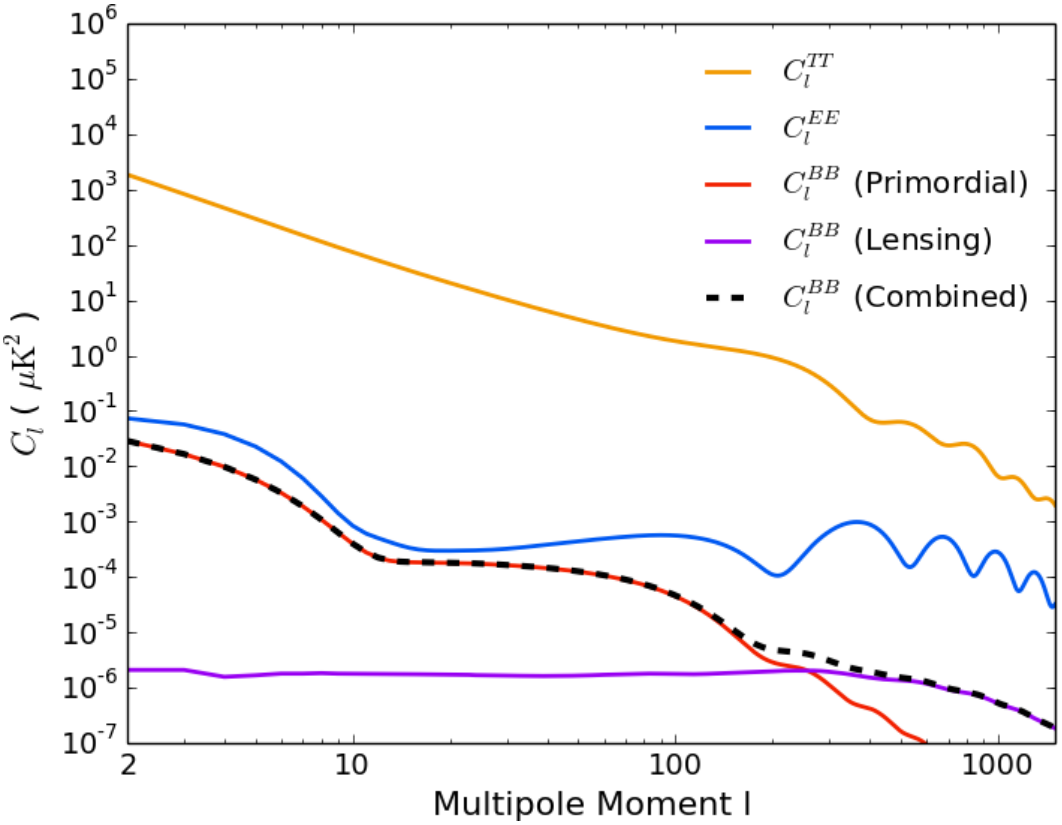

Figure 1.4: CMB angular power-spectra simulated using the `CAMB` (Lewis and Challinor, 2011) web interface at *lambda.gsfc.nasa.gov* using ΛCDM cosmology with a scalar-to-tensor ratio of $r = 1$. The primordial B-mode (BB) spectrum of the CMB is expected to be several orders of magnitude below the observed temperature spectrum and becomes dominated by lensing effects along the line-of-sight on small scales.

the B-mode signal is another order of magnitude below the E-mode spectrum. The scalar fluctuations that lead to the observed CMB temperature power-spectrum are expected to be the same as those that lead to the E-mode power spectrum. Therefore, measurements of the E-mode spectrum provide an independent measurement of the same cosmological parameters (Planck Collaboration et al., 2015e). The B-mode power-spectrum on the other hand (for large angular scales) is generated by tensor fluctuations thought to have arisen from primordial gravitational wave interactions during the inflationary epoch of the universe (e.g., Kamionkowski et al., 1997).

Detection of a B-mode power-spectrum would provide strong evidence that there was an early inflationary period in the history of the Universe (e.g., Dodelson et al., 2009). The critical parameter used to define the amplitude of the B-mode spectrum is

the tensor-to-scalar ratio (r), which is defined as the ratio between the amplitudes of the tensor and scalar CMB perturbations (Dodelson, 2003). Currently there have been no detections of the CMB B-mode signal however a 2σ upper limit of $r < 0.12$ has been set by combining measurements of baryonic acoustic oscillations, Type Ia supernovae and the latest *Planck* observations (BICEP2/Keck and Planck Collaborations et al., 2015b; Planck Collaboration et al., 2015e). Interestingly, a lower limit for the detectability of B-modes has also been estimated as $r \approx 10^{-4}$ (Knox and Song, 2002). At such a low value of r, the amplitude of the gravitational B-mode signal becomes confused with B-mode polarisation induced by second-order CMB density perturbations.

1.2.2 Thermal Bremsstrahlung Emission

Free-free emission from the unbound interactions of electrons in a Hydrogen or Helium plasma (Rybicki and Lightman, 1979). It is emitted from diffuse ionised gas in the interstellar medium (ISM) and HII regions. The gas in these regions is illuminated by nearby OB-type stars, meaning free-free emission typically correlates with the locations of star-forming regions along the plane of the Galaxy. Typically free-free emission only dominates the integrated emission of a galaxy within specific bright HII regions (Bennett et al., 2003).

The integrated flux density (S_{ff}) from a thermal free-free source can be modelled in the Rayleigh-Jeans regime as,

$$S_{ff} = \frac{2k_b T_{ff}}{\lambda^2}, \tag{1.4}$$

where k_b is the Boltzmann constant, λ is the observed wavelength, and T_{ff} is the brightness temperature of the free-free emission. The free-free emission brightness temperature is,

$$T_{ff} = T_e(1 - e^{\tau_{ff}}) \approx T_e \tau_{ff}, \tag{1.5}$$

for $\tau_{ff} \ll 1$ where τ_{ff} is the free-free optical depth and T_e is the electron temperature. For frequencies between $0.4-100\,\mathrm{GHz}$, which covers the QUIJOTE MFI bandpass, the free-free optical depth as derived in Dickinson et al. (2003) results in a free-free brightness temperature of,

$$T_{ff} = 8.235 \times 10^{-2} a(T_e, \nu) T_e^{-0.35} \nu_{\mathrm{GHz}}^{-2.1} (1 + 0.08) \mathrm{EM}_{\mathrm{pc\,cm^{-6}}}, \tag{1.6}$$

where EM is the emission measure, which is the integral of the electron density (n_e) squared along the line-of-sight (l), $\mathrm{EM} = \int \mathrm{n_e^2 dl}$. The factor of $(1 + 0.08)$ in Equation

1.6 accounts for the ionised Helium contribution. Equations 1.4 and 1.6 show that the free-free spectral energy density (SED) can be approximated by a power-law at GHz frequencies with a spectral index of $\alpha = -0.1$. Note that the factor $a(T_e, \nu)$ in Equation 1.6 does result in some weak spectral curvature dependent on frequency and electron temperature (Mezger and Henderson, 1967),

$$a(T_e, \nu) = 0.366 \nu_{\rm GHz}^{0.1} T_e^{-0.15} \times \left[\ln(4.995 \times 10^{-2} \nu_{\rm GHz}^{-1} + 1.5 \ln(T_e) \right]. \quad (1.7)$$

As free-free radio continuum emission is sub-dominant to other Galactic emission types such as synchrotron emission it is very challenging to uniquely isolate a map of radio free-free emission. Therefore, generating free-free emission maps of the whole sky relies upon the use of tracer emissions. At optical wavelengths the emission from the Hα transition (hydrogen $n = 3 \rightarrow 2$) can be used as a tracer of free-free (Dickinson et al., 2003). Optical Hα continuum maps, such as the composite all-sky free-free map shown in Figure 1.5, can be easily related to free-free emission at radio wavelengths in regions with a small Hα optical depth ($\tau_{\rm H\alpha} < 1$), which is limited to the sky far from the Galactic plane. The ratio of free-free to Hα emission is (Dickinson et al., 2003),

$$\frac{T_{ff}}{I_{\rm H\alpha}} = 8.396 \times 10^3 a(\nu, T_e)^{-2.1} T_4^{0.667} 10^{0.029/T_4} (1 + 0.08), \quad (1.8)$$

where $I_{\rm H\alpha}$ is the Hα brightness in Rayleighs (1 Rayleigh (R) $\equiv 10^6/4\pi$ photons s^{-1} cm^{-2} sr^{-1}), T_4 is the electron temperature in 10^4 K and all other parameters are as before.

In order to map free-free emission along the Galactic plane requires measuring an emission that traces HII regions but also passes through the dust within the Galaxy and is easily distinguished from other emission types. Hα radio recombination lines (RRL), which are very high Hα quantum number transitions, fit both criteria (e.g., Alves et al., 2012, 2015). The brightness temperature at the RRL centre, assuming the line is optically thin, is,

$$T_{\rm Line} = 1.92 \times 10^3 T_e^{-1.5} {\rm EM} \Delta\nu^{-1}, \quad (1.9)$$

where $\Delta\nu$ is the line-width in kHz. If both the line and continuum are assumed to be in local thermal equilibrium then the ratio of $T_{\rm Line}$ and the free-free continuum emission T_{ff} is found to be,

$$\frac{T_{\rm Line}}{T_{ff}} \Delta\nu = \frac{6.99 \times 10^3}{a(\nu, T_e)} \nu^{1.1} T_e^{-1.15} \frac{1}{1 + 0.08}. \quad (1.10)$$

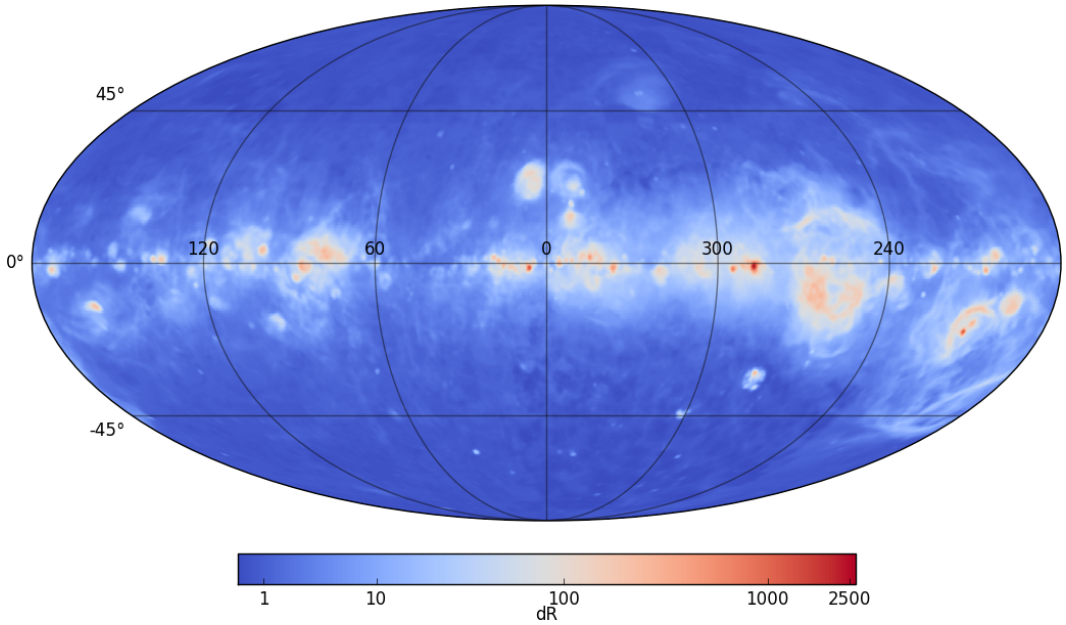

Figure 1.5: All-sky Hα map assembled by Finkbeiner (2003). Along the Galactic plane the optical Hα emission suffers from dust extinction along the line-of-sight. Some key Galactic plane structures such as Barnard's loop and M42 are clearly visibly on the *right* hand edge of the map. The image also shows how most of the Hα emitting gas is confined to the Galactic plane.

If the line emission is not in local thermal equilibrium then Equation 1.10 requires a more thorough treatment (see, e.g Rohlfs and Wilson, 2004). RRLs also have the benefit of providing Doppler information on the source being measured. This means that RRLs can also be used to ascertain the structure of the Galaxy (e.g. Georgelin and Georgelin, 1976; Paladini et al., 2004).

1.2.3 Synchrotron Emission

Synchrotron emission from the interaction of relativistic cosmic-ray electrons interacting with magnetic fields within the ISM (Rybicki and Lightman, 1979) dominates the integrated radio continuum of Milky Way type galaxies up to frequencies of $\nu \approx 30\,\mathrm{GHz}$ (Bennett et al., 2003). The primary source for the cosmic-ray electrons are supernovae remnants (SNR), but some may also be attributed to more exotic sources such as nearby pulsars (Atoyan et al., 1995), nearby active galactic nuclei or dark-matter annihilations (e.g. Garny et al., 2011). These electrons are then further accelerated by the shocks from other supernovae and from the radiation fields of the progenitor OB stars. As the typical lifetime of a cosmic-ray electron generated by a SNR is approximately 10^7 years (Garcia-Munoz et al., 1977), synchrotron can be a useful probe of recent star formation within a galaxy (e.g., Murphy et al., 2011).

The physical mechanism behind synchrotron emission has been understood for decades and detailed explanations can be found in the classic text Rybicki and Lightman (1979) and the more recent treatment can be found in Longair (2011). Here only a few choice equations will be taken from these texts in order to give a physical understanding of synchrotron emission. Synchrotron emission is generated from the gyration of relativistic cosmic-ray electrons. A single electron will, in this situation, emit a tight beam of photons distributed around a critical frequency (ν_c),

$$\nu_c \approx \left(\frac{E}{m_e c^2}\right)^2 \frac{eB}{2\pi m_e}\sin(\alpha), \tag{1.11}$$

where E is the energy of the electron, B is the magnetic field, m_e is the electron mass, e is the electron charge and α is the angle between the electron axis of rotation with the axis of the magnetic field. The total emissivity of many electrons will be proportional to the integration of the total power emitted per electron and the energy distribution of cosmic-ray electrons ($N(E)$),

$$\varepsilon(\nu) \propto -\frac{\mathrm{dE}}{\mathrm{dt}} N(E)\mathrm{dE}, \tag{1.12}$$

where $N(E)$ is often approximated to be a power-law distribution over a given range of energies, with a spectral index δ, of the form,

$$N(E) \propto E^{\delta}. \tag{1.13}$$

The emitted power per electron in Equation 1.12 is defined as,

$$-\frac{\mathrm{dE}}{\mathrm{dt}} \propto \nu_c B^2 \sin^2(\alpha), \tag{1.14}$$

where all the parameters are as before. Finally, integrating Equation 1.12 using the change of variable,

$$\mathrm{dE} \propto \nu^{-1/2} \mathrm{d}\nu, \tag{1.15}$$

the emissivity of the synchrotron emission per unit volume along a line-of-sight is

$$\varepsilon(\nu) \propto B^{(\delta+1)/2} \nu^{-(\delta-1)/2}, \tag{1.16}$$

which is a power-law relationship in the observed frequency. The previous discussion shows that the observed synchrotron emission brightness is dependent on two parameters, the local magnetic field strength and electron energy distribution. The observed synchrotron spectral energy distribution (SED) can then be described as a simple power-law of the form,

$$S_{\mathrm{sync}}(\nu) = S_0 \nu^{\alpha}, \tag{1.17}$$

where $S_{\mathrm{sync}}(\nu)$ is the measured synchrotron flux density, S_0 is an arbitrary constant that absorbs the magnetic field strength and α is the observed spectral-index of the emission related to δ by,

$$\alpha = (1 - \delta)/2 \tag{1.18}$$

The spectral index of Galactic cosmic-ray electrons has been measured by many space-based and balloon-based experiments (three recent space-based experiments are Aguilar et al. (AMS: 2002), Adriani et al. (PAMELA: 2009) and Atwood et al. (Fermi-LAT: 2009)). The mean all-sky spectral index of cosmic-ray electrons has been found to be 3.18 ± 0.05 by PAMELA (Adriani et al., 2011) and 3.19 ± 0.07 by Fermi-LAT (Ackermann et al., 2012). However, the generation of Galactic synchrotron emission depends on the mean all-sky spectral index of electron-positron energy spectrum that has been found to be 3.08 ± 0.05 (Abdo et al., 2009; Ackermann et al., 2010). Variations in the spectral index are expected because of the non-uniformity of the Galactic

magnetic field and the re-energisation of the cosmic-ray energy distribution from SNR shocks.

The observed diffuse synchrotron emission at radio frequencies is distributed across the entire sky as shown in the point-source subtracted Haslam 408 MHz all-sky map (Haslam et al., 1982; Remazeilles et al., 2015) in Figure 1.6. As the figure shows, most of the synchrotron emission from the Galaxy is concentrated along the Galactic plane but large scale features such as Loop I stretch over around half of the *North* Galactic sky. The synchrotron spectral-index α is found to vary across the sky between -1.5 (steep) and 0 (flat) (e.g., Lawson et al., 1987; Bennett et al., 2003; Platania et al., 2003). Figure 1.7 shows the distribution of synchrotron spectral-indices (Platania et al., 2003) as derived from the 408 MHz map and two other low frequency sky surveys (Reich and Reich, 1986; Jonas et al., 1998). These spectral-index measurements, and others derived from specific regions such as the North Celestial Pole (de Oliveira-Costa et al., 2008a), demonstrate that there is the expected frequency dependence on the synchrotron spectral index between 408 MHz and 33 GHz due to radiative losses. Note however, many of these results rely on the same low frequency sky-maps such as the Haslam 408 MHz map shown in Figure 1.6, a 1.420 GHz sky-map by Reich and Reich (1986) and a 2.326 GHz sky-map by Jonas et al. (1998). Higher frequencies around 30 GHz rely on *WMAP* or *Planck* observations. Experiments such as the QUIJOTE Multi-Frequency Instrument, which observes the Northern hemisphere between 10 GHz and 20 GHz, and the C-BASS experiment (King et al., 2010), which will observe the whole sky at 5 GHz, will be ideal for providing new insight into the synchrotron spectral-index distribution of the Galaxy (e.g, Irfan et al., 2015).

Synchrotron emission also has an intrinsic linear polarisation component that is generated perpendicular to the magnetic field lines along the line-of-sight. The polarisation fraction (Π) of the synchrotron emission is related to the cosmic-ray energy distribution spectral-index δ by (Rybicki and Lightman, 1979; Longair, 2011),

$$\Pi = \frac{\delta + 1}{\delta + \frac{7}{3}}, \tag{1.19}$$

which for the reported $\delta = 3.08$ from the previous page implies a polarisation fraction of approximately 75 %. On the sky this polarisation fraction is observed to be lower due to mixing between different magnetic fields integrated within the telescope beam, along the line-of-sight. However, some regions are observed to have very high polarisation fractions such as the North Polar Spur with a polarisation fraction of $\approx 40\%$

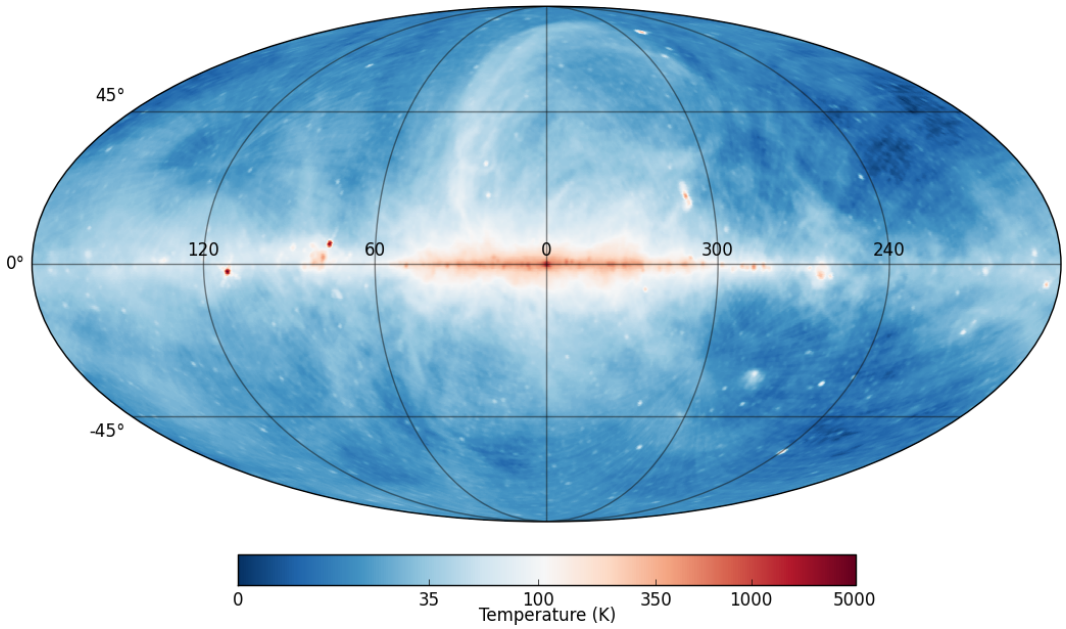

Figure 1.6: Reprocessed Haslam 408 MHz all-sky map from Remazeilles et al. (2015). The temperatures have been scaled logarithmically to emphasise the structure of the diffuse synchrotron emission.

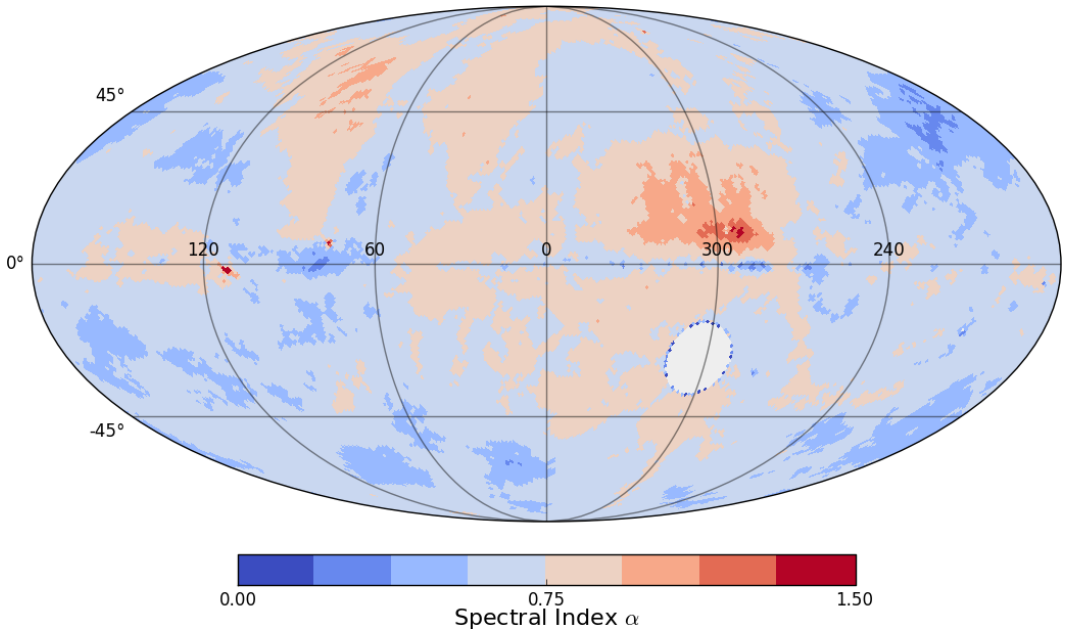

Figure 1.7: Synchrotron spectral-index map from Platania et al. (2003) derived using the 408 MHz (Haslam et al., 1982), 1.420 GHz (Reich and Reich, 1986) and 2.326 GHz (Jonas et al., 1998) all-sky maps. The map has been regridded into the Galactic coordinate system and the spectral-index changed to reflect Equation 1.17 instead of the temperature spectral-index quoted in Platania et al. (2003).

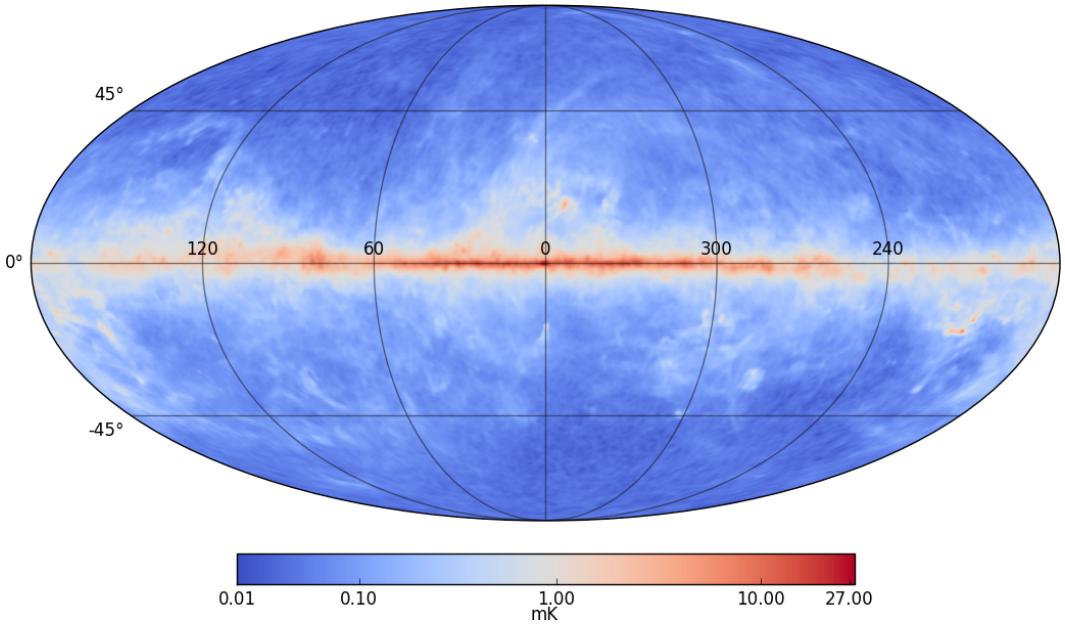

Figure 1.8: The *Planck* 353 GHz HFI all-sky map, which is largely tracing the cold, large dust grains in thermal equilibrium with the local radiation field.

(Macellari et al., 2011; Vidal et al., 2015). As synchrotron emission can potentially have such a high polarisation fraction it is a major foreground emission systematic contribution to measurements of polarised emission from the CMB (Dunkley et al., 2009). For this reason constraints on variations of Galactic synchrotron emission are major science drivers behind experiments such as the QUIJOTE MFI, C-BASS and S-PASS experiments.

1.2.4 Thermal Dust Emission

Dust is ubiquitous throughout the ISM, and affects the entire spectrum of the Galaxy. One critical role that dust serves is the absorption of energy from light emitted from stars then emitting that energy as infrared emission. The effect of dust on short-wavelengths is immediately apparent when viewing the Milky Way by eye, revealing the clumpy obscuration of the light originating from the embedded stars. Today, the large-scale distribution of Galactic thermal dust emission is known better than ever before thanks to instruments like the *Planck* high frequency instrument (HFI). Figure 1.8 shows the current all-sky HFI map at 353 GHz, which maps the distribution of cold dust in thermal equilibrium with the ISM.

Dust grain particles are generally modelled as belonging to one of three regimes: Large Grains with radius $a > 50\,\text{Å}$, very small grains (VSGs) with $a < 50\,\text{Å}$ and polycyclic aromatic hydrocarbon (PAH) molecules that contain $< 10^3$ carbon atoms (see e.g., Desert et al., 1990; Weingartner and Draine, 2001). The large dust grains are generally considered to be in thermal equilibrium with the interstellar radiation field and have grain temperatures of approximately 20 K (Mezger et al., 1982; Planck Collaboration et al., 2014b). The smaller grains (including the PAHs) are thought to be energised by single photons and as such have much higher grain temperatures that can be upwards of hundreds of Kelvin (Draine and Li, 2001). The grain composition of the ISM is identified as being composed of carbonaceous grains and silicate grains (Agladze et al., 1996; Mennella et al., 1998). Models of the grain size distribution of the silicate and carbonaceous grains are shown in Figure 1.9. These grain size distribution models were derived from observations of the Large Maganellic Cloud (Weingartner and Draine, 2001).

The integrated emission from an optically thin column of dust along the line-of-sight in the far-infrared between approximately 100 GHz and 6000 GHz is a modified black-body of the form (e.g., Planck Collaboration et al., 2014b),

$$S_{\text{dust}} = B_\nu(T_D)\tau_\nu \tag{1.20}$$

where the observed flux density of the dust column (S_{dust}) is the product of a black-body function B_ν at dust temperature T_D, and τ_ν is the infrared optical depth. The infrared opacities have a power-law form that can be parameterised using an emissivity index β as

$$\tau_\nu = \tau_{\nu_0}\left(\frac{\nu}{\nu_0}\right)^\beta, \tag{1.21}$$

where τ_{ν_0} is the infrared opacity at the frequency ν_0. The choice of the normalising frequency ν_0 is arbitrary and a commonly used value is 1200 GHz ($\lambda \approx 250\mu$m). The optical depth is related to the hydrogen column density N_H and the mean whole sky dust opacity $\sigma_e(\nu)$ by,

$$\tau_{\nu_0} = N_H\sigma_e(\nu_0). \tag{1.22}$$

Equation 1.20 is dominated by large grains with sizes $> 10\,nm$ with dust temperatures ranging from approximately 17 to 24 K. The emissivity index parameter has a typical value of $\beta \approx 1.8$ and an optical depth of 2×10^{-4} at 1200 GHz (Planck Collaboration et al., 2014a).

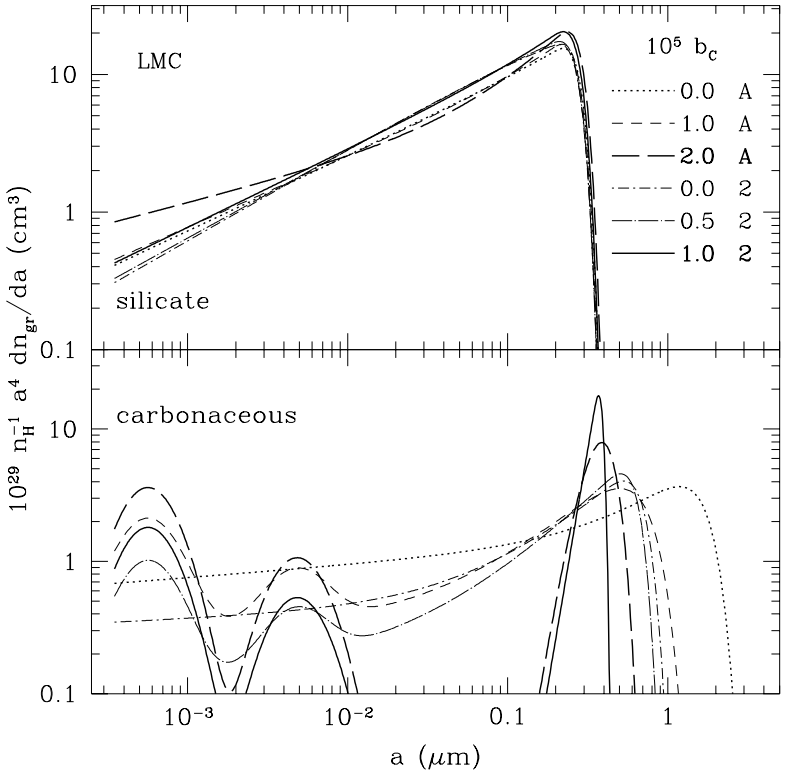

Figure 1.9: Silicate and carbonaceous dust grain size distributions derived for the nearby satellite galaxy the Large Maganellic Cloud taken from Weingartner and Draine (2001). The two log-normal bumps in the carbonaceous grain distribution are from the expected extra abundances of PAH molecules for small dust grains.

Polarisation due to thermal dust emission has been known for some time from measurements of the polarised light originating from stars obscured by dust (Gold, 1952). At far infra-red wavelengths, described by the emission model Equation 1.20, polarised emission has been observed by Archeops (Ponthieu and Archeops Collaboration, 2003) and *WMAP* (Gold et al., 2009), and could have a linear polarisation fraction up to approximately $\Pi = 10\,\%$ (Draine and Fraisse, 2009). However, the recent *Planck* results set a new upper limit for the polarisation fraction of thermal dust to be $\Pi = 19.8\%$ (Planck Collaboration et al., 2015b).

1.2.5 Spinning Dust Emission

After the first tentative hints of spinning dust emission emerged from the *COBE* all-sky observations as correlations between Galactic radio and dust emission, a wealth of supporting observational evidence began to build over the subsequent two decades. Today, evidence for spinning dust has been found in a large range of environments by many different instruments that include: HII regions (Dickinson et al., 2006, 2007, 2009; Todorović et al., 2010; Tibbs et al., 2012), Lynds dark nebulae (Casassus et al., 2006; AMI Consortium et al., 2009; Vidal et al., 2011, see also Chapter 7), molecular clouds (Tibbs et al., 2013b), a supernova remnant (Scaife et al., 2007), HII complexes (Irfan et al., 2015; Demetroullas et al., 2015), one external Galaxy (Murphy et al., 2010) and in the diffuse ISM at mid-to-high Galactic latitudes (Davies et al., 2006; Ghosh et al., 2012; Peel et al., 2012).

When first detected (Kogut et al., 1996; Leitch et al., 1997; de Oliveira-Costa et al., 1998), spinning dust emission from electric dipoles was referred to as *anomalous microwave emission* (AME). Several alternative mechanisms were proposed to describe AME, such as shock-heated HII (Leitch et al., 1997), which was discounted by energetic arguments (Draine and Lazarian, 1998a); spinning dust emission from magnetic dipoles (Draine and Lazarian, 1999), which has been discounted largely due to the observe low polarisation fraction of spinning dust regions (e.g. Rubiño-Martín et al., 2012); and ultra-compact HII (UCHII) regions, which may account for some compact spinning dust regions close to the Galactic plane but cannot explain the diffuse large-scale structure observed. The driving mechanism behind AME is still not entirely clear, with some evidence still in favour of magnetic dust grains (Hensley and Draine, 2015) and even HII shock-fronts (Paladini et al., 2015). However, given the body evidence in

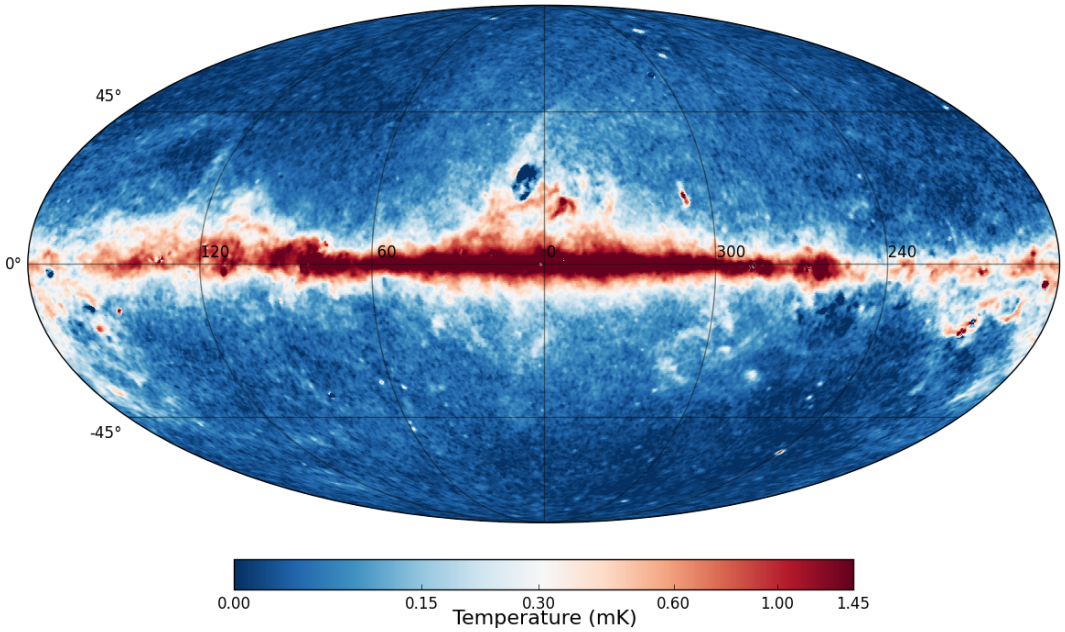

Figure 1.10: All-sky mollweide projection map in Galactic coordinates showing the distribution of spinning dust throughout the Galaxy at 28.4 GHz derived using the `Commander` algorithm, *Planck* and ancillary multi-frequency observations.

the previous paragraph, the results to be discussed in Chapter 7, and the nature of the regions that will be discussed, the *author* will refer to AME as spinning dust emission from here forward.

Observations from the *Planck* satellite in recent years have provided a wealth of new information on spinning dust emission. First, in Planck Collaboration Early XX (2011) definitive evidence for spinning dust emission was given for two previously identified spinning dust candidates, the Perseus and ρ-Ophiuchus molecular clouds (Watson et al., 2005; Casassus et al., 2008). A later *Planck* study looked at 98 discrete Galactic regions for evidence of spinning dust emission, of which 27 were deemed $5\,\sigma$ detections or better (Planck Collaboration et al., 2014d). Within the inner disk of the Galaxy ($300 < l < 60$ and $|b| < 0.5$), model fitting was used to find that spinning dust could contribute up to 50 % of the total observed emission at 28.4 GHz (Planck Collaboration et al., 2015c). Planck Collaboration et al. (2015d) derived an all-sky map of spinning dust emission using the Gibbs-sampling component separation algorithm `Commander` (Eriksen et al., 2008), shown in Figure 1.10, which revealed strong correlations between spinning dust and several other Galactic components at high Galactic latitudes.

The radio-dust correlations identified by *COBE* led to the first model for spinning

dust emission by Draine and Lazarian (1998a). The model proposes that the rapid rotation of the electric dipoles associated with the smallest dust grains in the ISM (PAHs and VSGs) can generate microwave frequency emission that peaks between 10 to 60 GHz. Since the Draine and Lazarian (1998a) model, significant refinements have been made to models of electric dipole spinning dust emission and now include: rotational grain excitation, a number of different damping processes, and grain rotation around an axis that does not have greatest inertia (Ali-Haïmoud et al., 2009; Hoang et al., 2010; Ysard et al., 2010; Silsbee et al., 2011). Many of these features are incorporated into the freely available Interactive Data Language (`IDL`) spinning dust model code, SpDust.

The total power emitted by a grain carrying an electric dipole grain is (Ali-Haïmoud et al., 2009)

$$P = \frac{2}{3}\frac{\mu^2\omega^4}{c^3}, \tag{1.23}$$

where P is the power, μ is the dipole moment of the grain, c is the speed of light, and ω describes the angular rotation rate of the grain. The frequency of the emitted photon is directly proportional to grain rotation rate. The distribution of rotational frequencies per grain at size a with a temperature T can be described under certain conditions as a Maxwell-Boltzmann distribution of the form

$$f_a(\omega) = \left(\frac{1}{2\pi x^2}\right)^{\frac{3}{2}} 4\pi\omega^2 e^{-\frac{\omega^2}{2x^2}}, \tag{1.24}$$

where $x = \sqrt{kT/I}$. The term k is the Boltzmann constant and I is the moment of inertia of the grain. Assuming that the grains are described well as flat disks or spheres, then the moment of inertia for grains of mass $m_{\rm g}$ is $I \propto m_{\rm g} a^2$. Taking the derivative of Equation 1.24 and finding where it is zero, results in an expression for the peak frequency as

$$\nu_{\rm peak} = \frac{1}{2\pi}\sqrt{\frac{2kT}{I}}. \tag{1.25}$$

Assuming typical grain sizes from Figure 1.9, and a range of grain temperature between 10 and 1000 K, the peak frequency of spinning dust grains is found to lie in the range $(10-100)\frac{a^{-1}}{\rm nm}$ GHz, decreasing linearly with grain size. As Equation 1.23 has the emitted power being proportional to ω^4, the smallest grains that rotate fastest dominate the generation of spinning dust emission. Note that this argument is extremely simplified but is still representative and should give an intuition as to how spinning dust

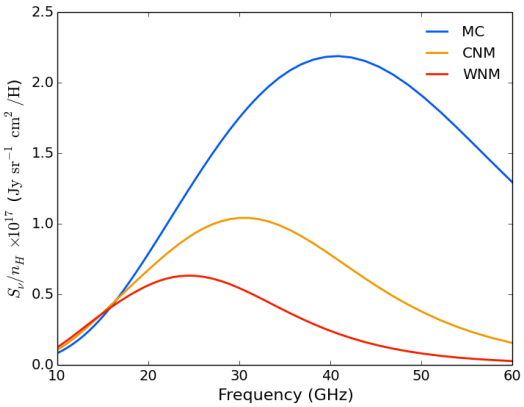

Figure 1.11: Three model spinning dust curves generated using the SpDust code using input parameters for the WNM, CNM and molecular clouds from Draine and Lazarian (1998a).

emission is generated. Figure 1.11 shows examples of several different spinning dust spectra derived for the warm neutral medium (WNM), cold neutral medium (CNM) and molecular cloud environments generated using the SpDust model `IDL` code. Note that the peak of the spinning dust spectrum is between 10 and 100 GHz.

As spinning dust grains are very small ($\ll 0.1\mu$m), grain alignment efficiency will be low implying that the polarisation fraction should be small. To date, no confirmed detection of polarised spinning dust emission has been made. The lowest upper limit on polarisation was set at $< 1\,\%$ using *WMAP* 7-year measurements of the Perseus molecular cloud (Battistelli et al., 2006; López-Caraballo et al., 2011; Dickinson et al., 2011). Similar upper limits have also been set for the ρ-Ophiuchus molecular cloud (Dickinson et al., 2011), LDN 1622 (Mason et al., 2009), LPH96 (Dickinson et al., 2006), the Helix planetary nebula (Casassus et al., 2004) and in the diffuse Galactic medium (Macellari et al., 2011). A review of spinning dust polarisation emission can be found in Rubiño-Martín et al. (2012). The most recent measurement of polarised spinning dust emission was of the HII region RCW175 at 21.5 GHz, which was reported by Battistelli et al. (2015) to have a polarisation fraction of 2.2%. However, Planck Collaboration et al. (2015d) proposed that much of the reported spinning dust polarisation in RCW175 could be due to synchrotron emission contamination. Models of spinning dust predict a polarisation fraction between 5 % (Lazarian and Draine, 2000) and 1 % (Hoang et al., 2013), which is in agreement with the currently available observations.

There are still many unanswered questions that remain regarding the nature and

ubiquity of spinning dust throughout the Galaxy. For low Galactic latitudes, the QUIJOTE Multi-Frequency Instrument (MFI) wide-survey of the Northern sky is well placed for constraining the rising spectrum between 10 to 30 GHz, a crucial part in distinguishing between spinning dust models and other Galactic emission.

1.3 Thesis Summary

This thesis describes the development of new methods of calibration and data reduction to address the challenges of modern single-dish radio observations over the frequency range of 5 to 20 GHz. A key development is an advanced map-making tool for removing correlated noise from radio time-ordered-data. This map-maker is shown to have the flexibility to be applied to the QUIJOTE MFI wide-survey observations of the whole Northern sky, as well as tight, arcminute resolution raster observations from the Robert C. Byrd Green Bank Telescope (GBT). The maps derived from these tools are used to investigate the prevalence of spinning dust emission throughout the Galaxy, which is crucial to studies of the CMB as well as the quantification of the integrated emission of the Galaxy.

- Chapter 2: An overview of the entire QUIJOTE project, scientific goals and observations summary.

- Chapter 3: This Chapter will describe the processes involved in calibrating the raw MFI voltages outputs on to a standard brightness temperature scale.

- Chapter 4: This Chapter will describe the methods used to minimise and remove various forms of poor MFI data and RFI contamination.

- Chapter 5: A description of the *authors* Destriping and Maximum-Likelihood map-making methods used to remove correlated *1/f* noise from TOD, applied both to the MFI and GBT.

- Chapter 6: A first look at the MFI wide-survey maps. This includes tests of the calibration and noise properties of the maps and early science possibilities with a specific focus on spinning dust emission in the Galaxy.

- Chapter 7: An investigation into the anomalous microwave emission originating from LDN 1622 at 5 and 14 GHz using the 100 m Robert C. Byrd Green Bank telescope.

Chapter 2

The QUIJOTE Project

> "To try to be happy is to try to build a machine with no other specification than that it shall run noiselessly."
>
> Robert J. Oppenheimer, *14 October 1929*

This Chapter will begin with an overview of the entire QUIJOTE project, including the collaborating institutions, scientific goals and a summary of the QUIJOTE instrumentation. The subsequent Sections will discuss the specifics of each phase of the QUIJOTE project and the current status of the project as of June 2015.

2.1 QUIJOTE Project Overview

The QUI-Joint Tenerife Experiment (QUIJOTE)[1] is a collaboration between over 50 researchers and engineers from the Jodrell Bank Centre for Astrophysics (JBCA); Instituto de Astrofísica de Canarias, Tenerife, Spain (IAC); Instituto de Física de Cantabria, Santander, Spain (IFCA); University of Cambridge, England; Departamento Ingeniería de Comunicaciones (DICOM) and IDOM. The primary mission goal of QUIJOTE is to measure the polarised CMB and polarised Galactic foregrounds, such as synchrotron emission, between the frequencies 10 to 42 GHz with a Full-Width Half-Maximum (FWHM) resolution of ≈ 1 degree.

The project is split into two phases consisting of three instruments, mounted in two identical alt-azimuth telescopes. The multi-frequency instrument (hereafter, MFI) was

[1]The QUIJOTE project is funded, in part, by an Exploring the Physics of Inflation (EPI) consolider grant.

Table 2.1: Summary of key instrumental parameters for the three QUIJOTE instruments. Values stated for the MFI have been derived from observations and values stated for the TGI and FGI are predicted values.

	MFI				TGI	FGI
Central Frequency (GHz)	11	13	17	19	31	42
Bandwidth (GHz)	2	2	2	2	10	10
Number of horns	2	2	2	2	31	31
Channels per horn	4	4	4	4	4	4
Beam FWHM (degrees)	0.94	0.94	0.64	0.64	0.37	0.28
T_{sys} (K)	~ 60	~ 47	~ 48	~ 47	35	45
NEP (μK s$^{1/2}$)	1336	1051	1073	1040	50	60
Sensitivity (Jy s$^{1/2}$)	1.7	1.4	1.5	1.1	0.06	0.06

the first to be completed and saw first-light in November 2012. The MFI is an intensity and polarised Galactic foregrounds experiment observing the frequency range of 10 to 20 GHz. The primary scientific objective of the MFI is to measure polarised, diffuse Galactic synchrotron in three regions of the sky far from the Galactic plane. The MFI measurements of Galactic emission will later be used by the QUIJOTE instruments at 31 GHz and 42 GHz to remove the polarised synchrotron foreground contamination from the polarised CMB signal. The 31 GHz instrument (the thirty-GHz instrument or TGI) at the current time has been installed at the observatory and will begin commissioning during autumn 2015. The 42 GHz instrument (the forty-GHz instrument or FGI) is expected to be operational sometime in 2016. Table 2.1 provides a summary of the sensitivities, system temperatures, Full-Width Half-Maximum (FWHM) resolutions and other instrumental parameters.

Both QUIJOTE telescopes are situated in the Northern hemisphere. The observing site is the Izaña observatory, Tenerife, at a longitude of 16°30′35″W and a latitude of 28°18′00″N. The observing site has an altitude of ~ 2400 m, which reduces the effects of atmospheric scattering and absorption compared to sea-level observatories. The telescopes are kept inside the enclosure shown in Figure 2.1. The enclosure is orientated *North* to *South* and can be remotely opened or closed. The enclosure limits the elevation range of the telescopes to > 30 degrees. The resulting potentially observable range of Declinations is -32 to $+88$ degrees.

Figure 2.1: The QUIJOTE enclosure at the Izaña observatory. Image credit: QUIJOTE Collaboration.

2.2 Phase I and the MFI

The first phase of the QUIJOTE project includes the construction and operation of a single alt-azimuth mounted telescope (QT1) and the MFI. The MFI is a composite of four coherent pseudo-correlation microwave receivers operating at four frequency bands between 10 and 20 GHz. The goal of the first phase is to characterise both the intensity and polarisation components of diffuse Galactic emission in the Northern sky at ~ 1 degree resolution. A 20000 degree^2 survey with a target to reach a sensitivity of 20 μK degree^{-2} in 5000 hours will be conducted. The data from the survey, coupled with the MFI frequency range, makes the MFI results a perfect complement to other major survey experiments such as *Planck* at frequencies greater than 30 GHz (Planck Collaboration et al., 2014c) and C-BASS at a frequency of 5 GHz (King et al., 2010). The MFI also serves as a precursor for the later Phase II instruments, which are primarily focused on measuring polarised CMB emission in several regions of low Galactic foreground emission covering ~ 3000 degree^2. The goal of the MFI is to measure the polarised Galactic synchrotron emission and estimate the foreground contamination at 31 and 42 GHz with a sensitivity of 5 μK degree^{-2}.

Figure 2.2 shows the first QUIJOTE telescope, QT1. Construction of the QT1

Figure 2.2: QUIJOTE QT1 alt-azimuth mounted telescope inside the dome at the Izaña observatory pointing towards the zenith position. The MFI receiver BEM is stored in the cabinets on the *right* side of QT1. Between the BEM cabinets is the MFI FEM and cryostat.

mount was outsourced to the industry firm IDOM[2]. The main design objectives of QT1 were dictated by the planned observing strategies. In order to conduct the Northern sky survey, QT1 can maintain stable continuous azimuthal rotation rate of 12 degree second^{-1}. The high rate of rotation helps to reduce the mixing of correlated noise with celestial signal, which will be discussed in Chapter 3. QT1 can also perform sky or azimuthal raster modes and tracking mode observations; a summary of the different observing modes can be found in Appendix A. The optical design is an offset Gregorian-Dragone scheme composed of a 2.25 m primary reflector and a 1.85 m secondary reflector. The offset Gregorian-Dragone optics minimises cross-polarisation to the -35 dB level and should produce more symmetric main beam shapes over a wider focal plane area. The optics are under-illuminated and contained within an radio absorbing shell to minimise contamination from radio-frequency interference and ground-spillover (Pérez-de-Taoro et al., 2014; Gomez et al., 2010).

Figure 2.3 show the MFI feed horns, front end module (FEM) and cryostat before installation into QT1. The four 10 to 20 GHz feed horns are distributed off-centre and can be seen at the front of the MFI in the figure. The smaller central feed horn was originally intended for a 30 GHz receiver, which was to be a testbed for the TGI and FGI receiver chain designs. Unfortunately, during the commissioning period, the MFI cryostat was found to not be able to achieve the desired 20 K cooling. As the 30 GHz feed was considered not crucial to the MFI mission goals it was therefore replaced to reduce the mass required to be cooled by the cryostat and was replaced with an improved cryostat coldhead. The cryostat can be seen in Figure 2.3 as the black cylinder towards the back of the MFI.

Figure 2.4 shows a schematic of an MFI receiver chain for one frequency. All components from the feed horn through to the cryogenically cooled 20 K FEM stage use waveguide components. The MFI feed horn propagates the incoming waves using the TM_{01} waveguide mode. The wave position angle orientation is then set by passing through the polar modulator. In the original MFI design the polar modulators at the front end of each horn were to rotate continuously. However, during commissioning of the MFI it was found that continuous rotation resulted in an increase in the cryostat temperature. Therefore in practice the polar modulators were set in one of several fixed positions prior to an observation and recovery of the polarisation signal was achieved by combining many observations during data processing. After the polar

[2]http://www.idom.com/

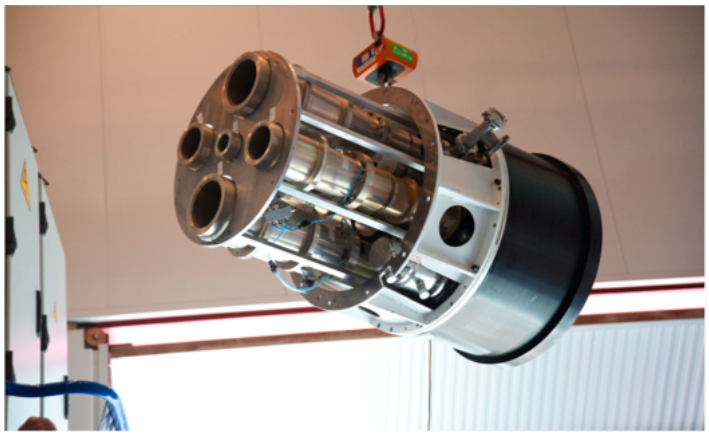

Figure 2.3: The MFI receiver before installation at the observatory. The black cylinder at the back of the MFI is the 20 K cryostat that houses the MFI LNAs. At the front end, the five original MFI receiver feed horns can be seen. The 10 to 20 GHz feeds are the four horns distributed off-centre. The smallest central horn was originally a 30 GHz feed that was removed before commissioning began. Image courtesy of the QUIJOTE Collaboration.

modulator, a ortho-mode transducer (OMT) (Cano et al., 2010) splits the measured signal into two orthogonal linear polarisation channels. The channels are amplified by two $6-20$ GHz monolithic microwave integrated circuit (MMIC) low-noise amplifiers (LNAs) with gains of 30 dB and noise temperatures <10 K (Pérez-de-Taoro et al., 2014). After the LNAs the channels enter the backend module (BEM). Note that the FEM amplifies the full 4 GHz bandpass, in the BEM the bandpass is split into two 2 GHz bandpasses that are 11 and 13 GHz, or 17 and 19 GHz depending on the receiver feed. After further amplification in the BEM, the channels are split again. Two of these channels are outputted directly and these are referred to as the uncorrelated channels. The other two split channels are passed through a 180 degree hybrid correlator circuit. Inside the hybrid both linear polarisations are added in and out of phase. The channels that have passed through the hybrid have correlated noise properties from the FEM LNAs in both channels and are therefore referred to as the correlated channels. The correlated channels have polarisation angles orthogonal to each other and are offset by 45 degrees from the uncorrelated channels. There are four MFI feeds, each of which has two frequencies with four different outputs, giving a total of 32 MFI output channels.

The outputs from the MFI for the uncorrelated and correlated channels for a single

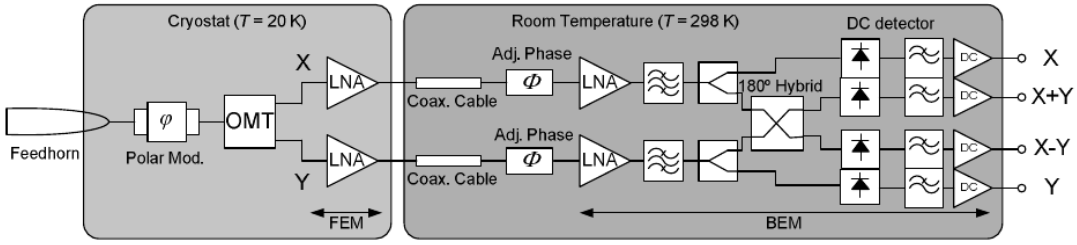

Figure 2.4: Schematic of the MFI receiver chain during Epoch 1 for a single frequency band. The OMT splits the incoming emission into two separate receiver chains to be amplified. There are four receiver outputs, two from the raw receiver chains and two that have been correlated using a 180 degree hybrid. Image courtesy of the QUIJOTE Collaboration.

frequency are defined as:

$$E_x^2 = \frac{1}{2}\left[I - Q\cos(4\psi) + U\sin(4\psi)\right], \tag{2.1}$$

$$E_y^2 = \frac{1}{2}\left[I + Q\cos(4\psi) - U\sin(4\psi)\right], \tag{2.2}$$

$$E_{x+y}^2 = \frac{1}{2}\left[I + Q\sin(4\psi) + U\cos(4\psi)\right], \tag{2.3}$$

$$E_{x-y}^2 = \frac{1}{2}\left[I - Q\sin(4\psi) - U\cos(4\psi)\right], \tag{2.4}$$

where E_x^2 and E_y^2 are the apparent x and y components of the incoming signal measured at the uncorrelated channel outputs. The outputs at the correlated channels are E_{x+y}^2 and E_{x-y}^2, which are the phase rotated sum and difference of the x and y components. The polar modulator angle of each feed is described by ψ. The terms I, Q and U describe the total intensity and linear polarisation Stokes parameters. To isolate the intensity component of an observed emission uncorrelated or correlated channel pairs must be summed. To isolate a single polarisation component the channel pairs are differenced. To isolate Q and U requires stacking many observations of a source with different ψ angles.

2.3 Phase II

Phase II of the QUIJOTE project is focused on polarised CMB science. Two instruments will be commissioned: the TGI, operating in the frequency band $26-36$ GHz and the FGI, operating in the frequency band $36-46$ GHz. Phase II also includes a

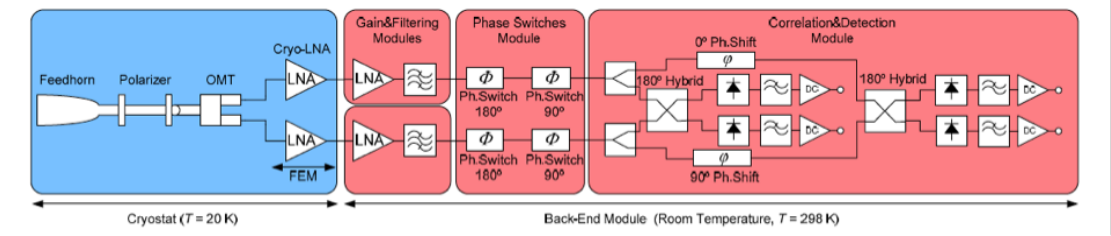

Figure 2.5: Schematic of the TGI receiver chain for a single frequency band. The crucial difference between the TGI and FGI receiver chains is the omission of the rotating polar modulator in favour of a fixed polariser. The use of two hybrid circuits and 90 degree phase switches means that the TGI and FGI will have instantaneous recovery of the linear polarisation Stokes parameters. Image credit: QUIJOTE Collaboration.

second QUIJOTE telescope (QT2) that has already been constructed and has near identical specifications to QT1. Phase II will survey 3000 degree^2 over three regions in the Northern sky that contain minimal Galactic foreground emission. The goal of Phase II is to be capable of achieving a $5\,\sigma$ detection on the tensor-to-scalar ratio at the level of 0.05. The time frame of the experiment will be $\approx$4 years, with the TGI operating three years and the FGI operating for 2 years. First-light for the TGI should be autumn 2015 and first-light for the FGI will be early 2016.

The TGI and FGI receivers are being designed to share a single 20 K Helium cooled cryostat that will be housed in QT2. The TGI and FGI receivers will be designed to be easily removed and replaced from the cryostat. In this way the TGI receivers will be slowly replaced with FGI receivers over the lifetime of the observations. Both TGI and FGI receivers will share the design shown in Figure 2.5. The measurement of polarisation by the TGI and FGI receivers is the primary difference when compared to the MFI receivers. The rotary polar modulator was removed and the OMT now splits the incoming signal into left-handed and right-handed circularly polarised channels. The linear polarised Stokes parameters Q and U are then measured by adding a second 180 degree hybrid to, what would have been, the uncorrelated channels and a 90 degree phase switch to one of the chains in the correlated channels. The TGI and FGI will have instantaneous measurements of the Stokes linear polarisation parameters. The LNAs in the TGI and FGI have been replaced with 100 nm metamorphic high electron mobility transistors (mHEMTs), which are being commissioned by Fraunhofer Institute of Freiburg (IAF), Germany.

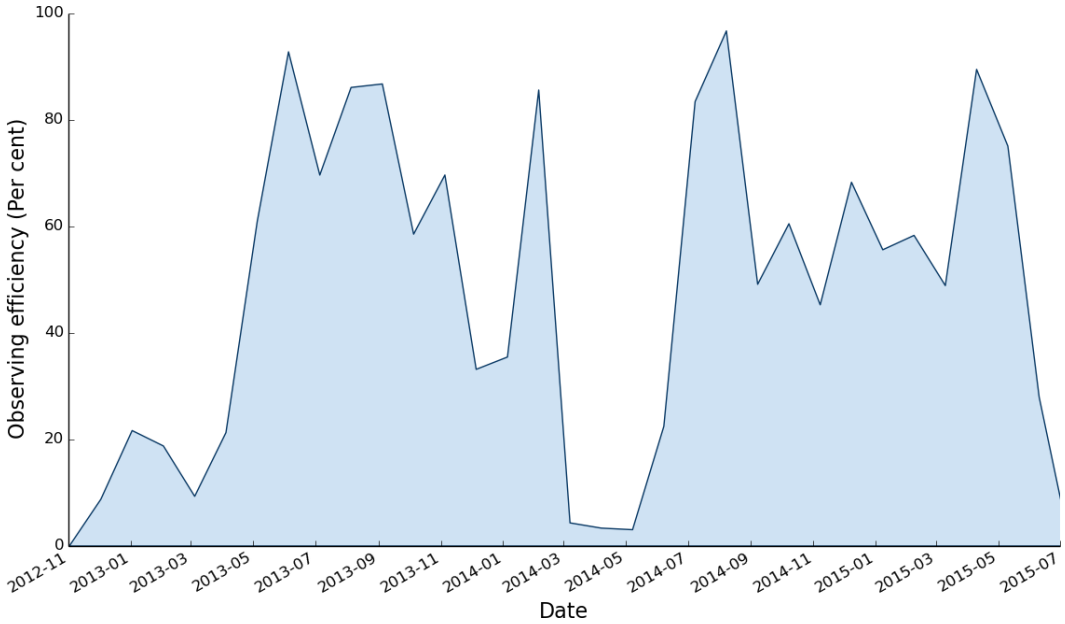

Figure 2.6: Percentage of the total number of hours that the MFI has observed since first light per month.

2.4 MFI Observations and Operations Summary

The QUIJOTE MFI has been observing since November 2012 and has observed approximately 10000 hours in total as of June 2015. The observations can be broadly characterised as four different types: Calibration, wide-survey and deep-surveys of cosmological and Galactic regions. The current global observing efficiency of the MFI since first light has been 48.6 %, which is measured from the number of hours observed in a month compared to the total number of hours per month. Figure 2.2 shows the month-by-month MFI observing efficiency. Note that some months are particularly low around April 2014 as significant changes to the MFI and QT1 were made. The other changes in the observing efficiency tend to correlate with the summer-winter cycle due to the generally poorer weather conditions during winter months at the Izaña observatory.

The calibration observations include twice daily measurements of primary MFI astronomical calibrator sources Cas A and Tau A, daily sky-dip observations to measure atmospheric absorption and maps of the local MFI sky. The deep-surveys are raster scan observations of three approximately 3000 degree^2 fields that have low Galactic emission. The deep-surveys constitute approximately 2200 hours of the total MFI

Table 2.2: Total hours spent observing each scientific field since MFI first light in November 2012.

Field	Hours
Wide-Survey	5443
Deep-Surveys	2233
Perseus	732
Haze	695
Fan	246
Taurus	364
W63	245
W44	209
IC443	244

observations to date. The wide-survey and raster observations of specific Galactic regions currently represent the largest scientific observing time contribution, which is currently in excess of 7000 hours as of June 2015. The goal of both of these sets of observations is to study regions near to the Galactic plane. Table 2.2 summarises the total hours devoted to each of the scientific observations.

Figure 2.7 summarises all the MFI scientific observing times and also marks the dates when key changes were made to the MFI or QT1. The commissioning period for the MFI and QT1 took place during the first five months of operation, from November 2012 until April 2013. During the commissioning period tests were made to ensure the functionality of the MFI, QT1 and the QUIJOTE enclosure. The following is a summary of the key points from the MFI commissioning period:

1. The absolute position of the horn 1 polar modulator was found to vary significantly when changing the relative polar modulator position.

2. The horn 4 LNAs were found to have system temperatures a factor two higher than expected.

3. The horn 3 correlated channels were exhibiting occasional periods of large, rapid gain fluctuations, which were later attributed to the horn 3 180 degree hybrids (see Section 4.2).

4. Far-sidelobe spillover from geo-stationary satellites was visible in the MFI low frequency channels (see Section 4.3).

5. An optical camera was used to make an initial estimate of the QT1 pointing model (see Section 3.3).

6. The calibration diode was installed behind the secondary reflector inside QT1 (see Section 3.5 for more details).

7. The receiver bandpasses were measured for horns 1, 2 and 3 (see Section 3.8).

Points 1 to 4 above were all MFI hardware-related issues. Point 1 was solved by fixing the horn 1 polar modulator into a single position, effectively making horn 1 unusable for polarisation measurements alone. Point 2 was resolved by simply not using any of the data taken by the horn 4 receivers. Point 3 and point 4 were problems that had to be solved during data processing, described in Chapter 4. These temporary solutions lasted for approximately 12 months, between April 2013 and April 2014. This period will be referred to as Epoch 1.

In April 2014 major changes were made to the MFI and QT1. Two 90 degree hybrids were added to the of the horn 1 receivers. The addition of the extra 90 degree hybrids to horn 1 meant that combining all four outputs from each frequency band could result in immediate determination of the I, Q and U Stokes parameters. Therefore the fixed horn 1 modulator was no longer a problem. The horn 4 LNAs were replaced and the new LNAs were found to have system temperatures comparable to the horn 2 LNAs. Finally, the far-sidelobe spillover was reduced by adding 1 m of extended shielding to the existing QT1 shielding. These changes marked such a significant change in the MFI system and data processing techniques that all observations taken after April 2014 are referred to as being in Epoch 2.

Two other smaller changes also occurred to the MFI system after the commissioning period ended. In February 2014 the cryostat compressor failed and was replaced with the compressor intended for the TGI cryostat. In October 2014 the horn 3 180 degree hybrid was replaced, correcting for the previously observed large drifts in the horn 3 correlated channels. Figure 2.7 summarises all the observations, changes and observing Epochs described in this Section.

2.5 Summary

This Chapter has summarised the QUIJOTE project instrumentation and scientific goals. The current status of the MFI observations has been discussed, along with

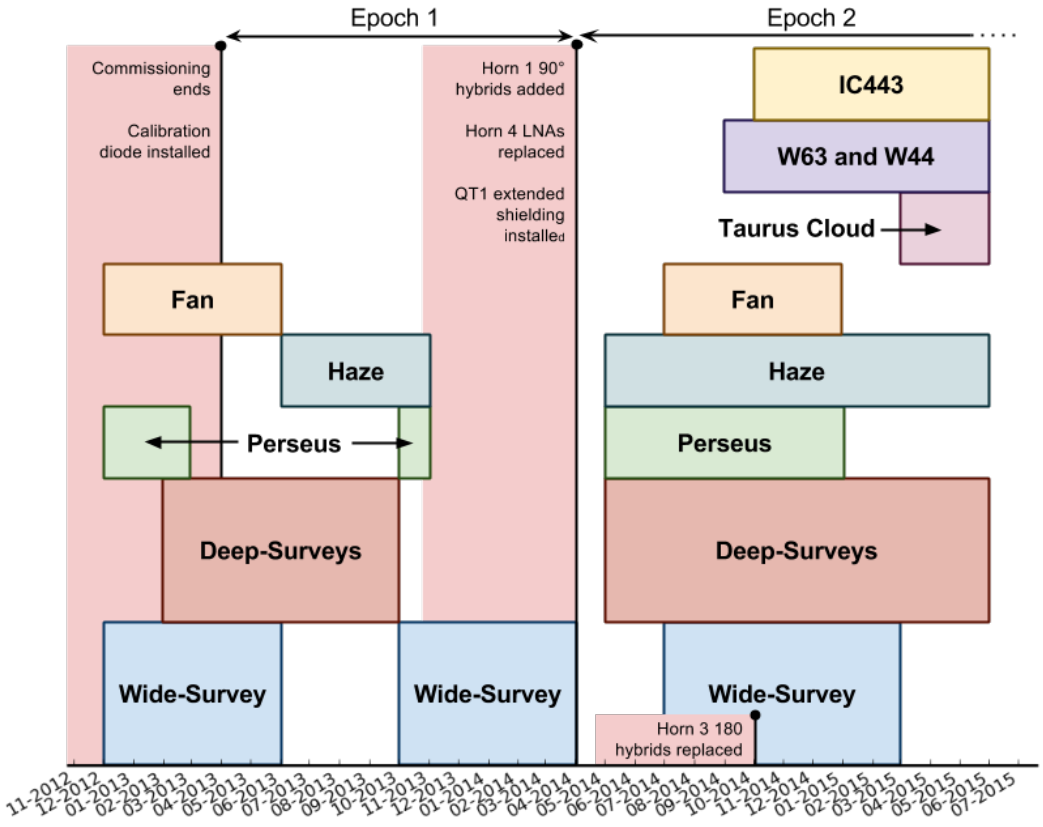

Figure 2.7: Timeline of all MFI scientific observations from first light until June 2015. Each block shows the beginning and end date of a series of observations on a particular field. The size of the blocks are not representative of the time observed.

several of the key points identified during the MFI commissioning period. Finally, the TGI and FGI were discussed as well as stating that both instruments are expected to be operational by early 2016.

Chapter 3

MFI Calibration

> "The more observations you make with an imperfect instrument the more it seems to be that the error in your conclusion will be proportional to the imperfection of the instrument..."
>
> Thomas Bayes, *Correspondence with Thomas Simpson, 1755.*

As postulated by Bayes in 1755, no instrument is perfect and therefore any measurement made with any instrument will be limited by some level of uncertainty. Careful understanding of the imperfections of an instrument can lead to some uncertainties being mitigated while other uncertainties must be accepted. This Chapter will discuss the properties of the MFI, discuss the imperfections in the instrument and show how the MFI time-ordered-data (TOD) are calibrated to a standard brightness temperature scale. The end goal of this Section will be to determine the calibration uncertainty in the MFI TOD and compare it to the calibration uncertainty goal of 1 per cent.

This Chapter principally focuses on the work of the *author* and the Manchester calibration pipeline. A similar calibration pipeline was developed at the IAC in parallel to the Manchester pipeline. Two pipelines were developed for calibration and data processing to determine and minimise any uncertainties introduced by the pipeline implementations.

Throughout this Chapter references are made to two different observing periods, before April 2014 and after April 2014. These two observing periods will be referred to as Epoch 1 and Epoch 2. For more details refer to Section 2.4.

3.1 Manchester Pipeline Tools

Before discussing the methods and results of the MFI calibration this Section will summarise all the external libraries used throughout Chapters 3 to 5.

The majority of the Manchester calibration pipeline is written in the `Python`[1] 2.7 programming language. The majority of the MFI calibration code is available online at `http://www.github.com/SharperJBCA`. The code makes extensive use of the `NumPy` (van der Walt et al., 2011) and `SciPy` (Jones et al., 2001–) libraries for many simple data analysis tasks. The Chapter 5 map-maker and some parts of the calibration pipeline are parallelised using the `MPI4Py` (Dalcin et al., 2005) which is a wrapper for the `C` based Message Passing Interface (`MPI`) libraries. Maps are generated using the `HEALPix` pixelisation scheme (Górski et al., 2005) unless otherwise stated.

The MFI pointing model described in Section 3.3 is written primarily in `Fortran` by the author and takes advantage of the `SLALIB` (Wallace, 1994b) library to perform horizon to sky coordinate transforms. The `Fortran` pointing model is linked to the `Python` calibration pipeline using the `F2Py` (Peterson, 2009) interface. Several other computationally intensive processes such as binning maps and down sampling data are also written in `Fortran` and connected to the calibration pipeline using `F2Py`.

3.2 Noise Properties

This Section discusses the MFI receiver noise properties. There are a number of reasons for measuring the MFI receiver noise properties. First, to characterise the fundamental system noise in the TOD and to determine of any temporal noise correlations that can be coupled to astronomical signal. Second, to identify any changes in the system noise properties, particularly between Epoch 1 and Epoch 2. Finally, to inform simulations of the TOD that are used to test data processing and map-making methods.

The characterisation of the receiver system temperature can be used to estimate the fundamental white-noise limit of the TOD. Stochastic variations in the amplifier current are characterised by the receiver system temperature $T_{\rm sys}$ using the radiometer equation (Rohlfs and Wilson, 2004)

$$\sigma_{\rm N} = K\frac{T_{\rm sys}}{\sqrt{\tau\Delta\nu}}, \tag{3.1}$$

[1] http://www.python.org

where σ_{N} is the white-noise level of the TOD, τ is the receiver sample rate and $\Delta\nu$ is the receiver bandwidth. The term K in Equation 3.1 is receiver dependent. For each of the MFI coherent pseudo-correlation receivers $K = \sqrt{2}$. Summing or differencing the MFI receiver outputs to isolate the intensity and polarisation components results in a further factor of $\sqrt{2}$ increase in the receiver noise, resulting in $K = 2$.

As well as system temperature variations, the MFI receiver outputs are subject to system gain variations. The output MFI receiver voltages can be defined as

$$V(t) = G(t)\left[T_{\mathrm{sys}}\right], \tag{3.2}$$

where $V(t)$ is the receiver TOD voltage response and $G(t)$ is the system gain, which can vary with time, t. If the variations in $G(t)$ are stochastic, then the fractional variance of the gain fluctuations can be added in quadrature to Equation 3.1(Burke and Graham-Smith, 1996),

$$\sigma_{\mathrm{N}} = KT_{\mathrm{sys}}\sqrt{\frac{1}{\tau\Delta\nu} + \left(\frac{\Delta G}{G}\right)^2}, \tag{3.3}$$

where ΔG describes the stochastic variations in the mean gain.

Unfortunately, for all radiometers the gain fluctuations will be correlated over some timescale. This results in the voltage TOD from the outputs of the radiometer to have a temporal power spectrum that can be approximately modelled by a reciprocal power-law. This type of correlated noise is known collectively as *1/f* noise and has the form (e.g., Maino et al., 1999; Seiffert et al., 2002; Meinhold et al., 2009),

$$P(\nu) = \sigma^2\left[1 + \left(\frac{\nu}{\nu_{\mathrm{knee}}}\right)^{\alpha}\right], \tag{3.4}$$

where $P(\nu)$ is the spectral power of each temporal mode, σ is the white-noise floor of the radiometer as described by Equation 3.1, ν is the temporal frequency, ν_{knee} is the temporal knee frequency where the correlated noise contributes an equal level of noise as the white-noise and α is the spectral index of the correlated noise. Typically the spectral index will vary between -1 and -2, where a spectral index of -2 describes a signal composed of Brownian noise. For an ideal receiver, ν_{knee} should be 0 Hz meaning that the receiver TOD is dominated by flat power-spectrum white-noise only.

The stability of the MFI noise properties can be quantified by the variation in the white-noise, knee frequency and spectral index over the lifetime of the experiment. The

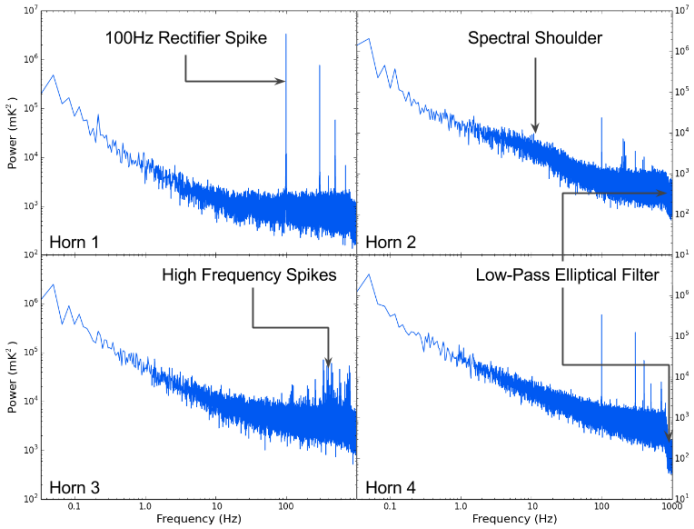

Figure 3.1: Representative power spectra measured from an observation of the deep survey field 1, July 2014 for each MFI pixel. The high frequency summed correlated channels are shown for horns 1, 2 and 4 and the uncorrelated channel for horn 3. Key spectral features are pointed out; see text for details.

knee frequency and white-noise levels will also provide important information on the quality of the data that can be expected from the MFI.

The power-spectra for one channel from each of the MFI feeds are shown in Figure 3.1. As well as the thermal noise and *1/f* noise properties of the receiver, there are also a number of other features. One of the most prominent features is the 100 Hz spike seen most clearly in the power-spectrum of the channels in horn 1. The spike is related to the 50 Hz "hum" of the mains supply to the MFI. The 50 Hz signal is filtered but the rectifier diode inside the power supply that transforms the mains supply from AC to DC generates an analogous 100 Hz signal. The 100 Hz spike is present in all MFI feeds but only in horn 1 is it particularly prominent. The spectral shoulder at ~ 10 Hz as indicated in the figure is a feature only seen in some MFI channels. A spectral shoulder can be generated by random on-off voltage switching. A similar effect was seen in the *Planck* HFI receivers and was referred to as "burst" or "popcorn noise". The exact origin of this noise is unknown, but is expected to be due to the receiver proximity to a component in the MFI BEM. The third feature referred to in Figure 3.1 are the high frequency spikes at approximately a few hundred hertz. The origin of these spikes are unknown and the brightness of the spikes depends both on the channel and time, the temporal component of the spikes implies the source may be local RFI. The final

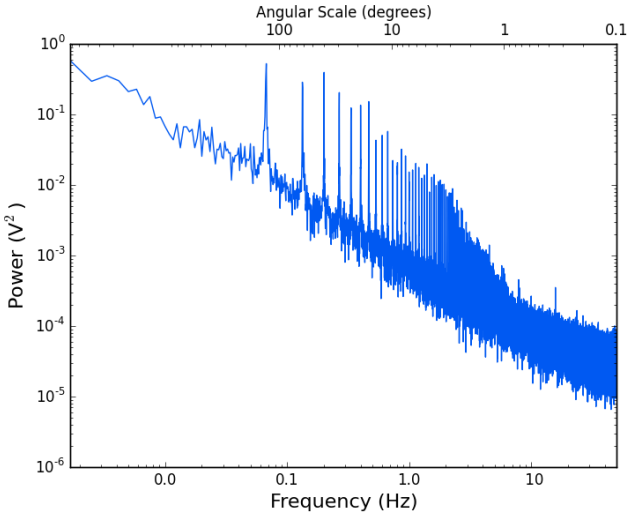

Figure 3.2: Mean power spectrum derived from 25 wide-survey nominal rings. The baseline slope is the receiver *1/f* noise. The spikes represent the Galactic plane transiting through the MFI beams at regular intervals along the nominal rings. The angular scales associated with each temporal frequency are estimated from the slew speed of QT1 at 12 degrees second^{-1}. Note angular scales are only illustrative as the true angular scale changes with azimuthal direction in the ring, current telescope elevation and slewing speed.

feature is a low-pass elliptical filter inside the MFI BEM that operates on frequencies higher than 800 Hz.

Figure 3.2 illustrates the importance of understanding the *1/f* noise properties of the MFI receivers. The figure shows the power spectrum of the Galactic plane transiting through the azimuthal scans of a MFI wide-survey observation. The Galactic emission from the plane forms spikes in the power spectrum of the TOD at regular frequencies that are dependent on crossing points of the Galactic plane on each azimuthal ring. For different observing strategies, telescope slewing speeds and pointing direction emission will be mapped to different temporal frequencies in the TOD power spectrum. Crucially, Figure 3.2 implies that higher knee frequencies will directly translate into greater uncertainty in the characterisation of larger scale emission. This is especially important when considering the MFI mission to characterise polarised diffuse Galactic emission in regions of weak Galactic emission.

The *1/f* noise parameters of the MFI receivers were measured using least-squares fitting to Equation 3.4. To avoid biasing the fit due to bright sources of emission in the sky the *1/f* properties are measured using the TOD obtained from observations of

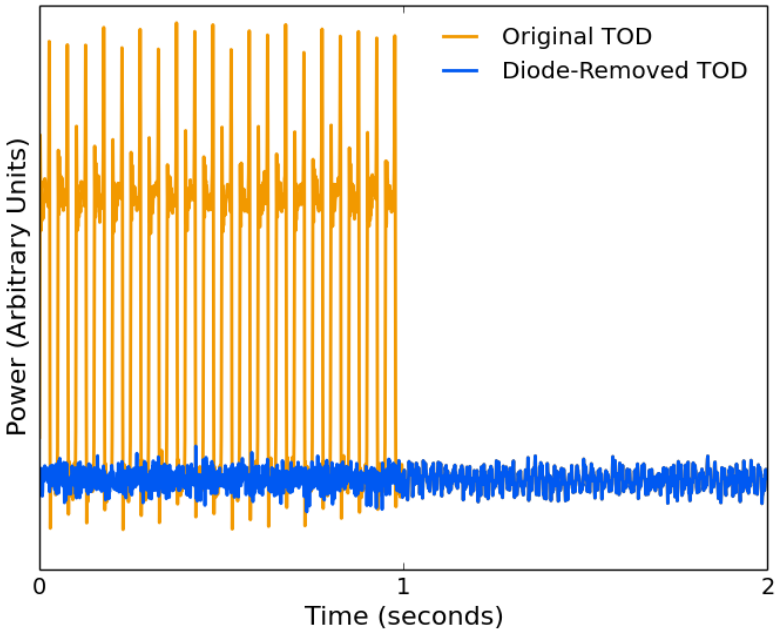

Figure 3.3: The calibration diode signal fires for 1 second every 30 seconds and is replaced by simulated white-noise derived from nearby TOD.

the cosmological fields. Before fitting for the *1/f* parameters the TOD had to first be preprocessed through several steps.

First the calibration diode signal had to be removed from the TOD. To maintain the temporal frequencies of any periodic function within the TOD the 1 second blocks containing the calibration diode signal were replaced with a computer generated white-noise signal that had the same variance as the nearby TOD as shown in Figure 3.3. As only $\sim$ 3 per cent of TOD was replaced using this method, the damping effect on the *1/f* noise power spectrum and spectral spikes was negligible.

The power spectrum is determined from the Fourier transform of the TOD,

$$P(\nu) = |\mathcal{F}(V_{\rm sys})|^2, \tag{3.5}$$

where $V_{\rm sys}$ is the recorded voltage TOD and $\mathcal{F}$ denotes the Fourier transform operation. The power spectrum was then binned into equally spaced logarithmic frequency bins. The binned power spectra were then least-squares fitted as shown in Figure 3.4. The uncertainty in the fitted parameters were determined using a jack-knifing method. The TOD was split into blocks of 60 seconds and each block was Fourier transformed

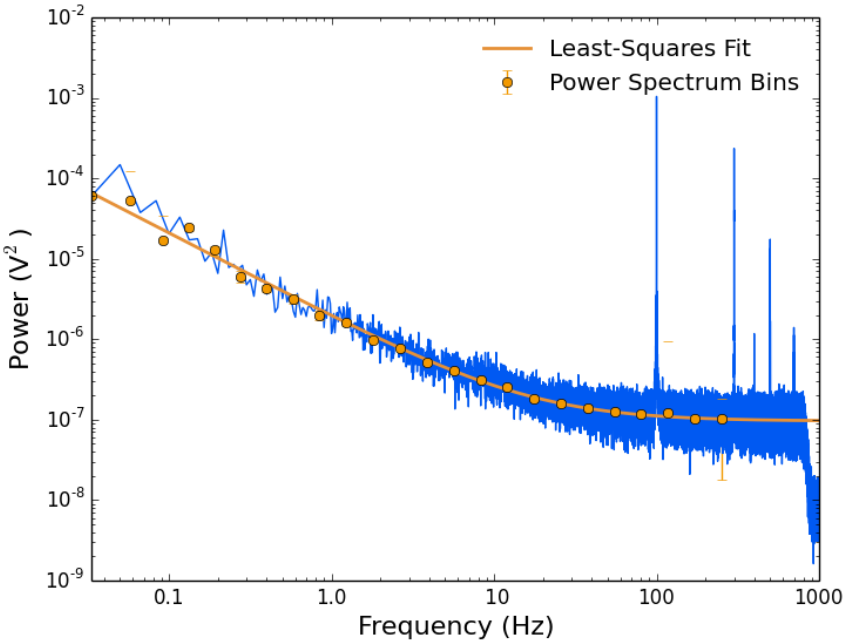

Figure 3.4: Example of a least-squares fit of the *1/f* model to the measured power-spectrum from a correlated 13 GHz channel in horn 1. The yellow line shows the best fit *1/f* spectrum and the yellow data points represent the bin centres.

into its power spectrum as described by Equation 3.5. The power spectra of a random selection of half of these blocks were averaged together and the best fit Equation 3.4 was determined. This procedure was repeated thousands of times in order obtain realistic estimates on the variance in each parameter for the *1/f* spectrum derived from the full TOD. The fitting procedure was tested by generating simulated *1/f* noise using Equation 3.4 and a range of knee frequencies between 0.1 Hz and 100 Hz. The fitting procedure was found to recover the *1/f* noise knee frequency with a 3 to 4 per cent uncertainty.

Measurements of the *1/f* parameters were made throughout Epoch 1 and Epoch 2. The mean fitted parameters per horn for the intensity component of the correlated MFI channel pairs are shown in Table 3.1. The uncertainties in the table are representative of the stability of each parameter over the Epoch. As the uncertainties in the values are measured over the entire Epoch, changes in atmospheric emission and changes in ambient temperatures can cause large shifts in the recovered knee frequencies. This is especially true of the higher frequency channels that are more sensitive to atmospheric fluctuations.

The polarisation *1/f* noise parameters were derived in a similar way. However, the channels had to be differenced and the correct *r-factors* applied to account for relative gain imbalance in the channel pairs (see Section 3.7). The typical knee frequencies for the correlated channels are approximately two orders-of-magnitude lower than the equivalent raw channel knee frequency. The polarisation *1/f* parameters are shown in Table 3.2. Unfortunately the knee frequencies for the high frequency MFI channels are still greater than 1 Hz, which is one of the primary sources of noise for the MFI polarisation observations. There are two reasons to expect lower knee frequencies in polarisation. The first is that the atmosphere is largely unpolarised at microwave frequencies and is removed when differencing the channels. The other is that the channels passing through the hybrid correlators have combined the gains from both FEM receivers and therefore differencing the correlated channels removes these long time scale drifts. Note that this implies that the uncorrelated channel polarisation knee frequencies are much closer to those measured in intensity and therefore are not stable enough for sensitive polarisation measurements.

One final point to consider when fitting the MFI *1/f* noise power spectra is the horn 2 spectral ledge that was shown earlier in Figure 3.1. To fit for the spectral ledge, two approaches are possible. One approach is to modify Equation 3.4 to allow for spectral

Table 3.1: Median knee frequency and spectral index for the MFI intensity *1/f* noise properties. Each frequency is derived from the sum of correlated channel pairs and observations of the cosmological fields. The uncertainty is derived from a Gaussian fit to a histogram distribution of the respective parameter and reflects the stability of the parameter.

	Epoch 1		Epoch 2	
Frequency (GHz)	ν_{knee} (Hz)	α	ν_{knee} (Hz)	α
Horn 1				
13	47±2	1.02±0.02	29±3	1.01±0.05
11	111±2	0.98±0.02	43±13	1.00±0.06
Horn 2				
19	228±14	1.07±0.04	120±64	1.3±0.5
17	185±3	1.09±0.03	106±55	1.3±0.6
Horn 3				
13	73±6	0.90±0.03	58±22	0.96±0.09
11	165±12	0.83±0.01	150±16	0.85±0.09
Horn 4				
19	188±20	0.92±0.03	275±106	0.84±0.09
17	306±14	0.92±0.05	278±46	0.86±0.02

Table 3.2: Median knee frequency and spectral index for the MFI polarisation *1/f* noise properties. Each frequency is derived from the difference of correlated channels and observations of the cosmological fields. The uncertainty is derived from a Gaussian fit to a histogram distribution of the respective parameter.

	Epoch 1		Epoch 2	
Frequency (GHz) (GHz)	ν_{knee} (Hz)	α	ν_{knee} (Hz)	α
Horn 1				
13	0.41±0.07	1.84±0.25	1.2±0.2	1.21±0.13
11	0.60±0.10	1.51±0.26	0.32±0.01	1.84±0.54
Horn 2				
19	5.0±2.6	1.4±0.8	7.4±1.0	1.8±1.1
17	3.15±0.09	1.8±1.0	5.3±4.2	1.6±1.2
Horn 3				
13	1.02±0.50	1.45±0.31	0.57±0.22	1.25±0.27
11	0.87±0.73	1.52±0.42	0.83±0.32	1.15±0.26
Horn 4				
19	1.63±0.59	1.48±0.23	1.53±0.1	1.06±0.05
17	1.29±0.18	1.09±0.07	0.70±0.09	1.02±0.04

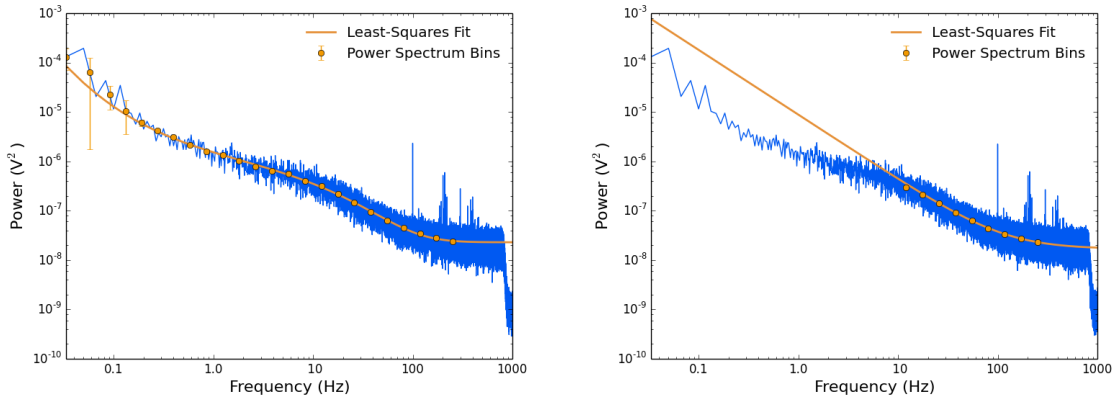

Figure 3.5: Example *1/f* fit to a horn 2 19 GHz power spectrum. Due to the spectral ledge in the horn 2 power spectra the *1/f* fitting procedure must be modified (see text). *Left*: Fitting using the modified *1/f* equation. *Right*: Fitting using a constrained range of frequencies.

curvature by adding a frequency dependent polynomial to the frequency spectral index as,

$$P(\nu) = \sigma^2 \left[1 + \left(\frac{\nu}{\nu_{knee}} \right)^{-\alpha - \sum_{i=1} a_i \log(\nu)^i} \right], \tag{3.6}$$

where a_i are the polynomial amplitudes and the number of extra terms required is $N_{\text{knees}} - 1$, where N_{knees} is the number of knee frequencies. Alternatively, the range of frequencies used to fit the power spectrum can be limited to those near the highest knee frequency. Both methods recover similar knee frequencies, however both do not consider the physical cause of the spectral slope. Therefore the knee frequencies of horn 2 are possibly being overestimated. Figure 3.5 demonstrates an example of both fitting procedures. For the power spectrum shown in the figure, $N_{\text{knees}} = 3$. The reported knee frequencies for horn 2 are derived from the fits using the limited frequency range method.

3.3 Pointing Model

The general pointing model for single-dish radio telescopes can be defined using seven physically motivated pointing parameters first derived by Stumpff (1972) and Ulich (1981). To derive the MFI pointing parameters, the general telescope pointing software `TPOINT` (Wallace, 1994a) was used. Measurements of the MFI pointing model were led

by Dr. Rubino Jose Alberto (IAC) and PhD student Denis Tramonte (IAC). The pointing parameters were initially derived from optical measurements of stars reported in the Hipparcos Catalogue (Perryman et al., 1997) using an optical camera fitted in the focal centre of the MFI. The pointing parameters were further refined per MFI feed using radio observations of the two primary calibrator sources Tau A and Cas A.

Using the IAC derived MFI pointing model, the author of this thesis determined the pointing uncertainty of QT1 and the MFI in the final MFI wide-survey maps. Pointing uncertainties do not affect the integrated flux density of a source in the final MFI wide-survey maps. However, pointing uncertainties can contribute to uncertainties in the amplitude determination of calibrator sources in a single observation and do change the effective beam size of the instrument in the final maps. The effective beam size in the final MFI maps will be dependent on position in the sky, scanning strategy and how evenly sampled a given region of sky is. Assuming the main beam of the MFI can be reasonably approximated by a Gaussian, the FWHM of the effective beam in the final maps is

$$\theta_{\rm eff}^2 = \theta_0^2 + \delta^2, \tag{3.7}$$

where $\theta_{\rm eff}$ is the effective FWHM of the MFI in the maps, θ_0 is the nominal MFI FWHM and δ is the pointing uncertainty. The maximum uncertainty in flux density can be estimated from the ratio of the nominal and effective FWHMs

$$\frac{\Delta S_\nu}{S_\nu} = 1 - \frac{\theta_0^2}{\theta_{\rm eff}^2} = 1 - \frac{\theta_0^2}{\theta_0^2 + \delta^2}, \tag{3.8}$$

where $\Delta S_\nu / S_\nu$ is the percentage uncertainty in the measured flux density.

The magnitude of the MFI pointing uncertainty was determined by differencing the true and reported coordinates of radio sources in the Revised 3C Catalogue of Radio Sources (Edge et al., 1959) that were detectable in the final MFI maps. Each 3C source was fitted for using a Gaussian beam model in the combined feed 1 and 3 11 GHz map and the combined feed 2 and 4 17 GHz map. Figure 3.6 shows the calculated offsets compared to the nominal FWHM of the 11 GHz and 17 GHz main beams. The measured dispersion in the difference between the true and observed 3C source coordinates was $\pm$ 5.2 arcmin in the 11 GHz map and $\pm$ 3.4 arcmin for the 17 GHz map. The resulting percentage flux density uncertainties can then be determined using Equation 3.8 and are found to be 0.8 per cent at 11 GHz and 0.8 per cent at 17 GHz.

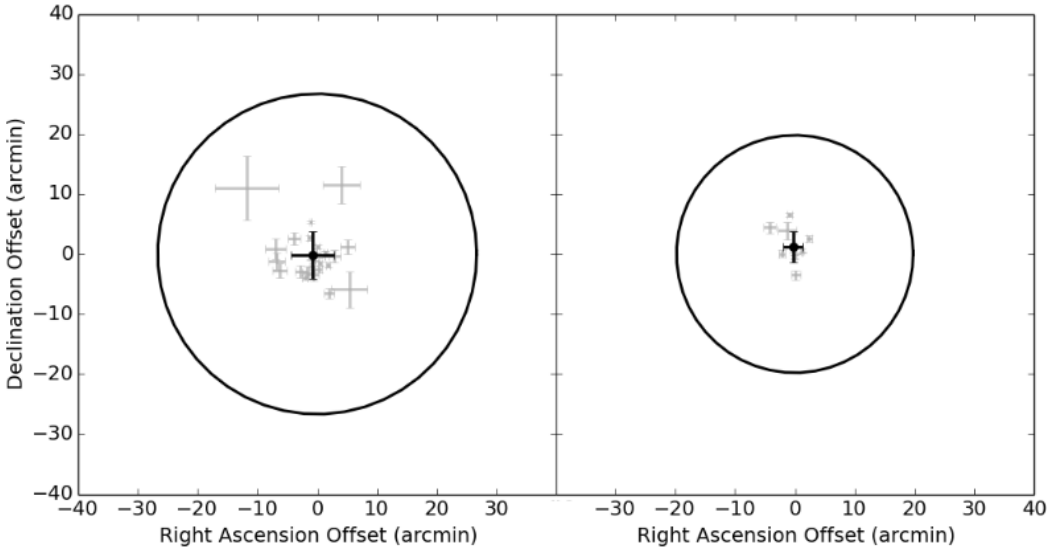

Figure 3.6: Scatter on 3C point sources measured across the sky in the 11 GHz (*left*) and 17 GHz (*right*) MFI wide-survey maps. The black circle in both images has a radius equal to half the typical beam FWHM for each frequency. The black point is the weighted mean location of all the points and the error bars are derived from the overall scatter of the points.

3.4 Beams

This Section will describe the total intensity power pattern response of the beams associated with the MFI feeds per frequency channel pair. The recorded antenna temperature (T_a) of the sky along a line-of-sight defined by θ_0 and ϕ_0 is the convolution of the beam and sky distributions described by (e.g., Rohlfs and Wilson, 2004),

$$T_a(\theta_0, \phi_0) = \frac{1}{\Omega_A} \int_{4\pi} P_N(\theta - \theta_0, \phi - \phi_0) T_b(\theta, \phi) \mathrm{d}\Omega, \tag{3.9}$$

where P_N is the power pattern of the MFI beam, $T_b(\theta, \phi)$ is the brightness distribution of the sky and Ω_A the full beam solid angle. The full beam solid angle is defined by integrating the power pattern over the whole sky,

$$\Omega_A = \frac{1}{P_{\max}} \int_{4\pi} P_N(\theta_0, \phi_0) \mathrm{d}\Omega, \tag{3.10}$$

where $P_{\max}$ is the maximum directional gain of the beam. The beam power pattern of the MFI can be divided into the main beam, near sidelobes and far sidelobes. These subdivisions of the beam are illustrated in Figure 3.7. Crucial beam characteristics to be discussed in this Section are the main beam FWHM, the main beam ellipticity

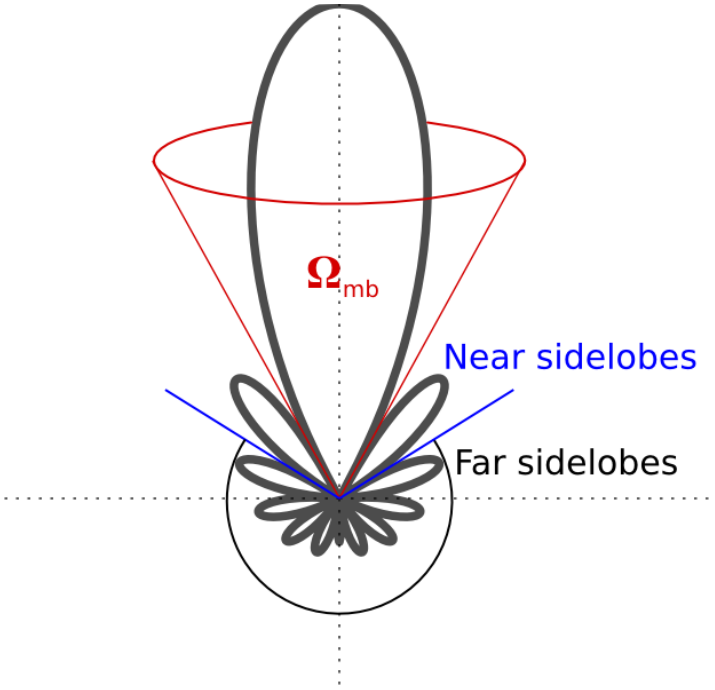

Figure 3.7: Illustrative beam pattern showing the definitions of the main beam area with solid angle $\Omega_{\rm mb}$. The first few brightest sidelobes are known as the near sidelobes and everything else is known as the far sidelobes.

and the ratio between the main beam and the full beam solid angles. There is also a discussion of the difference between the optical beam from a single pointing and the effective beam in the MFI maps after combining many observations.

Models of the MFI beam power patterns were generated by Roger Hoyland using the Computer Simulation Technology[2] (`CST`) software. The `CST` beam models use ray-tracing to define the QT1 optical paths from each feed through the secondary and primary reflectors. Analytical diffraction is then calculated and added to the ray edges. The `CST` models are expected to be accurate representations of the MFI main beam response, however the current `CST` models do not account for the QT1 shielding and therefore are not expected to reproduce the observed far sidelobe and spillover emission. Each beam model is normalised such that the maximum forward power of the main beam is the beam directivity ($\mathcal{D}$) defined as,

$$\mathcal{D} = \frac{4\pi}{\Omega_A}, \tag{3.11}$$

which is the ratio of the full sky solid angle over the full beam solid angle. The beam

[2]https://www.cst.com

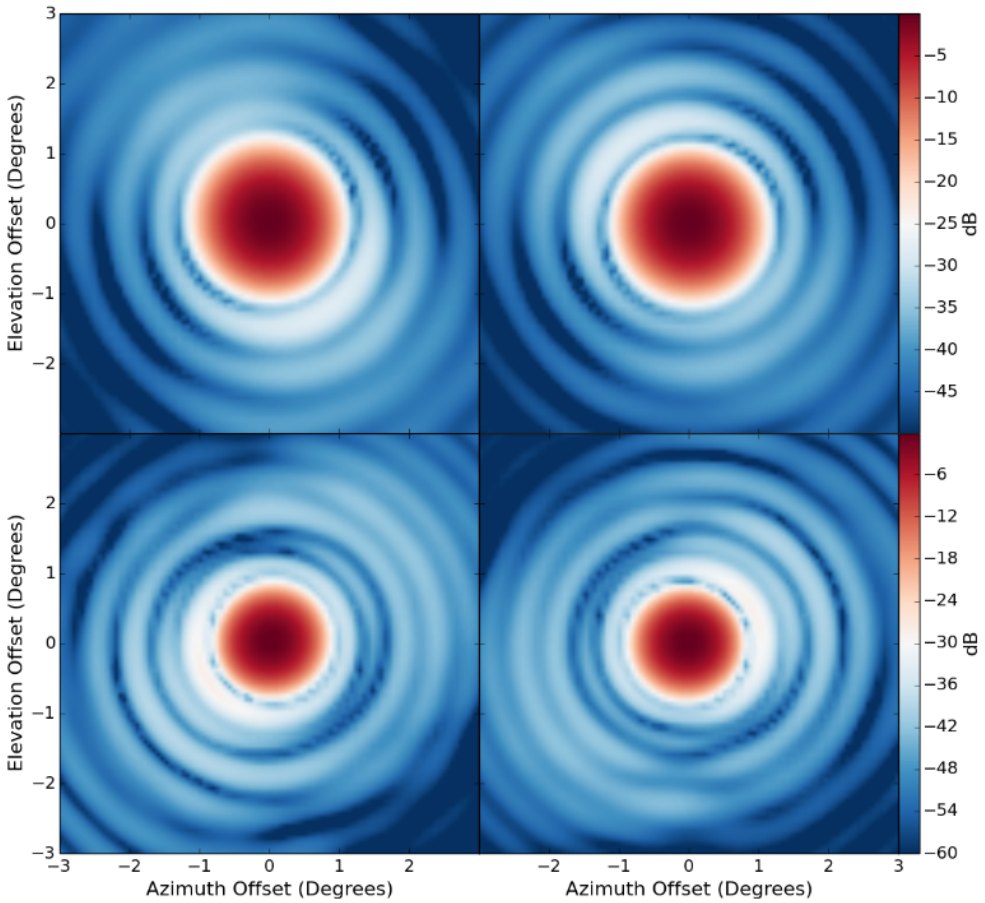

Figure 3.8: MFI beams simulated by the CST software package. The *top* row shows the feeds 1 and 3 models at 11 GHz and the *bottom* row shows the feeds 2 and 4 models at 17 GHz.

power pattern coordinate system was defined relative to the MFI focal centre, not the feed centres.

To analyse the MFI beam models the coordinate system of each raw CST beam output was first rotated to the centre of the peak power response of the beam. The CST beams were then regridded using linear interpolation into an all-sky map using the HEALPix pixelisation scheme with an N_{side} of 2048 ($\sim$ 1.7 arcmin pixels). Finally, the peak power response of each CST beam was normalised to unity. Figure 3.8 shows the main beam response for frequencies 11 GHz and 17 GHz of MFI feeds 1 to 4. Figure 3.8 shows that the brightest near sidelobe gain is expected to be between -25 dB and -30 dB below the main beam response.

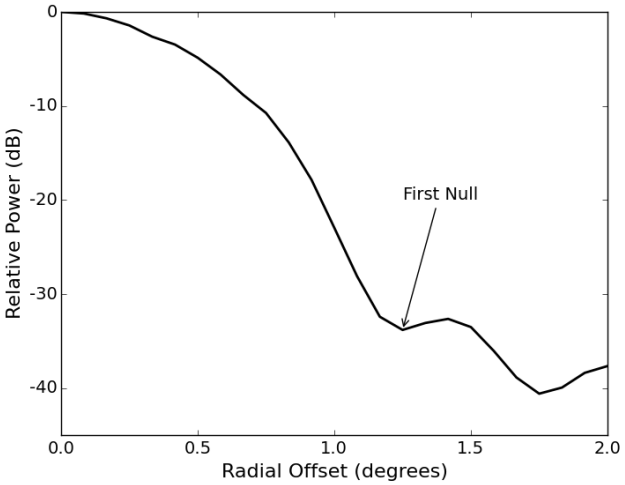

Figure 3.9: Radial profile of the horn 1 11 GHz `CST` beam. The location of the first null was used to define the radial extent of MFI main beams.

The `CST` beams were used to determine the main beam response ($\Omega_{\rm mb}$), the full beam response (Ω_A) and the main beam to full beam ratio (beam efficiency),

$$\eta_{\rm mb} = \frac{\Omega_{\rm mb}}{\Omega_A}. \tag{3.12}$$

Determination of $\Omega_{\rm mb}$ and $\eta_{\rm mb}$ are crucial to the MFI calibration pipeline as the MFI calibrates to the main beam temperature scale. Therefore the flux density measurements of extended emission, which will include MFI sidelobe contributions, will be overestimated by a factor of $\eta_{\rm mb}$. For the MFI, the main beam was defined as the power within the first null of the beam radial profile. The beam radial profile is derived from the mean power within annuli of a fixed width but with an increasing central radius. Figure 3.9 shows an example radial profile for the `CST` model of horn 1 at 11 GHz, and the location of the first null.

Table 3.3 summarises the beam model solid angles, $\eta_{\rm mb}$ and the first null distance. Ω_A was measured using the peak response of the beam model and the definition of directivity from Equation 3.11. The main beam solid angle was measured by numerical integration of the pixels in the regridded beam map using an aperture with a radius defined by the first null. Table 3.3 shows that the MFI beam efficiency is very high. For example, the MFI beam efficiency is much higher than many general purpose single-dish radio telescopes that may only achieve beam efficiencies between 55 to 70 per cent (e.g., Reich and Reich, 1985; Jonas et al., 1998; Jewell and Prestage, 2004), and is

Table 3.3: Beam parameters derived from the CST beam models. The first null is determined from the radial profile of the beam model and Ω_{mb} is the solid angle of the beam within the first null.

Frequency (GHz)	First Null (degrees)	Ω_{mb} 10^{-4} sr	Ω_A 10^{-4} sr	$\eta_{\rm mb}$
Horn 1				
13	1.27	2.95	3.04	0.973
11	1.27	2.92	3.02	0.967
Horn 2				
19	0.86	1.47	1.54	0.957
17	0.90	1.42	1.48	0.958
Horn 3				
13	1.31	2.87	2.95	0.958
11	1.27	2.85	2.95	0.966
Horn 4				
19	0.86	1.51	1.58	0.957
17	0.90	1.47	1.53	0.958

only slightly lower than the measured beam efficiencies of *Planck* at 99 to 99.5 per cent (Planck Collaboration et al., 2014g).

Measurements of the beam FWHM and beam ellipticity were made using Gaussian fits in the TOD of raster observations over Tau A. The observations were taken over a period between January 2014 and October 2014, which equates to approximately 150 unique observations. Gaussian fits were performed in the local coordinate frame of the telescope relative to the position of Tau A. Table 3.4 shows the measured FWHM and ellipticities. The FWHM was defined as

$$\mathrm{FWHM} = \sqrt{8\ln(2)\sigma_{\rm min}\sigma_{\rm max}}, \tag{3.13}$$

where $\sigma_{\rm min}$ and $\sigma_{\rm max}$ are the smallest and largest main beam widths respectively. The beam ellipticity (e) was defined as,

$$e = \frac{\sigma_{\rm min}}{\sigma_{\rm max}}, \tag{3.14}$$

where an ellipticity of 1 would describe a perfectly circular beam. The uncertainties in Table 3.4 are derived from the sample variance to account for systematic uncertainties associated with the fit. The results of Table 3.4 show that the MFI main beam response

Table 3.4: The FWHM and ellipticities of the MFI beams derived from TOD level Gaussian fits to intensity calibrated Tau A observations.

Frequency (GHz)	FWHM (degrees)	Ellipticity
Horn 1		
13	0.94±0.02	0.99±0.04
11	0.94±0.02	0.99±0.04
Horn 2		
19	0.64±0.03	0.85±0.17
17	0.65±0.02	0.97±0.08
Horn 3		
13	0.94±0.02	0.98±0.06
11	0.94±0.02	0.99±0.04
Horn 4		
19	0.63±0.03	0.80±0.5
17	0.62±0.03	0.91±0.14

is highly symmetrical. The implication of a symmetrical main beam response means that the effective main beam in the map should be the same as the optical main beam derived from a single observation.

Stacking the Tau A observations in relative azimuth and elevation coordinates was used to compare the observed main beam response of the MFI feeds with the main beam response of the `CST` models. Figure 3.10 shows the radial profile of the Tau A stacked observations overlaid with the radial profile of the `CST` beam models for feeds 1 to 4 at 11 GHz and 17 GHz.

A second check of the `CST` beam models and a cross-check of the main deviations can be performed for the low frequency MFI channels using emission from geostationary (GSO) satellites. The GSO satellite used in this analysis has a longitude of 40.5 W. The GSO satellite was chosen as it was bright enough to observe the first near sidelobes but not so bright that the main beam saturated the receiver. There was not another GSO satellite within 4 degrees of the GSO satellites main beam response. Figure 3.11 shows the comparison between the radial profiles of the satellite and the model. From the figure, it is clear that the beam model agrees with the true main beam response. The predicted observed near sidelobe responses seem to deviate outside of 1.25 degrees. Both appear to have the same peak sidelobe response around 1.5 degrees, but the nulls

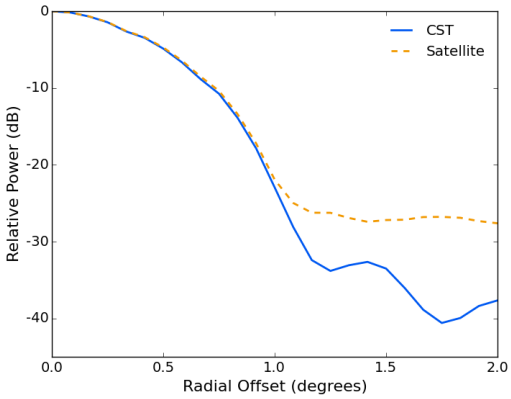

(a) Horn 1 11 GHz.

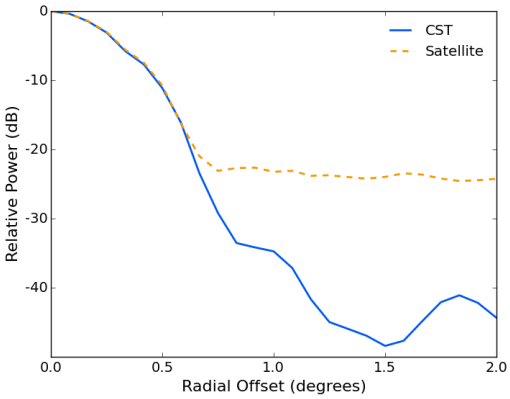

(b) Horn 2 17 GHz.

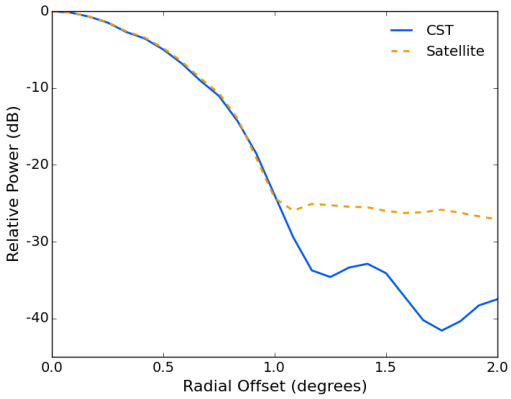

(c) Horn 3 11 GHz.

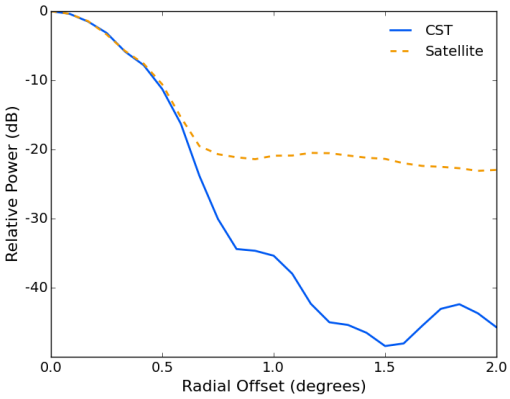

(d) Horn 4 17 GHz.

Figure 3.10: Comparison between the radial profile of the model `CST` beam with stacked observations of Tau A from throughout 2014.

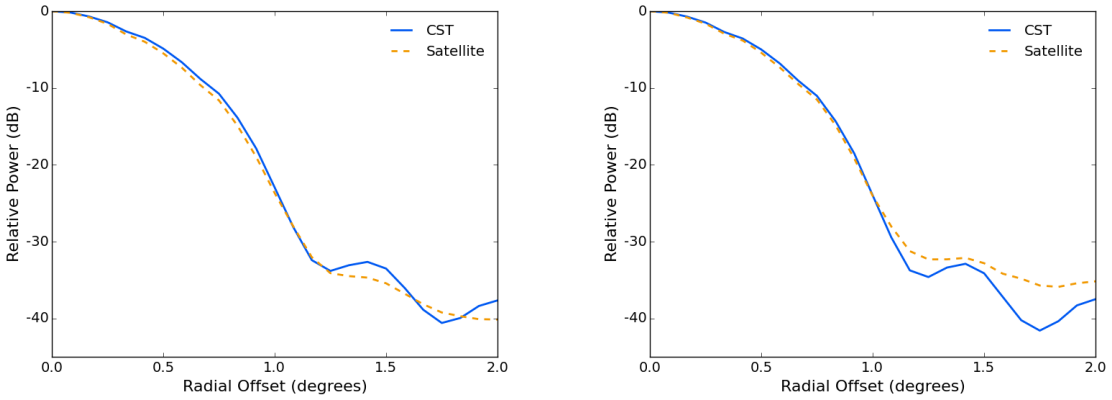

(a) Horn 1 11 GHz. (b) Horn 3 11 GHz.

Figure 3.11: Radial profile of the model `CST` beams overlaid with a profile of a moderately bright geostationary satellite observed by MFI Horn 1 and horn 3 at 11 GHz.

either side of the peak in the observed beam are significantly higher the and sidelobe far less defined. The explanation of these differences include pixel aliasing effects, intrinsic smoothing of the beam due to the source angular size and pointing inaccuracies.

Using the GSO satellite and the stacked Tau A observations, the observed main beam solid angles $\Omega_{\rm mb}$ were estimated by normalising the main beam peak response to unity and performing aperture photometry to the first null. For horn 3 at 11 GHz the GSO satellite measured main beam solid angle was $(2.6 \pm 0.2) \times 10^{-4}$ sr and the Tau A stacked solid angle was found to be $(2.82 \pm 0.03) \times 10^{-4}$ sr. Comparing these measurements to the reported main beam solid angle in Table 3.4 reveals that the measured main beam solid angles are consistent with the main beam model. The GSO satellite measurement slightly underestimates the beam solid angle due to a combination of the *1/f* noise in the map and the presence of near sidelobes from other nearby GSO satellites. The uncertainty of the GSO satellite measurements attempts to account for the presence of these spurious signals. As there were no bright GSO satellites observed in the 17 GHz bandpass, the horn 2 main beam solid angle was estimated from Tau A alone. The measured Tau A main beam solid angle was $(1.40 \pm 0.02) \times 10^{-4}$ sr, which again agrees with the measured main beam solid angle. These measurements are crucial as they demonstrate that the beam efficiency measured from the `CST` beam models are reliable at the 1.1 per cent level for the low frequency channels and 1.4 per cent reliable for the high frequency channels.

This Section has introduced the MFI beams and validated the reliability of the

CST beam models as being representative of the observed main beam responses. The main beam response at both frequencies is found to be consistent with the CST beam models. The near sidelobes appear less accurately modelled, however the amplitude of the sidelobes were found to be representative of the measured sidelobe emission. No direct comparison of the model far sidelobes and true far sidelobes responses have been shown. However, from the design of the model it is expected that the model far sidelobes will not be representative. More discussion on the MFI far sidelobe emission can be found in Section 4.3 that discusses the integrated far sidelobe pick up from GSO satellites.

3.5 Calibration Diode

As discussed in Section 3.2 on MFI noise properties, the stability of a radiometer is dependent on variations in the system gain. Tracking and minimising changes in the receiver gain is critical for determining accurate flux density measurements of celestial emission. The MFI tracks receiver gain fluctuations by making regular measurements of the emission from an external calibration diode shown in Figure 3.12. The calibration diode generates a circularly polarised, flat spectrum signal with a brightness temperature of the order 10^4 K. The beam FWHM of the calibration diode is > 90 degrees, meaning the diode signal should be approximately the same brightness across all four MFI feeds. The calibration diode is located just behind the secondary reflector as illustrated in Figure 3.13.

The calibration diode generated bursts of 20 pulses over one second, once for every 30 seconds of TOD and could be clearly identified above the TOD thermal noise as shown in Figure 3.14. Parallel to the TOD, a Boolean array was used to track the one second intervals containing the calibration diode bursts. This array will be referred to as the diode array. The amplitude of the calibration diode is measured as the difference between the mean signal when the calibration diode was switched on relative to the mean value when the calibration diode was off. However, large instabilities were seen to occur in the calibration diode signal that limited the samples that could be used to determine the calibration diode voltage response. These instabilities can be seen in Figure 3.15 as ripples occurring up to 10 ms after turning the diode on and after the large spike and subsequent ripples from 27 ms. The additional TOD noise increase for samples injected with the calibration diode due to the increased system temperature

Figure 3.12: The MFI calibration diode before installation into QT1.

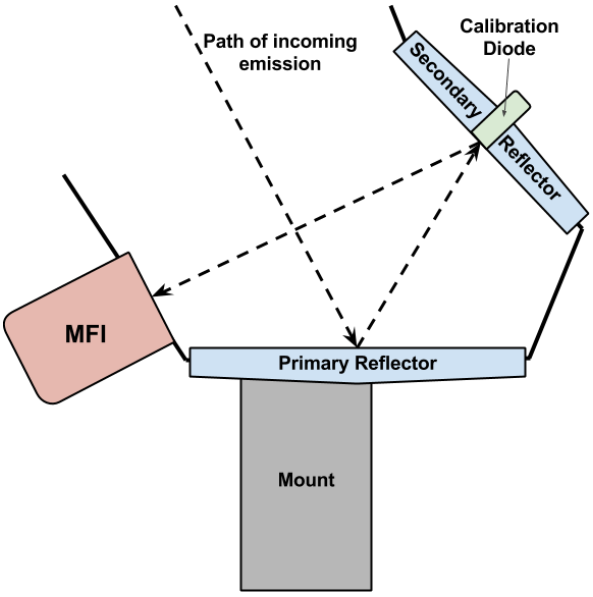

Figure 3.13: Schematic diagram of QT1 marking the location of the calibration diode in the centre of the secondary reflector.

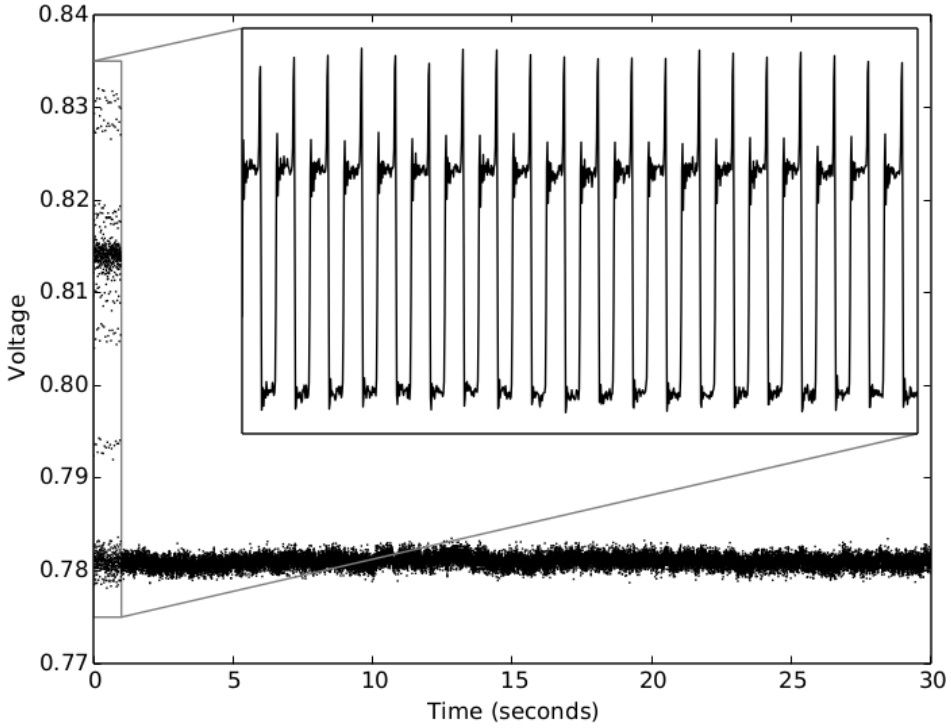

Figure 3.14: Example of calibration diode signal. Twenty pulses are fired in one second. Each group of pulses is fired once in every 30 seconds.

were less than 6 per cent.

The voltage response of every calibration diode pulse was recorded independently along with the corresponding Julian date. As each voltage response occupied the same 50 ms block, the voltage response could be measured by stepping through every 50 samples of the TOD that were flagged by the diode array as containing a calibration diode pulse. A small complication with this method was that sometimes a 1 second burst of calibration diode pulses would be recorded as lasting 1001 ms instead of 1000 ms. If these extra 1 ms intervals were not accounted for then the regions used to measure the voltage response shown in Figure 3.15 would slowly drift towards the left of the diode pulse signal. To correct for this effect, the areas used to measure the voltage response were always performed relative to the voltage spike at 27 ms, which was found to always occur at the same relative instant of time.

To remove gain drifts from the MFI receivers the TOD are divided by the calibration diode, the voltage response is divided by the calibration diode voltage,

$$V' = \frac{V_{\rm sys}}{V_{\rm dio}}, \tag{3.15}$$

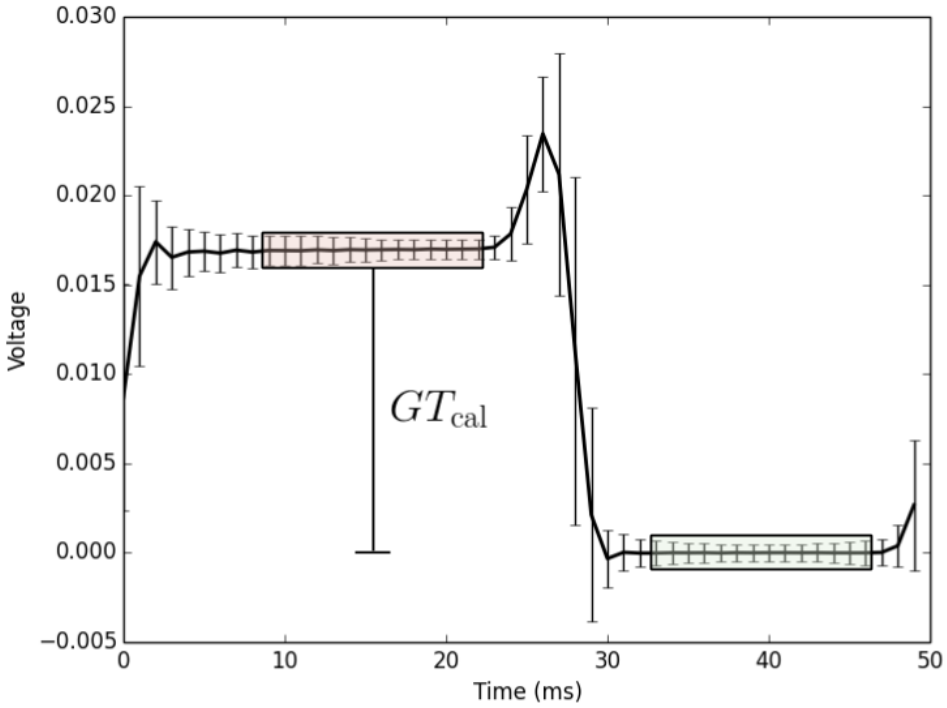

Figure 3.15: Cross-section of a single calibration diode on-off pulse. The calibration diode voltage GT_{cal} is defined as the difference between the diode signal plateau and the background signal.

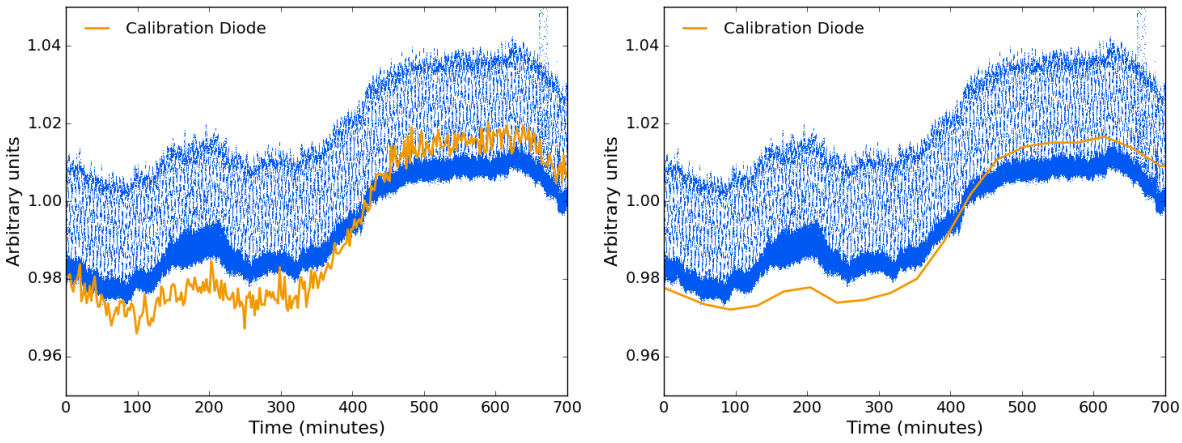

(a) (b)

Figure 3.16: Gain models derived for a single 75 degree elevation wide-survey observation over a 700 minute interval. *Left*: Gain model derived using 1.5 minute averages of the calibration diode voltage. *Right*: Gain model derived using 30 minute averages of the calibration diode voltage.

where $V_{\rm sys}$ and $V_{\rm dio}$ are the system and calibration diode voltage responses and V' is the gain corrected voltage response in units of calibration diode brightness. $V_{\rm dio}$ for all TOD samples can be determined using linear interpolation between blocks of calibration diode bursts. As V' is determined from the ratio of the system and diode voltages, the resulting uncertainty is the sum of both the variance in the system and the diode. Ideally, $V_{\rm dio}$ should not add any appreciable additional noise to the system voltage uncertainty. However, the uncertainty in a single calibration diode pulse will be only slightly smaller than the system noise. Therefore to reduce the noise of the calibration diode response, many 1 second bursts are averaged together over a 24 minute interval.

Figure 3.16 demonstrates the difference between averaging calibration diode bursts spanning 1.5 minutes of TOD and averaging calibration diode bursts spanning 24 minutes. From Figure 3.16 it can be seen that short averaging times for the calibration diode will add significant extra noise to the MFI TOD. By effectively mean smoothing the calibration diode voltages to a timescale of 24 minutes, small scale noise variations are reduced and the diode voltage primarily traces the receiver gain.

A major systematic effect of the calibration diode identified at the end of the MFI commissioning phase is that the circularly polarised emission from the diode induced an apparent linear polarisation response in the MFI receivers. The linear polarisation

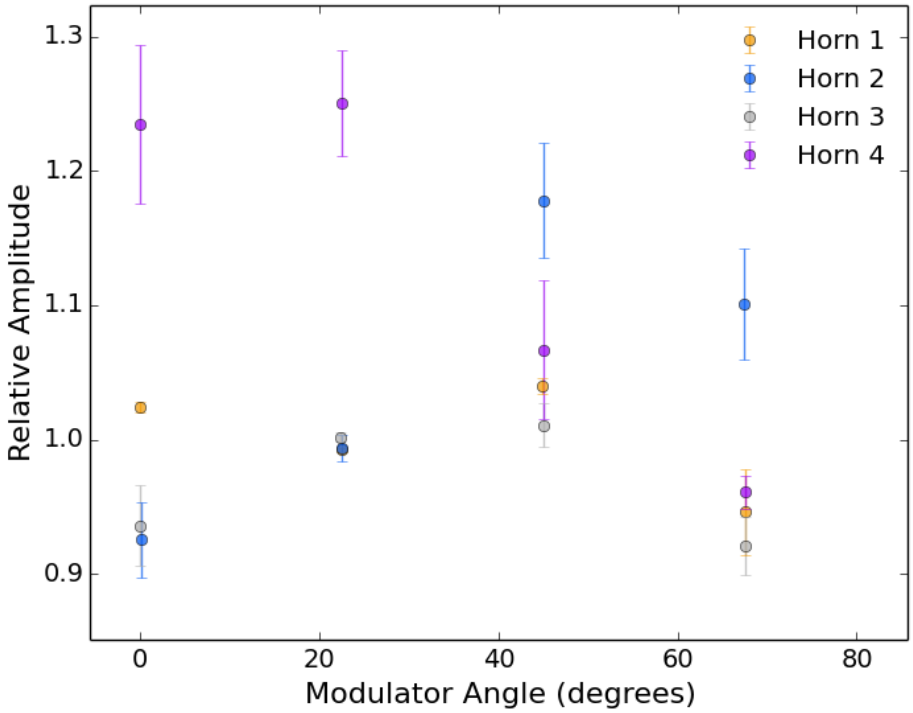

Figure 3.17: Variation in the calibration diode signal with modulator angle for observations taken during Epoch 1.

response can be clearly seen in all four horns. Figure 3.17 shows the mean relative change in amplitude of the calibration diode for different modulator angles at 11 and 17 GHz in all MFI horns for observations taken during Epoch 1. The figure shows that the apparent diode polarisation varies by 5 to 10 per cent depending on horn and frequency.

To quantify the apparent linear polarisation response of the diode, the diode signal was modelled as

$$T_{\rm dio} = I_{\rm dio}\left[1 + P_{\rm dio}\cos(4\phi + \psi)\right], \tag{3.16}$$

where $I_{\rm dio}$ is the diode intensity signal, $P_{\rm dio}$ is the diode polarisation fraction, ϕ is the modulator angle and ψ is an arbitrary phase offset.

During Epoch 2, two dedicated observations on 5^{th} and 6^{th} November 2014 were made to quantify the polarisation response of the diode. The dedicated observations in Epoch 2 decreased the time between diode bursts to just 1 second, QT1 was pointed towards the NCP and the feed modulator positions were rotated 22.5 degrees every

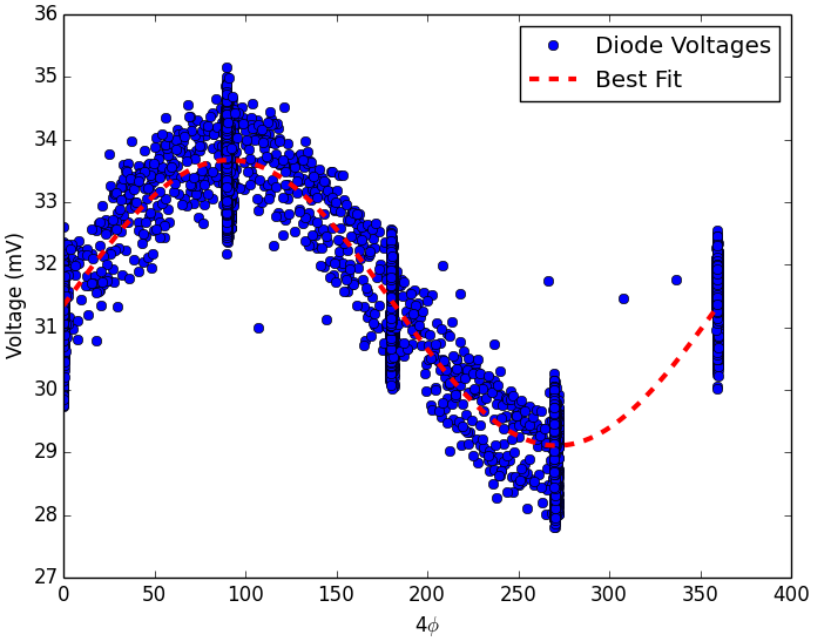

Figure 3.18: Change in the voltage response of a MFI 13 GHz horn 3 correlated channel with modulator angle taken on the 5^{th} November 2014. A fit of Equation 3.16 is shown overlaid.

Table 3.5: Weighted averages of the apparent diode polarisation for feeds 2 to 4. All measurements were determined from fixed pointing observations of the NCP taken on 5^{th} and 6^{th} November 2014. Horn 1 polarisation fractions are not reported as the feed 1 polar modulator is in a fixed position.

Frequency (GHz)	Polarisation Fraction (%)
Horn 1	
13	–
11	–
Horn 2	
19	10±3
17	13±2
Horn 3	
13	9.4±0.4
11	6.3±0.9
Horn 4	
19	15±3
17	6±2

2 seconds. These observations provided very robust solutions to the calibration diode polarisation signal. Figure 3.18 shows an example of how the diode polarisation response at 13 GHz in horn 3 changed with modulator angle. The figure shows a clear sinusoidal voltage response from the calibration diode caused by the apparent diode polarisation. Table 3.5 shows the average diode polarisation fractions derived from these observations per MFI horn and frequency. Feed 1 polarisations are reported as the feed 1 polar modulator is in a fixed position. Unfortunately during Epoch 1, dedicated observations made to quantify the apparent polarisation of the calibration diode were not made and as there were such significant system changes between both Epochs the polarisation information of the diode cannot be reliably extrapolated retrospectively to the Epoch 1 observations. Similarly there have not been any repeat observations to date in Epoch 2 to validate whether the apparent diode polarisation is stable with time. For these reasons the Manchester calibration pipeline does not remove the apparent calibration diode polarisation using the model described by Equation 3.16. Instead the apparent calibration diode polarisation signal is removed by simply determining the relative gains of the receiver channel pairs (see Section 3.7) and summing the channels

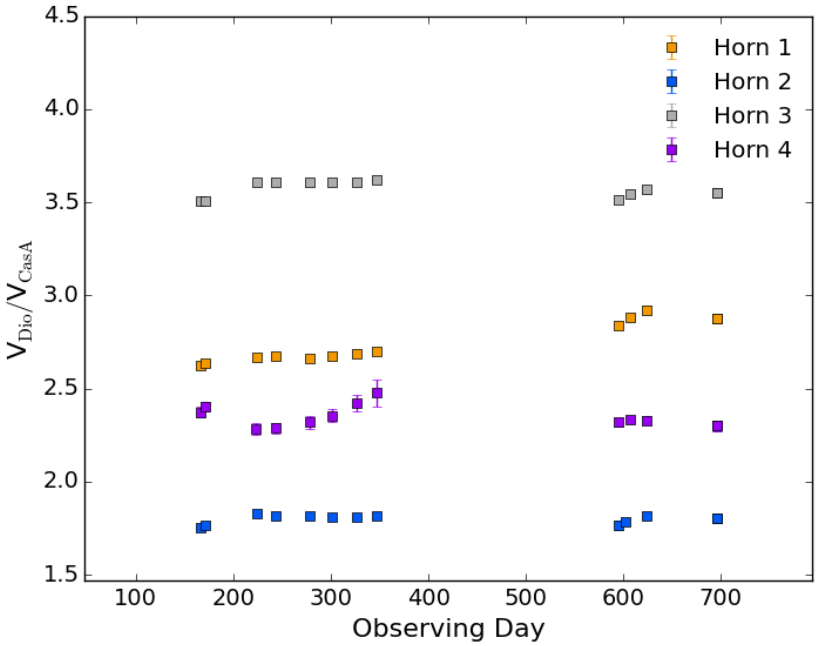

Figure 3.19: Mean monthly measurements of the ratio between the calibration diode and fitted Cas A amplitudes for horns 1 to 4 and frequencies 11 GHz and 17 GHz.

to keep only the intensity component. Summing the channels will also eliminate the uncharacterised polarisation component associated with the MFI channels in feed 1.

The apparent brightness of the calibration diode as recorded by any MFI output channel depends not only on the intrinsic brightness of the diode but also on the near-field interaction between the MFI and diode beams, the relative position of each MFI horn, the power spectrum of the diode signal and the signal attenuation occurring in each radiometer. The calibration diode is housed in a temperature stabilised environment and therefore the apparent brightness temperature of the calibration diode on short timescales is expected to be constant. However, comparing the monthly ratios of the mean calibration diode amplitude with the mean measured Cas A amplitudes shown in Figure 3.19 reveals that on long timescales apparent brightness of the calibration diode is not stable. Table 3.6 shows the complete list of the reported percentage deviations in the apparent calibration diode temperature over the period April 2013 to April 2014. However, long-term variability in the apparent brightness of the calibration diode is not critical as long timescale calibration is performed using astronomical calibrator sources, which is discussed in the next Section.

Table 3.6: Percentage uncertainty in the reported calibration diode apparent brightness per MFI frequency channel pairs over the period April 2013 to April 2014. The upper two rows per horn are correlated channel pairs and the lower two rows are the uncorrelated channel pairs.

Frequency (GHz)	Uncertainty (per cent)
Horn 1	
13	0.93
11	1.20
13	0.93
11	0.84
Horn 2	
19	2.83
17	1.85
19	2.84
17	1.40
Horn 3	
13	1.63
11	1.29
13	1.61
11	1.22
Horn 4	
19	2.22
17	2.35
19	2.80
17	2.68

This Section has introduced the MFI calibration diode and shown how the diode is incorporated into the MFI calibration pipeline. The primary features of the calibration diode were shown including several systematic effects that required correcting before implementation in the calibration pipeline. The calibration diode has been demonstrated to be effective at removing gain variations on timescales of approximately 24 minutes. Over very long timescales, approaching a year, the diode apparent brightness is stable to within a few per cent at all frequencies.

3.6 Astronomical Calibrators

In the previous Section, the TOD are calibrated relative to the apparent brightness of the calibration diode. The next step is to calibrate the TOD to the main beam brightness temperature scale. Regular measurement of astronomical calibrators can be used to put the MFI TOD onto a standard brightness temperature scale. This Section will discuss in detail the two primary MFI calibrator sources, the Crab nebula (Tau A) and Cassiopeia A (Cas A) supernova remnants (SNRs). This is followed by a description of how the source amplitudes were fitted for using analytical Gaussian beams and the `CST` beam models. Fitting uncertainties will also be defined in this Section, which will contribute to the final calibration uncertainty in Section 3.10.

The principle emission mechanism at the MFI frequencies for both Cas A and Tau A is non-thermal synchrotron. A general parameterised form for the spectral energy density (SED) of integrated synchrotron emission is a curved power-law (e.g. Baars et al., 1977; Hafez et al., 2008; Weiland et al., 2011),

$$\left(\frac{S_\nu}{\mathrm{Jy}}\right) = \left(\frac{S_{1\,\mathrm{GHz}}}{\mathrm{Jy}}\right)\left(\frac{\nu}{\mathrm{GHz}}\right)^{\alpha+\beta\log\left(\frac{\nu}{\mathrm{GHz}}\right)}, \tag{3.17}$$

which can also be written in log form as,

$$\log\left(\frac{S_\nu}{\mathrm{Jy}}\right) = \log\left(\frac{S_{1\,\mathrm{GHz}}}{\mathrm{Jy}}\right) + \alpha\log\left(\frac{\nu}{\mathrm{GHz}}\right) + \beta\log^2\left(\frac{\nu}{\mathrm{GHz}}\right), \tag{3.18}$$

where $S_{1\,GHz}$ is the brightness of the source at 1 GHz, ν is the observing frequency, α is the spectral index and β describes the curvature of the spectrum.

Table 3.7: SED models of Tau A from the literature. All models have been normalised to the same reference brightness at 1 GHz.

	α	$\frac{S_{1\,\mathrm{GHz}}}{\mathrm{Jy}}$	$\frac{\mathrm{Frequencies}}{\mathrm{GHz}}$	Epoch
Baars et al. (1977)	-0.299±0.009	1042±77	1−35	≈1970
Hafez et al. (2008)	-0.278±0.007	986±2.1	1−353	2003
Macías-Pérez et al. (2010)	-0.296±0.006	973±19	1−353	2003
Weiland et al. (2011)	-0.302±0.005	977±7	1−353	2005

3.6.1 Tau A

Tau A, also known as Messier 1 or the Crab nebula, is an expanding young pulsar wind driven filled-centre SNR with an angular size of 5×7 arcmin (Green, 2009). The progenitor star to Tau A died approximately 1000 years ago and is thought to be linked to the *guest-star* noted in the records of Chinese astrologers in the year 1054 AD (Hubble, 1928; Breen and McCarthy, 1995). The SED of Tau A has been found to be very accurately represented by a power-law up to frequencies as high as a few hundred GHz (Baars et al., 1977; Hafez et al., 2008; Macías-Pérez et al., 2010; Weiland et al., 2011).

Several recent measurements of the Tau A SED have been made over the frequency range of 1 to 353 GHz using a combination of historical flux density measurements compiled by Baars et al. (1977), *WMAP* 5-year and 9-year data from Macías-Pérez et al. (2010) and Weiland et al. (2011) and a 34 GHz Very Small Array (VSA) measurement by Hafez et al. (2008). Table 3.7 summarises each of the derived Tau A SED models. The disagreement in the expected Tau A flux densities between each of the SED models derived in Hafez et al. (2008), Macías-Pérez et al. (2010) and Weiland et al. (2011) does not exceed 1 per cent at MFI frequencies. Ultimately, the Macías-Pérez et al. (2010) Tau A SED model was adopted for the Manchester calibration pipeline because the flux densities were measured using aperture photometry.

Pulsar wind driven SNR of the age of Tau A are expected to exhibit a secular increase in brightness of 0.16−0.4 per cent year^{-1} (Reynolds and Chevalier, 1984). The secular decay of Tau A can be modelled as a exponential decay of the form,

$$\frac{S}{S_0} = e^{-a(T-T_0)}, \tag{3.19}$$

where a is the half-life of the decay with units of years^{-1}, T is the fractional year the

Table 3.8: Models of the percentage secular decrease in the brightness of Tau A.

Reference	Weiland et al.	Aller and Reynolds	Hafez et al.
Frequency (GHz)	23	8	34
Epoch	2002−2008	1968−1985	2002−2004
a (% year^{-1})	-0.21±0.01	-0.167±0.015	-0.22±0.07

observation was made and T_0 is the year the SED model was normalised to. Observations of the radio flux density of Tau A over the period 1969−85 at 8 GHz found a secular decrease of $a = -0.167 \pm 0.015$ per cent year^{-1} (Aller and Reynolds, 1985). This is the secular decay model adopted by Macías-Pérez et al. (2010). The more recent VSA and *WMAP* measurements of Hafez et al. (2008) and Weiland et al. (2011) found that the secular decay of Tau A over the period 2001−2008 was approximately $a = -0.22$ per cent year^{-1}. The secular decay of Tau A measured by Hafez et al. (2008) and Weiland et al. (2011) were adopted into the MFI calibration pipeline because both measurements are independent, agree at the $1\,\sigma$ level and represent a more recent epoch.

The final SED model for Tau A used to calibrate the MFI observations was,

$$\frac{S_\nu}{\mathrm{Jy}} = \frac{979 \pm 19}{\mathrm{Jy}} \left(\frac{\nu}{\mathrm{GHz}}\right)^{-0.296\pm0.006} e^{-0.0022\pm0.0001(T-2000.0)}, \tag{3.20}$$

where the Macías-Pérez et al. (2010) SED model amplitude has been normalised to the year 2000. Figure 3.20 shows all the literature values of Tau A overlaid with the model described by Equation 3.20, all normalised to the year 2014 to be representative of the expected Tau A SED during the MFI observing period.

As well as being bright, Tau A is also linearly polarised at the 7−8 per cent level at cm-wavelengths (e.g. Page et al., 2007). Figure 3.20 shows the Tau A polarisation fraction, defined as the ratio of the polarised flux density over the intensity flux density, from 1 to 100 GHz. At frequencies of around 5 GHz and below, evidence of depolarisation starts to occur, however at higher frequencies the integrated polarisation fraction of Tau A appears very stable. Taking the weighted average of the polarisation fraction measurements above 8 GHz from Table B.1 gives an expected polarisation fraction of $\Pi = 7.4 \pm 0.14$ per cent over the MFI frequencies. The position angle of Tau A was taken from *WMAP* measurements in Page et al. (2007) that found it to be 150±2 degrees in celestial coordinates and -88±2 degrees in the Galactic coordinate

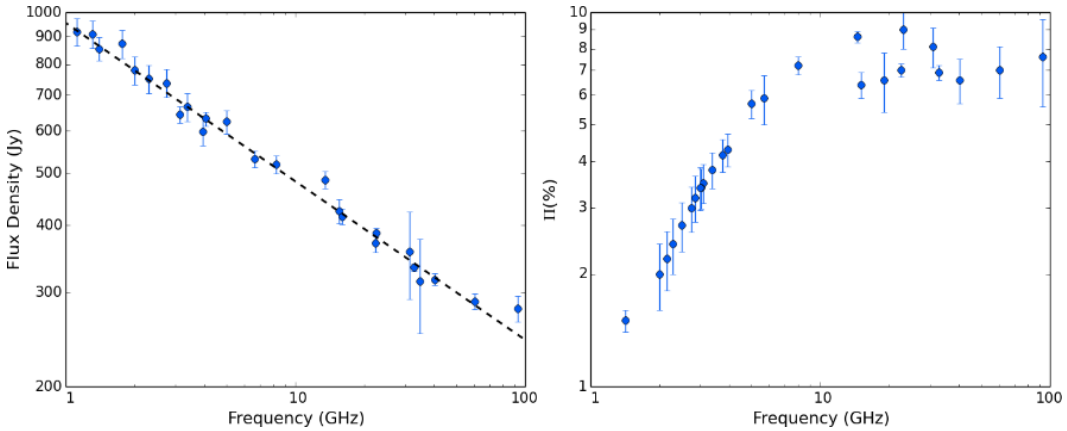

Figure 3.20: Polarisation fraction spectrum of Tau A derived from *WMAP* and other ground based observations. A weighted line of best fit is used to estimate the polarisation fraction at MFI frequencies. For a full list of polarisation fraction references see Appendix B, Table B.1.

frame. The well constrained polarisation properties of Tau A were used to calibrate the absolute modulator positions of the MFI polarimeters.

3.6.2 Cas A

The second primary MFI calibrator source is Cas A. Cas A is a shell-like SNR that is only a few hundred years old and has an angular extent of 5 arcmin (Bell, 1977; Green, 2009). Cas A has a much steeper spectrum than Tau A with a spectral index of approximately $\alpha = -0.770 \pm 0.007$ (Baars et al., 1977). High-resolution 5 GHz Very Large Array (VLA) observations of Cas A at 5 GHz found embedded structures within Cas A that exhibit a range of spectral indices between -0.75 and -0.9 (Anderson and Rudnick, 1996). The integrated effect of these embedded structures within Cas A results in a spectral curvature in the Cas A SED and a frequency dependence in the secular variation of the flux density.

The model for the synchrotron emission that dominates the Cas A SED below 90 GHz can be described using Equations 3.17 and 3.18. Recent measurements of the Cas A SED can be found in Weiland et al. (2011) that uses *WMAP* data, and Hafez et al. (2008) that uses VSA observations. A summary of historical measurements of the Cas A SED can also be found in Baars et al. (1977). Table 3.9 summarises the SED model parameters from all three sources. Over the MFI frequency range, both Baars et al. (1977) and Hafez et al. (2008) model the Cas A SED as a straight power

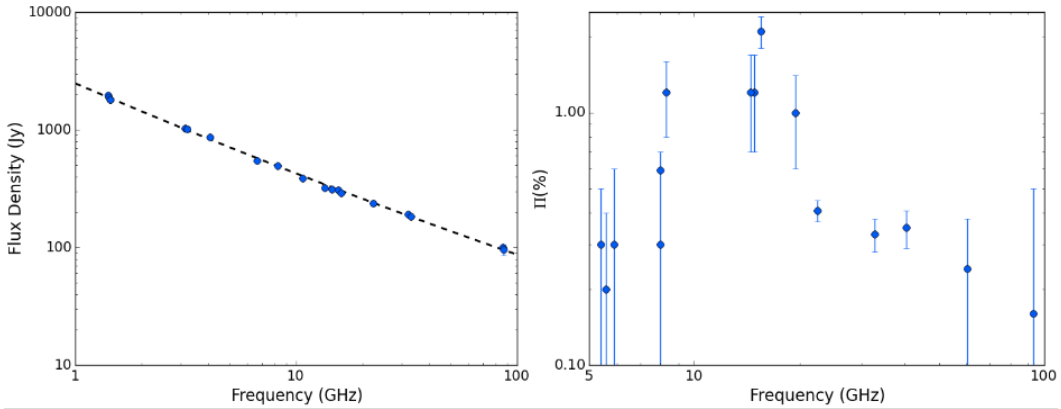

Figure 3.21: *Left*: Integrated flux density measurements of Cas A corrected to the year 2000 taken from Hafez et al. (2008) overlaid upon the Cas A SED model derived in Weiland et al. (2011). *Right:* Literature measurements of the integrated polarisation fraction of Cas A between 1960 and 2005.

Table 3.9: SED models of Cas A from the literature. All the model values have been recalculated to be normalised to the flux density at 1 GHz.

Reference	α	β	$S_{1\,\mathrm{GHz}}$ (Jy)	ν (GHz)	Epoch
Baars et al.	-0.770±0.007	–	2722±150	1–35	≈1980
Hafez et al.	-0.69±0.02	–	2031±57	1–353	2003
Weiland et al.	-0.804±0.011	0.038±0.008	2478±19	1–353	2005

law. However, both acknowledge the possibility of spectral curvature. The analysis in Weiland et al. (2011) found that when combining literature values for Cas A between 1 and 353 GHz along with *WMAP* seven year measurements, the curved spectral SED model provided the best representation of the observations. As the Cas A SED is expected to exhibit some spectral curvature due to significant variations in spectral index within the embedded structures of the SNR the Weiland et al. (2011) Cas A SED model was chosen as the best physical representation of the Cas A SED and was used for MFI calibration. The Weiland et al. (2011) SED model is shown in Figure 3.21 with literature values of Cas A extrapolated to the expected flux densities in 2014.

The secular variation of Cas A has for a long time been known to vary with frequency (Dent et al., 1974; Baars et al., 1977). The Cas A secular variation can be modelled by including a frequency dependence in the exponent of Equation 3.19. The modified

frequency dependent, a, for Cas A can be written as,

$$\frac{a(\nu)}{\text{year}^{-1}} = \theta_a - \theta_b \log\left(\frac{\nu}{\text{GHz}}\right), \tag{3.21}$$

where θ_a and θ_b are constants to be determined. However, there has been some suggestion that the model for the secular decrease of Cas A is more complicated than Equation 3.21 implies (Vinyaikin, 2014). This has not been considered at present for the Manchester MFI calibration pipeline. Hafez et al. (2008) determined θ_a and θ_b using VSA observations of Cas A over a period of 3 years between 2001 and 2004. Equation 3.21 from Hafez et al. (2008) takes the form,

$$\frac{a(\nu)}{\text{year}^{-1}} = \frac{1}{100}\left[0.68 \pm 0.04 - 0.15 \pm 0.04 \log\left(\frac{\nu}{\text{GHz}}\right)\right]. \tag{3.22}$$

The result for a from Equation 3.22 can then be substituted into Equation 3.19 to determine the fractional change in flux density for any epoch.

High resolution polarisation measurements of Cas A reveal that the polarisation vectors at microwave frequencies align parallel to the exterior of the Cas A shell (e.g. Mayer and Hollinger, 1968). Therefore when integrating the entire Cas A shell, all the polarisation vectors should cancel resulting in a net zero polarisation fraction. Figure 3.21 shows a number of historical integrated polarisation fractions measured between 1960 and 2005. In general, these measurements imply an integrated polarisation fraction of ≈ 0.5 per cent over the MFI frequencies. However, a number of historical measurements over 1 per cent can be seen between 8 GHz and 20 GHz in Figure 3.21 but these observations have far larger uncertainties and are still consistent within $3\,\sigma$ with no polarisation from Cas A. For polarisation calibration Cas A is used as a null test to determine the I to Q/U leakage terms for the MFI polarimeters. Ideally, calibration of polarisation leakage would be obtained from bright HII regions but unfortunately the region of sky around the brightest HII region M42 in Orion is heavily contaminated by GSO satellite emission. Other HII regions such as NGC 7027 are embedded in the Galactic plane and cannot be easily distinguished from other nearby Galactic emission at MFI resolutions and frequencies.

3.6.3 Secondary Calibrators

As well as Tau A and Cas A there are several secondary calibrators available to the MFI that are useful for cross-checking the calibration in the final MFI maps. The

brightest secondary calibrator is Cygnus A (Cyg A), which is also the brightest radio Galaxy in the sky. The reason why Cyg A was not used a primary calibrator is that it is approximately half the brightness of Tau A at the MFI frequencies and is situated very close to the bright diffuse Galactic emission of the Cygnus region. The other secondary calibrator available is the giant elliptical galaxy 3C274, which has approximately 10 per cent of the brightness of either of the primary calibrators. Models for the SEDs of both of these two sources can be found in Baars et al. (1977), Ott et al. (1994) and Weiland et al. (2011).

3.6.4 Calibrator Source Measurements

Calibrator observations of Tau A and Cas A are conducted once each, daily. Fixed elevation raster scans are used for Tau A calibration observations and fixed Right Ascension sky raster scans are used for Cas A calibration observations (see Appendix A for a summary of single-dish observing modes). The time for the calibrator source observed to transit the main beam of all four MFI feeds required a minimum observing time of 20 minutes and a sky coverage of 10×10 degrees^2.

As each individual calibrator observation was taken using multiple raster scans all orientated in the same direction, obtaining a solution to the *1/f* noise using the Destriping map-maker was not possible. Instead of Destriping the calibrator raster TOD, the background *1/f* noise was removed by smoothing the TOD using a box kernel with a timescale of 0.1 seconds, which was interpolated through samples within 1.5 FWHM of the source central position. Figure 3.22 shows an example of an 11 GHz Tau A observation in both the map domain and time domain with the smoothed background noise signal overlaid onto the TOD. The `CST` beams were used to generate noiseless simulations of the Tau A calibration observations. The lost calibrator flux density after passing the simulated TOD through the above process was found to be less than 0.04 per cent. The simulations also revealed that the Gaussian fits to the beam overestimate the main beam amplitude by 1.75 per cent.

Calibrator source amplitudes were measured in the local frame of the telescope relative to the local position of the source in the sky. The TOD were transformed from the sky by

$$\Delta\mathbf{A}(t) = \left[\mathbf{A}(t) - \mathbf{A}_{\mathrm{src}}(\alpha, \delta, t)\right] \cos(\mathbf{E}), \tag{3.23}$$

$$\Delta\mathbf{E}(t) = \left[\mathbf{E}(t) - \mathbf{E}_{\mathrm{src}}(\alpha, \delta, t)\right], \tag{3.24}$$

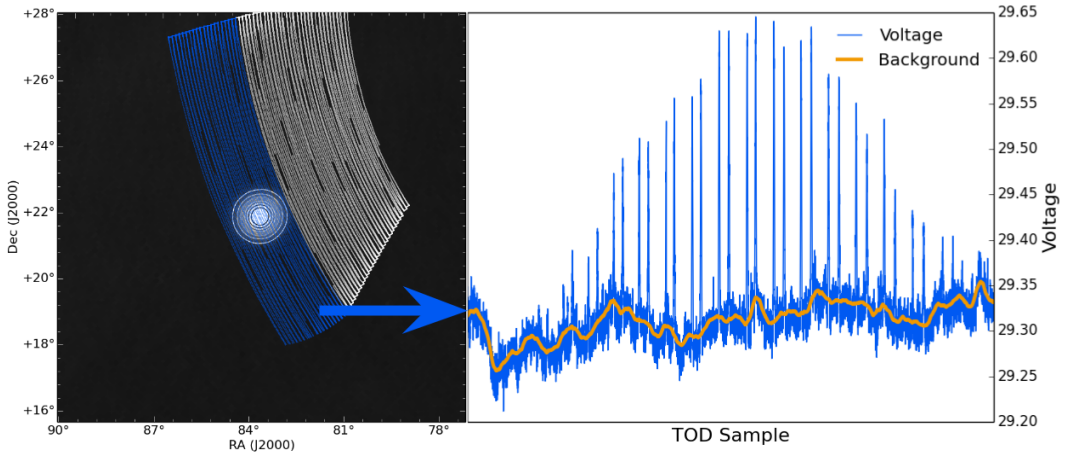

Figure 3.22: *Left:* Image of Tau A from the MFI 11 GHz wide-survey with the scan tracks of a single drift raster scan overlaid. Contours are used to highlight the position of Tau A. *Right:* The measured TOD voltages from a MFI horn 1 11 GHz channel from the blue scan tracks on the image.

where $\Delta\mathbf{A}$ and $\Delta\mathbf{E}$ are the relative azimuth and elevation of the telescope pointing to the calibrator source position; $\mathbf{A}$ and $\mathbf{E}$ are the absolute pointing positions of the MFI and $\mathbf{A}_{\rm src}$ and $\mathbf{E}_{\rm src}$ are the expected absolute azimuth and elevation of the observed source with a Right Ascension (α) and Declination (δ) at time t. The principle benefit of working in the relative local frame is that the MFI beam response will stack with the same orientation regardless of the parallactic angle of the source at the time of observation.

Four methods were implemented into the MFI calibration pipeline for measuring point-like calibration sources. Three methods were based on least-squares fitting of a beam model that was either a Gaussian or derived analytically using the `CST` software. The fourth method used aperture photometry to measure the source flux. Each method has advantages and disadvantages, which will be discussed.

Gaussian Fitting

The QT1 main beam response can be reasonably approximated using a Gaussian model of the form,

$$P_N(\theta,\phi) = Ae^{-0.5\left[\left(\frac{\theta-\theta_0}{\sigma_\theta}\right)^2+\left(\frac{\phi-\phi_0}{\sigma_\phi}\right)^2\right]}+b, \tag{3.25}$$

where θ and ϕ are the offset in elevation and azimuth respectively; A defines the main beam amplitude; σ_θ and σ_ϕ define the width of the main beam response limited to ± 5 per cent of the measured beam FWHM; θ_0 and ϕ_0 can vary by the pointing

uncertainty and define the relative position of the source from the focal centre and b accounts for any arbitrary offset in the background. Equation 3.25 was fitted to MFI observations of the calibrator sources in both the map and TOD domains. Fits in both domains were found to be consistent within the measured amplitude uncertainties.

Beam Model Fitting

Instead of approximating the main beam as a Gaussian, fits could be performed using the `CST` beam models. The main beam response of the `CST` beam models were normalised to unity. Two-dimensional linear interpolation was used to transform the `CST` beam model into a TOD domain representation of the beam using the telescope pointing information for a given observation. The least-squares fit for the `CST` beam model was then dependent only on two parameters, the source amplitude and background emission. Note that the MFI beam will be convolved with the intrinsic calibrator source angular extent of approximately 5 arcmin for Tau A and Cas A. However, the change in the beam FWHM will be less than 1 per cent at 19 GHz and therefore was considered negligible.

When fitting for the source amplitudes, only a limited annulus within the main beam and an annuli far from the main beam were used to perform the fitting procedure. The edges of the MFI main beam can diverge from the `CST` beam models as shown in the radial profiles of Section 3.4 and the beams diverge significantly from being Gaussian outside of the main beam FWHM. By limiting the fitting area, the model fits were found to be less biased. The fitting region was determined by Gaussian fitting to the `CST` beam and measuring the divergence in the fitted Gaussian beam amplitude from unity.

When least-squares fitting to Cas A, special consideration was given to the bright background emission from the nearby HII regions. The HII regions near to Cas A have a peak brightness between 15 per cent to 20 per cent of the peak brightness of Cas A as shown in Figure 3.23. To account for these HII sources a mask is generated from *WMAP* data to identify the lines-of-sight contaminated with bright background emission and the samples that lie within the extent of the background emission are ignored during the fit.

Aperture Photometry

An alternative to model fitting is to use aperture photometry in the map domain to measure the main beam response of a calibrator source. Accurate aperture photometry measurements require complete source sampling, high signal-to-noise per pixel and

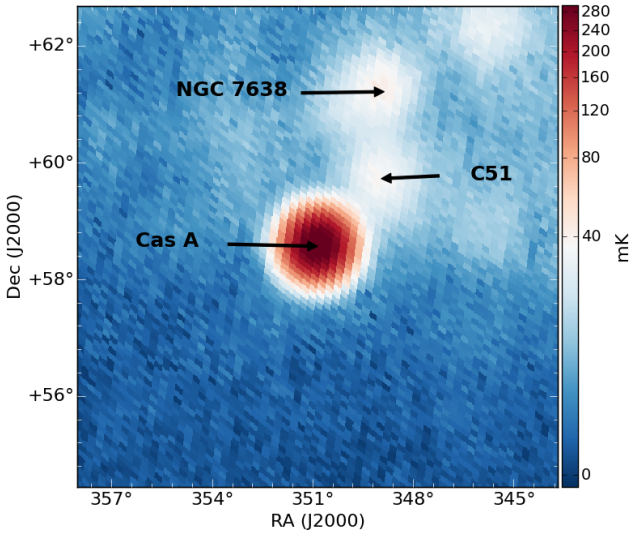

Figure 3.23: Cas A as seen at 11 GHz by the MFI. The bright HII region C51 is very close to Cas A. C51 has a peak amplitude of ∼ 15 per cent of the peak amplitude of Cas A at 11 GHz and ∼ 20 per cent of the Cas A peak amplitude at 19 GHz. C51 must be masked when fitting Cas A to avoid biasing the best fit parameters.

small pixel sizes to avoid aliasing effects. Aperture photometry of a source in the map domain is defined as

$$S_{\rm src} = \sum_{\rm aper} S_{\rm pix}\Omega_{\rm pix} - \langle S_{b,{\rm pix}}\rangle\, N_{\rm aper}, \tag{3.26}$$

where $S_{\rm src}$ is the integrated source flux density in the map, $S_{\rm pix}$ is the flux density contribution of each pixel, Ω_{pix} is the solid angle of the pixels in the map, $\langle S_{b,{\rm pix}}\rangle$ is the mean background pixel flux density contribution and $N_{\rm aper}$ is the number of pixels within the aperture.

Aperture photometry per calibrator observation was performed by binning the TOD into `HEALPix` maps with $N_{\rm side} = 256$ (a pixel size of ∼ 13.74 arcmin). The source flux density was measured within an aperture of radius 0.75 FWHM and the background estimated from an annulus larger than 1.5 FWHM. The integrated flux density of a source is related to the source peak amplitude ($S_{\rm peak}$) by

$$S_{\rm peak}\Omega_{\rm mb} = \sum S_{\rm pix}\Omega_{\rm pix}. \tag{3.27}$$

Aperture photometry typically has a much higher uncertainty than the model fitting methods and for this reason was only used as a cross-check of the fitted amplitude

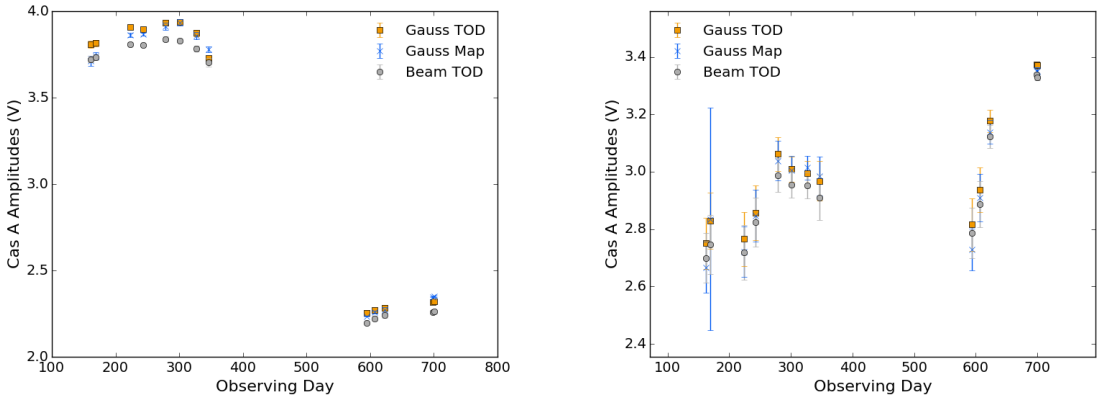

(a) Horn 1 13 GHz. (b) Horn 3 13 GHz

Figure 3.24: Measured raw voltage amplitudes of Cas A at 13 GHz as seen by the difference correlated channels in MFI feeds 1 and 3.

measurements.

Figure 3.24 shows the measured voltage amplitudes of Cas A as seen by the 13 GHz correlated difference channels of MFI feeds 1 and 3. Each data point in Figure 3.24 represents the mean voltage amplitude over approximately 30 days of Cas A observations. The associated observing day of each point is the mean Julian date of the Cas A observations within the bin. The uncertainty associated with each data value is calculated from a Gaussian fit to a histogram of all the measurements within each data point. To avoid biases due to outliers, the Gaussian fit was performed iteratively.

A point to note in Figure 3.24 is that the Gaussian fits in the TOD and map both seem to systematically estimate the amplitude of the calibrator source voltage higher than the `CST` beam model fits by 2.3 ± 0.5 per cent. This is consistent with the 1.7 per cent amplitude overestimate predicted by fitting Gaussian beam models to the `CST` beam models by just over $1\,\sigma$. The general fluctuations in the measured voltage amplitudes from all four methods are largely consistent within the uncertainties of each 30 day bin. From this point forward all discussion of calibrator source measurements use measurements derived using the `CST` beam model fitting method.

The fitting uncertainties associated with each MFI feed are listed in Table 3.10. The fitting uncertainties are estimated from the mean uncertainty associated with each of the 30 day bins and are shown in Figure 3.24 for the correlated MFI channels. Values are given separately for Epoch 1 and Epoch 2. The factor of two improvement in the fitting uncertainty for horn 4 is expected due to the replacement of the FEM LNAs.

Table 3.10: Mean fitting percentage uncertainties derived from measurements of Cas A voltage amplitudes over approximately 30 day intervals as measured by the correlated MFI channels.

	Epoch 1	Epoch 2
Horn 1	0.42 %	0.40 %
Horn 2	1.16 %	1.03 %
Horn 3	0.53 %	0.44 %
Horn 4	2.33 %	0.98 %

This Section has discussed in detail the SED models of the MFI flux density calibrators and also the methods used to fit for the observed main beam amplitude of point sources. The work in this Section will be used later to describe the MFI relative monthly gain corrections. The main contribution to the calibration uncertainty in this Section are the fitting errors described by Table 3.10. These uncertainties describe the knowledge of MFI gain at a given instance of time.

3.7 r-Factors

Each MFI receiver can be imagined as being composed of two individual sections. The first section includes all the components in the MFI FEM up until the 180 degree hybrid in the BEM. The second section includes all the components after the 180 degree hybrid. For the horn 1 receivers during Epoch 2 the same division can be imagined to occur before and after the second 90 degree hybrid. Gains in the first section of the receiver are principally due to the LNAs in the FEM and are referred to as g_x and g_y. Gains from the second half of each receiver have contributions from components such as the square-law detectors or analogue-to-digital converters. These gains are unique to each channel output and are referred to as s_x and s_y for the uncorrelated channels and s_{x-y} and s_{x+y} for the correlated channels. The voltage outputs per channel for the MFI can therefore be written as

$$V_x = s_x g_x^2 \frac{T_{\rm sys}}{2}, \tag{3.28}$$

$$V_y = s_y g_y^2 \frac{T_{\rm sys}}{2}, \tag{3.29}$$

$$V_{x-y} = s_{x-y}\frac{g_x^2 + g_y^2}{2}\frac{T_{\rm sys}}{2}, \tag{3.30}$$

$$V_{x+y} = s_{x+y}\frac{g_x^2 + g_y^2}{2}\frac{T_{\rm sys}}{2}, \tag{3.31}$$

for all the receivers apart from the horn 1 receiver in Epoch 2. For the horn 1 Epoch 2 receivers the x and y channels are also correlated and therefore are defined as

$$V_x = s_x\frac{g_x^2 + g_y^2}{2}\frac{T_{\rm sys}}{2}, \tag{3.32}$$

$$V_y = s_y\frac{g_x^2 + g_y^2}{2}\frac{T_{\rm sys}}{2}. \tag{3.33}$$

Equations 3.28 to 3.33 are strictly true for an unpolarised source. If the source is polarised the channel outputs will have polarised terms with gain combinations of $0.5(g_x^2 - g_y^2)$ and $g_x g_y$, which are omitted here for clarity.

To combine MFI channels to isolate the intensity or polarisation components of the observed emission, the relative fractional gains or *r-factors* between channels must be determined. The *r-factors* for the MFI uncorrelated and correlated channel pairs are defined as

$$r_u = \frac{s_x g_x^2}{s_y g_y^2}, \tag{3.34}$$

$$r_c = \frac{s_{x-y}}{s_{x+y}}, \tag{3.35}$$

where r_u and r_c are the *r-factors* for the uncorrelated and correlated channels respectively. For pseudo-correlation receivers that use reference loads, such as *Planck*, the determination of channel *r-factors* are related to the minimisation of *1/f* noise (e.g., Mennella et al., 2003, 2010). For most channel pairs in the MFI, *r-factors* minimise Stokes parameter leakage terms. However for the correlated polarisation MFI channel pairs, which will be differencing the same gain fluctuations, the optimum determination of the channel pair *r-factor* also minimises *1/f* noise contributions. For example, Figure 3.25 shows how the correlated polarisation MFI channel pair in horn 3 at 13 GHz has a clear minimum when the two channels are balanced at around $r = 0.83$. For comparison the figure also shows that the knee frequency of the intensity or uncorrelated channel outputs are largely unaffected by changes in *r-factor*.

The *r-factors* for channel pairs can be derived using a bright, unpolarised source. For example, the *r-factors* for the uncorrelated MFI channels when the MFI is pointing

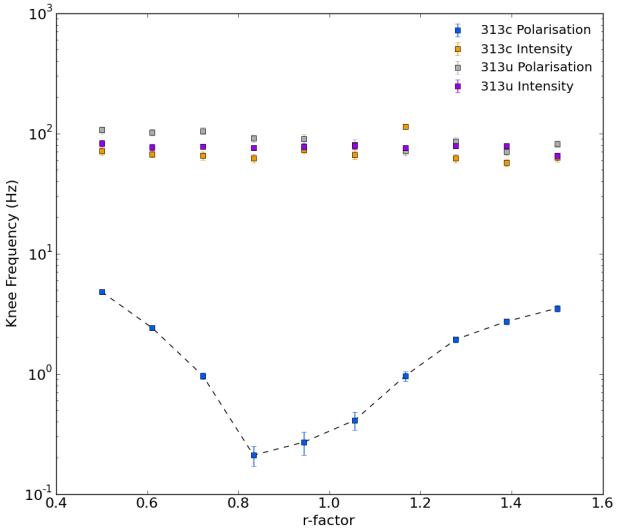

Figure 3.25: Change in the best fit knee frequencies of combined MFI horn 3 channels at 13 GHz from an observation of a clear region of sky in Epoch 2. Intensity and uncorrelated channel pairs are largely unaffected by changing *r-factors*. However, the *1/f* noise in correlated polarisation channel pairs is highly dependent on the *r-factor* determination.

at Cas A is,

$$r_u = \frac{V_x}{V_y} = \frac{s_x g_x^2 T_{\mathrm{CasA}}}{s_y g_y^2 T_{\mathrm{CasA}}}, \tag{3.36}$$

where the terms are as before in Equation 3.34 and T_{CasA} is the antenna temperature of Cas A, which will be almost identical in both channels except for a small (< 0.1 per cent) difference due to the slightly different channel amplifier bandpass responses.

Figure 3.26 shows four lines indicating the change over time in the recorded MFI *r-factors* for the 13 GHz and 17 GHz correlated channels of horns 1, 2, 3 and 4. The line is derived from the mean *r-factor* in approximately 30 day bins, using the same binned measurements of Cas A from the previous Section. A key feature in the plot to notice is dramatic change in the relative amplifier gains of the channels in horn 1 and horn 4 between Epoch 1 and Epoch 2 due to large changes in the system. The *r-factors* derived for horn 2 and horn 3 seem to remain stable throughout the lifetime of the MFI. However, the dispersion of the *r-factors* within Epochs is not insignificant, with variations approaching 5 per cent for some channel pairs. Table 3.11 lists the mean *r-factors* associated with Epoch 1 and Epoch 2.

Table 3.11: Mean *r-factors* per MFI channel pair for Epoch 1 and Epoch 2. The uncertainty is the standard deviation in all the measured *r-factors* in each respective Epoch.

Channel Pair	Epoch 1	Epoch 2
Horn 1		
13 GHz r_c	0.959±0.014	0.787±0.004
11 GHz r_c	1.015±0.004	0.994±0.002
13 GHz r_u	1.035±0.026	0.854±0.009
11 GHz r_u	1.235±0.036	0.935±0.009
Horn 2		
19 GHz r_c	0.731±0.004	0.744±0.006
17 GHz r_c	0.965±0.002	0.955±0.003
19 GHz r_u	0.963±0.035	0.944±0.041
17 GHz r_u	1.369±0.025	1.352±0.014
Horn 3		
13 GHz r_c	0.898±0.007	0.902±0.015
11 GHz r_c	0.905±0.004	0.910±0.003
13 GHz r_u	1.000±0.018	0.992±0.008
11 GHz r_u	1.105±0.017	1.097±0.008
Horn 4		
19 GHz r_c	1.059±0.010	0.937±0.012
17 GHz r_c	0.863±0.010	0.941±0.008
19 GHz r_u	1.184±0.062	0.820±0.031
17 GHz r_u	1.024±0.060	0.841±0.016

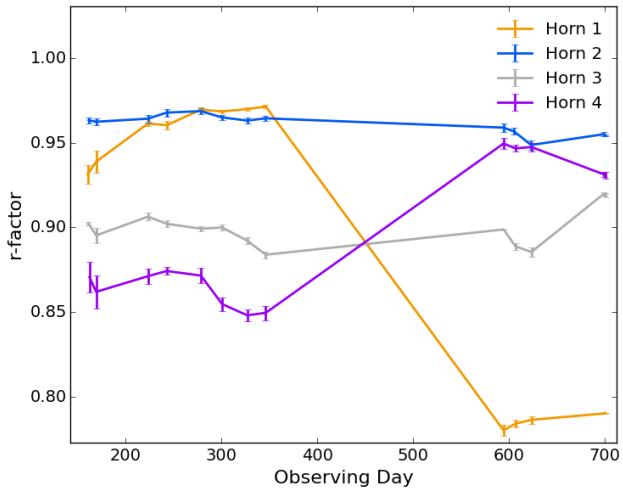

Figure 3.26: MFI *r-factors* calculated using ratios of beam model fitted Cas A voltage amplitudes for the horns 1, 2, 3, and 4 correlated channels at 13 GHz and 17 GHz. The large change in *r-factors* before and after 514 days for horns 1 and 4 is due to the significant modifications to the receivers that occurred.

The relative gains of the *r-factors* appear to change significantly over long time scales. Therefore the pseudo-monthly *r-factor* measurements for every channel pair are saved in a `FITS` table. When combining the MFI channel pairs from scientific observations, the *r-factor* at the time of the observation is determined using nearest neighbour interpolation of the *r-factors* derived from Cas A. As shown earlier these changes in the *r-factor* of channel pairs should not affect the receiver noise properties for the MFI intensity channel pairs.

This Section has discussed how the MFI *r-factors* for each channel pair were determined and summarised how the *r-factors* are included into the Manchester calibration pipeline. Accurate determination of the MFI *r-factors* is critically important for accurate flux density calibration and minimising leakage between intensity and polarisation. The variations in the MFI *r-factor* are a significant contribution to the calibration uncertainty. The maximum uncertainty due to the *r-factors* can be approximated from the statistical uncertainty of each monthly *r-factor* measurement and the mean change in the *r-factors* between bins. This is discussed more in Section 3.10.

3.8 Colour Corrections

Colour corrections are factors that account for the difference in the observed frequency (ν_o) or flux density of a source compared to an arbitrary reference frequency (ν_c) or flux density at a reference frequency due to the receiver bandpass (e.g., Jarosik et al., 2003; Leahy et al., 2010; Zacchei et al., 2011). The flux density of a source at an MFI channel output is defined as:

$$S = \int G(\nu)S(\nu)\mathrm{d}\nu, \tag{3.37}$$

which is the integration of the product of the bandpass (G) and the source SED ($S(\nu)$). The measured flux density of the source is then

$$S_\nu = \frac{\int G(\nu)S(\nu)\mathrm{d}\nu}{\int G(\nu)\mathrm{d}\nu}. \tag{3.38}$$

For a flat spectrum source, the flux density is the same at all frequencies regardless of the receiver bandpass. Therefore the colour correction factor would be unity at all reference frequencies, ν_c. Figure 3.27a shows the interaction between a flat receiver bandpass and a flat spectrum source SED. The observed frequency (ν_o) of the source flux density is always equal to the arbitrary reference frequency (ν_c) flux density. However, if the source has a steep spectrum SED such as in Figure 3.27b, the observed source frequency will be weighted towards one side of the receiver bandpass. In this case the choice is either change the reference frequency to match the observed source frequency or change the observed flux density to match the expected flux density at the reference frequency. For the MFI calibration pipeline, colour corrections are applied to the source flux densities. The choice of reference frequency (ν_c) will dictate the magnitude of the flux density colour corrections. The choice of reference frequency should be informed by the receiver bandpass to minimise the size of the colour corrections needed. One possible method for choosing the reference frequencies is to calculate the weighted central frequency per receiver bandpass using,

$$\nu_c = \frac{\int G(\nu)\nu\mathrm{d}\nu}{\int G(\nu)\mathrm{d}\nu} \tag{3.39}$$

however the problem with this is that every channel will be calibrated to a slightly different reference frequency. Instead, the Manchester calibration pipeline simply uses the nominal MFI bandpass frequencies of 11 GHz, 13 GHz, 17 GHz and 19 GHz.

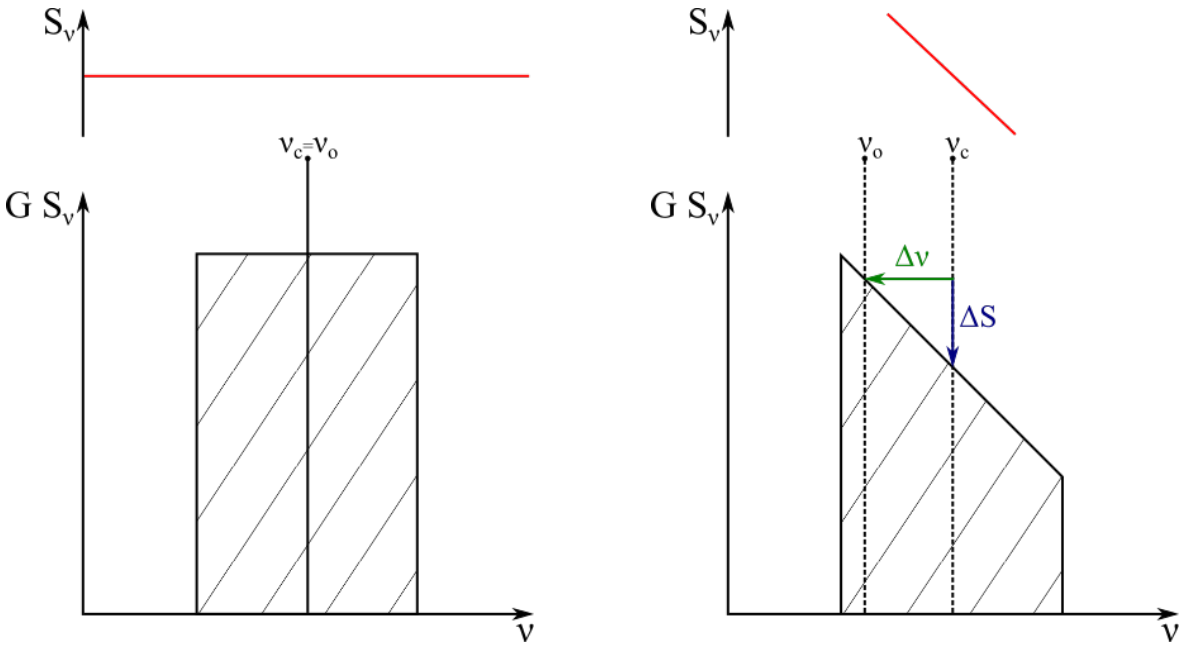

Figure 3.27: Illustrative example of colour corrections for a (*Left*) flat and (*Right*) steep spectrum source interacting with a square spectrum bandpass. The red line indicates the model source spectrum and the black rectangle is the convolution of the source spectrum with the bandpass. Distances have been exaggerated for clarity.

The definition for colour correction is simply the ratio between the expected flux density at the reference frequency and the expected flux density at the observed frequency,

$$C(\alpha) = \frac{S_{\nu_c}}{S_{\nu_o}}, \tag{3.40}$$

where C is the colour correction factor, which is dependent on the spectral index (α) of the observed source SED. Substituting the observed source flux density with Equation 3.38 gives the full general form for colour correction,

$$C(\alpha) = S(\nu_c)\frac{\int G(\nu)\mathrm{d}\nu}{\int G(\nu)S(\nu)\mathrm{d}\nu}, \tag{3.41}$$

where $S(\nu)$ is a model describing the SED of the source being observed and S_{ν_c} has been replaced by $S(\nu_c)$ describing the model SED flux density at the frequency ν_c. A further simplification of Equation 3.41 can be made if the source SED is expected to be modelled by a simple power-law over the receiver bandpass frequencies, meaning that,

$$S(\nu) = S_0\nu^{\alpha}, \tag{3.42}$$

where α is the source spectral index and S_0 is an arbitrary scaling constant. Substituting Equation 3.42 into Equation 3.41 gives,

$$C(\alpha) = \nu_C^{\alpha}\frac{\int G(\nu)\mathrm{d}\nu}{\int G(\nu)\nu^{\alpha}\mathrm{d}\nu}. \tag{3.43}$$

Using Equation 3.43 the typical magnitude of the MFI colour corrections can be estimated for a range of sources with different spectral indices. Table 3.12 shows the average colour correction required per MFI horn for the 13 GHz and 19 GHz channels assuming a flat-spectrum calibrator source. Note that the MFI calibration pipeline colour corrects astronomical calibrator sources to appear as flat-spectrum sources. Typical sources observed by the MFI will have a spectral index range of $\alpha = -1$ due to synchrotron emission to $\alpha = 2$ due to spinning dust emission or potential calibrator sources such as Jupiter. The corresponding systematic error in the flux density of a source that is accounted for with colour corrections is not expected to exceed the 2 per cent level.

To perform colour corrections on the measured flux densities of observed sources requires measuring the MFI bandpass responses ($G(\nu)$) for every MFI channel. The bandpasses were measured during the MFI commissioning phase by connecting a spectral analyser to a pre-bandpass integration output from the MFI BEM. During the

Table 3.12: Colour correction factors for the 13 and 19 GHz MFI uncorrelated channels of horns 1, 2 and 3. Horn 4 colour corrections are calculated assuming a model top-hat bandpass.

α	-2	-1	0	1	2
Horn 1	0.968	0.985	1	1.013	1.024
Horn 2	0.976	0.988	1	1.010	1.019
Horn 3	0.972	0.988	1	1.009	1.015
Horn 4	0.997	0.999	1	1.000	0.999

bandpass measurements, QT1 was pointed at an empty region of sky. The measurements of the MFI bandpasses were undertaken by Roger Hoyland. Figure 3.28 shows the bandpasses for the correlated channel frequencies of horn 1 and horn 2. The bandpasses have been normalised to an integrated area of unity. Note that the bandpass for horn 4 has never been measured for either Epoch and therefore horn 4 colour corrections assume a model top-hat bandpass response, which from visual inspection of Figure 3.28 should be a reasonable approximation. Also note that no repeated bandpass measurements have been made of the horn 1 receivers after being extensively changed during Epoch 2. Therefore horn 1 colour corrections may be unreliable for Epoch 2 observations. Finally, Figure 3.28 shows that the 11 and 13 GHz bandpasses have large tails that are far broader than the expected 2 GHz bandwidth that are approximately a factor of 20 below the peak bandpass response. Bandpass tails are less than ideal but should be accounted for by the colour correction factors.

For sources with an unknown SED, the colour corrections need to be calculated using a simple iterative procedure:

- Fit an SED model to measured flux densities.
- Determine the local spectral index around each measurement.
- Apply colour corrections to each measurement and repeat.

Typically the iterative procedure above will converge within just a few steps.

This Section has discussed the concept of colour corrections for sources that vary across the receiver bandpass. The magnitude of colour corrections for the MFI are not expected to exceed 2 per cent for any given astronomical source. Therefore calibration uncertainties associated with the MFI bandpasses are expected to be much smaller than 2 per cent, even for horn 1 Epoch 2 and horn 4 where the bandpass responses are

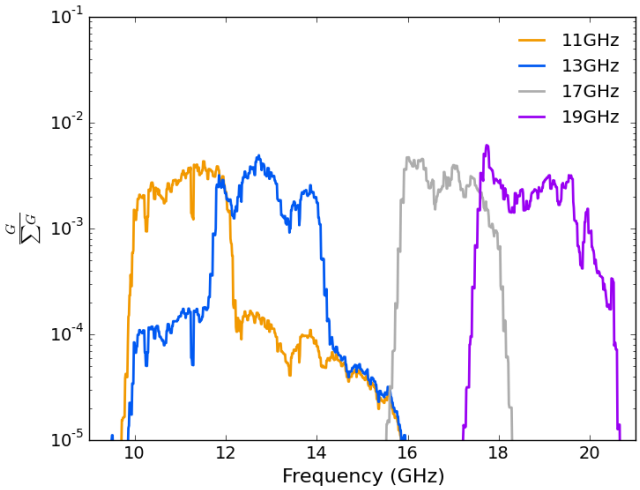

Figure 3.28: MFI bandpasses for 11, 13, 17 and 19 GHz for the correlated channels of horn 1 and horn 2.

only approximately known.

3.9 Atmosphere

For terrestrial observations the atmosphere appears as a source of large-scale black-body emission with a brightness temperature of a few Kelvin at microwave frequencies. However, the atmospheric brightness temperature increases rapidly near to the 22 GHz water line, meaning that the higher MFI frequency channels are expected to be the most affected by atmospheric effects. On smaller scales, the spatial inhomogenities in the atmosphere can imprint *1/f* type noise in the TOD. The atmosphere is also a source of absorption for celestial sources, the amount of absorption being dependent on atmospheric water content and observing elevation angle. The atmosphere is not expected to have any intrinsic contribution to the polarisation observations at MFI frequencies (e.g., Hanany and Rosenkranz, 2003) but is still important as a contribution to I to Q/U leakage.

The contribution of atmospheric emission to the receiver system temperature can be modelled using radiative transfer (e.g., Rohlfs and Wilson, 2004),

$$T_{\rm sys} = T_r + T_{\rm atm}\left[1 - e^{-\tau_0 \mathrm{A(el)}}\right] \tag{3.44}$$

where $T_{\rm atm}$ is the black-body temperature of the atmosphere, τ_0 is the zenith opacity of

the atmosphere and A(el) is the airmass along the line-of-sight for elevation el. As the atmosphere is optically thin, a Taylor expansion can be performed on the exponential term resulting in,

$$T_{\rm sys} = T_r - T_{atm}\tau_0 A(\mathrm{el}), \tag{3.45}$$

where $T_{atm}\tau_0 A(\mathrm{el})$ is the atmospheric brightness temperature. For elevations between 10 degrees and 80 degrees the airmass of the atmosphere can be approximated as an infinite, uniform slab. The airmass can therefore be defined as the cosecant of the elevation angle,

$$\mathrm{A(el)} = \csc(\mathrm{el}). \tag{3.46}$$

Absorption of celestial emission can be modelled as,

$$T'_{\rm src} = T_{\rm src} e^{-\tau_0 \mathrm{A(el)}} \approx T_{\rm src}\left[1 - \tau_0 A(\mathrm{el})\right], \tag{3.47}$$

where $T'_{\rm src}$ is the recorded antenna temperature of the source being observed and $T_{\rm src}$ is the intrinsic source antenna temperature.

The two principal contributions to atmospheric emission and absorption at radio wavelengths are from oxygen and water. Atmospheric water content is usually quantified using precipitable water vapour (PWV). Predictions for the atmospheric opacity were made using the `am` atmospheric model (Paine, 2004) and measurements of PWV from a meteorological station near to the Izana observatory. The atmosphere above the Izana observatory was modelled assuming the U.S. standard atmosphere (on Extension to the Standard Atmosphere et al., 1976), a water vapour scale height of 2 km and an atmospheric pressure and temperature of 755 mbar and 284 K respectively. Figure 3.29 shows the difference between the expected zenith opacity over the Izana observatory between 10 and 20 GHz for a dry oxygen only atmosphere and an atmosphere containing the median Izana PWV content of 3.7 mm. For the 11 and 13 GHz channels, water content has a small affect on zenith opacity, with the typical opacity value of $\tau_0 \approx 6 \times 10^{-3}$. At 17 and 19 GHz zenith opacity exhibits large variations between $\tau_0 \approx 7 \times 10^{-3}$ and $\tau_0 \approx 1 \times 10^{-2}$. The contribution of atmospheric emission at MFI frequencies, assuming an air temperature of 284 K, is approximately 2 K.

Dedicated atmospheric observations were made by the MFI daily using sky-dips. The sky-dip observations were performed with QT1 pointing towards 270 degrees azimuth while continuously slewing in elevation. Figure 3.30 shows an example of the MFI channel voltage response during a sky-dip observation with time at 11 GHz and

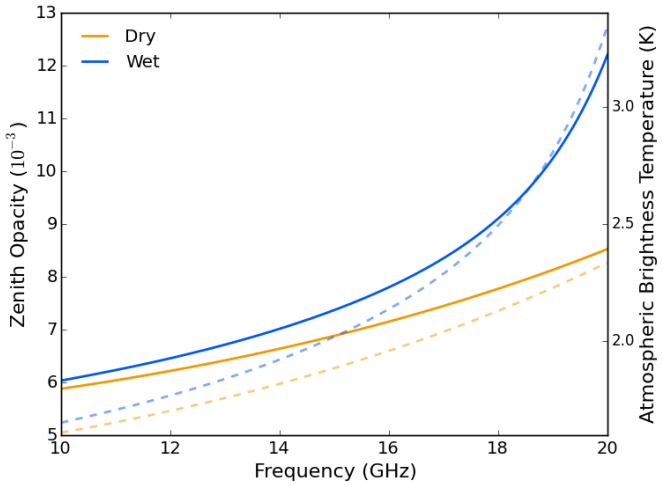

Figure 3.29: Properties of the atmosphere above the Izana observatory as predicted by the `am` atmospheric model. The solid lines show the zenith opacity for a dry atmosphere and an atmosphere with 3.7 mm PWV with frequency. The dashed lines show the change in the expected atmospheric brightness temperature with frequency.

Table 3.13: Range of PWV values recorded at the AEMET-Izana meteorological station situated ~ 1 km from the Izana Observatory. The median recorded atmospheric PWV between November 2012 and April 2015 was 3.7 mm. The station temperature is ~ 283 K and the pressure is ~ 772 hPa.

Percentage Time	<25 %	<50 %	<75 %	<99 %
PWV (mm)	2.1	3.7	6.3	11.0

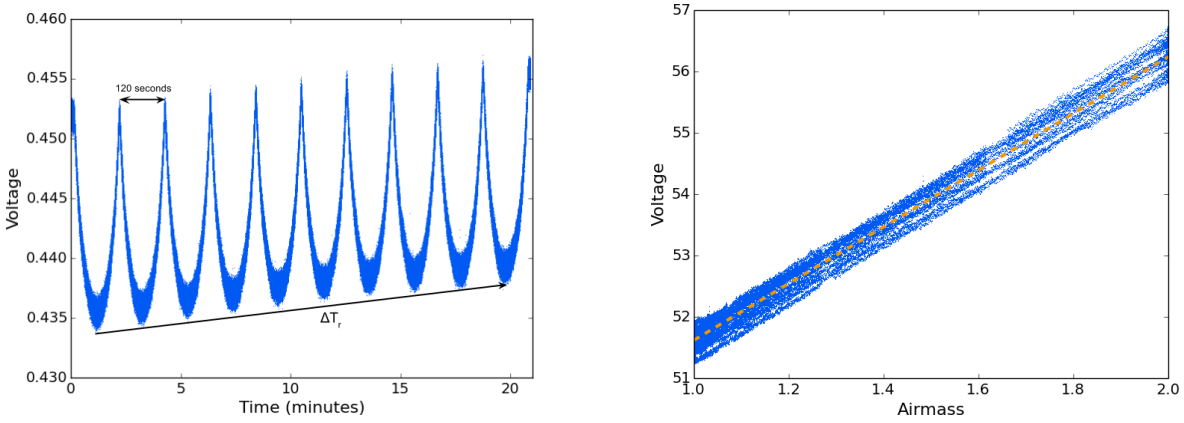

Figure 3.30: *Left*: Change in an 11 GHz channel voltage response with time. Note that the baseline system temperature ΔT_r is changing with time and must be corrected for. A complete up-and-down sky-dip would take 120 seconds to perform. *Right*: Change in MFI voltage response in a 19 GHz MFI channel with airmass. A linear best fit model is overlaid.

airmass at 19 GHz. The atmospheric brightness temperature, $T_{\rm atm}\tau_0$, was determined from the gradient between the MFI voltage response and airmass by performing a linear fit to Equation 3.45 as shown by the dashed line in the figure.

An important quantity to determine for MFI calibration is the atmospheric transmission at the zenith defined as $\mathrm{T} = 1-\tau_0$. Figure 3.31 compares the measured median atmospheric transmission at MFI frequencies with the atmospheric transmission predicted by `am` for 0, 3.7 and 11.1 mm PWV. The uncertainties in the figure represent the total range of transmission measured from 323 sky-dip observations spanning the lifetime of the MFI. At 11 and 13 GHz the `am` model predictions for atmospheric transmission appear to agree with those observed assuming the median atmospheric PWV of 3.7 mm. The 17 and 19 GHz channels are more closely represented by 11.1 mm PWV. Crucially, the general trend of the predicted atmospheric transmission is observed.

At present the effects of atmospheric absorption were not included into the MFI calibration pipeline. This will result in a minimal addition of a 0.5 per cent calibration uncertainty in the 11 and 13 GHz channels, a 1 per cent calibration uncertainty at 17 GHz and a significant calibration uncertainty of 2 per cent at 19 GHz. However, these additional uncertainties are all lower than other sources of uncertainty at each frequency. Note also that periods of high atmospheric PWV are typically also more noisy and are flagged during data processing and therefore do not contribute to the final calibrated MFI TOD.

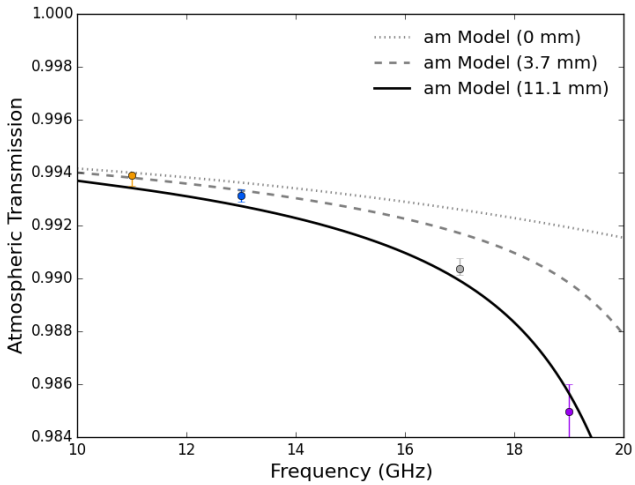

Figure 3.31: Comparison between measured transmission assuming $T_{\mathrm{atm}} = 284\,K$ and atmospheric transmission predicted by the `am` atmospheric model.

3.10 Calibration Overview

In this final Section, the methods and results of the previous Sections will be combined to determine the final calibration of the MFI TOD and an overview of the Manchester calibration pipeline steps is shown. Finally, at the end of this Section the total calibration uncertainty will be estimated using the contributions from all previous Sections and compared with the desired calibration uncertainty goal of 1 per cent.

Before describing the Manchester MFI calibration procedure one final calibration tool must be derived. In Section 3.5 it was shown how the MFI TOD are calibrated in terms of apparent diode temperatures on timescales of 24 minutes. To put the TOD onto the main beam brightness temperature scale, a monthly relative calibration function was determined using Tau A and Cas A. The calibration model is defined as

$$R = \frac{\langle V_{\mathrm{cal}} \rangle \, S_{\mathrm{src}}(\nu)}{\langle V_{\mathrm{src}} \rangle \, C(\alpha)}, \tag{3.48}$$

where $\langle V_{\mathrm{cal}} \rangle$ and $\langle V_{\mathrm{src}} \rangle$ are the mean diode and source voltages over periods of approximately 30 days. The $S_{\mathrm{src}}(\nu)$ and $C(\alpha)$ are the source SED model and bandpass colour corrections as defined in Sections 3.6 and 3.8. Figure 3.32 shows the raw individual measurements of R using Cas A and Tau A using the correlated 11 GHz horn 1 channel pair and also the 17 GHz horn 2 correlated channel pair. There is a small divergence of 1 per cent between the Cas A and Tau A measurements that becomes clear when the

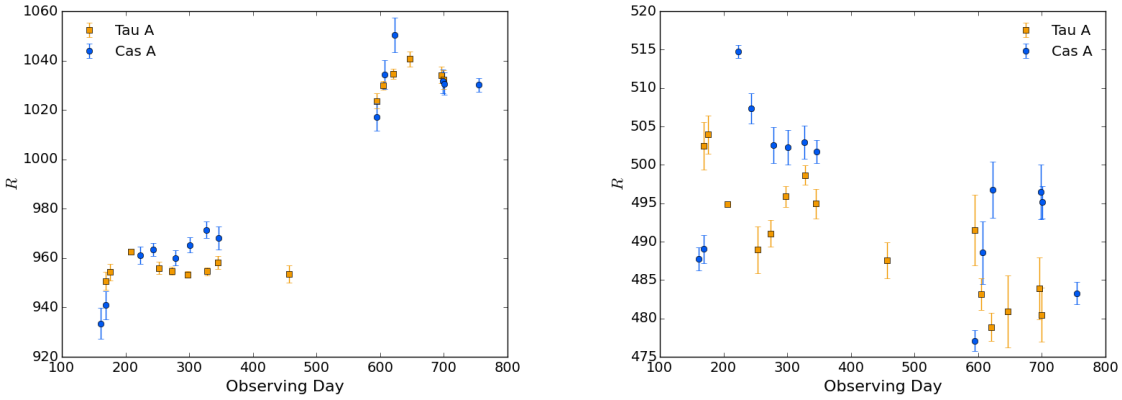

(a) (b)

Figure 3.32: The relative calibration model is derived from the combination of Tau A and Cas A observations. Here the monthly relative calibration model is derived separately from the Tau A and Cas A observations. *Left*: Horn 1 11 GHz. *Right*: Horn 2 17 GHz.

calibrator amplitudes are binned per month as shown in the figure. The source of the divergence was attributed to a systematic fitting offset in the Cas A amplitude due to the bright HII regions near Cas A.

Incorporating R into the Manchester calibration pipeline, the full calibration procedure applied to all MFI TOD is:

- Determine *r-factor* for a channel pair at the time of the observation.
- Sum TOD pairs using *r-factor*.
- Sum diode voltage pairs using *r-factor*.
- Define a gain model using the summed diode voltages as in Section 3.5.
- Divide summed TOD with linear interpolated gain model.
- Determine the value of R for the channel pair at the time of the observation.
- Multiply TOD by R calibrating the TOD into units of $\mathrm{Jy\,beam^{-1}}$.
- Convert to main beam brightness temperature scale using the main beam size derived in Section 3.4.

The TOD were converted to the main beam brightness temperature scale using (Rohlfs and Wilson, 2004)

$$T_{\mathrm{mb}} = \frac{\lambda^2}{2k}\frac{S_\nu}{\Omega_{\mathrm{mb}}}, \tag{3.49}$$

where T_{mb} is the main beam brightness, S_ν is the flux density in $\mathrm{Jy\,beam^{-1}}$, Ω_{mb} is the main beam solid angle, λ is the observed wavelength and k is the Boltzmann constant.

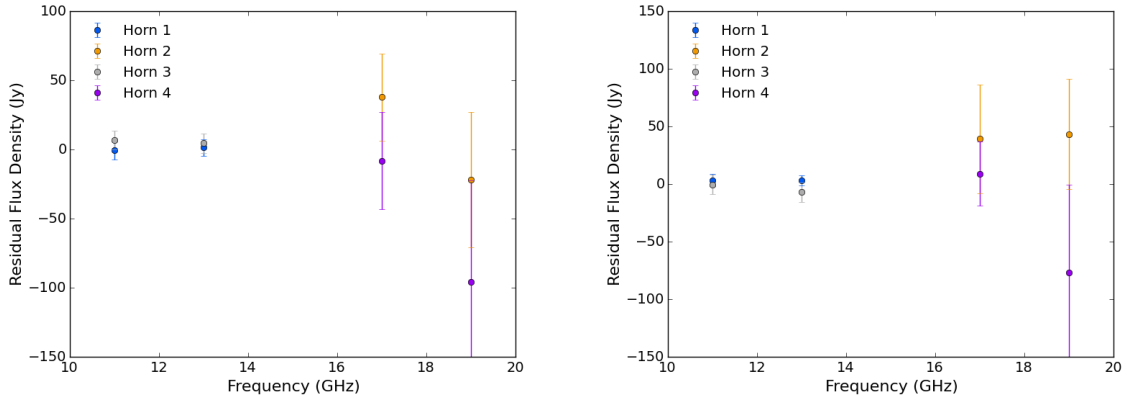

Figure 3.33: Residual flux densities of bright point sources from a difference map generated from elevation 60 degrees wide-survey maps from Epoch 1 and Epoch 2. *Left*: Tau A. *Right*: Cyg A.

In the final MFI maps the integrated flux density of point-sources calibrated to the main beam brightness scale will be correct but extended sources will have overestimated flux densities equal to beam efficiency of each horn and frequency.

To test the calibration stability, difference maps were generated using wide-survey observations at 60 degrees elevation taken between April 2013 to April 2014 containing approximately 350 hours of data, and between April 2014 to December 2014 containing approximately 150 hours of data. The residual flux density of Tau A and Cyg A were measured using aperture photometry in the wide-survey maps. Cyg A was chosen over Cas A, as Cas A is not visible by all MFI feeds at elevation 60 degrees. Figure 3.33 shows the residual flux density of the two sources. The uncertainties are calculated from the pixel noise. The residual flux densities are all consistent with zero however it is clear from the figure that the 17 and 19 GHz channels are pixel noise dominated.

Another test of the calibration stability is to cross check the calibration between horns. Figure 3.34 shows the residual flux of Tau A and Cyg A when differencing data taken during the same Epoch but observed with different MFI feeds at the same frequency. Again most of the points are consistent with no residual flux. However, the dispersion is slightly larger, the reason for this being a combination of slightly different main beam shapes and small systematic pointing inconsistencies between the feeds resulting in a measurable dipole in the difference map. The dipole is shown in Figure 3.35 as a slice through the residual map between horn 1 and horn 3 around

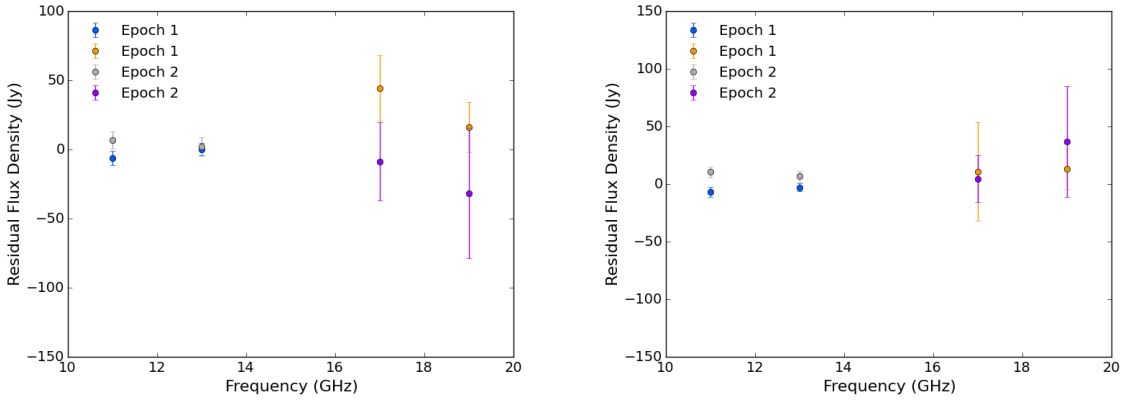

(a) (b)

Figure 3.34: Residual flux densities of Tau A and Cas A after differencing maps from different MFI feeds at the same frequency during Epoch 1 and Epoch 2. *Left*: Tau A. *Right*: Cyg A.

Tau A at 11 GHz. The residual dipole amplitude is approximately 25 mK or around 6 per cent of the Tau A amplitude. The pointing offset that equates to a 6 per cent dipole can be calculated by simply differencing two Gaussians with a FWHM equal to the MFI beam widths. The pointing offset was found to be 5 arcmin, which is just below the $1\,\sigma$ pointing uncertainty calculated in Section 3.3. In general these pointing uncertainties are flux preserving but when measuring sources in the final MFI maps it must be considered that the effective beam size will be different to the true beam size discussed in Section 3.4.

Throughout this Chapter, the effect of each Section on the calibration uncertainty budget was discussed. At the beginning of this Chapter a calibration uncertainty goal of 1 per cent was set for measurements made between adjoining frequency bands. The principle contributor to the calibration uncertainty is the method used to fit to the amplitude of calibrator sources, which is dependent on the beam model accuracy, the receiver noise properties and the telescope pointing. The other principal contribution to the calibration uncertainty comes from atmospheric absorption. The calibration uncertainty can be estimated from the combined uncertainty of the receiver *r-factors*, the relative calibration model and the atmosphere.

The calibration uncertainty from *r-factors* and the relative calibration model can be estimated from the mean uncertainty associated with each monthly measurement. This uncertainty is a combination of the statistical uncertainty in the bins, added in

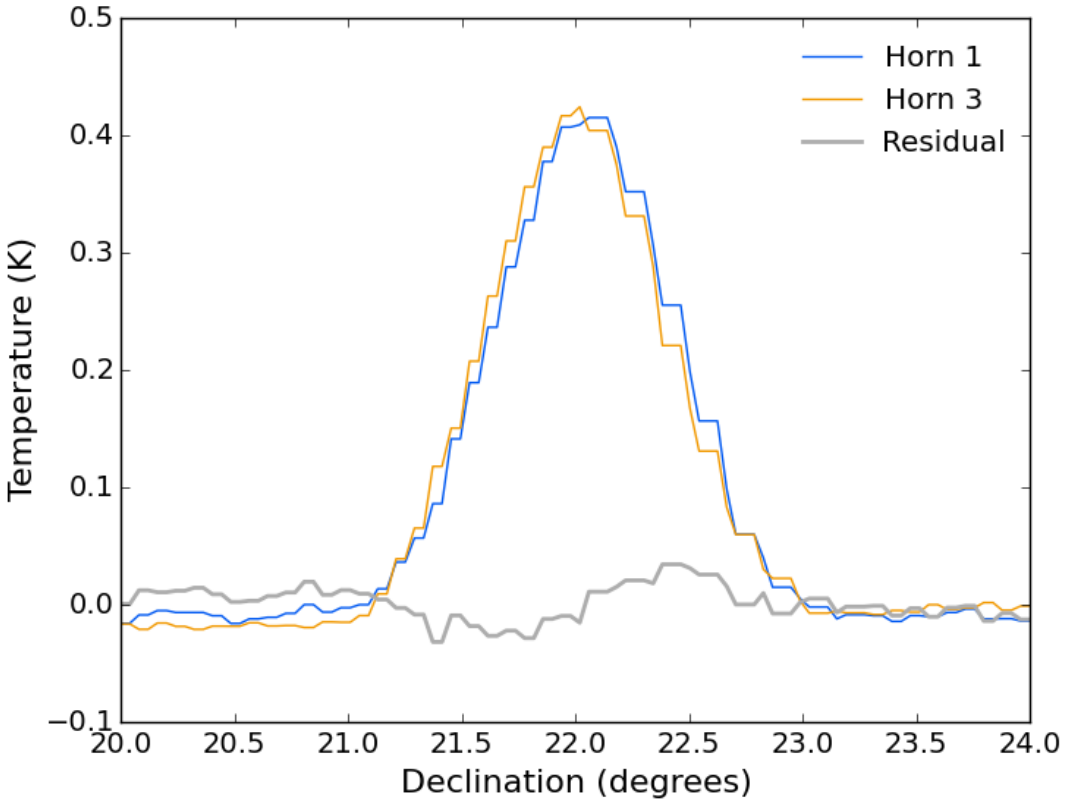

Figure 3.35: Slice through the elevation 60 degrees wide-survey maps from horn 1 and horn 3 at 11 GHz centred in Right Ascension on Tau A. The grey line shows the residual dipole from differencing the horn 1 map with the horn 3 map.

quadrature to the intrinsic fitting uncertainties,

$$\sigma_{\rm bin} = \sqrt{\sigma_{\rm n}^2 + \sigma_{\rm fit}^2}, \tag{3.50}$$

where $\sigma_{\rm bin}$ is the uncertainty in the binned monthly measurement of the *r-factors* or relative calibration model, $\sigma_{\rm n}$ is the normally distributed uncertainty in the mean value of a given bin, and $\sigma_{\rm fit}$ is the systematic fit uncertainty. All the σ values are percentage uncertainties. For the *r-factors*, which were derived using Cas A observations alone, an additional 1 per cent uncertainty should be added to $\sigma_{\rm fit}$ to account for the possible systematic offset in the Cas A amplitudes discussed earlier in this Section.

A second contribution to the *r-factor* and relative calibration model uncertainty comes from using nearest neighbour interpolation to determine the value of each at any point in time. This uncertainty can be quantified as the ratio of the mean change in the model over the mean absolute value of the model during a single Epoch,

$$\sigma_\tau = \sqrt{\frac{\langle \Delta x \rangle}{\langle x \rangle}}, \tag{3.51}$$

where σ_τ is the model temporal uncertainty, $\langle \Delta x \rangle$ is the mean of the difference between adjacent model bins and $\langle x \rangle$ is the mean model value. The uncertainty σ_τ is then added in quadrature to the statistical uncertainty in each bin ($\sigma_{\rm bin}$).

Table 3.14 lists the calibration uncertainties derived for each MFI feed. The uncertainties due to the atmosphere and pointing are taken from Sections 3.9 and 3.3. For the low frequency MFI horns, the calibration uncertainty is approximately 0.5 per cent higher than the target 1 per cent calibration uncertainty. However, a calibration uncertainty between 1 and 3 per cent is still sufficient for scientific outputs discussed in Chapter 6 using the MFI wide-survey maps. The horn 2 and 4 calibration uncertainties are approaching or in excess of 4 per cent. This implies that the 17 and 19 GHz MFI data will be far more limited than the 11 and 13 GHz data.

From this point forward the MFI TOD are considered to be calibrated to the main beam brightness temperature scale. In the next Chapter these calibrated TOD will be processed to remove samples containing spurious emission not of celestial origin. In Chapter 6 the calibration uncertainties will be used to determine the flux density uncertainties of regions measured in the final MFI wide-survey maps.

Table 3.14: Average calibration uncertainties for each MFI feed from the combination of the uncertainties in R and *r-factor* models. Total uncertainties are the added in quadrature value of the other uncertainty components. Calculated from observations taken during Epoch 1. The total uncertainty for horn 4 in Epoch 2 is 3.7 per cent. Note, in Epoch 2 the horn 4 LNAs were replaced, the total uncertainty horn 4 subsequently decreased to 3.7 per cent.

	R (%)	*r-factors* (%)	Atmosphere (%)	Total (%)
Horn 1	0.7	1.4	0.5	1.6
Horn 2	1.8	2.5	1.5	3.4
Horn 3	1.0	1.2	0.5	1.6
Horn 4	3.1	4.9	1.5	5.9

3.11 Summary

This Section has described the Manchester calibration pipeline and the key systematics associated with each of the crucial areas of MFI calibration. The work outlined in this Section is tailored specifically towards the MFI however many of the methods and fundamental concepts discussed are quite general and could be applied to other single-dish radio telescopes and instruments. At the end of this Section the final calibration uncertainties of the MFI were derived as less than 2 per cent for the 11 and 13 GHz channels and less than 4 per cent for the 17 and 19 GHz channels. To some extent calibration uncertainties are indicative of the notion that the calibration of an instrument is never complete. This is true also of the MFI and there are a number of areas of calibration that could still be improved. Specifically better characterisation of the atmosphere in both absorption and emission could be improved and would be most beneficial to the higher frequency MFI channels. Another area that could use improvement is the determination of the gain model described in Section 3.5. The calibration diode uncertainty on timescales shorter than 24 minutes is not ideal. However, recently it has been found that the MFI BEM temperature sensors correlate with the MFI gain variations and could potentially be used to track the MFI gain variations. The other two areas that could use general improvements are the measurement of the MFI bandpasses, as this has not been repeated since the changes in the receivers in April 2014 and to revisit the MFI pointing model, perhaps by installing a new optical

camera into the focal centre of the MFI.

Chapter 4

MFI Data Processing

"No data is better than bad data."

Anon. *An approach to data analysis.*

This Chapter will discuss the Manchester pipeline data processing of calibrated TOD before map-making and the post-processing of the MFI maps that occurs after map-making. The first two Sections principally discuss the methods used to mask TOD contaminated with non-celestial emission. The final Section gives a detailed discussion of the effect of geo-stationary satellites on the MFI TOD and demonstrates several methods for mitigating the effects of geo-stationary satellites.

4.1 Sun, Moon and Jupiter

This Section will discuss how daily masks of the Sun, Moon and Jupiter were generated using the `SLALIB` ephemeris routines. A mask was generated per observation by generating a `HEALPix` map with all pixels set to unity; pixels in the sky contaminated by the emission from the Sun, Moon or Jupiter are set to zero. The mask is then sampled using feed pointing information to generate a Boolean mask array to match the TOD.

Figure 4.1 shows an example of a mask map generated for a 24 hour long wide-survey observation taken on the 6^{th} September 2014. The position of each source is calculated at the beginning and end of the observation. Interpolation of the source position is then used to determine the pixels in the map through which the source transits. For each unique pixel transited by the source, an aperture is calculated to flag out any data

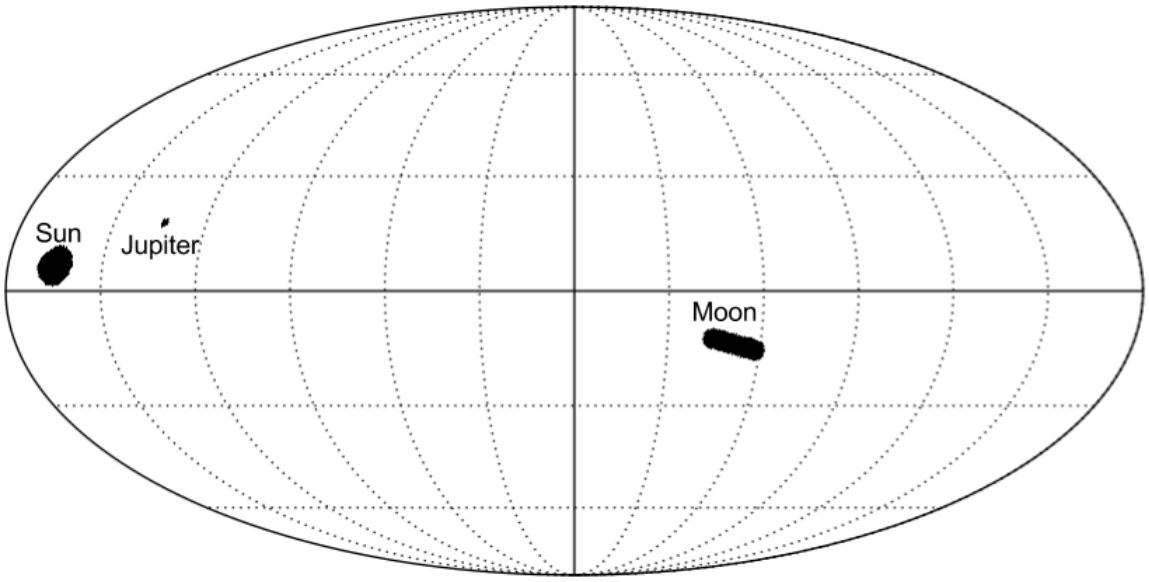

Figure 4.1: Example mask map generated for planet positions on the 6^{th} September 2014 taken over 24 hours of data. Each source mask is generated from the interpolated transit of the source from the beginning and end of the observation.

within that region of the sky. Note that the moon transits approximately 12 degrees per day, hence the Moon mask is highly elongated, whereas the Sun and Jupiter transit only 1 degree.

The radius of the masking aperture is calculated using the `CST` beam models and an estimate of the antenna temperature of each source at 11 GHz. Sources such as the Sun, Moon and Jupiter can be modelled as flat discs with a constant surface brightness temperature. Therefore, the antenna temperature (T_a) can be calculated using (Rohlfs and Wilson, 2004),

$$T_a = \frac{\int\limits_{\text{src}} P_n(\theta,\phi)\mathrm{d}\Omega}{\int\limits_{4\pi} P_n(\theta,\phi)\mathrm{d}\Omega} T_b = \frac{\Omega_{\text{src}}}{\Omega_{\text{A}}} T_b, \tag{4.1}$$

where Ω_{A} is the full beam solid angle of the telescope, T_b is the brightness temperature of the source and Ω_{src} is the projected solid angle of the source. The solid angle of the source can be calculated by integrating the conic sections of a sphere resulting in

$$\Omega_{\text{src}} = 2\pi r \left[\frac{1}{r} - \frac{1}{\sqrt{R^2 + r^2}}\right] f_o, \tag{4.2}$$

where r is the source distance, R is the source equatorial radius and f_o accounts for the source oblateness, which is the ratio of the polar radius over the equatorial radius.

Using Equation 4.2, the solid angles of the Sun, Moon and Jupiter are $\Omega_{\text{Sun}} \approx 6.8 \times 10^{-5}$ sr, $\Omega_{\text{Moon}} \approx 6.4 \times 10^{-5}$ sr and $\Omega_{\text{Jup}} \approx 4.1 \times 10^{-8}$ sr, where Jupiter is assumed to be at 4.08 AU. The brightness temperature of the Sun is ≈ 6000 K, the Moon is ≈ 210 K (Burke and Graham-Smith, 1996) and Jupiter at 11 GHz is ≈ 185 K (Klein and Gulkis, 1978). Using this information and Equation 4.1 the approximate peak antenna temperature response for the Sun, Moon and Jupiter are 1511 K, 53 K and 28 mK respectively. The maximum contribution from each source is set to be 0.1 mK, which is a factor of 100 below the low frequency TOD white-noise level. Therefore the Sun must be masked out to -60 dB, the Moon to -40 dB and only the main beam response needs to be masked for Jupiter. Visual inspection of the low frequency `CST` beam models suggests that a radius of 5 degrees is required to mask out all the solar near sidelobe contributions; 2.5 degrees is required for the Moon and the beam FWHM for Jupiter.

This Section has summarised the method for masking bright, celestial objects from the MFI TOD. The implementation in the Manchester pipeline involved generating daily mask maps in the celestial coordinate frame. These mask maps were then sampled to generate time-ordered-masks of the Sun, Moon and Jupiter.

4.2 Flagging Noise and RFI Contamination

This Section will discuss the methods in the Manchester pipeline for removing bad quality or RFI contaminated TOD from the calibrated MFI TOD. Historically, the removal of poor quality data would be done by visual inspection. However, with modern radio instruments the volume of the data produced is vast and therefore the only way to remove poor quality data is to use an automated method. In recent times automatic flagging of data has become a topic of interest in relation to general purpose interferometric instruments because of the large volumes data produced per observation. Some examples of current automatic flagging software are `SERPent` (Peck and Fenech, 2013) used by *e*-MERLIN, `AOFlagger` (Offringa et al., 2010) used by LOFAR and `FlagCal` (Prasad and Chengalur, 2012) used by the GMRT. Just as for single-dish TOD, interferometric datasets are flagged in the time domain. Therefore, the research into effective automatic flagging methods has a general application to all aspects of radio astronomy.

The three principal types of poor data removed by the MFI automatic TOD flagging

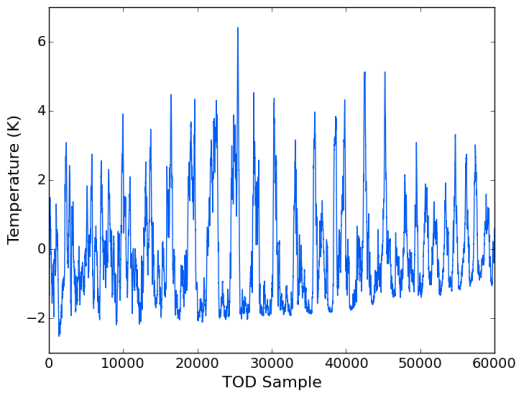

(a) Correlated RFI.

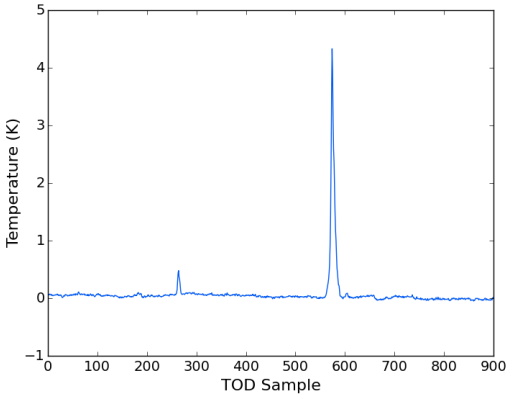

(b) RFI spikes.

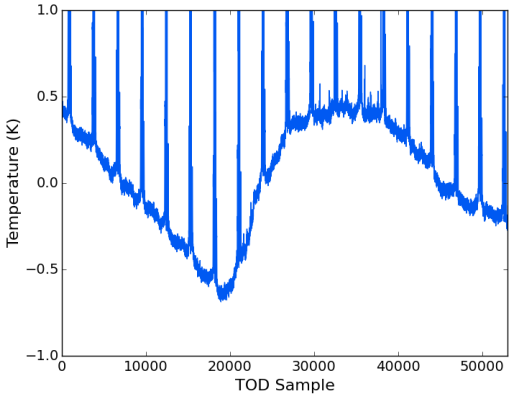

(c) Horn 3 baseline drifts.

Figure 4.2: Examples of the three principal types of bad data to be removed during the flagging procedure. Note the scales in these figures are K and that the brightest astronomical signal is of the order a few 100 mK. The correlated RFI shown in Figure 4.2a occurs for extended periods and is the most important RFI to identify and remove from the TOD. RFI spikes can vary in brightness between a few tens of mK to several K as shown in Figure 4.2b. Figure 4.2c shows the correlated channels of Horn 3 in Epoch 1, which experience periods of rapid baseline variations with amplitudes of a few K over timescales of minutes.

are shown in Figure 4.2. Figure 4.2a shows an example of a bright, correlated RFI signal. The typical apparent brightness of the correlated RFI can approach tens of K and can extend over periods of minutes to hours, occurring at random intervals throughout all MFI TOD. The accurate identification and removal of the correlated RFI signal is crucial to high quality map-making and astronomical signal recover covered in Chapters 5 and 6, respectively. Figure 4.2b shows an example of RFI spikes measured in the feed 1 11 GHz TOD. The RFI spikes have been found to vary between a few tens of mK to several K in apparent brightness. Figure 4.2c shows two final examples of bad MFI TOD. The first is a rapid baseline variation seen in the Horn 3 correlated channels. As the figure shows, the variations can have amplitudes around a few K, changing on a timescale of ten to twenty minutes. The rapid baseline variations were attributed to a problem with the Horn 3 180 degree hybrid correlators. These were replaced in Epoch 2, therefore correcting the effect. The other RFI source seen in Figure 4.2c are periodic spikes occurring as the azimuthal slewing of QT1 transits the MFI beam through bright geostationary satellite emission; geostationary satellites are addressed in detail in Section 4.3.

Removal of the transient RFI spikes involves a two step iterative process. A threshold for identifying spikes is defined, which for the first step is equal to the brightest observed Galactic emission at a given frequency over the whole observable sky. The spikes in the TOD are then removed iteratively using the following process:

- Identify the index of the brightest spike in the TOD above the threshold value.
- Isolate all the TOD samples 10 minutes either side of the spike.
- Find the samples that are within 2 degrees of the spike.
- Mask the samples and repeat until all samples are below the threshold.

The reason for flagging any TOD that are within 2 degrees of the spike is to catch any slow, transiting RFI sources that are then measured in subsequent wide-survey azimuthal scans but at diminishing brightness that may not be detected by the spike finding algorithm. TOD are also selected within a 20 minute temporal window; this avoids flagging all TOD that observe that region of sky. The final step is to decrease the threshold to five times the effective noise level of the TOD, followed by masking the Galactic plane and repeating the process above.

All other forms of bad TOD, which includes the correlated RFI, Horn 3 baseline drifts and any stochastic increase the effective noise of the TOD due to variations in *1/f* properties were removed using noise threshold cuts. The noise threshold was

determined from visual inspection of the calibrated TOD overlaid with the measured uncertainties per 60 seconds of TOD that were mean-smoothed using a 30 minute mean filter. Trial-and-error was employed to find the optimum threshold for each MFI frequency that resulted in no correlated RFI contamination shown in Figure 4.2a being left in the final MFI datasets. This is a relatively standard technique for automatic TOD flagging. The primary difference of this method to those discussed at the start of this Section is that no dynamic determination of the flagging threshold is performed based on the background noise measured using the Median Absolute Deviation (MAD) (e.g. Fridman, 2008) statistic. In the case of the MFI, because the scientific goal is always the same, and the calibrated TOD noise level for good TOD is constant, a single threshold that is typically a factor of ten higher than the effective noise was used.

Figure 4.3 shows two naively binned mollweide projections of the whole sky in the celestial coordinate system using the `HEALPix` pixelisation scheme. The data used to generate the maps are from two days of wide-survey observations taken on July 6^{th} 2013 and November 22^{nd} 2013. Figure 4.3a shows the map as it would appear if no TOD were flagged. The bright ring of emission labelled correlated RFI is an example of the RFI shown in Figure 4.2a when binned into a wide-survey map. Comparing the correlated RFI ring to the bright Galactic emission of the Cygnus region shows how the real signal could easily be dominated by the RFI signal. Figure 4.3b shows the same TOD set after flagging was performed to remove poor quality TOD. In this example approximately 50 % of the total data have been flagged as bad. This example demonstrates that the automatic flagging does remove bad and RFI contaminated TOD. However, the cost of removing the RFI and bad quality TOD is that some of the good quality data in Figure 4.3a has also been lost. The reason for this is that the variance threshold chosen per frequency is a pessimistic estimate to ensure that no correlated RFI passes through the RFI flagging method. For a typical wide-survey observation approximately 35 % of the TOD will be flagged, with some bad quality observations having up to 80 % of the TOD flagged. Later, in Chapter 6, the total observing efficiency after TOD flagging will be calculated per MFI frequency channel.

This Section has demonstrated the challenges faced with removing RFI and poor quality TOD from the MFI observations. The philosophical question posed when writing an automatic RFI flagging method is how much bad TOD can be absorbed into the final dataset while simultaneously factoring in the cost of how much good TOD will be lost. The approach described here favoured the sacrificing of some good TOD in an

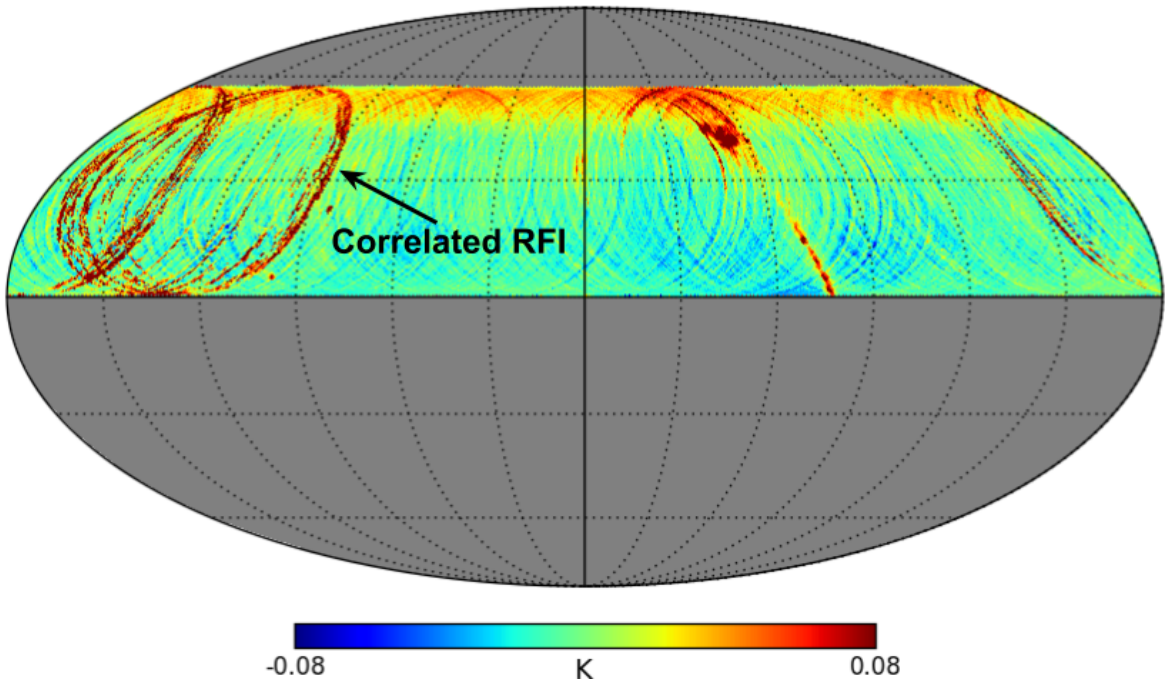

(a) Non-flagged map.

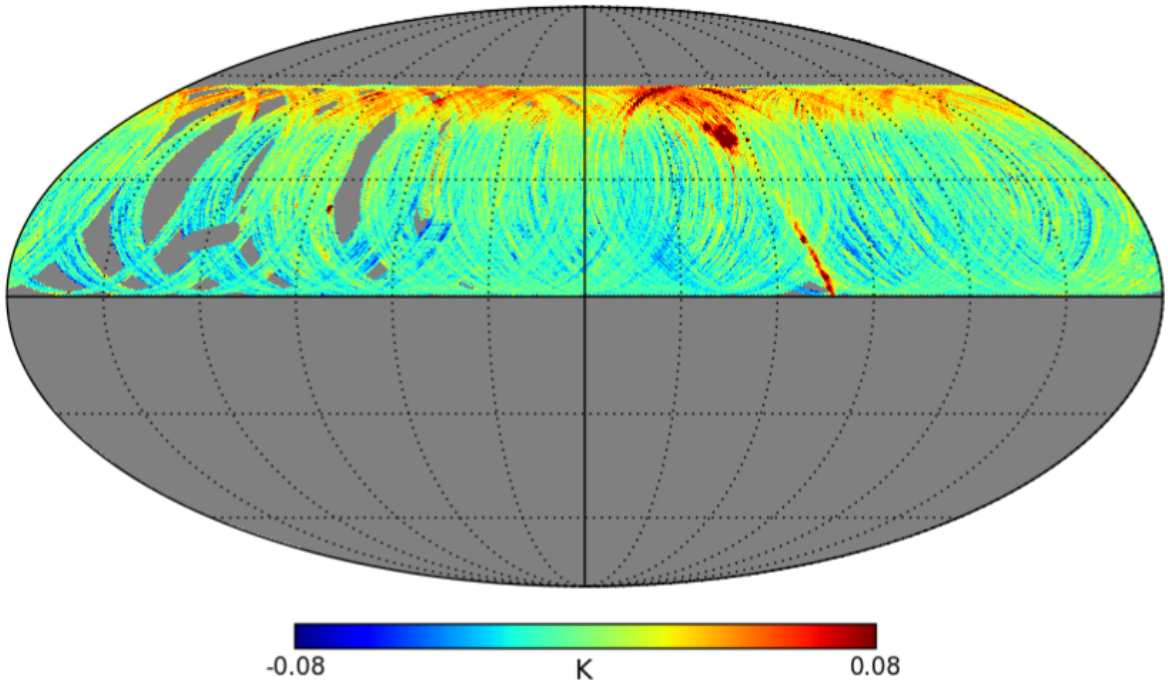

(b) Flagged map.

Figure 4.3: An example of the results of binning wide-survey observations into an all-sky map that has not been flagged (*Top*) and has been flagged (*Bottom*) for bad TOD.

effort to ensure that the worst RFI does not make it through the automatic flagging routine. This is important for the MFI as the map-maker described in Chapter 5 relies on the noise statistics of the TOD to be constant with time. Bright spikes or correlated RFI noise can severely change the noise properties of the TOD. The final result would be that the map-making solution for the receiver *1/f* will be poor and artefacts, such as large-scale negatives, can become manifest in the final maps.

4.3 GSO Satellite Emission

Figure 4.4 shows the local sky as seen by MFI feeds 1 and 2 at 11 GHz and 17 GHz respectively for Epoch 1 and Epoch 2. The Galactic plane can be seen in the figures to span the sky from *North* to *South*; the Cygnus region in particular can be clearly seen at the 60 degree elevation line. From *East* to *West* the bright emission of the geostationary orbit (GSO) satellites can be seen in the 11 GHz images. The 11 GHz Epoch 1 map also shows integrated effect of the QT1 far sidelobe pick-up near the zenith of the map as a large-scale diffuse emission. The emission from the GSO satellites is also highly polarised, with polarisation fractions approaching 90 % and polarisation angles that can vary with time. Therefore, at low frequencies, the emission from GSO satellites is the principal source of RFI for both total intensity and polarisation measurements. In the 17 GHz MFI channels, the GSO satellites are not observed at all. Meanwhile in the 19 GHz MFI channels, only several faint GSO satellites are observed but unlike in the lower frequencies, no near or far sidelobe pick-up was detected. For this reason this Section will only discuss the effect of the GSO satellite emission in the low frequency MFI channels and the methods for modelling the GSO satellite emission.

Some GSO satellites have brightnesses that are comparable to the Sun and can be measured in a single pass out to the fifth near sidelobe at around -60 dB of the main beam power. The integrated effect of the near sidelobes in the low frequency channels can be seen in the *West* of Figure 4.4 as a large-scale emission that has a brightness that exceeds most of the brightest diffuse emission along the Galactic plane. For MFI feed 1, the integrated effect of the far sidelobe pick-up can also be seen, forming an arc around the zenith above 60 degrees elevation. This integrated far sidelobe pick-up also has a brightness that is comparable to the diffuse Galactic plane emission. For MFI feed 3, the far sidelobe emission is an order-of-magnitude fainter but is still observable in the full integrated wide-survey maps if not subtracted.

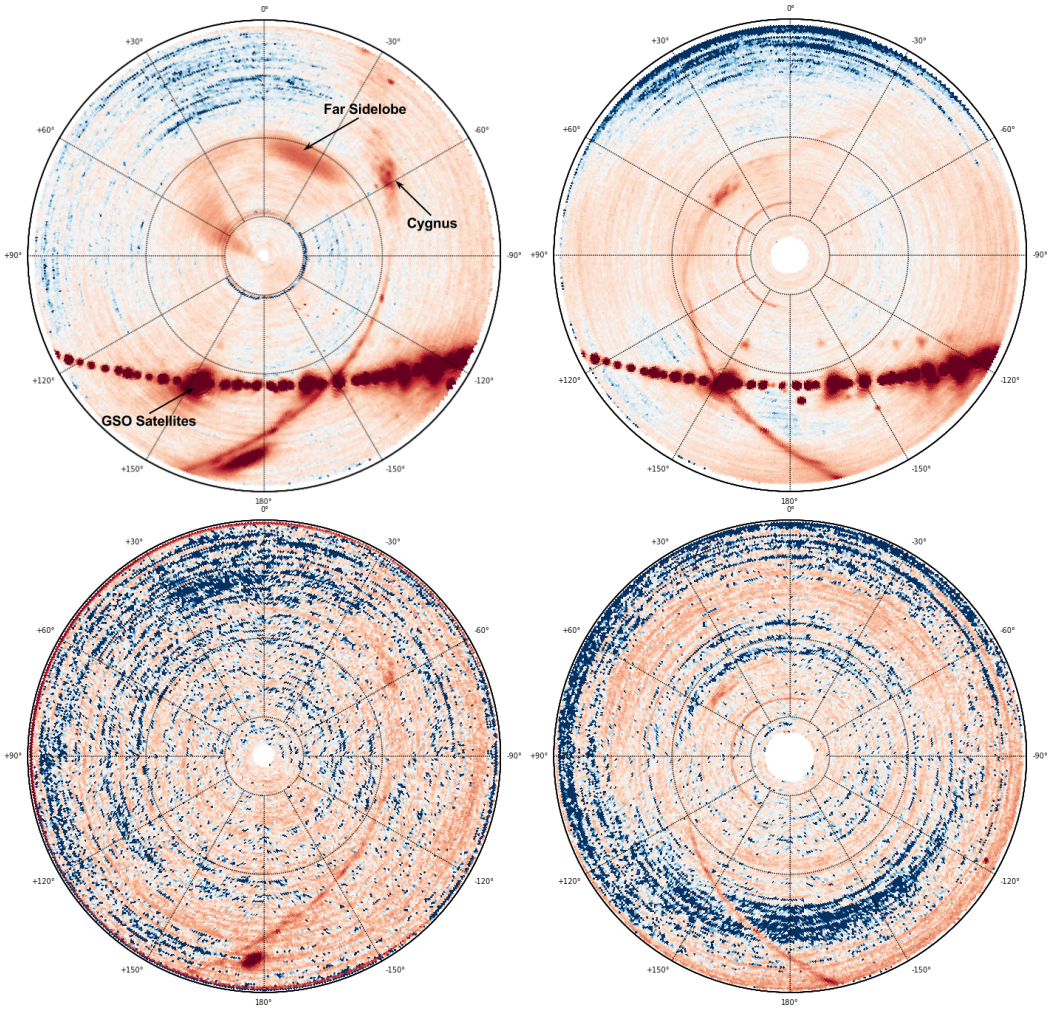

Figure 4.4: Local emission as seen by the MFI between elevations 30 degrees and 90 degrees. The *left* maps show the sky as seen before the extended shielding and the *right* maps show the sky as seen after the extended shielding. The *top* maps show the local sky as seen by the MFI feed 1 at 11 GHz and the *bottom* maps are the local sky emission seen at 17 GHz by MFI feed 2.

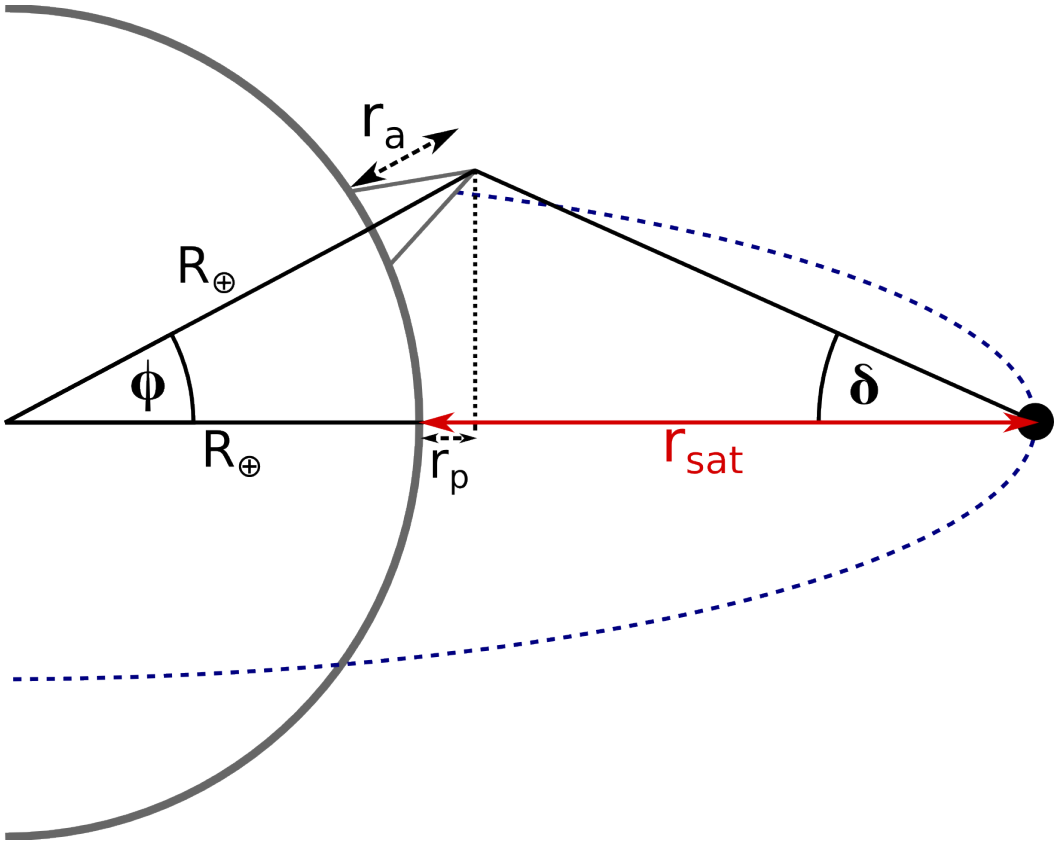

Figure 4.5: As geostationary satellites are nearby sources of emission, parallax affects the satellites apparent Declination (δ) and is dependent on the latitude ϕ and altitude r_a of the observing site.

Geostationary satellites are fixed sources in the local frame of the telescope and are distributed along a band at a single Declination. The Declination of the GSO satellite band is dependent on the latitude (ϕ) and altitude (r_a) of the observer and can be easily formed into the parallax problem shown in Figure 4.5. The Earth will be assumed here to be a sphere, but a more accurate treatment would include modelling the Earth as an ellipsoid (e.g Bate et al., 1971). First, the projected distance of the observing site on the equator (r_p) is calculated as,

$$r_p = [R_\oplus + r_a]\cos(\phi) - R_\oplus, \tag{4.3}$$

where $R_\oplus$ is the radius of the Earth. The distance between r_a and r_p is simply $(R_\oplus + r_a)\sin(\phi)$. The apparent Declination (δ) of the geostationary satellites is then

$$\delta = \arctan\left(\frac{[R_\oplus + r_a]\sin(\phi)}{r_{\rm sat} - r_p}\right), \tag{4.4}$$

where $r_{\rm sat}$ =35786 km, the typical height of the GSO satellite above the equator of the Earth. For the Izana observing site the expected Declination of the GSO satellites is calculated to be -4.7 degrees. This value agrees with the observed Declination of the GSO satellites to within a few per cent and is illustrated by Figure 4.6.

As the GSO is a unique and important orbit, the International Telecommunications Union (ITU) was established to impose international regulations on the orbital solutions of all GSO satellites. GSO satellites must not deviate more than ± 0.1 degrees in longitude when crossing the celestial equator and must not deviate more than ± 5 degrees in latitude (ITU, 1992). The nominal pointing direction of the satellite must be maintained within ± 5 per cent of the main beam FWHM or 0.2 degrees, whichever is greater (ITU, 1995). The fuel cost in maintaining these criteria are the primary limitation on the lifetime of a GSO satellite. The GSO of a satellite will gradually degrade due to perturbation forces caused by distortions in the Earth's gravitational field, solar radiation pressure, and Moon-Sun tidal forces. Without regular corrections the inclination, i, of a GSO satellite will change by 0.75 degrees to 0.95 degrees per year, which in turn increases the libration motion of the satellite up to $\pm\,(i^2/4)(\pi/180)$ degrees over the course of half a sidereal day. Ultimately, these variations in position and pointing of the GSO satellite could result in variations in the apparent brightness of GSO satellite emission by the MFI.

The brightest GSO satellite seen by the MFI is Telstar 12 at longitude 15 degrees *West*. The emission from this satellite alone is expected to be contributing most of

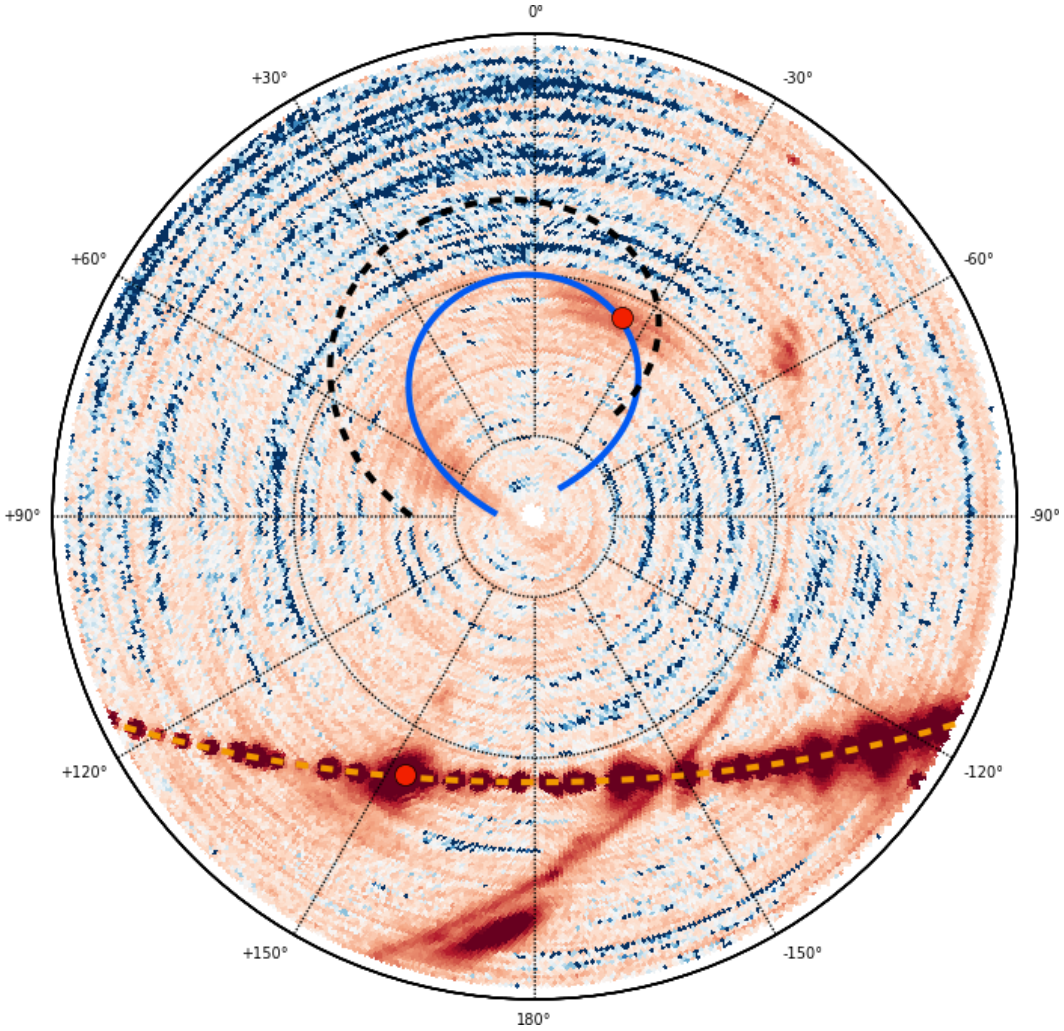

Figure 4.6: Polar map of the local sky as seen by the 11 GHz channels in the MFI feed 1, observed during the MFI commissioning. The dashed yellow line marks the geostationary satellites at Declination −4.72 degrees. The black dashed line shows the expected position of the far sidelobe pickup as predicted by the CST beam model. The blue line shows the observed position of the far sidelobe pickup. The red marker on the satellite band is the position of Telstar 12 and the other red marker is the far sidelobe pickup associated with Telstar 12.

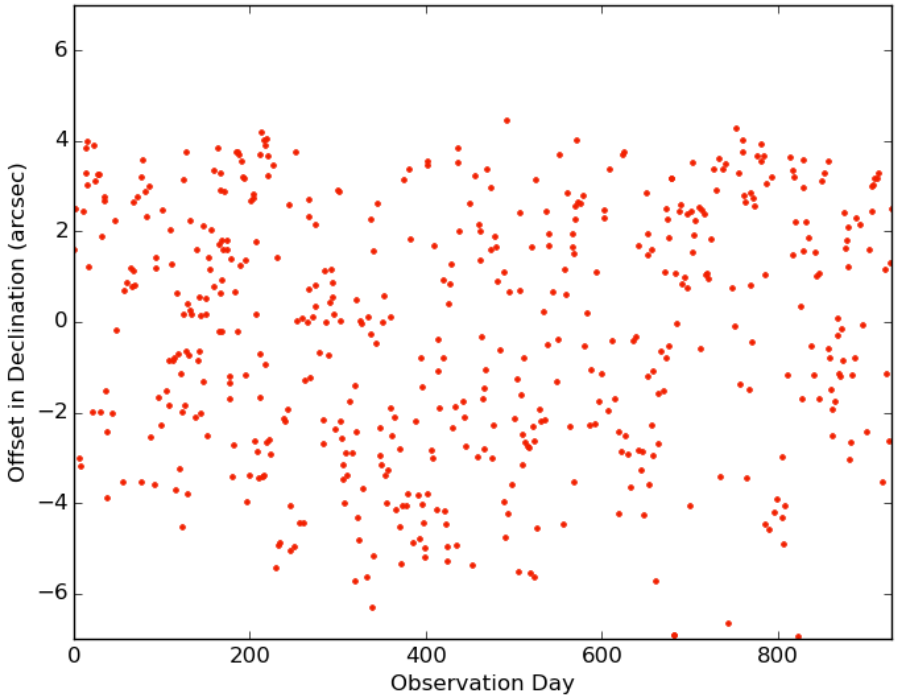

Figure 4.7: Deviations in the apparent Declination of the geostationary satellite Telstar 12, the brightest MFI RFI source at the low frequencies. The deviations are derived from the satellites two line elements taken from the NORAD archive at *www.space-track.com*.

the observed far sidelobe emission seen in Figure 4.4. The NORAD satellite tracking archive *www.space-track.com* provides daily two-line elements (TLEs) describing the orbit of known near Earth objects. These TLEs can be converted into instantaneous position and velocity vectors using the method described in Bate et al. (1971, Chapter 2). The variations in the apparent satellite Declinations can then be found using Equation 4.4. Figure 4.7 shows the Declination deviations in the position of Telstar 12 between MFI first light and June 2015 and is seen to have an amplitude of ± 5 arcsec. These deviations are small enough to assume that the satellite is a fixed source in the frame of the telescope, implying that the far sidelobe emission and other near sidelobe emission are also fixed. Several other of the brighter GSO satellites were tested, and the maximum deviation over the observing period of the MFI was less than ± 10 arcsec.

Using the `CST` beam models and the known positions of the GSO satellites in the local coordinate frame it should be possible to derive a template of the integrated GSO satellite emission. Formally, each TOD sample can be written as

$$\mathbf{d} = \mathbf{s} + \mathbf{n} + \mathbf{P}_{\mathrm{L}}\mathbf{m}_{\mathrm{L}}, \tag{4.5}$$

where $\mathbf{d}$ is the TOD, $\mathbf{s}$ is the signal detected along the pointing direction, $\mathbf{n}$ is an instantaneous noise contribution and $\mathbf{P}_{\mathrm{L}}$ is a pointing matrix that unrolls a map of the local sky, $\mathbf{m}_{\mathrm{L}}$, into TOD data. Together, $\mathbf{P}_{\mathrm{L}}\mathbf{m}_{\mathrm{L}}$ is the emission template of the GSO satellites and the azimuthal ring emission. There are two methods for generating $\mathbf{m}_{\mathrm{L}}$. The `CST` beam model can be used with measurements of the main beam amplitudes of the GSO satellites to derive a noiseless model of the integrated GSO satellite sidelobe pick-up across the whole local sky. The full sky model would then be sampled per observation using the pointing matrix $\mathbf{P}_{\mathrm{L}}$, and the result subtracted from $\mathbf{d}$. Alternatively, $\mathbf{m}_{\mathrm{L}}$ can be derived from the observations by stacking the observations in the local coordinate frame. The only requirement of both methods is that the uncertainty in the template emission must be equal to or less than the uncertainty in the final MFI maps to ensure no additional systematic noise is added.

There are several sources of uncertainty to consider when generating the satellite emission template. When generating the beam model analytically, the accuracy of the beam model in reproducing the true MFI beam must be considered. Generating the template from the observations is limited by the integration time per beam in the local coordinate frame. The final source of uncertainty, important to both methods, is the variability in the apparent brightness of the geostationary satellite emission. The

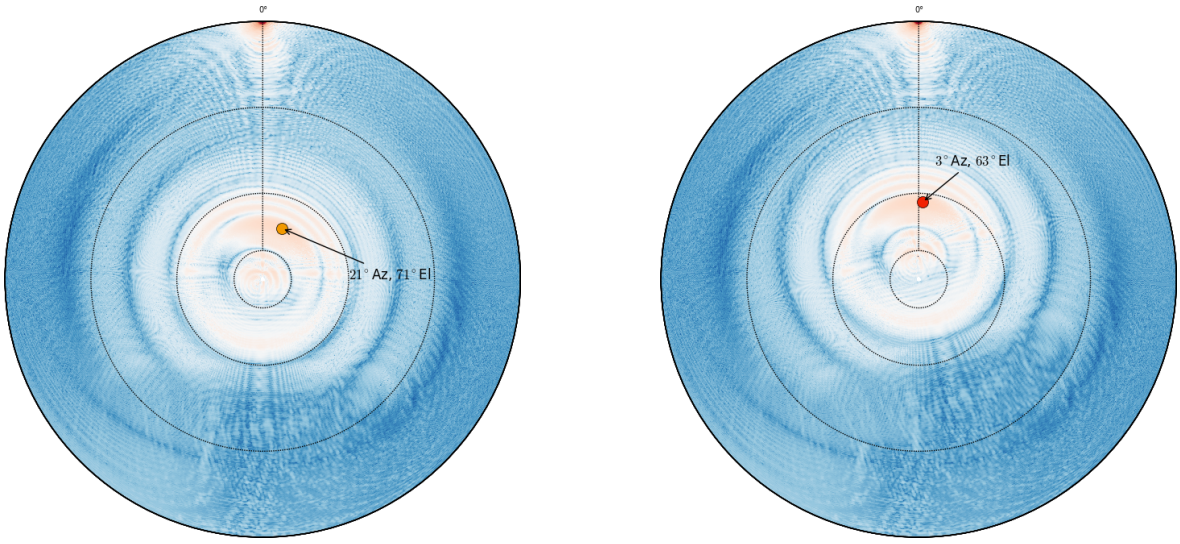

(a) Original CST beam model.

(b) Rotated CST beam model.

Figure 4.8: Polar projection of the original and rotated CST full MFI beam models for feed 1 at 11 GHz. The view is offset +90 degrees from the main beam centre. The main beam is seen 0 degrees longitude at the top of both plots. The marker in both indicates the location of the brightest emission in the far sidelobe.

variability of the geostationary satellite emission will also limit the longest integration time possible when generating a template from the observations.

As discussed in Section 3.4 the MFI beam models were generated using CST software by Roger Hoyland at the IAC. Figure 4.8a shows a polar projection of the full MFI 11 GHz beam derived using CST offset 90 degrees in elevation from the main beam, which is at the 0 degrees position. The structure shown in the plot is the expected MFI far sidelobe emission caused by spillover emission reflected by the secondary dish into the MFI feeds. The marker on the left image of Figure 4.8 is the position of the brightest pixel inside the far sidelobe structure. The far sidelobe is offset from the main beam by 21 degrees in azimuth and 71 degrees in elevation. The brightest region of the far sidelobe is approximately an order-of-magnitude brighter than the rest of the far sidelobe emission at around -40 dB of the forward beam power.

Figure 4.6 shows the Epoch 1 MFI feed 1 11 GHz local sky from Figure 4.4 but with several additional annotations. The yellow dashed line marks the expected local coordinates of the GSO satellite band. The black dashed line, near the zenith, marks the location expected to trace the brightest emission from the far sidelobe. The expected position is calculated by rotating the line marking the GSO satellite band by

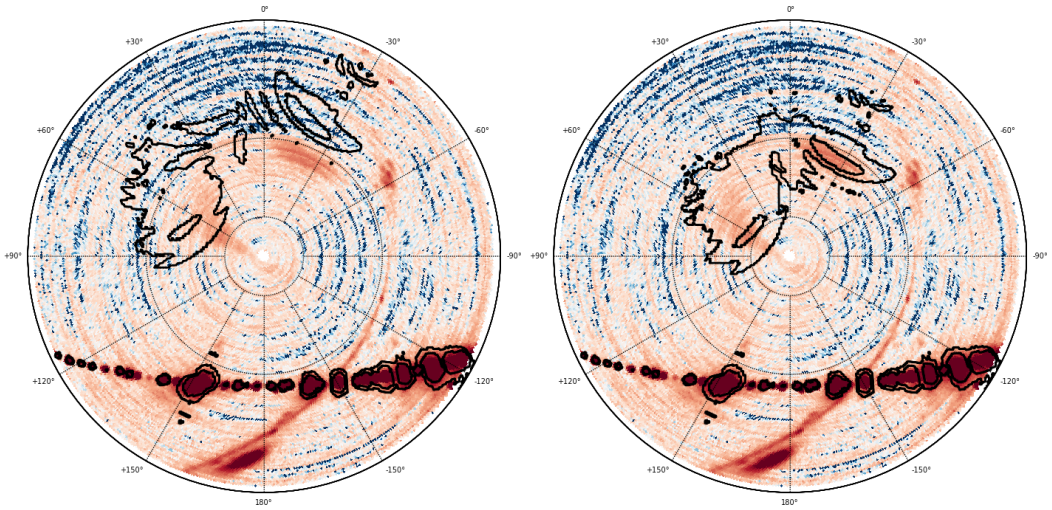

Figure 4.9: Polar maps of the local sky as seen at 11 GHz by feed 1 during Epoch 1. *Left*: Overlaid contours showing the integrated emission of the far sidelobes generated using the original `CST` beam model. *Right*: Overlaid contours showing the integrated emission of the far sidelobes generated using the rotated `CST` beam model.

the offset of brightest emission in the far sidelobe. It is clear from Figure 4.6 that the black dashed line does not agree with the position of the observed far sidelobe emission. However, by varying the offset rotation angle it was found that the location of the integrated far sidelobe emission could be reconstructed by rotating the GSO satellite band by 4 degrees in azimuth and 63 degrees in elevation, which is represented by the solid blue line in Figure 4.6.

The principal reason for the discrepancy between the `CST` beam model predictions and the observed far sidelobe emission is because the `CST` does not account for the QT1 shielding. The far sidelobe emission is modelled as a spillover picked up by the secondary reflector from a source approximately +90 degrees in elevation from the main beam pointing centre. Roger Hoyland is currently working on improving the CST beam model to include the QT1 shielding, both for QT1 and QT2, but this improved beam model is, as of writing, not available. Lacking the improved beam model, the original beam model was modified by rotating the far sidelobe in Figure 4.8a such that the brightest point in the far sidelobe was offset from the main beam centre by 4 degrees in azimuth and 63 degrees in elevation. The rotated beam model is shown in Figure 4.8b. The rotated beam model will be very inaccurate but the morphology of the integrated far sidelobe emission generated using Figure 4.8b should be reasonable for illustrating that the GSO satellites are the origin of the observed far sidelobe emission.

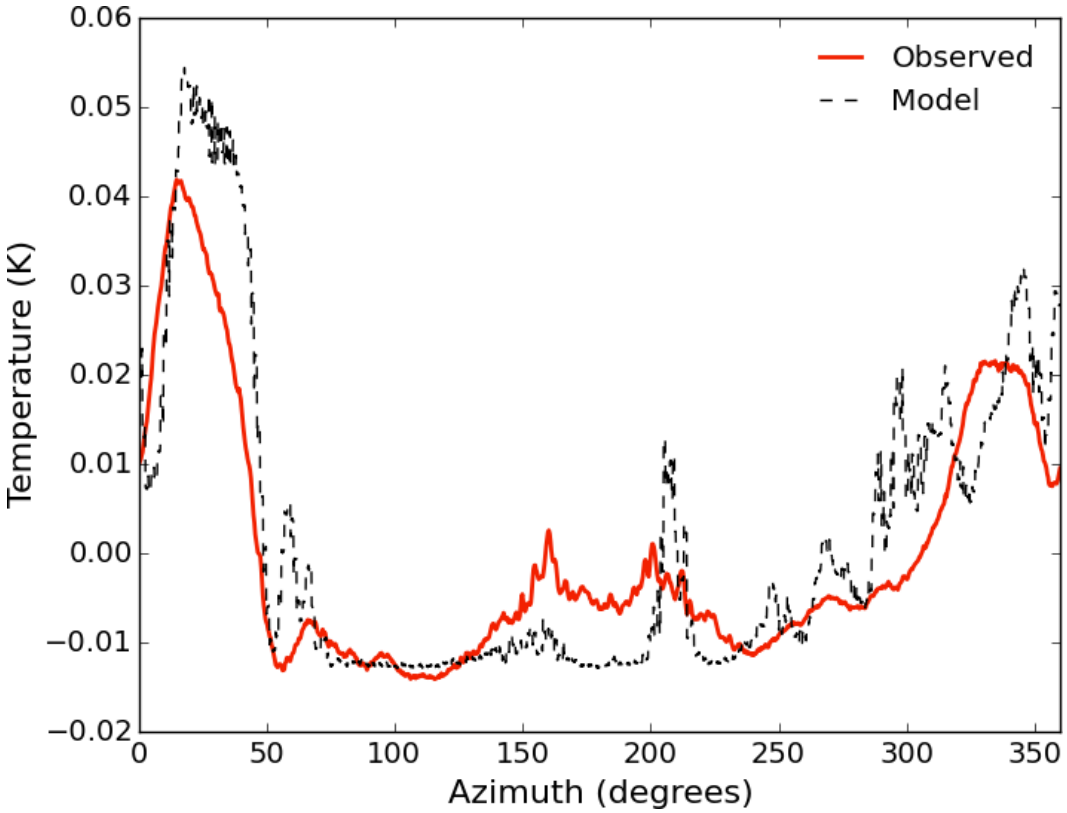

Figure 4.10: The solid red line shows the measured azimuthal variations of an elevation 60 degrees wide-survey observation and the black dashed line shows the simulated azimuthal emission predicted by the simulated local sky model.

To test that rotating the `CST` beam model far sidelobe is a reasonable estimate of the true MFI feed 1 far sidelobe pick-up, the original and rotated beam models were convolved with the measured positions and amplitudes of the GSO satellites. By convolving the GSO satellites with the beam models a simulated local sky map of the integrated GSO satellite emission could be generated. Figure 4.9 shows the comparison between the original and rotated integrated GSO satellite emission in contours overlaid onto the 11 GHz observed local sky. It is clear from the figure that the rotated beam model does make a reasonable estimate of the observed integrated far sidelobe emission.

The simulated local sky map is shown in Figure 4.9 to broadly replicate the observed integrated far sidelobe emission. However, when the simulated sky map is sampled to generate a TOD emission template $P_L m_L$ only broad comparisons can be made between the observed and simulated emission. Figure 4.10 compares the observed and simulated emission as seen by MFI feed 1 during wide-survey observations at a fixed 60 degrees

elevation. The observed azimuthal ring template is generated from a stack of 6 hours of observations and bright sources such as the Sun or Galactic plane are masked. In both the model and the observed TOD the integrated far sidelobe emission can be seen as broad large-scale emission below 100 degrees and above 250 degrees. Similarly, both TOD show the same general structure for the near sidelobe emission pick-up between 100 degrees and 250 degrees. However, the amplitude and morphological differences between the observed and simulated templates have differences far larger than the uncertainty in the MFI maps meaning the simulated template is unusable in the present form. One particularly useful piece of information to note about Figure 4.10 is the extent of the GSO integrated sidelobe pick-up extends across the entire sky when observing at 60 degrees elevation. The same plot at other elevations shows similar levels of contamination. This is important because it is an indication of why improving the MFI beam models will be needed to probe weak and diffuse Galactic emission at high Galactic latitudes with the MFI.

For the wide-survey a template of the GSO satellites could be generated *in-situ* from the observations. This is because the wide-survey nominal mode observing strategy repeatedly observes the same azimuth and elevation coordinates over hundreds of hours and therefore the wide-survey survey can be stacked into azimuthal rings with a very high signal-to-noise on the azimuthal emission. As indicated earlier, the uncertainty in the template must be at least equal to or less than the uncertainty in the final maps, which is principally dependent on the integration time per beam in the template. Limitations on the integration time are caused by how much TOD must be masked to avoid bright sources and also the timescale of the variability of the emission from the GSO satellites.

Figure 4.11 shows a wide-survey observation taken at elevation 40 degrees that has been reprojected into the time-azimuth plane. Each pixel in the map represents a single ring of MFI TOD, which in Epoch 2 is 30 seconds of observations. The regions shown in white are masked samples containing the Galactic plane, the Moon, non-geostationary satellites and the calibration diode signal. From the figure it can be seen that for some azimuths almost 50 per cent of data has been masked due to the Galactic plane. The total area masked is also dependent on the elevation being observed during the wide-survey. The effect of requiring more of the sky to be masked is that the integration time per beam in the stacked azimuthal ring will be reduced. However, the effect of masking will be a minimal increase in uncertainty if all the azimuthal rings can be

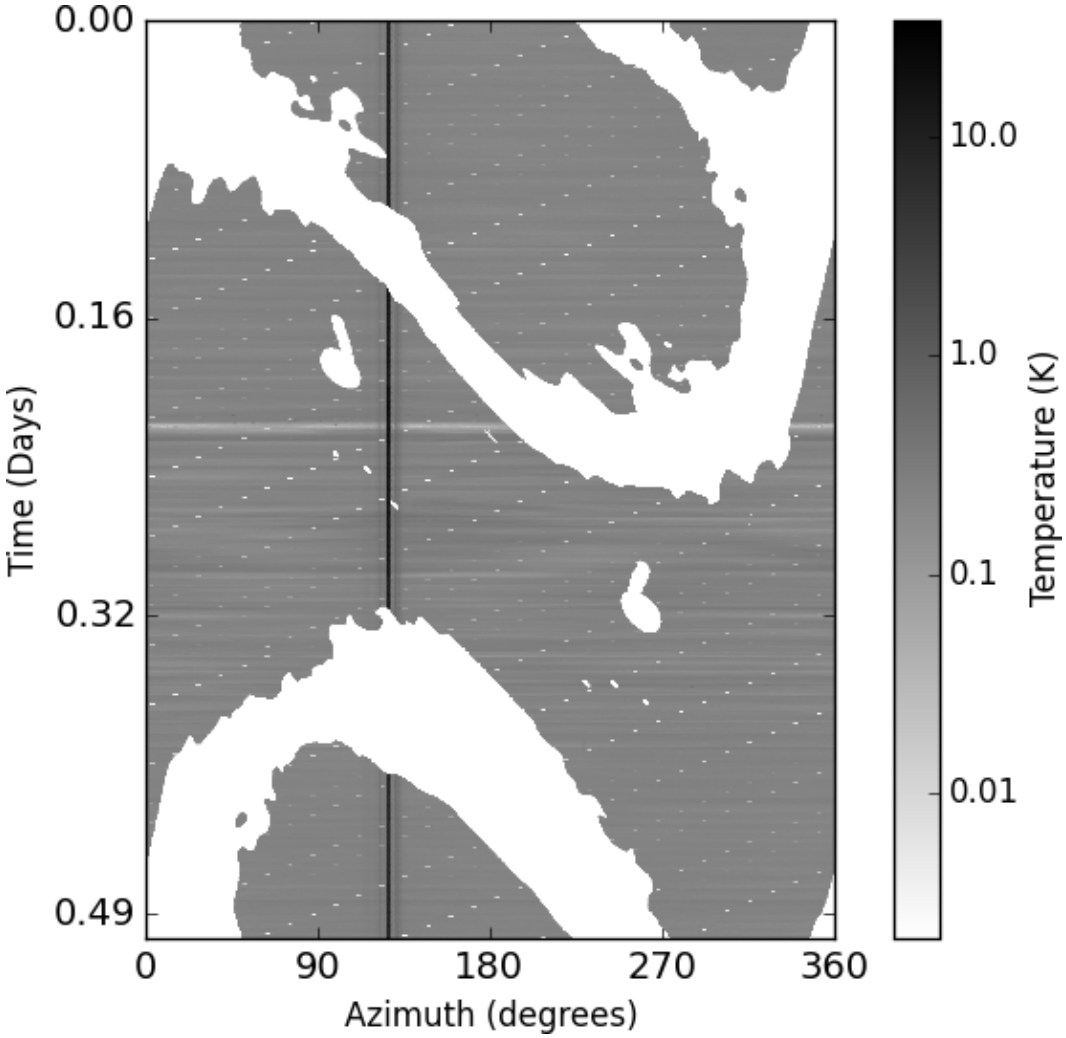

Figure 4.11: Variations in the azimuthal signal of an elevation 40 degree wide-survey observation taken in Epoch 2. White regions are masking bright non-local emission.

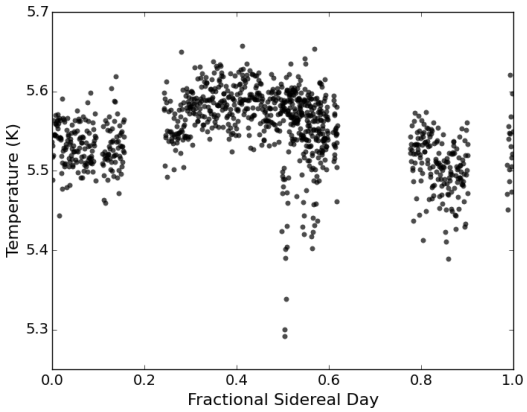

(a) GSO near sidelobe.

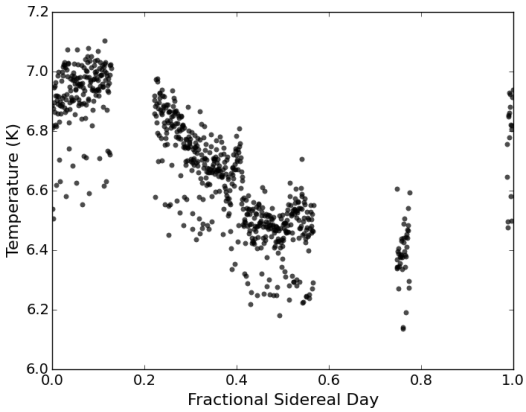

(b) GSO faint main beam.

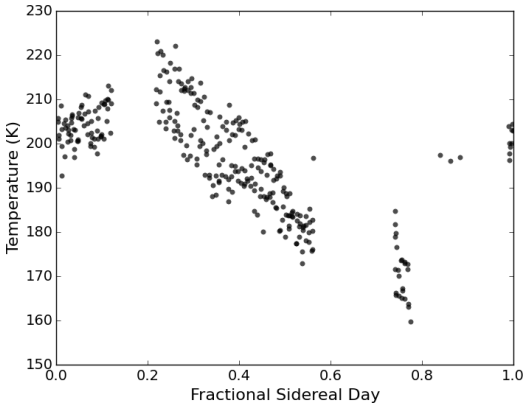

(c) GSO moderately bright main beam.

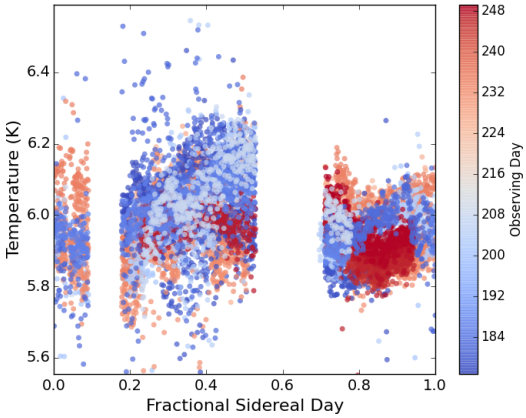

(d) Near sidelobe Long timescale variations.

Figure 4.12: Figures 4.12a, 4.12b and 4.12c show variations in the brightness of the GSO satellites with sidereal day. Figure 4.12d shows the variations in the near sidelobe pickup from one GSO satellite over several months.

stacked to produce an azimuthal template.

The other question that dictates the integration time per beam in the template is the variability of the GSO satellite emission. At the beginning of this Section it was shown that most of the brightest GSO satellites are effectively fixed in the local sky and therefore the integrated sidelobe pick-up will also be fixed. However, GSO satellites all have an associated beam pattern, which can be as large as 17.4 degrees FWHM for a GSO satellite with full coverage of one side of the Earth. Generally though most GSO satellites have beam FWHM that are much smaller. The tidal forces acting on the GSO satellites will cause variations in the pointing direction of the satellite with sidereal day and variations over longer timescales due to man-made corrections to the

pointing to keep the satellite within ITU pointing regulations discussed earlier. The result of these variations is that the main beam pointing directions between the MFI and the GSO satellite will change resulting in a change in the apparent brightness of the GSO satellite. As the tidal forces predominantly originate from the Sun and Moon the satellite apparent brightness variations is correlated with sidereal day.

Variations in the apparent brightness of the GSO satellites is supported by the MFI observations. All the elevation 60 degrees wide-survey TOD were transformed into the time-azimuth frame such as for the elevation 40 degrees wide-survey observation shown in Figure 4.11. Variations in the GSO satellite emission could then be measured by extracting columns at a single azimuth from the image. Figures 4.12a, 4.12b and 4.12c show the emission from a satellite near sidelobe, the main beam of a dim geostationary satellite and the main beam of a moderately bright geostationary satellite. All three were found to vary with the sidereal day but each with different phases. The phase of the oscillation is related to the longitude of the satellite and the current geocentric position of the Sun and Moon. The observations in Figures 4.12a, 4.12b and 4.12c were all taken within a single week. Over longer timescales of several months the apparent amplitude and phase of the geostationary satellites were also found to vary, as shown in Figure 4.12d. The magnitude of the variations in the satellites on short time-scales is $1-2\,\%$, however the variations on longer timescales approach $10\,\%$.

Variations of just $1\,\%$ over 12 hours in the apparent brightness of the GSO satellites near and far sidelobe emission can be equivalent to a temperature variation of $\pm\,1$ mK, which is comparable to the diffuse emission from the Galaxy. To achieve variations of just 0.1 mK per beam would require generating a template from the observations around every 1.2 hours. However, Figure 4.11 shows that on these short timescales a lot of the azimuthal data is likely to be masked due to contamination from the Galaxy. Also, the uncertainty in the template from the integration of 1.2 hours of azimuthal rings would not be able to trace variations on the 0.1 mK scale. Unfortunately, for these reasons using templates derived from observations to remove the integrated near and far sidelobe contamination from GSO satellites was not possible with the MFI. Another common use for generating azimuthal templates is to model the ground spillover signal, however this is not possible with MFI TOD for the same reasons that a GSO satellite emission template cannot be made.

An alternative to modelling the GSO satellite emission in the TOD is to model the integrated effect of the emission in the map domain. If no corrections GSO satellites is

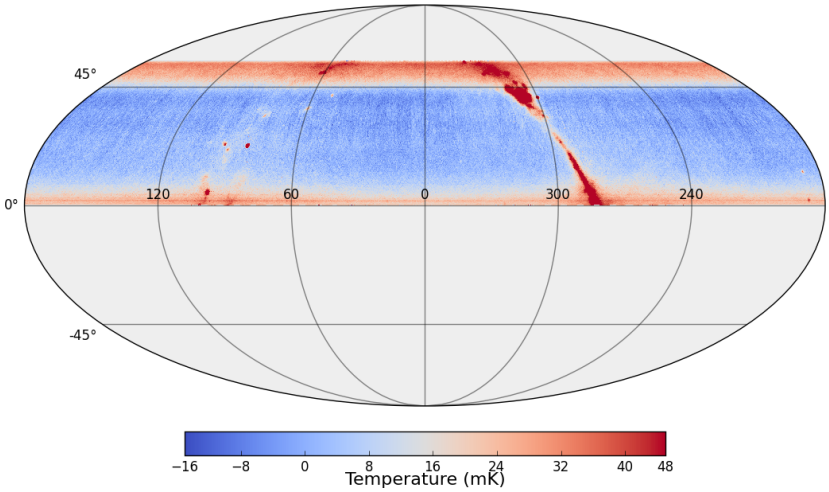

(a)

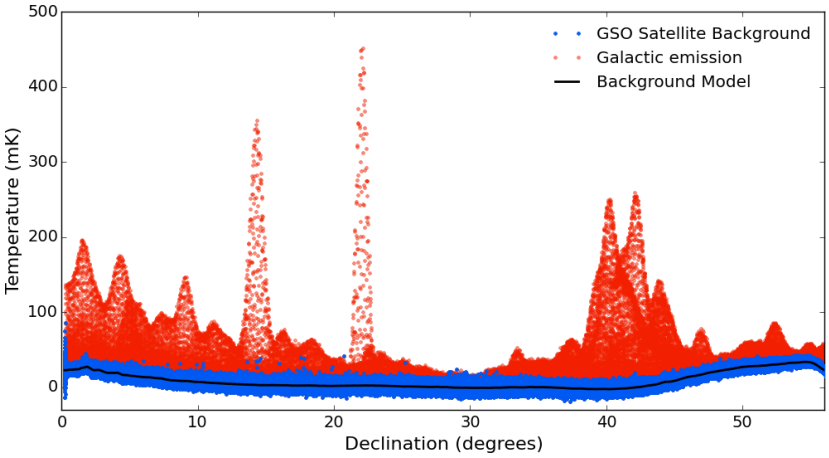

(b)

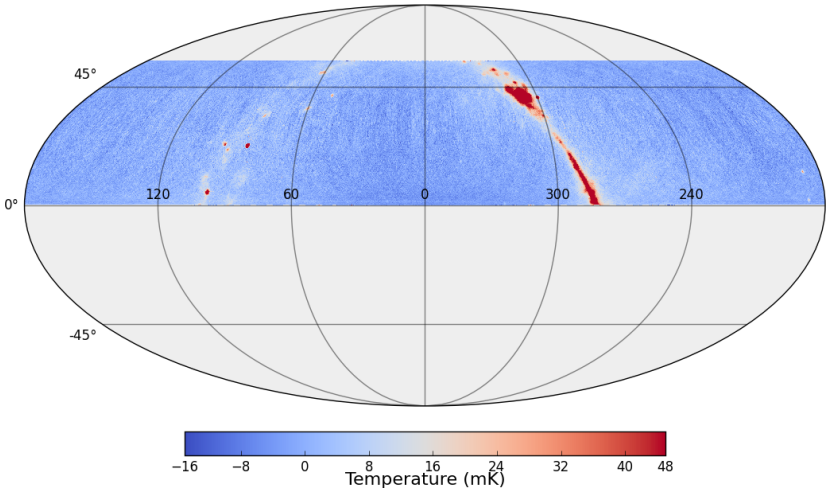

(c)

Figure 4.13: Example of removing the integrated GSO satellite emission in the map domain. *Top*: Before subtracting the GSO satellite emission. *Middle*: Projection of the map pixels along Declination. *Bottom*: After subtracting the GSO satellite emission.

made the *North* and *South* edges of the Epoch 1 maps are heavily contaminated by the GSO satellite emission as shown in Figure 4.13a. The integrated emission of the GSO satellites after performing destriping map-making (see Chapter 5) is a smoothly varying large-scale systematic. The integrated effect of the GSO satellite emission in Figure 4.13a can therefore be modelled by weighted binning the map pixels in Declination and masking any bright radio emission. Interpolating between the weighted bins results in a model of the GSO satellite background emission as shown by the solid black line in Figure 4.13b. Subtracting the model from the map in Figure 4.13a results in Figure 4.13c, which significantly reduces the effect of the integrated GSO satellite emission.

There are several issues with subtracting the integrated GSO satellite emission in the map domain. One is related to the possible suppression of real large-scale structure from the Galaxy, another is that for the GSO emission to be smooth in Declination requires that the two azimuthal locations associated with each Declination to be both sampled per pixel on the sky and the last is that the solution must be found per elevation. The suppression of large-scale structure can be tested using a noiseless simulation. Simulated wide-survey pointing information was used to transform the 11 GHz simulated local sky emission template into TOD, which was then binned into a sky map. Signal was added using the *WMAP* 22.8 GHz map. Figure 4.14a shows the resulting noiseless sky map. Figure 4.14a was then processed to remove the GSO satellite emission using the method discussed earlier. Figure 4.14b shows the comparison between the original *WMAP* 22.8 GHz input signal and the recovered signal. Figure 4.14b shows that only the very largest scales are affected by the removal of the GSO satellite emission. Note that unequal sampling of the azimuthal local emission is an issue as it can result in the residual integrated GSO satellite emission to beat in the Right Ascension direction. The variations may be expected to be as large as the sidereal variations in the satellite brightness but in the final integrated MFI wide-survey maps the variations are not seen to exceed 1 mK. However, this is still a problem when trying to recover weak Galactic emission far from the plane using the wide-survey map and will even be a problem when measuring emission observed in the cosmological fields.

The removal of the GSO satellite emission in the map domain is not perfect and typically the *North* and *South* edges will still have some residual GSO satellite contamination that manifest as stripes in Right Ascension as seen in Figure 4.15. The effect of these residual stripes are typically constrained to be within several degrees of the edges, where the GSO satellite contamination was brightest. To correct for this effect

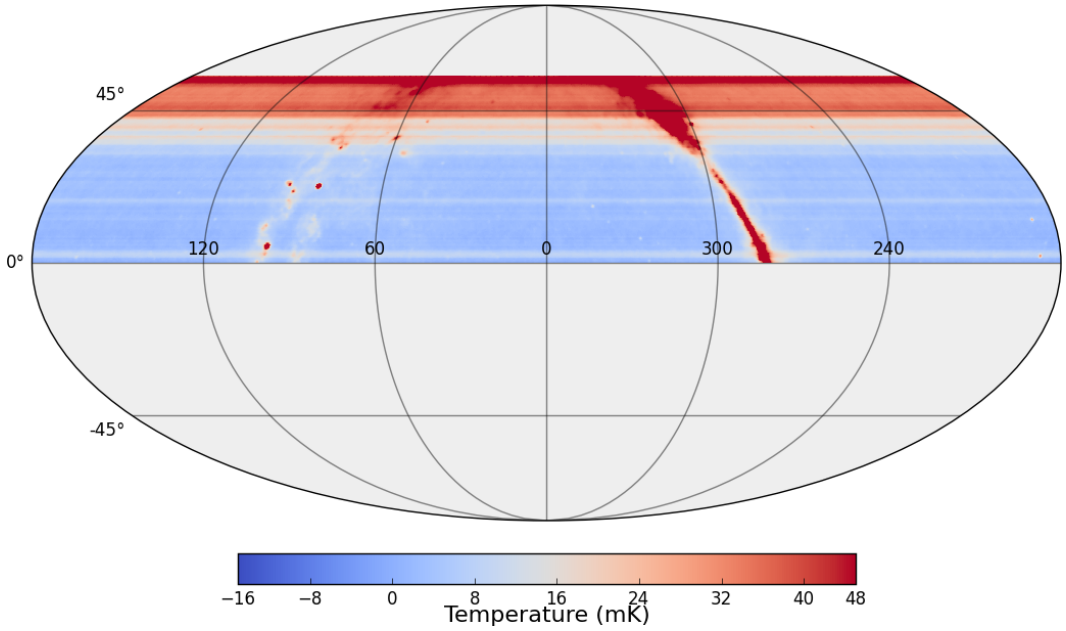

(a)

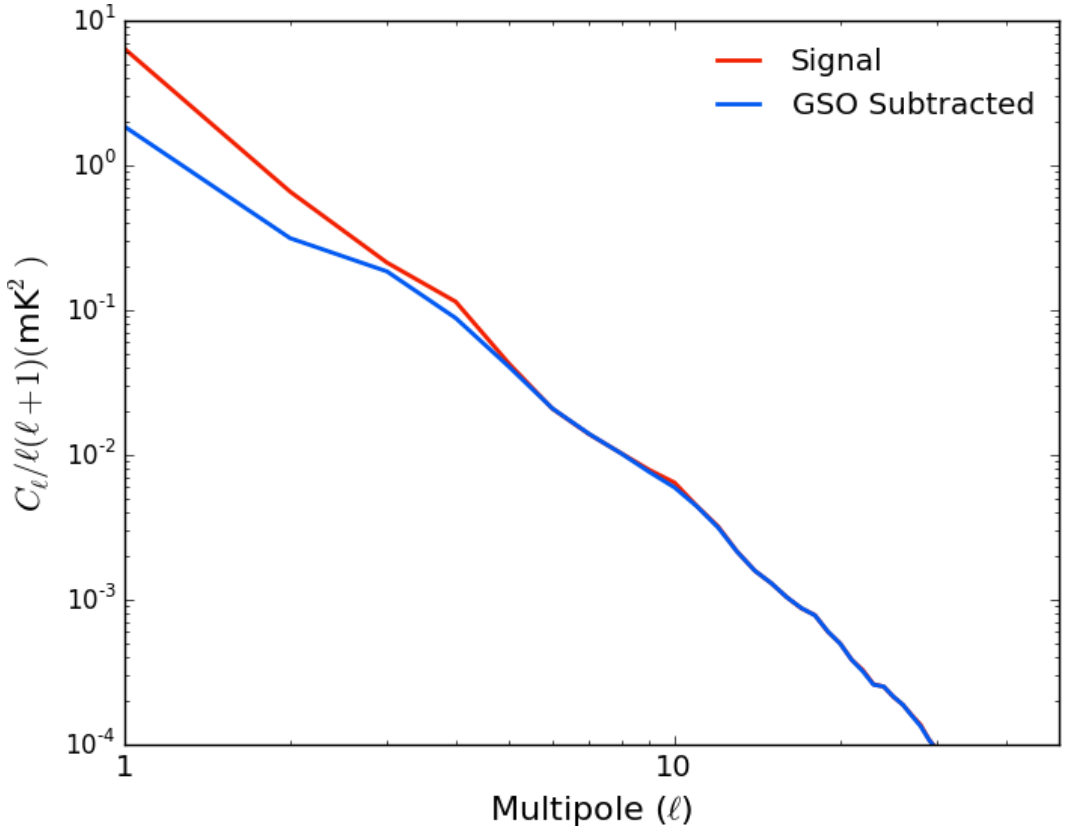

(b)

Figure 4.14: *Top*: Simulated noiseless input map showing a GSO satellite emission signal evenly distributed across the sky and Galactic emission from *WMAP* 22.8 GHz. *Bottom*: Comparison between the noiseless signal-only angular power spectrum and angular power-spectrum of the simulated map after correcting for the simulated GSO satellite emission.

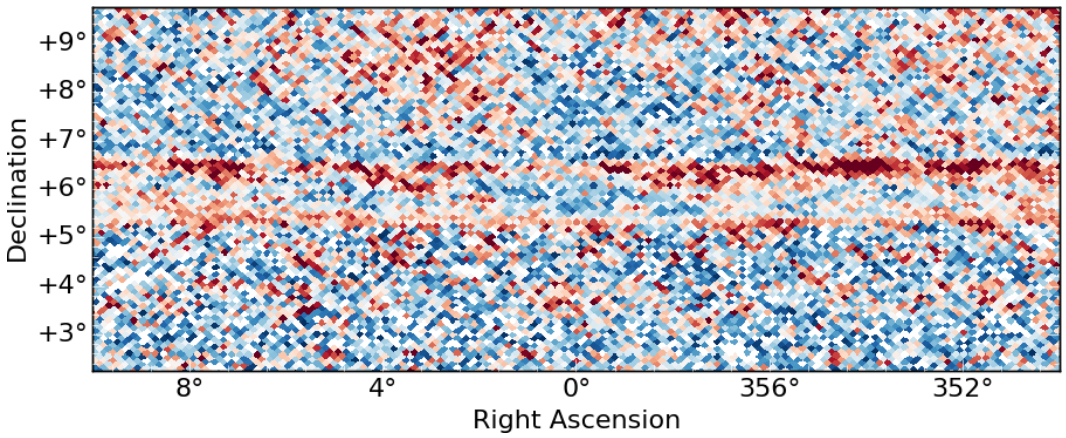

Figure 4.15: When combining wide-survey maps at different elevations residual GSO emission forms low level striping artefacts that can be removed by down weighting the edges of maps at the cost of an increase in noise.

MFI wide-survey maps are generated for each elevation, the large-scale GSO satellite emission is subtracted as above and then all the elevations are combined using weights that are smoothly tapered to zero, 3 degrees from the minimum and maximum Declinations. The tapered weights do remove the stripes at the edges of each elevation map but the trade off is a small increase in the pixel white-noise. However, a slight increase in white-noise is preferred to the correlated noise contribution that was removed.

For the main beam response of many of the GSO satellites and associated sidelobe pick-up, the apparent brightness of the RFI is too high to be modelled and may even saturate the receivers. For the emission from these GSO satellites the only option is to flag the contaminated TOD completely. For the brightest GSO satellites a local sky mask is generated, as in Section 4.1. Figure 4.16 is a mollweide projection of the MFI local sky with black discs marking the location of the bright GSO satellites. The size of the aperture is dependent on the extent of the observed near sidelobes. When processing the MFI TOD the sky map in Figure 4.16 is sampled using the local feed centre pointing information. Less bright GSO satellites and sidelobe pick-up is masked using the spike masking method described in Section 4.2. Dynamic flagging of less bright GSO satellite emission was chosen because of the variability of the GSO satellite emission. Therefore at specific elevations and times regions of the sky normally unobservable become observable resulting in greater complete converge of the Northern sky emission.

This Section has focused on methods for subtraction of the GSO satellite emission

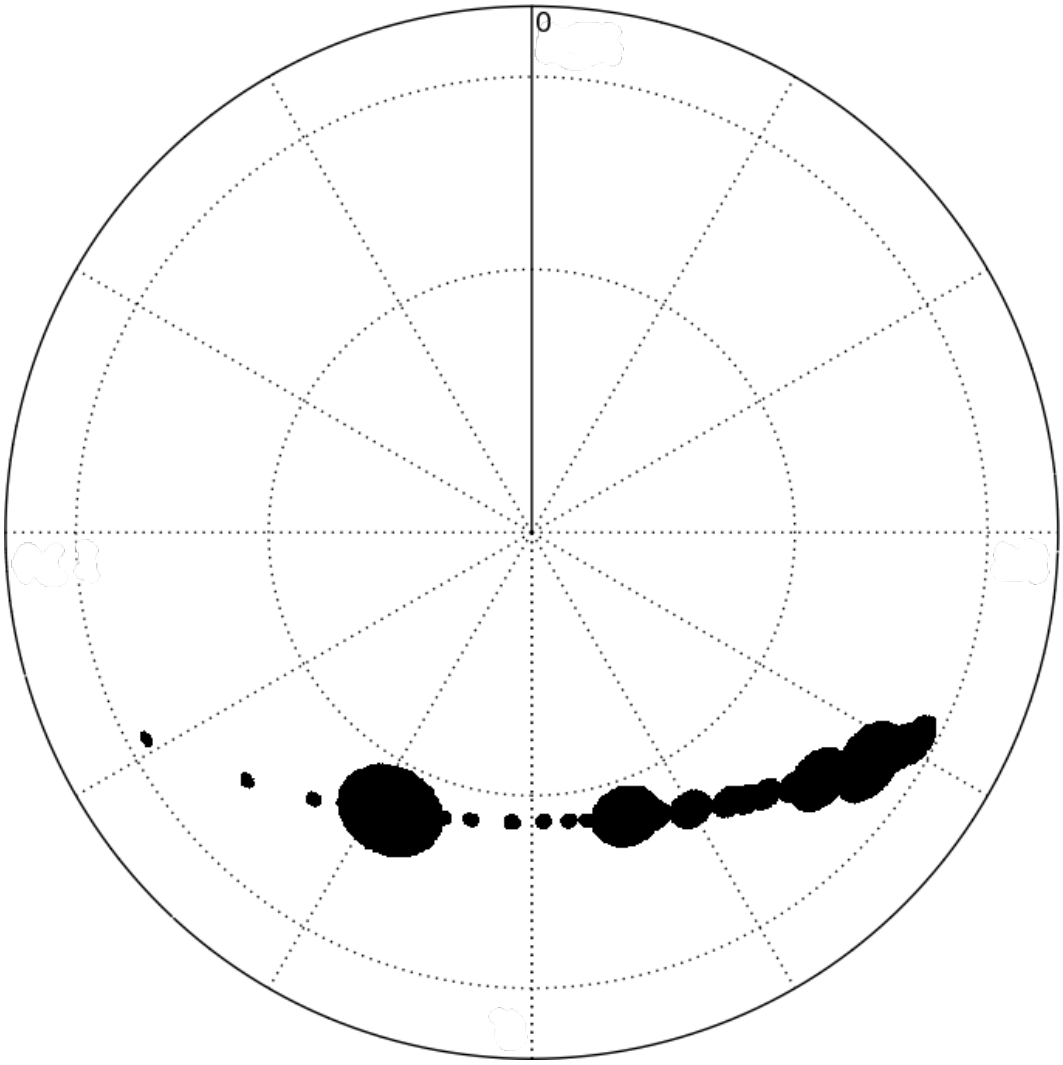

Figure 4.16: Orthographic projection of the bright GSO satellite mask in local coordinates looking up at the zenith. Black apertures mark the locations of GSO satellites and the aperture size reflects the GSO satellite brightness.

from the MFI low frequency observations. Several methods for removing the near and far sidelobe contamination were discussed. Template fitting in the TOD using the MFI beam models seemed promising but the currently available beam models do not adequately recreate the observed far sidelobe pick-up. Template fitting from the observations was found to not be suitable to remove the GSO satellite emission sidelobe pick-up due to the variations in the emission limiting the total available integration time. Fitting for smooth variations in Declination after map-making for each elevation of the wide-survey was found to be the most effective way of removing the integrated GSO satellite sidelobe emission.

4.4 Summary

This Chapter has outlined the various sources of TOD contaminants from the receiver, RFI and astronomical sources. At low frequencies the key source of TOD contamination in the low frequency MFI bands was identified as GSO satellite emission, both in the near and far sidelobe pickup. Unfortunately, for the low frequency MFI bands precise removal of GSO satellite emission at the present time is not possible and will require both improved models of the MFI beams and of the GSO satellite emission. This means that weak emission from the large-scale structures of the Galaxy far from the plane will not be reliable. This will also be true for polarisation observations at low frequencies due to the highly polarised nature of GSO emission. However, the methods described to mitigate GSO satellite emission are sufficiently accurate to recover large-scale emission near the Galactic plane. Chapter 6 will discuss the final TOD flagging efficiency in respect to the MFI wide-survey observations.

Chapter 5

Map-Making

> "If your experiment needs statistics, you ought to have done a better experiment."
>
> Ernest Rutherford.

This Chapter will discuss the general principles of map-making - the process of converting TOD into images of the sky - in the context of the author's own map-making implementation. The author's map-making code is described in this Chapter and used to generate maps from both the MFI wide-survey observations (see Chapter 6) and GBT arcminute resolution raster observations (see Chapter 7). Fundamentally, the task of the author's map-maker is to remove correlated *1/f* noise drifts from TOD without compromising the celestial signal being observed. Secondary goals were to design the implementation such that it was flexible enough to be applied to many different instruments, scalable to handle both small and large datasets, and easily expandable to implement future developments in map-making methods.

As careful validation of the map-making methods described in this Chapter are so important, the Chapter begins with a description of the author's single-dish radio telescope simulation code used to test the map-maker capabilities. Following this a is a general review of current map-making methods. Finally, the author's map-making code implementation is described in detail, along with the results of simulations used to test the map-making codes integrity.

5.1 Radio Telescope Simulation

A single-dish alt-azimuth mounted focal plane array telescope simulation code was written by the author to simulated realistic TOD for testing the integrity of the map-making making code. Simulated TOD was principally used for testing the map-maker but has also aided in the analysis in other Chapters such as the integrated emission from GSO satellites in Section 4.3. The simulation code was written primarily in `Python`. The code utilised the MFI pointing model to generate realistic pointing information and Equation 3.4 to generate *1/f* noise contaminated TOD.

Figure 5.1 shows a schematic of the telescope simulation code. The user would provide the arrangement of the focal plane array, a map of the sky in either `FITS` or `HEALPix` format, and the noise properties of the receivers. Additional parameters such as maps of the local RFI emission or atmospheric emission could be flagged on or off.

Each module of the telescope simulation was tested to ensure it was producing similar TOD to that produced by a real telescope. The scanning module was tested by reproducing the scan tracks from observations of LDN 1622 by the twin-feed Ku-Band receiver on the 100 m Green Bank Telescope (GBT). The Ku-Band receiver has one receiver at the focal centre of the GBT and one receiver offset in the positive azimuth direction by 300 arcsec. The observations were raster scans in Right Ascension and Declination taken at multiple elevations, before and after culmination of LDN 1622 (see Chapter 7). Figure 5.2 shows the comparison between the real scan tracks and those reproduced by the telescope simulation. The difference in density of the tracks in the real and simulated data is because the real data contains many more rasters. The level of accuracy of the reproduced scan tracks was considered sufficiently accurate for the purposes of the simulated telescope.

5.2 Review of Map-Making Methods

The topic of map-making is concerned with the process of generating noise optimal images from TOD. In the simplest case of TOD with only Gaussian distributed noise, the optimal image is obtained from the weighted averaged of the TOD per pixel. If the TOD has correlated *1/f* noise properties then the resulting images are sub-optimal and will contain stripes along the telescope slewing directions that can dominate the astronomical signal. Simple map-making methods subtract *1/f* noise from TOD by

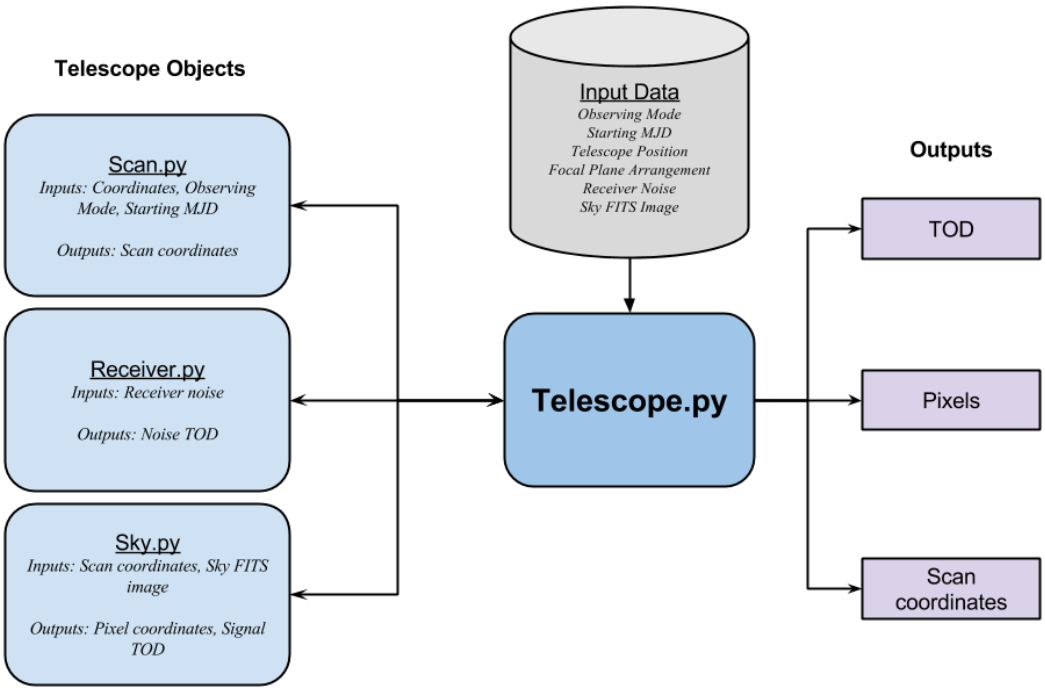

Figure 5.1: Schematic of simulated telescope code. The user would define a parameter file that included maps of the sky to be sampled, the arrangement of the focal plane array and receiver noise properties. The telescope simulation code would use this information to output realistic TOD and pointing information.

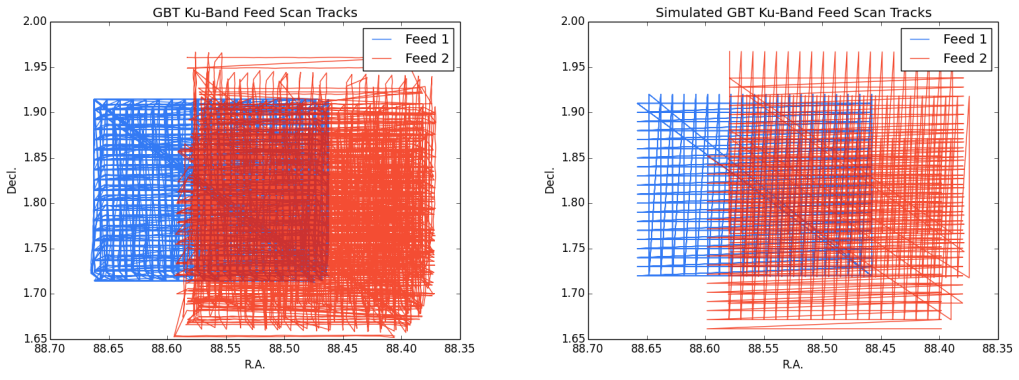

Figure 5.2: Comparison between the real GBT Ku-band pointing information (*left*) and the telescope simulations Ku-band pointing information (*right*).

fitting for polynomials (e.g., Finkbeiner et al., 2002) or Fourier filtering the TOD (e.g., Watson et al., 2005). Another method of removing *1/f* noise proposed by Emerson and Graeve (1988) was to combine the Fourier components of two orthogonal scans, this was the method used by SCUBA (Jenness and Economou, 2004). Unfortunately, all these methods are sub-optimal and would generally compromise the astronomical signal being observed. The maximum entropy method was implemented by some experimenters as a non-linear optimal map-making solution, which has been used by a large range of single-dish (e.g., Watson et al., 1992) and interferometer experiments (e.g., Casassus et al., 2006). However, as the method is non-linear deriving uncertainties can be challenging. This Chapter will describe the linear Bayesian approach to the map-making problem of making optimal images from TOD contaminated by correlated noise.

The TOD (given by $\mathbf{d}$) measured by a receiver can be defined as the linear equation:

$$\mathbf{d} = \mathbf{S} + \mathbf{n} = \mathbf{A}\mathbf{m} + \mathbf{n}. \tag{5.1}$$

The elements of the TOD vector $\mathbf{d}$ are the sum of two components, a vector containing the signal as it changes with the pointing position of the telescope ($\mathbf{S}$) and a vector containing the associated noise measured by the receiver ($\mathbf{n}$). The measured signal $\mathbf{S}$ is the product of a vector containing an optimal pixelised map of the sky ($\mathbf{m}$) and a pointing matrix that transforms the sky-map into TOD ($\mathbf{A}$). The number of rows in the pointing matrix is equal to the number of TOD elements in $\mathbf{d}$ ($N_{\rm tod}$) and the number of columns is equal to the number of pixels in the map $\mathbf{m}$ ($N_{\rm pix}$). Figure 5.3 shows an example of a pointing matrix derived from an 8 element TOD array sampling a four pixel sky-map. As the Figure shows, each row of the pointing matrix will contain mostly zeros and a single one that signifies the pixel to which a given TOD element belongs.

A solution for $\mathbf{m}$ can be found via the minimisation of $\mathbf{n}$ using the Generalised Least-Squares (GLS) equation:

$$\chi^2 = (\mathbf{d} - \mathbf{A}\mathbf{m})^T \mathbf{C}_N^{-1} (\mathbf{d} - \mathbf{A}\mathbf{m}). \tag{5.2}$$

Here $\mathbf{C}_N^{-1}$ defines the covariance matrix of the noise. It is also assumed that the vectors are column vectors and that the transpose is a row vector. Minimising Equation 5.2 with respect to $\mathbf{m}$ gives:

$$\frac{\partial \chi^2}{\partial \mathbf{m}} = \mathbf{A}^T \mathbf{C}_N^{-1} \mathbf{A}\mathbf{m} - \mathbf{A}^T \mathbf{C}_N^{-1} \mathbf{d} = 0, \tag{5.3}$$

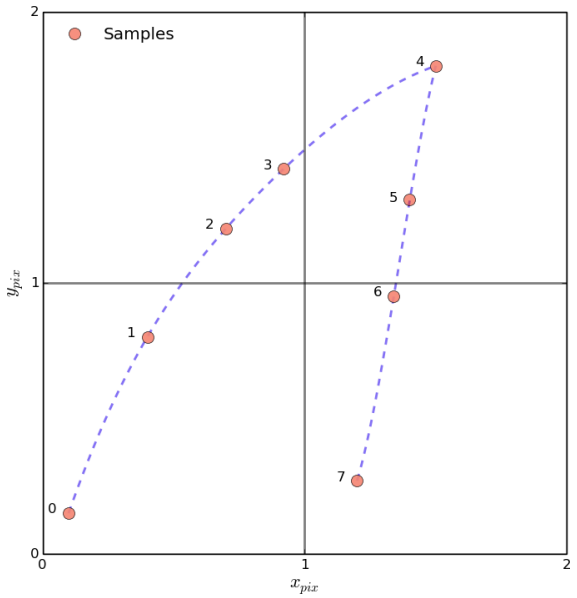

$$\mathbf{A} = \begin{vmatrix} 1 & 0 & 0 & 0 \\ 1 & 0 & 0 & 0 \\ 0 & 1 & 0 & 0 \\ 0 & 1 & 0 & 0 \\ 0 & 0 & 1 & 0 \\ 0 & 0 & 1 & 0 \\ 0 & 0 & 0 & 1 \\ 0 & 0 & 0 & 1 \end{vmatrix}$$

Figure 5.3: How the samples within pixels on the sky (*left*) map to positions in the pointing matrix $\mathbf{A}$ (*right*).

$$\mathbf{m} = (\mathbf{A}^T \mathbf{C}_N^{-1} \mathbf{A})^{-1} \mathbf{A}^T \mathbf{C}_N^{-1} \mathbf{d}. \tag{5.4}$$

This is the optimal minimum-variance solution for the map $\mathbf{m}$. If the noise vector $\mathbf{n}$ only contains uncorrelated Gaussian white-noise then the covariance matrix $\mathbf{C}_N^{-1}$ is simply a diagonal matrix of variances in the form $\mathrm{diag}(\sigma^2)$. This reduces Equation 5.4 to the weighted average of the vector $\mathbf{d}$ into the pixels in the map $\mathbf{m}$. This proves the earlier statement that in the case of only Gaussian noise, the weighted averaging the data is the optimal strategy. For the situation when the noise is correlated, the covariance matrix $\mathbf{C}_N^{-1}$ will not be diagonal and will contain many non-zero cross-terms. In this case the solution for $\mathbf{m}$ can only be found by performing the inversion of the matrix $\mathbf{A}^T \mathbf{C}_N^{-1} \mathbf{A}$ in the linear Equation 5.4.

There have been two schools of thought proposed to find the optimal solution for $\mathbf{m}$. The first will be referred to as maximum-likelihood (ML) map-making (in the literature this may also be referred to as optimal solution map-making), and the other is Destriping map-making. The goal of both methods are to generate models that trace baseline offsets in TOD. Figure 5.4 shows an example of the authors implementation of both methods (see Section 5.3) traces the *1/f* variations in a simulated set of TOD. The Destriping solution is fitting linear *baselines* to the TOD, in this case of 500 samples long, and the ML solution is estimating the baseline drifts per sample. In the limit that the baseline length of the Destriper is one, the solution should be identical to the

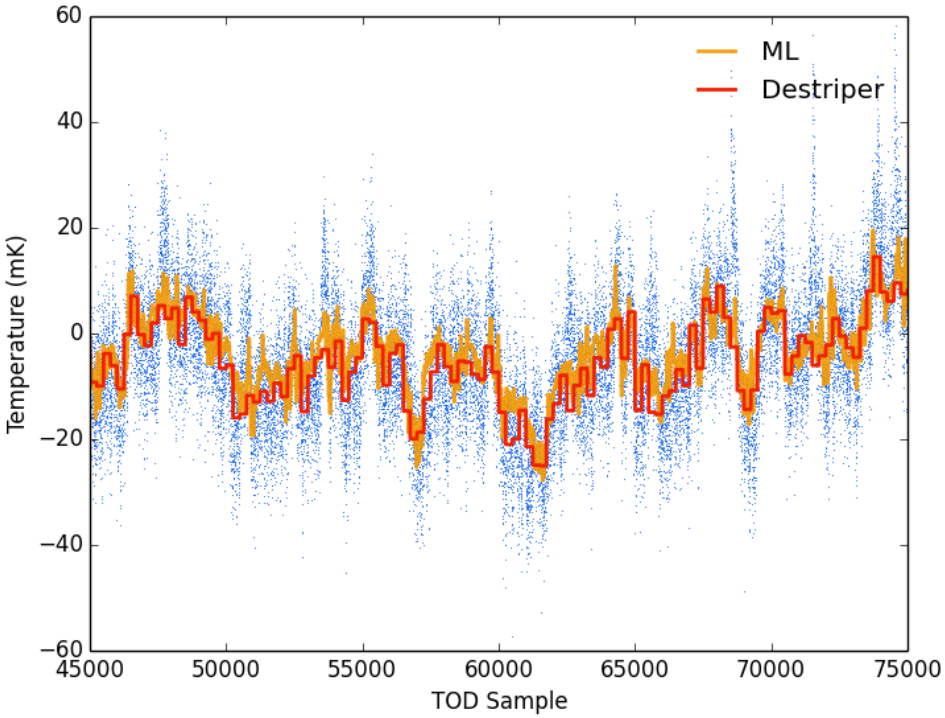

Figure 5.4: The Destriper and ML fits to the correlated *1/f* noise for some example simulated TOD.

ML solution.

5.2.1 Maximum-Likelihood Map-Making

In practice, solving Equation 5.4 by the brute force inversion of $\mathbf{A}^T\mathbf{C}_N^{-1}\mathbf{A}$ is impossible for images of even moderate size. The reason for this is that brute force methods, such as LU Decomposition, require $O(N_{\rm pix}^3)$ operations (Press et al., 1992). A common method for maximum-likelihood (ML) map-making codes is to perform the inversion using the Conjugate Gradient Method (CGM), typically with some form of preconditioner matrix to whiten the noise. Currently there are several optimal map-making codes discussed in the literature, some of which are publicly available, for example `mapCUMBA` (Doré et al., 2001) and `MADmap` (Cantalupo et al., 2010), and others that were developed internally, such as `ROMA` (Natoli et al., 2001). A detailed description of ML map-making is given in the context of the authors map-making implementation (see Section 5.3).

5.2.2 Destriping Map-Making

Destriping map-making was pioneered by Delabrouille (1998) and Maino et al. (1999) as an alternative to the ML map-making implementations. The benefits of Destriping map-making is that it is less computer resource intensive and does not relying on computing the full noise covariance matrix. The cost of these benefits is that Destriping efficiency is far more dependent on telescope scanning strategy and does not always result in the optimal minimum-variance solutions for $\mathbf{m}$.

Following the formalism set out in Sutton et al. (2009) and Keihänen et al. (2010), Destriping map-making modifies the data vector $\mathbf{d}$ such that the noise term $\mathbf{n}$ is composed of two parts: a white noise component $\mathbf{n}_w$ and a correlated noise component $\mathbf{n}_c$. The correlated noise component can be decomposed into a series of linear offsets in the TOD that is described by a series of amplitudes $\mathbf{a}$ and a *folding matrix* $\mathbf{F}$ that either stretches $\mathbf{a}$ out into $\mathbf{d}$ or folds $\mathbf{d}$ into $\mathbf{a}$. Equation 5.1 can be rewritten as:

$$\mathbf{d} = \mathbf{Am} + \mathbf{Fa} + \mathbf{n}_w. \tag{5.5}$$

Equation 5.2 is then written in terms of just $\mathbf{n}_w$ resulting in:

$$\chi^2 = (\mathbf{d} - \mathbf{Am} - \mathbf{Fa})^T \mathbf{C}_N^{-1} (\mathbf{d} - \mathbf{Am} - \mathbf{Fa}). \tag{5.6}$$

Unlike with ML map-making, Destriping seems to find a solution for the correlated noise offsets $\mathbf{a}$ in the TOD. The first step, as before, is to minimise the GLS Equation 5.6 with respect to $\mathbf{m}$:

$$\frac{\partial \chi^2}{\partial \mathbf{m}} = \mathbf{A}^T \mathbf{C}_N^{-1} \mathbf{Am} + \mathbf{A}^T \mathbf{C}_N^{-1} \mathbf{Fa} - \mathbf{A}^T \mathbf{C}_N^{-1} \mathbf{d} = 0, \tag{5.7}$$

$$\mathbf{m} = (\mathbf{A}^T \mathbf{C}_N^{-1} \mathbf{A})^{-1} \mathbf{A}^T \mathbf{C}_N^{-1} (\mathbf{d} - \mathbf{Fa}). \tag{5.8}$$

Substituting Equation 5.8 into Equation 5.6 and defining $\mathbf{Z} = \mathbf{I} - \mathbf{A}(\mathbf{A}^T \mathbf{C}_N^{-1} \mathbf{A})^{-1} \mathbf{A}^T \mathbf{C}_N^{-1}$ gives:

$$\chi^2 = (\mathbf{Zd} - \mathbf{ZFa})^T \mathbf{C}_N^{-1} (\mathbf{Zd} - \mathbf{ZFa}). \tag{5.9}$$

Finally, minimising Equation 5.9 with respect to $\mathbf{a}$ gives:

$$\frac{\partial \chi^2}{\partial \mathbf{a}} = \mathbf{F}^T \mathbf{Z}^T \mathbf{C}_N^{-1} \mathbf{ZFa} - \mathbf{F}^T \mathbf{Z}^T \mathbf{C}_N^{-1} \mathbf{Zd} = 0, \tag{5.10}$$

$$\mathbf{a} = (\mathbf{F}^T \mathbf{Z}^T \mathbf{C}_N^{-1} \mathbf{ZF})^{-1} \mathbf{F}^T \mathbf{Z}^T \mathbf{C}_N^{-1} \mathbf{Zd}. \tag{5.11}$$

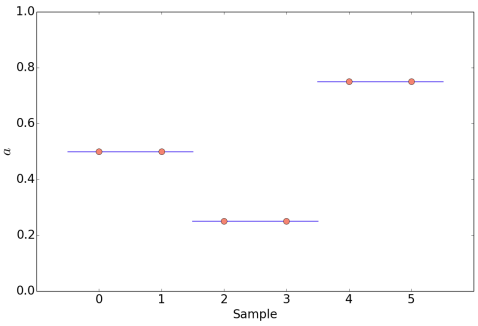

$$\mathbf{F} = \begin{vmatrix} 1 & 0 & 0 \\ 1 & 0 & 0 \\ 0 & 1 & 0 \\ 0 & 1 & 0 \\ 0 & 0 & 1 \\ 0 & 0 & 1 \end{vmatrix} \qquad \mathbf{a} = \begin{bmatrix} 0.5 \\ 0.25 \\ 0.75 \end{bmatrix}$$

Figure 5.5: How the samples within baselines (*left*) map to positions in the folding matrix $\mathbf{F}$ (*right*).

The offsets derived from Equation 5.11 can then be substituted back into Equation 5.8 to find the solution for $\mathbf{m}$.

A large number of Destriping map-making codes have been developed and used by a number of current instruments. For example, `Descart` (Sutton et al., 2009, 2010) used by the C-BASS collaboration (King et al., 2014), and `MADAM` (Keihänen et al., 2004, 2010), which is implemented into the *Planck* LFI data processing pipeline (Planck Collaboration et al., 2014i). Unfortunately neither of these map-making codes at the time of writing are publicly available. Details of the author's Destriping map-making implementation are described in Section 5.3.

5.3 Map-Making Implementation

This Section will discuss the implementations of ML map-making and Destriping map-making by the author. First, the shared code frameworks will be discussed, followed by specific details required to implement both map-making methods.

5.3.1 Conjugate Gradient Method

The backbone of the author's ML and Destriping map-making algorithms is the author's custom CGM implementation, optimised for the map-making problem (Press et al., 1992). The CGM method iteratively solves for the minimum of quadratic equations of the form:

$$f(\mathbf{x}) = \frac{1}{2}\mathbf{x}^T\mathbf{B}\mathbf{x} + \mathbf{b}\mathbf{x}, \tag{5.12}$$

which have a minimum when

$$f'(\mathbf{x}) = \mathbf{b} - \mathbf{B}\mathbf{x} = 0. \tag{5.13}$$

A condition required for the CGM to correctly minimise is that $\mathbf{B}$ is a symmetric positive-definite matrix. In this instance, symmetric refers to a matrix that is mirrored along the diagonal, and positive-definite meaning $f(\mathbf{x}) >= 0$ for all values of $\mathbf{x}$. If $\mathbf{A}$ in Equation 5.12 is poorly sampled, then the matrix can become very ill-conditioned or even singular, resulting in a failed solution from the CGM implementation. In terms of map-making this would be similar to the sky being very poorly sampled with few crossings between telescope slews. Typically, $\mathbf{B}$ must also be sparse; while the CGM method will solve a dense matrix $\mathbf{B}$, it will be no more efficient than more brute force methods.

There are several definitions required to understand the CGM method. The first is the residual vector:

$$\mathbf{r}_i = \mathbf{b} - \mathbf{B}\mathbf{x}_i. \tag{5.14}$$

Where the $\mathbf{r} \cdot \mathbf{r}$ defines how far away Equation 5.12 is from the solution. Another definition is the search vector $\mathbf{s}$, which describes the direction that Equation 5.12 steps towards on each iteration. The CGM method forces all search vectors to be orthogonal. The vector $\mathbf{Bs}$ is the conjugate search vector of $\mathbf{s}$.

The iterative steps behind the CGM implementation are shown in Figure 5.6. Stopping the iterative process is a user defined choice depending on the accuracy of the solution required. The CGM is stopped when the product of the residual vectors $r_i^T r_i$ is less than $r_0^T r_0/c$, where c is an arbitrary constant typically set between 10^{10} to 10^{20}. The novel difference with this CGM implementation is that the sparse matrix $\mathbf{B}$ and the vector $\mathbf{b}$ are not required to be known. Instead, the CGM code expects two user-defined functions. One function must define $\mathbf{b}$ for a given input vector $\mathbf{x}$, and the second function returns the matrix multiplication of the argument by the matrix $\mathbf{B}$.

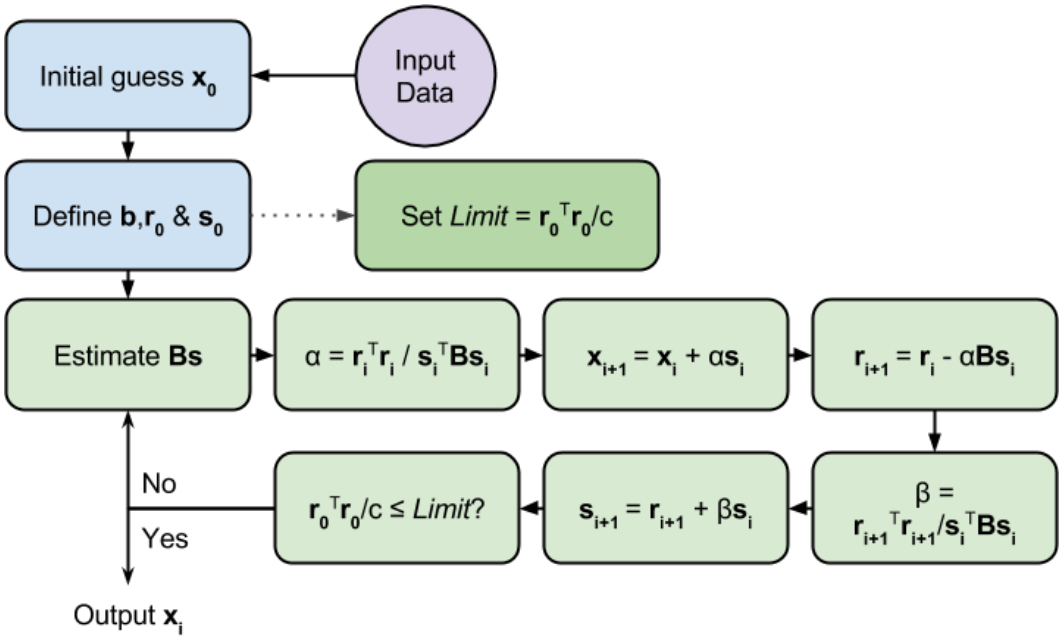

Figure 5.6: Flow chart representation of the implementation of the CGM method. The input data includes the TOD, a function that defines $\mathbf{b}$ and a function that defines the operation $\mathbf{Bx}$.

The definitions of these two functions will be discussed in the context of Destriping and maximum likelihood map-making in the proceeding Sections.

5.3.2 Destriping Map-Making Implementation

The author's Destriping algorithm implementation $\mathbf{b}$ (from the previous subsection) is defined as

$$\mathbf{b} = \mathbf{F}^T\mathbf{Z}^T\mathbf{C}_N^{-1}\mathbf{Z}\mathbf{d}, \tag{5.15}$$

and the vector $\mathbf{Bx}$ is

$$\mathbf{Bx} = \mathbf{F}^T\mathbf{Z}^T\mathbf{C}_N^{-1}\mathbf{Z}\mathbf{F}\mathbf{a}, \tag{5.16}$$

and the vector $\mathbf{Bs}$ is

$$\mathbf{Bs} = \mathbf{F}^T\mathbf{Z}^T\mathbf{C}_N^{-1}\mathbf{Z}\mathbf{F}\mathbf{s}. \tag{5.17}$$

The Destriping implementation requires the definition of two functions, both of which contain a near identical algorithm. For the first function, the TOD is binned into a naive, weighted average map via the operation:

$$\mathbf{m}_n = (\mathbf{A}^T\mathbf{C}_N^{-1}\mathbf{A})^{-1}\mathbf{A}^T\mathbf{C}_N^{-1}\mathbf{d}, \tag{5.18}$$

where $\mathbf{m}_n$ is the naive map. Next the naive map is sampled using pixel coordinates (e.g., the operation $\mathbf{Am}$) in order to stretch it to the length of the TOD. This vector is then summed into chunks of data using the folding matrix:

$$\mathbf{e}_n = \mathbf{F}^T\mathbf{A}\mathbf{m}_n, \tag{5.19}$$

where $\mathbf{e}_n$ is the resulting vector. The vector $\mathbf{e}_n$ is subtracted from a vector containing the weights for each baseline resulting in the solution:

$$\mathbf{b} = \mathbf{F}^T\mathbf{Z}^T\mathbf{C}_N^{-1}\mathbf{Z}\mathbf{d} = \mathbf{F}^T\mathbf{C}_N^{-1}\mathbf{d} - \mathbf{e}_n. \tag{5.20}$$

The second function follows a series of very similar steps to the first. The offsets are stretched out to the length of the TOD:

$$\mathbf{w}_n = \mathbf{F}\mathbf{a}, \tag{5.21}$$

where $\mathbf{w}_n$ is the stretched out offsets vector. The weighted average of $\mathbf{w}_n$ is then calculated for each pixel in a map:

$$\mathbf{m}_n = (\mathbf{A}^T\mathbf{C}_N^{-1}\mathbf{A})^{-1}\mathbf{A}^T\mathbf{C}_N^{-1}\mathbf{w}_n. \tag{5.22}$$

This map is then subsequently sampled using the telescope pointing information to generate a vector of length equal to the TOD, this vector is then summed into a set of baselines (e.g., as in Equation 5.19):

$$\mathbf{e}_n = \mathbf{F}^T\mathbf{A}\mathbf{m}_n. \tag{5.23}$$

This results in the final step, where the vector $\mathbf{e}_n$ is subtracted from the vector containing the weights for each baseline:

$$\mathbf{B}\mathbf{x} = \mathbf{F}^T\mathbf{Z}^T\mathbf{C}_N^{-1}\mathbf{Z}\mathbf{F}\mathbf{a} = \mathbf{F}^T\mathbf{C}_N^{-1}\mathbf{F}\mathbf{a} - \mathbf{e}_n - \sum_{i=0}^{N_a} a_i. \tag{5.24}$$

This final step deviates slightly from Equation 5.20, as the sum of the offsets is also subtracted. This change to the Destriping algorithm was first outlined in Keihänen et al. (2004) and ensures that the background offsets of the Destriped maps are zero.

To ensure that the Destriping implementation described here is scalable to any possible future instrumentation it is parallelised using `MPI4Py` (Dalcin et al., 2005), which is a wrapper for the `C` based Message Passing Interface (`MPI`) libraries. The

`MPI` implementation ensures that the TOD are shared across many different machines. This is important because the total data rate of focal plane arrays can rapidly increase. For example, each receiver pair output from the MFI has a 50 Hz downsampled data rate of 20 MB per hour (include TOD, pointing information and masks), which for the approximately 5000 hours of data is 20 GB. This is a relatively manageable data size but when combining all the MFI TOD at one frequency this increases to 80 GB, which is beyond the memory capacity of a typical modern computer. This problem becomes worse for more large focal plane arrays such as the TGI, which has 31 horns, resulting in 1240 GB of TOD for a 5000 hour survey. A general outline of how the MPI-ready Destriping implementation works is shown in Figure 5.7. The key change for the MPI implementation is that each node processing the data must share the map of the offsets generated in Equation 5.22 for each iteration of the CGM method.

5.3.3 Maximum-Likelihood Map-Making Implementation

The ML map-making implementation is slightly more complicated than the Destriping implementation because it requires two loops. The inner loop is the CGM method and the outer loop is used to estimate the noise covariance matrix. The principal difficulty in implementing a ML map-making code is performing the inversion of the covariance matrix, $\mathbf{C}_N$. This problem will be addressed first. Once the covariance matrix can be inverted, solving for ML map follows a similar solution to the Destriping map-maker.

Each row of the covariance matrix can be defined as the auto-covariance function of $\mathbf{n}$ in Equation 5.1,

$$C_N(\tau + j \mod N_{\rm tod}, j) \approx \sum_{i=1}^{N_{\rm tod}} n_i n_{i+\tau}, \tag{5.25}$$

where τ is a displacement of the samples running from 0 to $N_{\rm tod}$ and j is the current row of the covariance matrix. Note that the columns change according to $\tau + j \mod N_{\rm tod}$, which implies that the covariance matrix will be a *circulant* matrix and also imposes the condition that the noise properties of $\mathbf{n}$ be stationary. Figure 5.8 shows an example of a circulant matrix.

A useful property of linear equations containing circulant matrices is that they can be solved by simply multiplying the Fourier transform of the first row of the circulant

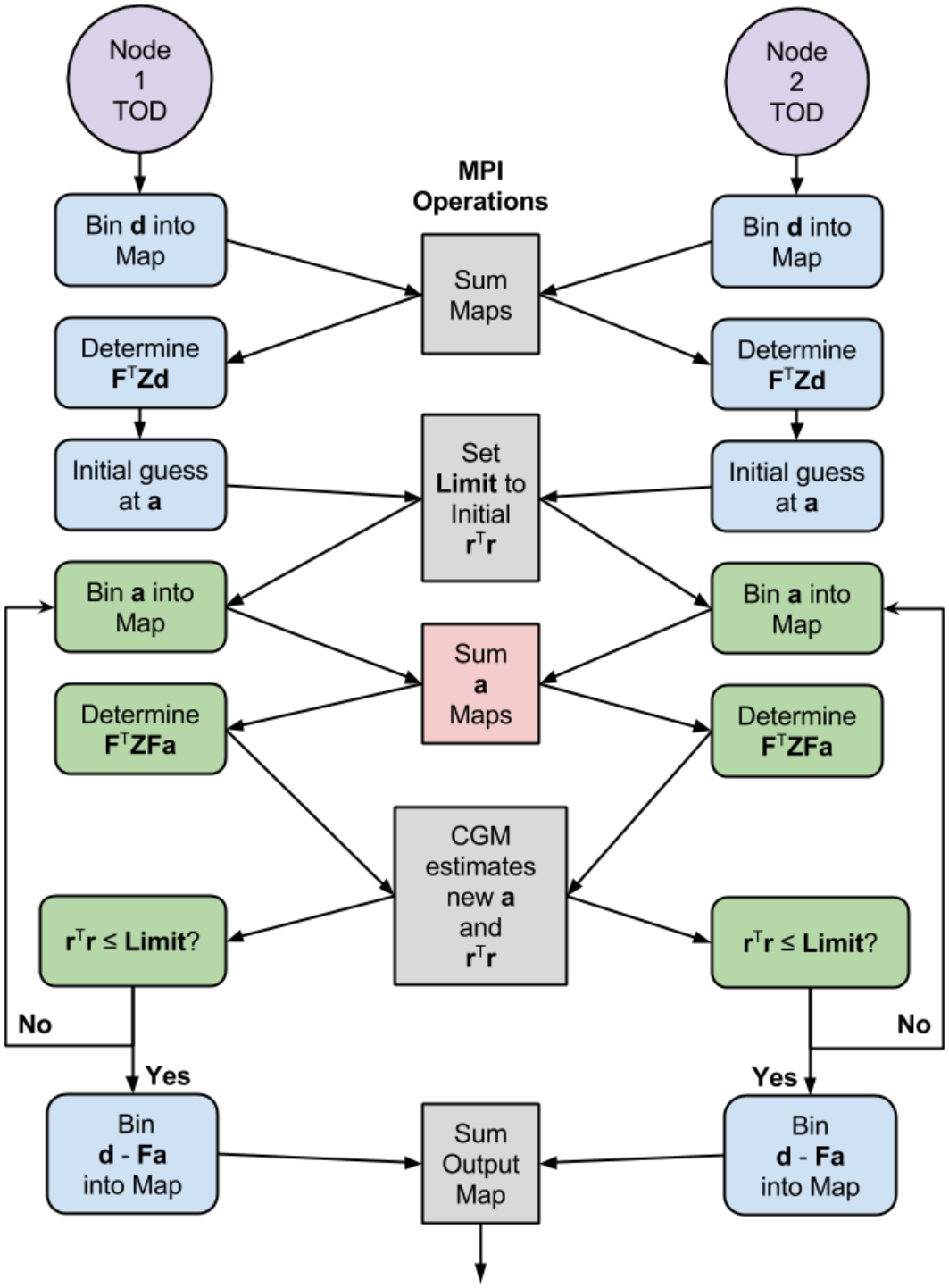

Figure 5.7: Flow chart representation of the MPI-ready Destriping algorithm. Green boxes indicate operations within the CGM code and the red box indicates the primary inefficiency in the MPI implementation.

$$\mathbf{C}_N = \begin{vmatrix} 1 & 2 & 3 \\ 3 & 1 & 2 \\ 2 & 3 & 1 \end{vmatrix}$$

Figure 5.8: The covariance matrix of the TOD is assumed to be a circulant matrix. A circulant matrix simply means that each column element will shift one column to the right with each row.

matrix with the Fourier transform of the TOD vector (Natoli et al., 2001):

$$\mathbf{C}_N^{-1} d = \mathcal{F}^{-1} \left\{ \frac{\mathcal{F}\{\mathbf{d}\}}{\mathcal{F}^{-1}\{\mathbf{C}_N\}} \right\}. \tag{5.26}$$

This technique can be further optimised by noting that the Fourier transform of the noise vector auto-covariance function is the noise vector power spectral density (PSD) function or $\mathcal{F}\{\mathbf{C}_N\} = |\mathcal{F}\{\mathbf{n}\}|$. The PSD of $\mathbf{n}$ has the advantage that it is far quicker to compute than the auto-covariance of $\mathbf{n}$. When using the PSD, Eqn. 5.26 can be written as,

$$\mathbf{C}_N^{-1}\mathbf{d} = \mathcal{F}^{-1} \left\{ \frac{\mathcal{F}\{\mathbf{d}\}}{|\mathcal{F}\{\mathbf{n}\}|} \right\}. \tag{5.27}$$

A way of interpreting this operation is to think of the PSD of $\mathbf{n}$ as a low-pass spectral filter being applied to the TOD. The effects of the filtering on the signal in the data are undone when the data are binned into the map.

Once the noise covariance matrix is known, and the method for inverting it is implemented, the solution to Equation 5.4 can be found using the CGM method. Again, two functions are passed to the CGM code, where one defines:

$$\mathbf{b} = \mathbf{A}\mathbf{C}_N^{-1}\mathbf{d}, \tag{5.28}$$

and the other defines both

$$\mathbf{B}\mathbf{x} = \mathbf{A}^T\mathbf{C}_N^{-1}\mathbf{A}\mathbf{m}, \tag{5.29}$$

$$\mathbf{B}\mathbf{s} = \mathbf{A}^T\mathbf{C}_N^{-1}\mathbf{A}\mathbf{s}. \tag{5.30}$$

Where each of the above will involve an FFT to invert and multiply the covariance matrix with a given vector.

In situations when the exact PSD function of $\mathbf{n}$ is unknown, it must be estimated from the TOD. The noise PSD can be iteratively estimated from the TOD via the following steps. On the first iteration the *residual* noise vector is assumed to be the input TOD,

$$residual = \mathbf{d}. \tag{5.31}$$

The residual will therefore contain both signal and correlated noise. The PSD of the initial *residual* will look like Figure 3.2. This PSD is then binned and a model of noise spectrum is derived using linear interpolation in log-space. This model noise spectrum is then used as the first row of the covariance matrix, and is used to generate the initial estimate of the map vector $\mathbf{m}$. The next iteration, the *residual* vector is estimated as

$$residual_i = \mathbf{d} - \mathbf{A}\mathbf{m}_{i-1}, \tag{5.32}$$

where i describes the number of the current iteration. The last best estimate of the map vector is subtracted from the TOD and therefore the *residual* vector should contain principally just the correlated noise component. This is again used to derive a new noise model and the process is repeated. Typically between three and four iterations are required before the system converges to the optimal solution. A summary flow diagram of the ML map-maker is shown in Figure 5.9.

5.3.4 Polarisation Map-Making

The current map-making implementation does not extend to polarisation map-making, in part because polarisation measurements are not the focus of this thesis. However, the current map-making framework lends itself well to adding polarisation map-making in the future. This subsection will therefore briefly discuss the foundations of how to perform polarisation map-making, with a specific focus on the MFI.

In Chapter 2 the fundamental components of the MFI output channels were stated in terms of the Stokes parameter components. Assuming that all of the TOD has been calibrated to a standard brightness temperature scale, the correlated channel outputs of the MFI are defined as:

$$T_s(\chi) = \frac{1}{2}\left[I + Q\sin(\chi) + U\cos(\chi)\right], \tag{5.33}$$

$$T_d(\chi) = \frac{1}{2}\left[I - Q\sin(\chi) - U\cos(\chi)\right], \tag{5.34}$$

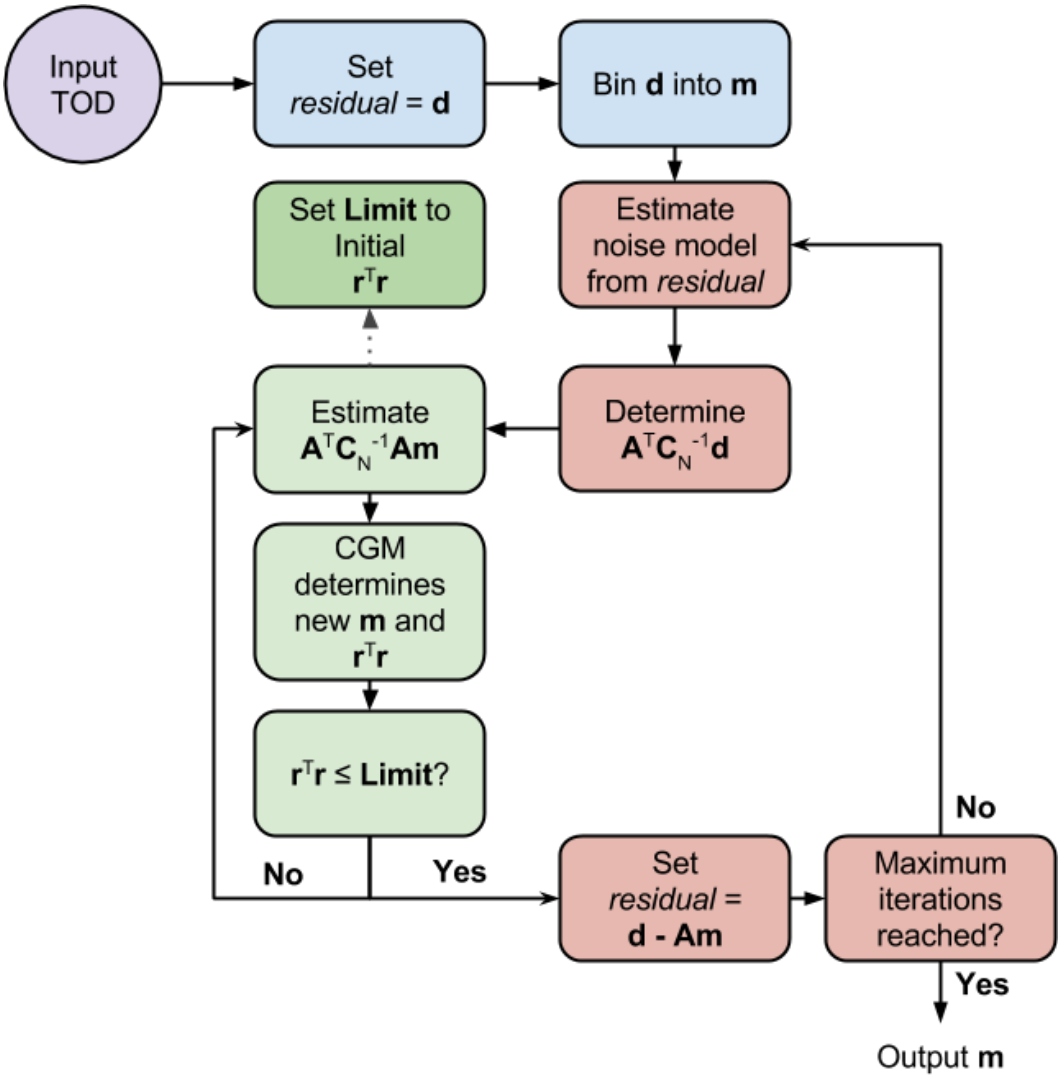

Figure 5.9: Flow chart representation of the ML map-making algorithm. Red boxes indicate the outer loop needed to estimate the covariance of the noise and the green boxes indicate the CGM code.

where T_s and T_d are the summed and differenced correlated channel outputs respectively. Both output channels are a function of χ, which is defined as

$$\chi = 4(\psi + \psi_0) + 2P_a, \tag{5.35}$$

where ψ is the relative angle of the MFI polar modulator, ψ_0 is the absolute polar modulator angle and P_a is the parallactic angle of the source on the sky.

As discussed in earlier Chapters, the polarisation component of the MFI can be isolated by differencing channel output pairs. Differencing the MFI correlated channels results in:

$$T_p(\chi) = T_s(\chi) - T_d(\chi) = [Q\sin(\chi) + U\cos(\chi)] \tag{5.36}$$

where $T_p(\chi)$ is the polarisation response in the local frame of the telescope. It is useful to rewrite Equation 5.36 as a vector equation:

$$T_p(\chi) = \begin{bmatrix} \sin(\chi) & \cos(\chi) \end{bmatrix} \begin{bmatrix} Q \\ U \end{bmatrix}. \tag{5.37}$$

Taking Equation 5.37 and multiplying it by the transpose of $\begin{bmatrix} \sin(\chi) & \cos(\chi) \end{bmatrix}$ results in a linear equation:

$$\begin{bmatrix} T_p(\chi)\sin(\chi) \\ T_p(\chi)\cos(\chi) \end{bmatrix} = \begin{bmatrix} \sin^2(\chi) & \sin(\chi)\cos(\chi) \\ \sin(\chi)\cos(\chi) & \cos^2(\chi) \end{bmatrix} \begin{bmatrix} Q \\ U \end{bmatrix}. \tag{5.38}$$

The terms Q and U in Equation 5.38 refer to the brightness of either linear polarisation component for a given pixel line-of-sight in two separate linear polarisation maps. To isolate the Q and U components per pixel requires averaging observations that have a well sampled distribution of χ and then solving the linear equation. This results in each pixel of Q and U being calculated as:

$$\begin{bmatrix} Q_{pix} \\ U_{pix} \end{bmatrix} = \frac{1}{\langle \mathrm{s}^2 \rangle \langle \mathrm{c}^2 \rangle - \langle \mathrm{sc} \rangle^2} \begin{bmatrix} \langle \mathrm{c}^2 \rangle & -\langle \mathrm{sc} \rangle \\ -\langle \mathrm{sc} \rangle & \langle \mathrm{s}^2 \rangle \end{bmatrix} \begin{bmatrix} \langle T_p \mathrm{s} \rangle \\ \langle T_p \mathrm{c} \rangle \end{bmatrix} \tag{5.39}$$

where all the sine and cosine terms have been abbreviated to s and c, all terms on the right are assumed to be functions of χ, each term refers to a single pixel, and $\langle\rangle$ indicates the mean value within a pixel. For a well sampled distribution of χ_{pix}, $\langle \mathrm{c}^2 \rangle$ and $\langle \mathrm{s}^2 \rangle$ terms tend to a half, and the $\langle \mathrm{sc} \rangle$ terms tend to zero. If χ is very poorly sampled then $\langle \mathrm{s}^2 \rangle \langle \mathrm{c}^2 \rangle \approx \langle \mathrm{sc} \rangle^2$, making the matrix singular. Therefore any polarisation map-making code must include a mask that avoids pixels with poor χ angle sampling.

5.4 Map-Maker Integrity Simulations

Two sets of simulations will be used to test the quality of the Destriping and ML map-making algorithms. The first set of simulations will compare the quality of the Destriping and ML map-making for MFI nominal survey mode observations. The second set of simulations will test the map-makers capabilities for small field raster scan observations taken with the MFI and GBT receivers.

5.4.1 MFI Wide-Survey Simulations

A set of 96 hour long 60 degree wide-survey MFI observations generated using the telescope simulation code will be used to test the map-making performance. The simulation generated two sets of TOD with noise properties similar to those expected from the MFI Horn 11 GHz channels. Both simulated TOD datasets shared the same noise equivalent power (NEP) of $800\,\mu\mathrm{K\,s^{1/2}}$, a *1/f* spectral index of 1.25, and the sample rate of 50 Hz. One set of simulated TOD has a knee frequency of 10 Hz and the other 80 Hz. The slewing speed of the telescope was set to $6\,\mathrm{degrees\,s^{-1}}$ and the observations were split into contiguous 6 hour blocks. The longitude and latitude were set to match the geodetic position of the QUIJOTE MFI. To minimise the amount of data being generated only a single receiver was simulated, positioned in the MFI focal centre. The horn position will have no effect on the *1/f* noise solutions. The Galactic emission was simulated using the *WMAP* 22.8 GHz all-sky signal map (Bennett et al., 2013) extrapolated to the expected 11 GHz brightness assuming a frequency power law with a spectral index of -0.15 for the whole sky.

Figure 5.10a shows the naively binned, weighted average Mollweide all-sky map in celestial coordinates. The Galactic plane in this image can be seen arching up towards the north celestial pole. The ringing in the map is the result of the 80 Hz knee frequency *1/f* noise contamination. Note that the amplitudes of these *1/f* noise rings are higher than most of the mid-to-high Galactic emission. This is especially obvious for the outer Galactic region seen in the *East* of the image. Figures 5.10c and 5.10d show the residual maps of the ML and Destriping map-making solutions with the noiseless signal map. The Destriping solution used a baseline length of 500 samples or 2.5 seconds. Visual inspection of both images shows that both maps are now dominated by white noise and no obvious ringing effects of *1/f* noise can be seen. Note also that these figures have a colour scale that is a factor of two smaller than the colour scale in Figure 5.10a. Figure

5.10b is the residual map between the ML map-making solution and the Destriping map-making solution. As both input datasets to the map-makers shared the same white noise properties, this residual map is revealing the residual correlated noise rings that could not be removed by the Destriper. Where the scan tracks of the telescope are almost parallel (between Declinations $\approx 15^\circ$ to 45°) the residual ringing is worse. This is because between this range the angle between scan crossings become very acute and as stated earlier the Destriping solution is highly dependent on the quality of the crossing between telescope scans.

A crucial problem to solve for the Destriping map-making is to determine the optimum baseline length to use to generate the MFI wide-survey maps. To determine the optimum baseline length, Destriping solutions for a range of baselengths between 1 and 160 seconds were generated, for both the 10 Hz and 80 Hz simulated TOD. The noise levels in these maps were then divided by the expected white noise level, had there been no *1/f* noise contamination. The Destriping solutions were also compared to the noise level of ML map solution at both knee frequencies. Figure 5.11 shows how the noise level of the entire map changes with Destriping baseline length, and for the ML solutions when the *1/f* noise knee frequency is 10 Hz or 80 Hz. The noise at both knee frequencies minimises for a baseline length of 10 seconds (or 500 samples at 50 Hz). Above 40 seconds the noise properties of the map appear not to change; this is because at this point the Destriper is simply adjusting the offsets for single of sets of scan rings. At shorter baseline lengths the noise climbs because the solution to the correlated noise is poorly constrained. The ML solution for both maps, which is effectively a baseline length of 1 sample, typically has a 10 per cent lower noise level than the lowest noise Destriping solution. An interesting point to note is that the noise level of the ML solution is not equal to the theoretical white noise level. This is because the ML solution is limited at some point by the sampling rate of the TOD.

Another important property of the Destriping map-maker is to determine whether the quality of the solution is the same across the whole map. From Figure 5.10b it was implied that the Destriping solution quality degraded in regions of the map where scan crossings are close to parallel. Figure 5.12 compares the noise level in the Destriping and ML maps along different bands. Figure 5.12a measures the noise in the maps above a Declination of 45°. In this case the Destriping map-making solution is found to be largely the same as in Figure 5.11 and minimised at a baseline length of 10 seconds. However, in the region of poor crossings, between Declinations 15° to 45° and shown in

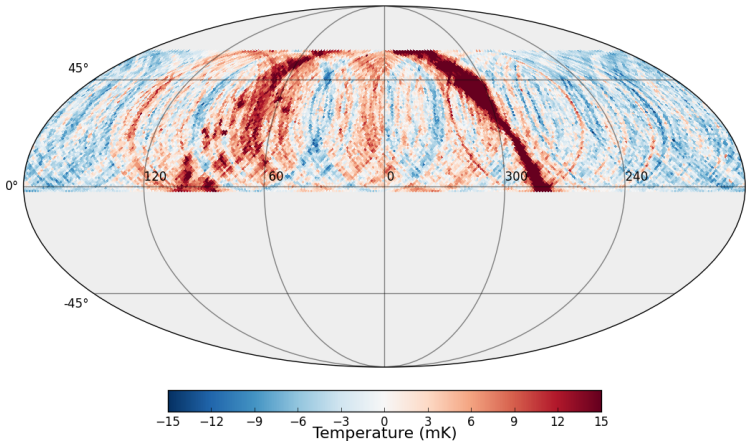

(a) Input sky map.

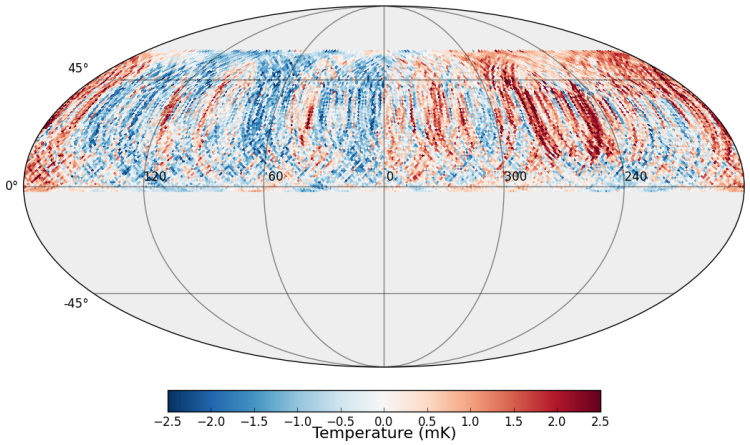

(b) ML and Destriper residual.

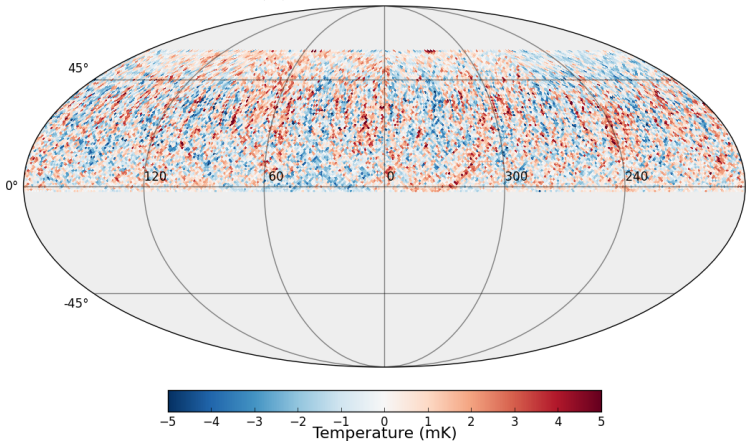

(c) ML residual.

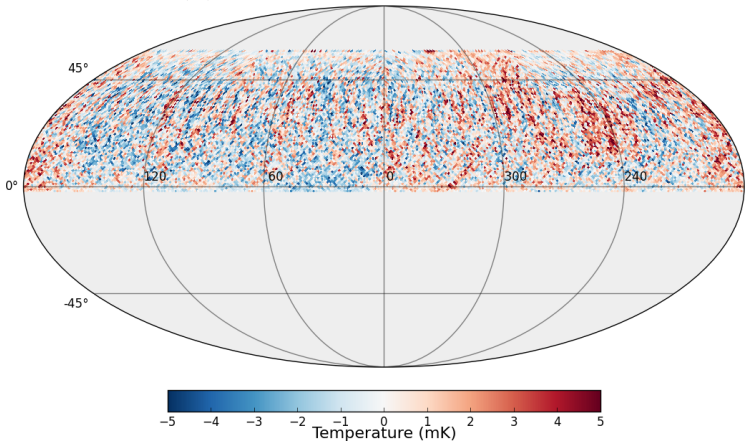

(d) Destriper residual.

Figure 5.10: Comparison of noise levels of the input simulation map with the output residual maps from ML and Destriping map-making. The Destriping baseline was 10 seconds. Note the different scales on the maps, the stripe amplitude in the input map is twice the noise level of the residuals. *Top-Left*: Input simulation including Galactic plane. *Top-Right*: Residual of ML and Destriping output maps. *Bottom-Left*: Residual of ML output and noiseless sky signal. *Bottom-Right*: Residual of Destriping output and noiseless sky signal. All maps presented are in the Celestial coordinate frame.

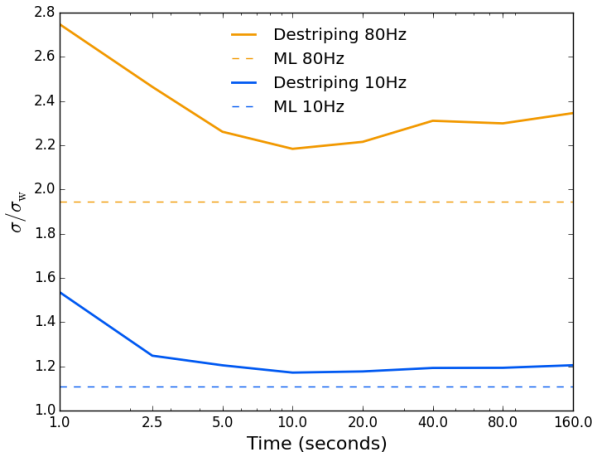

Figure 5.11: Comparison between the noise levels different Destriping solutions and the ML solution for TOD with either 10 Hz or 80 Hz knee frequency. In both cases the optimal Destriping baseline length is found to be at 10 seconds.

Figure 5.12b, the baseline length of 10 seconds seems to shows little or no improvement over longer baseline lengths. From this analysis it can be concluded that in general, the optimum baseline length of the author's Destriping implementation is 10 seconds. This information is used later to produce the final MFI wide-survey maps presented in Chapter 6.

Finally, the Destriper performance was compared with naive median baseline subtraction. Figure 5.13 shows the pseudo-C_ℓ power spectra of simulated 60 degree nominal observations. The two plots in the figure clearly show how the measured Galactic emission signal is lost with decreasing median baseline length. The Destriper however has negligible effect on the large scale diffuse Galactic emission while still achieving similar levels of noise to the median baselines at the smallest scales. This is because Destriping and ML map-making use all the available information. The only advantage of fitting median, or even polynomial, baselines is that the solution is extremely quick to calculate, making it ideal for rapid inspection of the data quality. Also, if the knee frequency of the instrument was sufficiently low, such that it had a timescale of many scans, then median subtraction should have a minimal effect on the large-scale structure according to Figure 5.13.

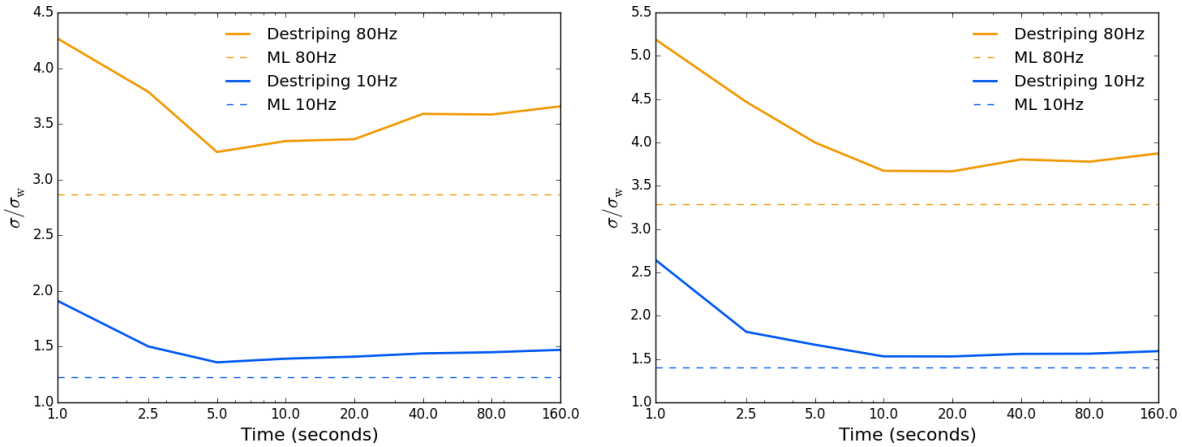

(a) Good Crossings. (b) Poor Crossings.

Figure 5.12: Comparison between the Destriping and ML solutions in regions of the sky that have large crossing angles between scans (*top*) and small crossing angles between scans (*bottom*). The results from two sets of TOD are shown, one has a knee frequency of 10 Hz and the other 80 Hz.

5.4.2 GBT Raster Simulations

These second set of simulations will focus on the application of the author's map-maker to small field raster observations taken by the GBT. Two sets of simulated observations were generated. The first simulates the single feed GBT C-Band or X-Band receivers. The second simulates the seven feed GBT K-Band Focal Plane Array (KFPA) receiver. The feeds in the KFPA are arranged with six feeds forming a close packed hexagon around a single central feed and typical feed angular separation of ≈ 90 arcsec. Each simulated receiver had a NEP=$983\,\mu\mathrm{K\,s^{1/2}}$, a knee frequency of 1 Hz (unless otherwise stated), a sample rate of 5 Hz and a *1/f* spectral index of 1.25. These parameters were chosen based on the measured noise properties of the C-band receivers discussed in Chapter 7. The observations are two orthogonal sky rasters, with one observation scanning in the Right Ascension direction and the other in the Declination direction. The time to complete each raster was 54 seconds, which is slow for a typical GBT mapping observation, but was chosen here to increase the effective *1/f* contamination per scan. Figure 5.14 shows the raster scan coverage and associated hit map of the simulated observations for the single feed GBT C/X-band receiver. Figure 5.15 shows the same but for the KFPA receivers.

The reason for simulating the single feed C/X-band receiver and the multi-feed

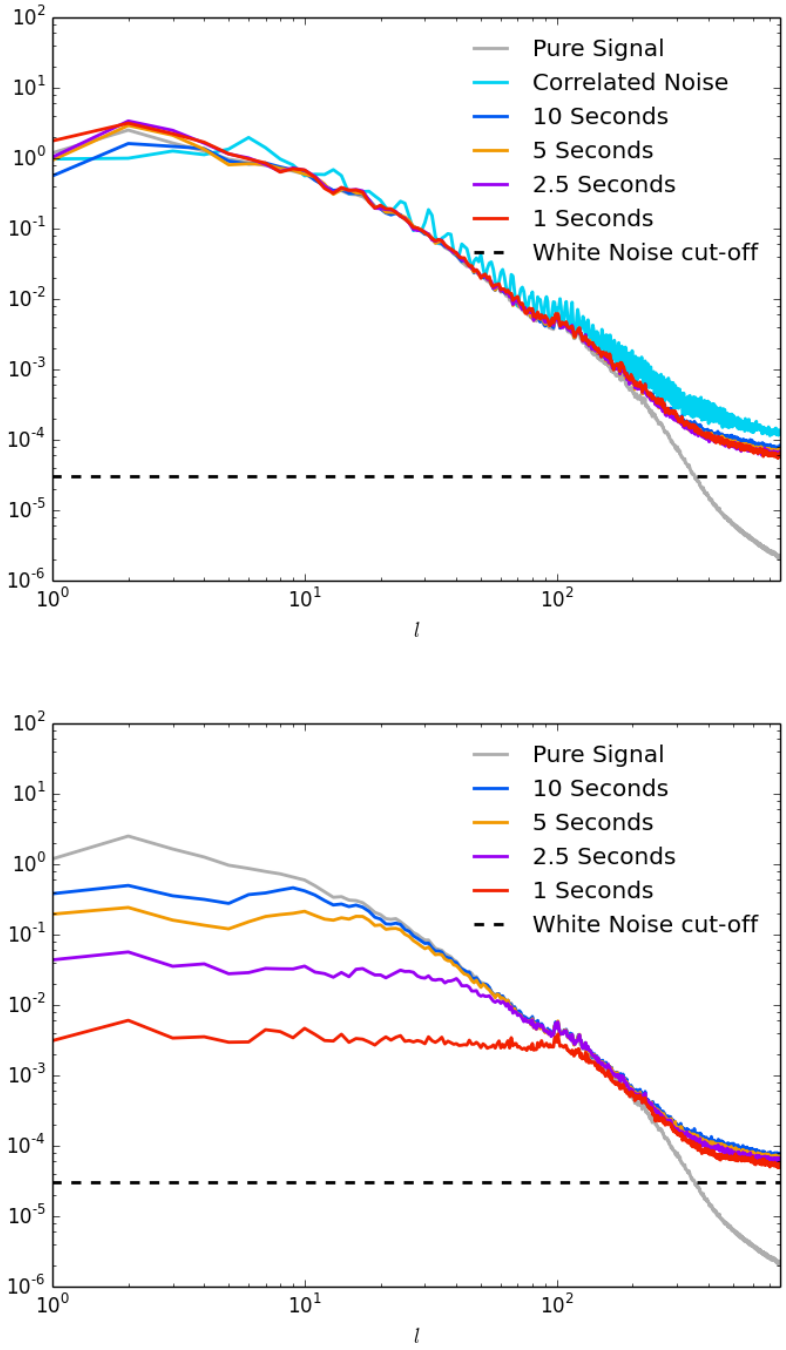

Figure 5.13: Pseudo-C_l power spectra of the Galactic foregrounds of simulated maps for baseline lengths of $0.5 - 10$ seconds. Note how the Destriping solution maps do not compromise the astronomical signal. *Top*: Destriped maps. *Bottom*: Median baseline maps.

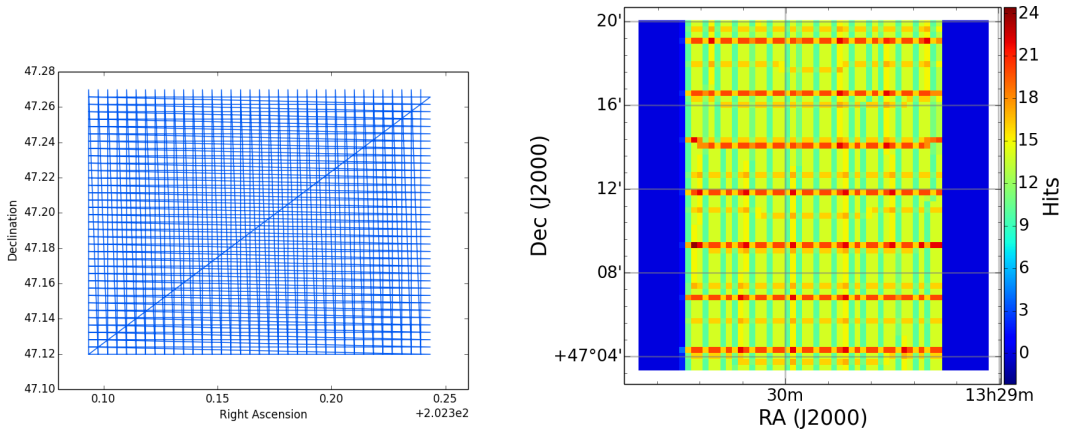

Figure 5.14: Coverage of orthogonal GBT raster scan observations for a focal-centre receiver. *Left*: Telescope scan tracks. *Right*: Hit map coverage.

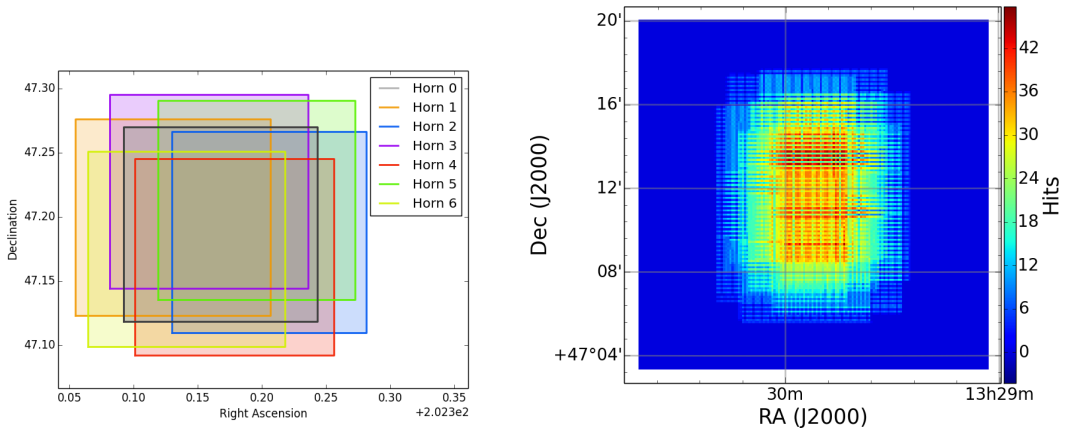

Figure 5.15: Simulated coverage of the seven feed GBT KFPA receiver for an orthogonal Right Ascension and Declination raster scan observation. *Left*: Sky coverage of each receiver. *Right*: Combined hit map coverage for all seven receivers.

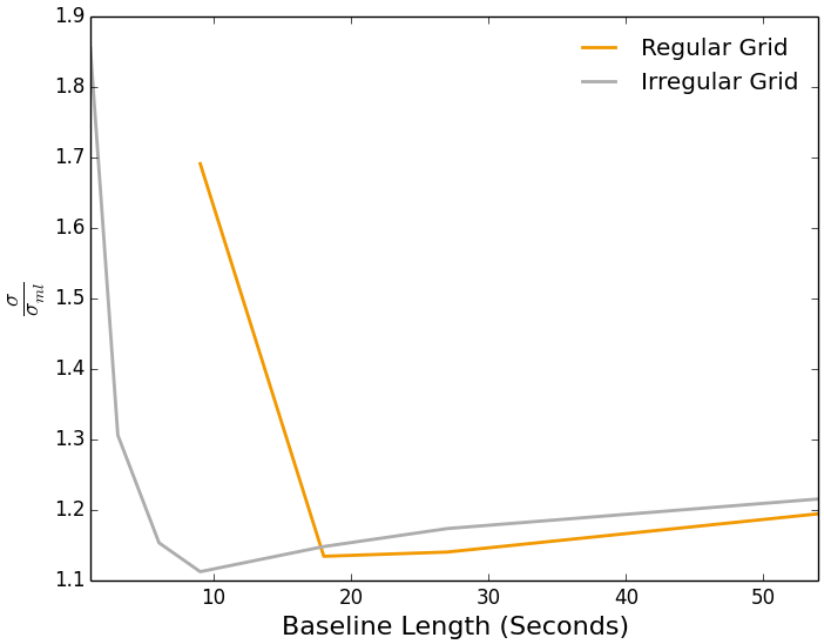

Figure 5.16: Ratio of noise measured in Destriped maps over the noise in the ML map for different baseline lengths.

KFPA receivers is to compare the quality of the *1/f* noise removal when TOD is regularly gridded (as with the single feed receiver) or irregularly gridded (as with the KFPA). Figure 5.16 compares the noise ratio of the Destriping solution to the ML solution in the centre of the simulated C/X-band and KFPA maps. The figure shows that for irregularly gridded data, the increased quality of the scan crossings in the raster map means that baselines a factor of two shorter can be used. Another effect to consider when Destriping regularly gridded TOD is to avoid picking baseline lengths that are integer multiples of each scan length. This is because under this condition regular portions of the TOD will be independent of all other portions, potentially resulting in the map having many different zero level offsets. Note also that as before with the wide-survey simulations, the Destriping solution does not achieve the same minimum noise level as the ML map-making solution.

It has been stated several times throughout this Chapter that the quality of the Destriping solution depends on the quality of the scan crossings within a dataset. The simulated C/X-band raster scan observations are ideal for demonstrating this effect. This is because the simulated observations have regularly gridded TOD slewing in

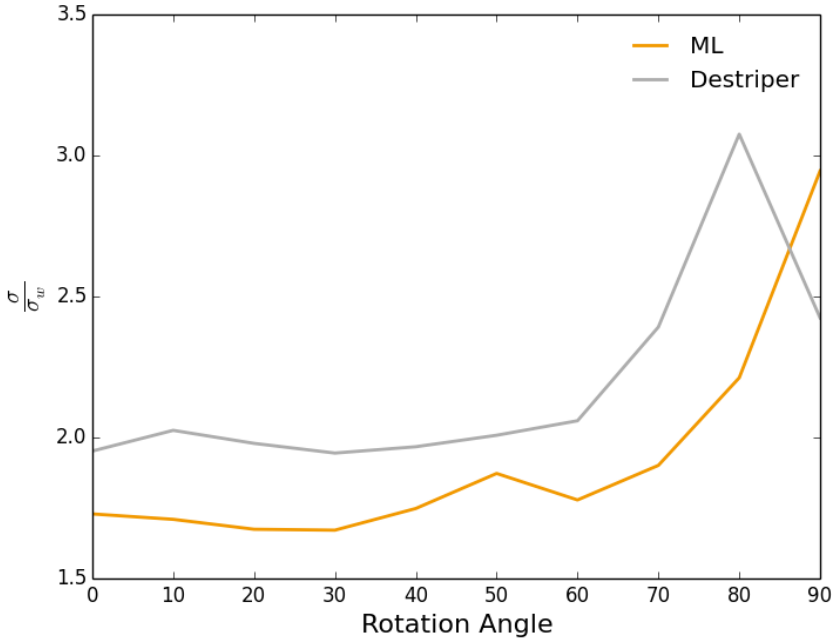

Figure 5.17: Ratio of noise measured in the ML and Destriper maps over the noise measured in a map containing only white noise. At a rotation angle of 0 the scan direction are orthogonal and at 90 the scans are parallel.

Right Ascension only and regularly gridded TOD slewing in Declination only. This represents the optimal crossing situation. However, if the Declination direction scans are incrementally rotated relative to the Right Ascension scans around the centre of the field, it is possible to determine the crossing angle that results in the failure of the Destriping and ML map-making solutions. Figure 5.17 demonstrates this effect by rotating the Declination scans in 10 degree steps relative to the Right Ascension scans. The figure shows that when the Declination scans are rotated 60 degrees (resulting in a 30 degree crossing angle) the noise level rapidly increases until at 90 degrees (parallel scans) the solution is completely unreliable. For the ML map-making solution the rotation angle has a similar effect. However, even with parallel scans a ML solution is possible, if noisy. In real observations, the crossing angles of a region of sky can be estimated from the mean parallactic angle along that line-of-sight.

5.5 Summary

This Chapter has discussed in detail two methods of single-dish map-making that can recover optimal or close-to-optimal images of the sky for data contaminated with *1/f* noise. The author's implementation of these two methods was discussed, including the optimised CGM custom implementation and the framework for the map-making code that will allow for the map-maker to scale to future instruments. Polarisation map-making was highlighted as an area of future expansion for the map-making code. However, other areas of improvement include optimising the `MPI` routines for Destriping and implementing `MPI` into the ML map-making code. The map-making code is available online along with a tutorial and simulated example wide-survey TOD [1].

Simulations of the MFI wide-survey and small field GBT raster scans were used to test the capabilities of the map-maker. In both cases the map-making codes were demonstrated to effectively reduce *1/f* noise without compromising the astronomical signal. Comparing the Destriping solutions to the ML solutions revealed that the ML solutions had noise levels approximately 10 per cent better than the best possible Destriping solution. Unfortunately, due to the size of the MFI wide-survey observations, the current implementation of the ML map-maker could not be used. Instead the MFI wide-survey TOD were reduced using the Destriping map-maker with the optimal baseline length of 10 seconds. For the GBT raster observations in Chapter 7 the total size of the TOD is small enough to be easily processed on a single machine and therefore the GBT maps are generated using the ML map-making code.

[1] `http://www.github.com/SharperJBCA/MapMaker`

Chapter 6

MFI-Wide Survey: A First Look

"By a small sample we may judge the whole piece."

Don Quixote, *Miguel de Cervantes*

This Chapter will present the final MFI maps generated using the calibrated TOD derived from the calibration and processing Chapters 3 and 4 and transformed into the map-domain using the map-maker in Chapter 5. To begin, the combined frequency maps are shown and several tests of the final survey sensitivity, calibration accuracy and observing efficiency are discussed. The results of parametric model fitting to the SEDs of one tentative and three known spinning dust emission sources will be discussed. Followed by the discussion of spectral index maps of the Galactic plane generated using a combination of the MFI wide-survey 11 and 13 GHz maps and ancillary data.

6.1 Overview of Wide-Survey Maps

Figures 6.1 and 6.2 show the final combined MFI wide-survey maps observed between November 2012 and December 2014 for the 11 and 13 GHz channels. The maps are presented in a Mollweide, all-sky projection in the Galactic coordinate frame where Sagittarius A* is at the origin of the image. The low frequency maps presented still show some residual systematic noise from GSO satellites and *1/f* noise, which is especially evident at mid-to-high Galactic latitudes. For example, two large-scale features caused by near-sidelobe pickup from GSO satellites can be seen around $l \approx 20^{\circ}$ and again at $l \approx 220^{\circ}$, both features extend tens of degrees above or below the Galactic plane.

Table 6.1: Total number of effective hours observed per combined MFI frequency map and the subsequent TOD efficiency relative to the total possible effective observing hours.

Frequency	Total Map Time (hours)	TOD Efficiency (%)
11 GHz	4216	52 %
13 GHz	5092	63 %
17 GHz	3452	42 %
19 GHz	2632	32 %

At low Declinations ($240^\circ < l < 20^\circ$ on the Galactic plane) bright stripes left over from the *1/f* noise removal in the map-making process clearly dominate the noise. A similar effect is seen around the *North Celestial Pole* (NCP) where *1/f* noise stripes are the main noise contribution. However, the Galactic plane at low latitudes ($|b| < 15^\circ$) can clearly be seen, including many interesting specific regions such as the Perseus molecular cloud and the inner Galactic disk region.

The high frequency 17 and 19 GHz maps shown in Figure 6.3 have significantly higher noise characteristics than the low frequency maps. Only very bright features such as the Cygnus region, the inner Galactic disk and the calibrator sources, Cas A, and Tau A can be seen. The cause of this is due to the far higher *1/f* noise properties of the 17 and 19 GHz TOD, which raises the effective noise of the data. Additionally, another small increase in noise can be attributed to the shorter effective integration times caused by more of high frequency TOD being flagged.

The total observing time in each map is 2028 hours per horn per channel pair, spread over approximately 18 months. The total number of integrated samples per frequency after flagging poor data are shown in the hit distribution maps of Figures 6.4 and 6.5. Table 6.1 shows the total number of effective hours per map and the accompanying TOD efficiency, which is the ratio of the measured samples over the total possible samples. Typical TOD efficiency is around 50 % for all frequencies after flagging.

The noise distribution of the MFI wide-survey maps is highly variable due to the inhomogeneous distribution of TOD samples and RFI across the sky. The noise in the MFI wide-survey maps was derived by subtracting the maps derived from the correlated channels from maps derived from the uncorrelated channels. The resulting residual map should have statistically similar noise to the final wide-survey maps including

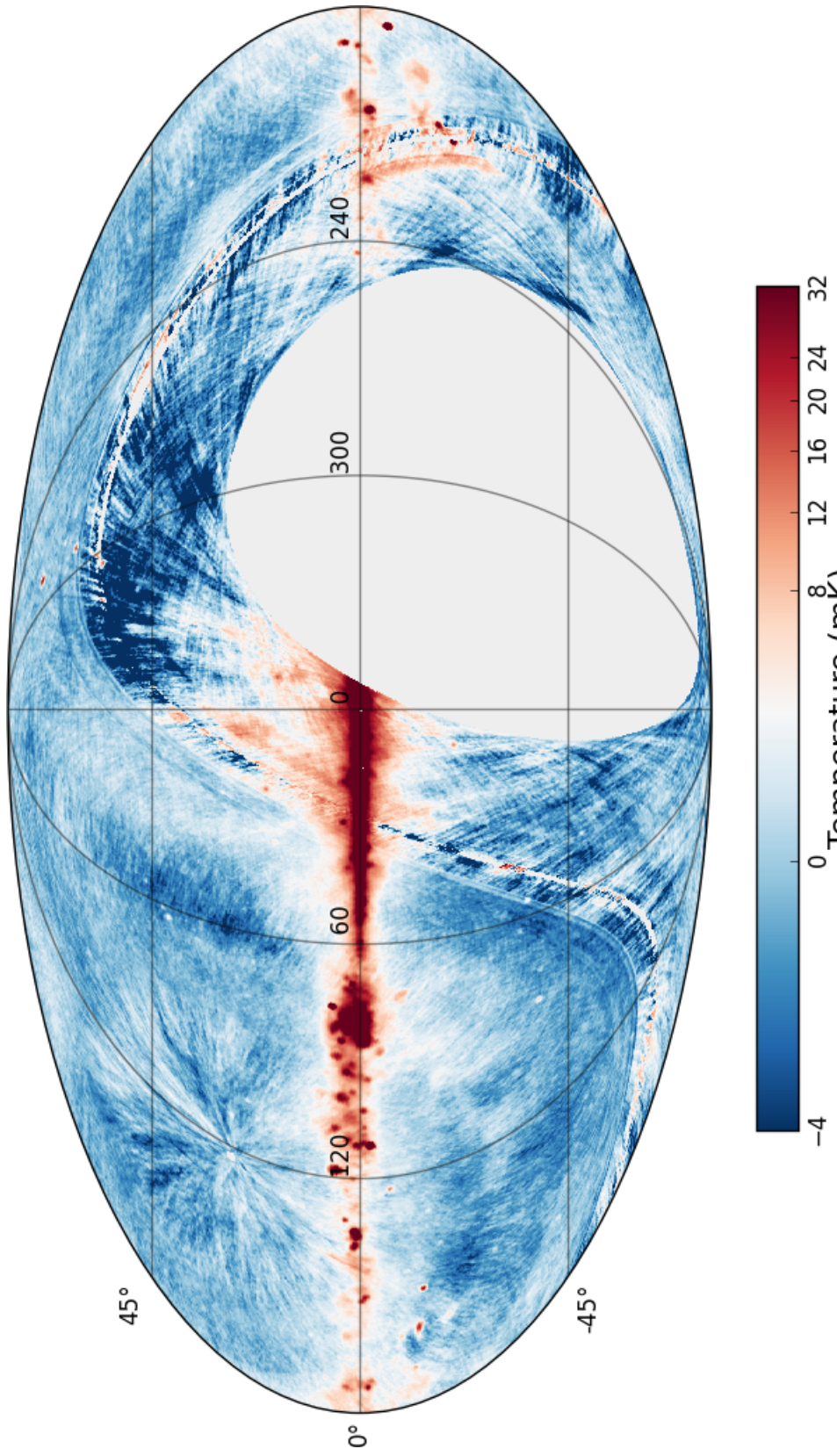

Figure 6.1: Combined MFI Wide-Survey 11 GHz Map in Galactic coordinates. The 11 GHz wide-survey map suffers from the worst residual RFI noise contamination of all four wide-survey maps. This is especially obvious around regions such as Orion and Barnard's loop at $l \approx 210°$. This image uses an arcsinh colour scaling and saturates bright regions to exaggerate the map noise contamination and weaker diffuse sources.

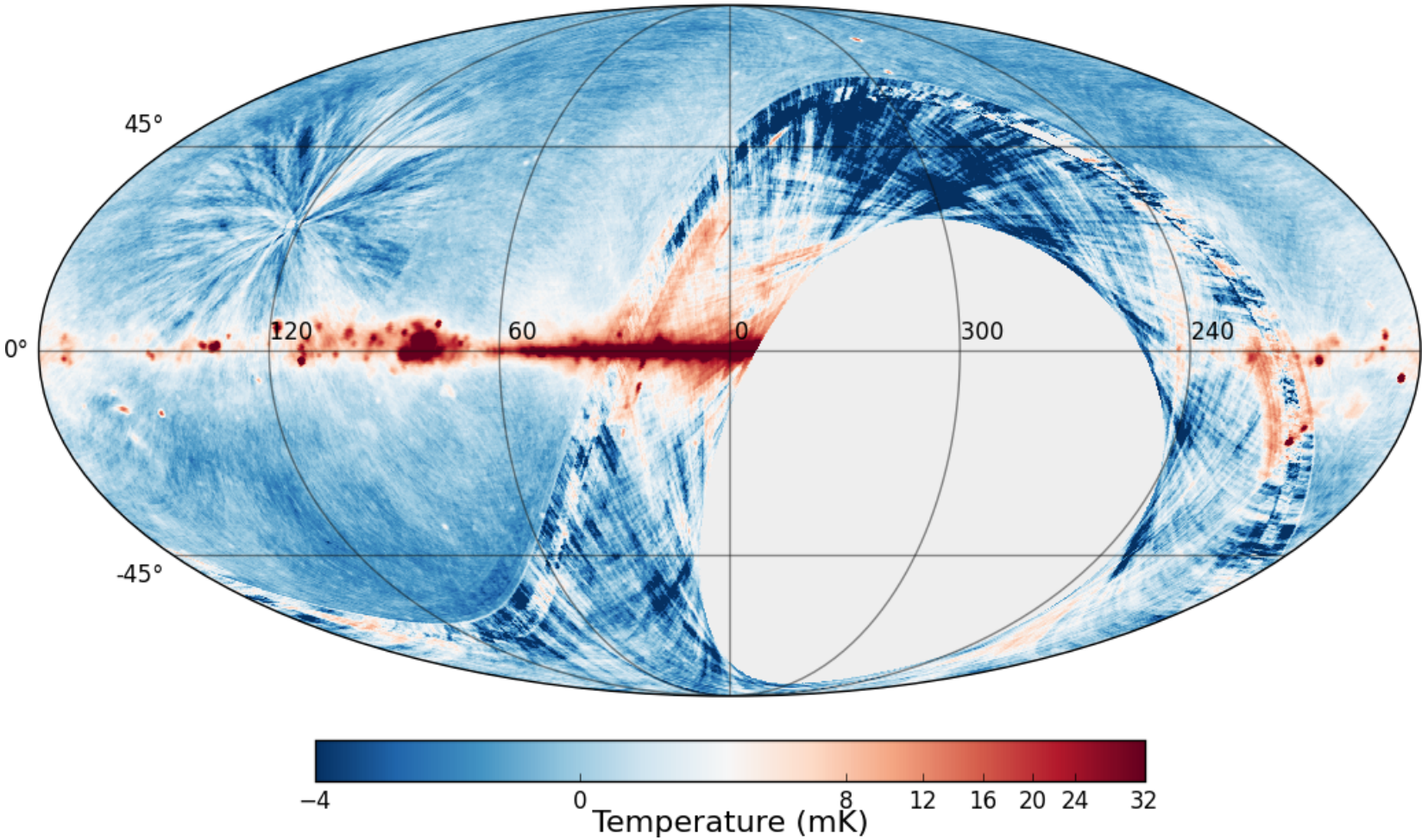

Figure 6.2: Combined MFI Wide-Survey 13 GHz Map in Galactic coordinates. The 13 GHz wide-survey map has the best noise properties of all the wide-survey maps. Lots of large-scale structure away from the Galactic plane can be seen, such as the low Galactic latitudes of the North Polar Spur.

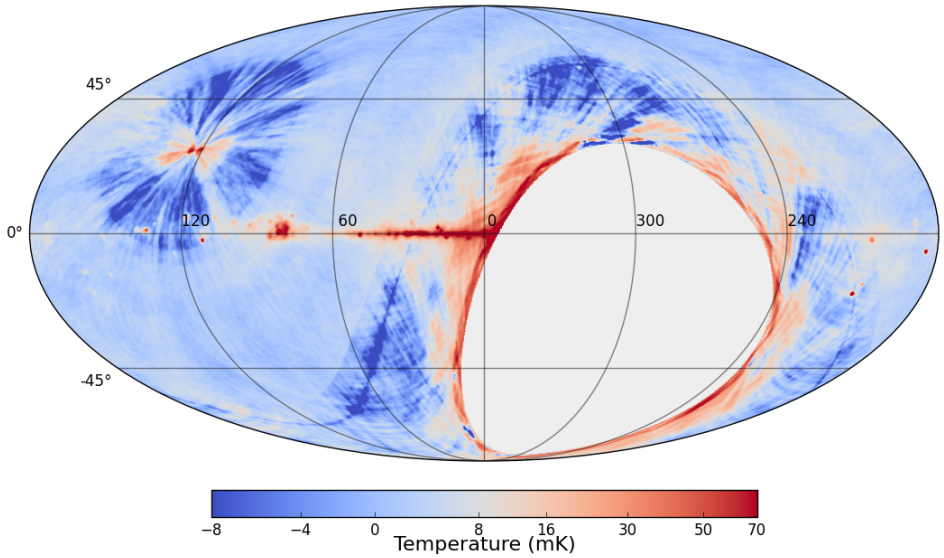

(a) .

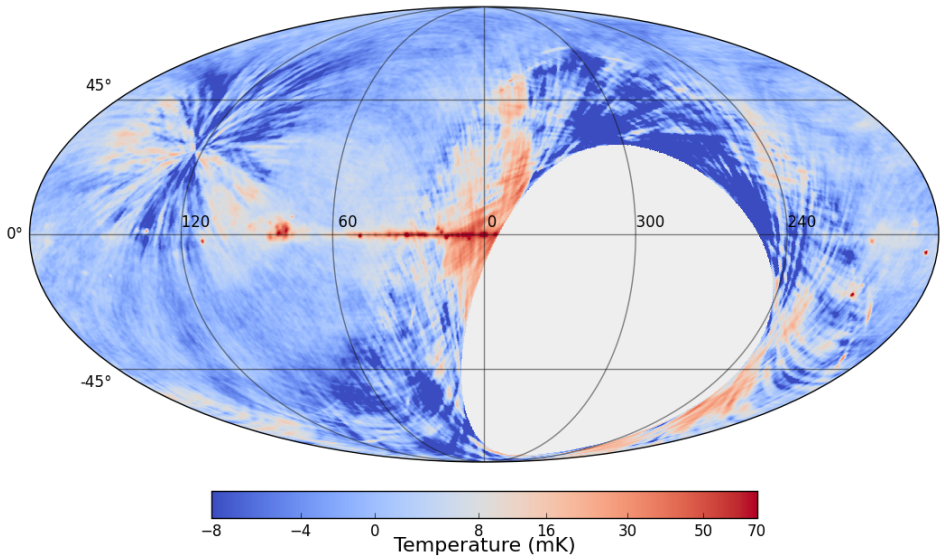

(b) .

Figure 6.3: Combined MFI Wide-Survey maps at 17 GHz (*top*) and 19 GHz (*bottom*) in Galactic coordinates. Both high frequency MFI wide-survey maps are contaminated by very high levels of *1/f* noise and high calibration uncertainties ($> 6\%$) making these maps unreliable. However, some bright regions along the Galactic plane are still visible, especially in the 17 GHz map.

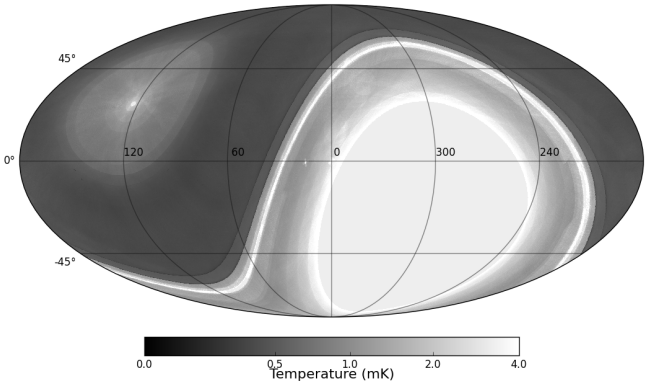

(a) 11 GHz Noise Map.

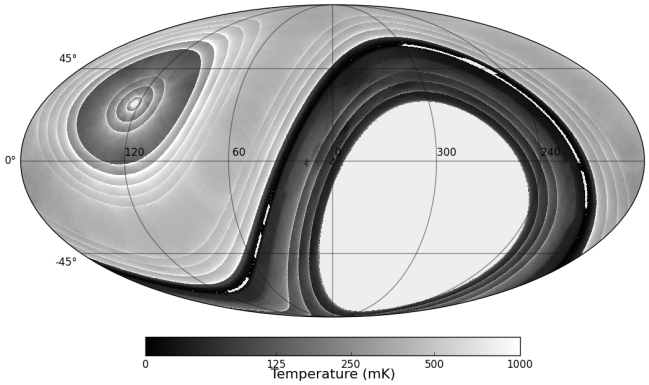

(b) 11 GHz Hits Map.

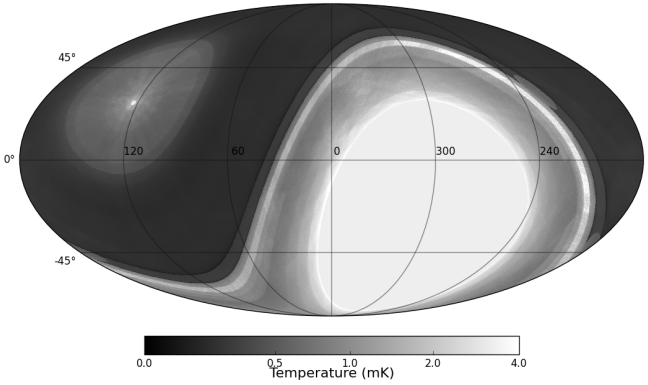

(c) 13 GHz Noise Map.

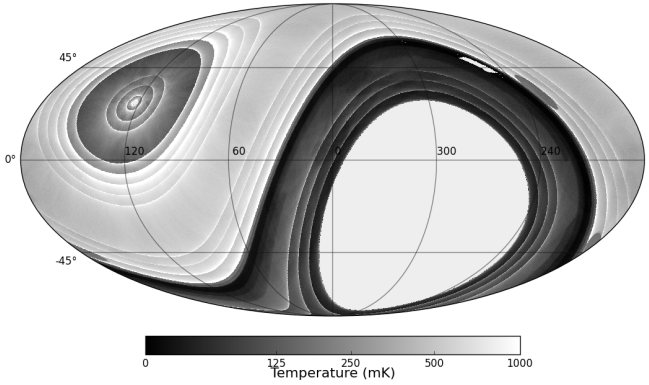

(d) 13 GHz Hits Map.

Figure 6.4: Combined MFI Wide-Survey 11 and 13 GHz Noise and Hits Maps.

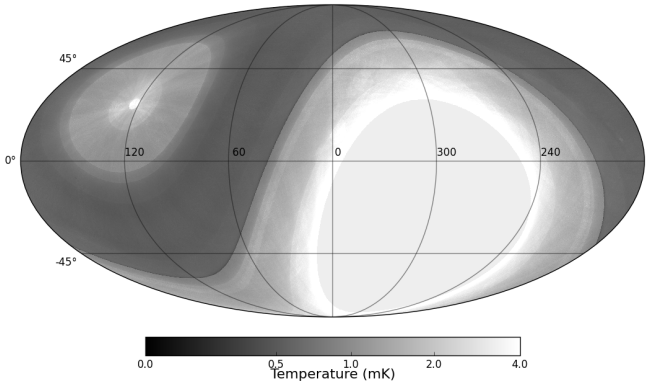

(a) 17 GHz Noise Map.

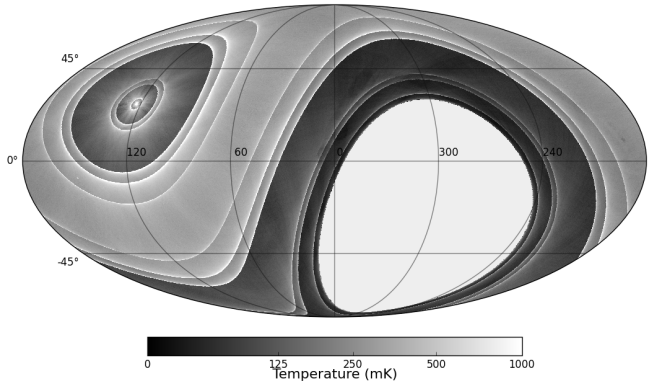

(b) 17 GHz Hits Map.

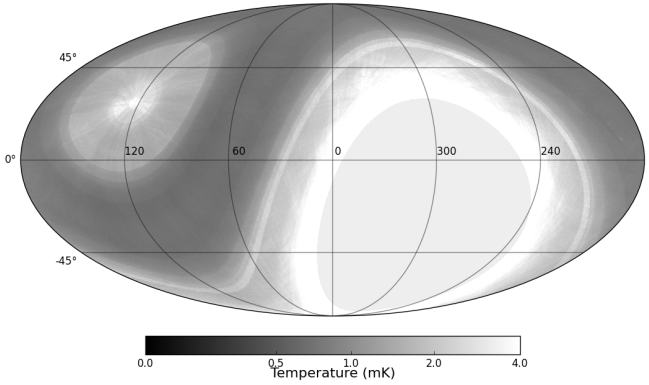

(c) 19 GHz Noise Map.

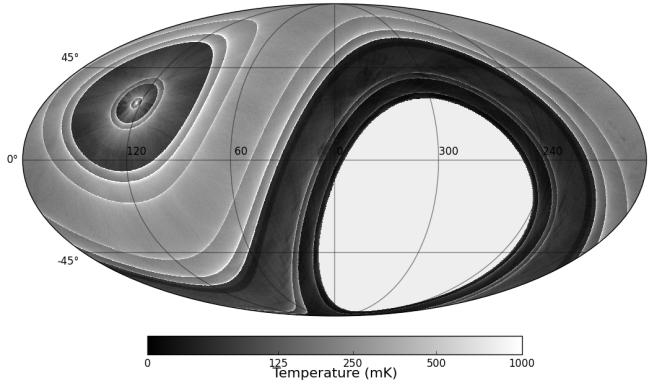

(d) 19 GHz Hits Map.

Figure 6.5: Combined MFI Wide-Survey 17 and 19 GHz Noise and Hits Maps.

Table 6.2: Noise properties of the MFI wide-survey maps. The map sensitivity describes the effective noise in the maps per one second integration time. The NEP factor is the ratio of the map sensitivity over the theoretical thermal noise limit of the receivers quoted in Table 2.1.

Frequency	Map Sensitivity (μK s$^{-1/2}$)	NEP Factor
11 GHz	3867	2.9
13 GHz	2596	2.5
17 GHz	5188	4.8
19 GHz	8260	7.9

any residual *1/f* noise. The noise in the residual map was defined as the standard deviation of the pixels within a 6 degree band, centred on Declination 28°. The map sensitivity quoted in Table 6.2 is the measured *map sensitivity*, which accounts for the mean number of samples per pixel and the 50 Hz sample rate of the TOD. The map sensitivity in the table was also compared to the NEP derived from the TOD stated in Table 2.1. These ratios of the effective noise over the thermal noise show that the 11 and 13 GHz channels have a factor of 2 to 3 more noise as a result of *1/f* contamination. The effective noise in the 17 and 19 GHz maps are 5 to 8 times higher than predicted by the thermal noise level. From Table 6.2, and visual inspection of Figures 6.1, 6.2 and 6.3, it is clear that the 13 GHz MFI wide-survey map has the lowest *1/f* noise contamination.

6.2 Calibration Integrity

In Chapter 3, a thorough treatment of the MFI TOD calibration was given as well as the final calibration uncertainties per MFI horn. In this Section, a jack-knife analysis of the individual MFI wide-survey observations is performed to check the robustness of the relative changes in the absolute calibration.

The term jack-knife refers to the splitting of the MFI data into sets with differing properties and measuring the properties of the residuals of each set. To test the integrity of the MFI relative calibration uncertainty for the wide-survey maps, the wide-survey data are split into `HEALPix` maps derived from individual observations. In each map the pixels within a 2 degree diameter aperture centred on 307.5° Right Ascension and

41° Declination were summed. This aperture was chosen as all the pixels contain a contribution from the bright extended emission of the Cygnus region. This region is clearly visible at all MFI frequencies, has a predominantly flat spectrum and fills the MFI beams.

The sum over all the pixels within the aperture can be defined as

$$\sum_{i}^{\mathrm{N_{pix}}} T_i = \sum T_b \left[1 + \delta(t)\right] + n, \tag{6.1}$$

where T_i is the brightness temperature of each pixel, N_{pix} is the number of pixels in the aperture, and n is the noise contribution of each pixel with a mean of zero. In each of the daily wide-survey maps, the source contribution of each pixel will be a combination of the intrinsic source brightness (T_b) plus a small change in the relative calibration $1 + \delta(t)$. The term $\delta(t)$ accounts for any relative changes in the absolute flux density calibration of the MFI, which could be due to changes in receiver gain, the atmosphere, or pointing.

Randomly selected pairs of aperture sums taken on different days in a single horn, or taken on the same day from different horns are subtracted from each other. This results in the residual function:

$$D = \frac{\sum T_b(\delta(t_1) - \delta(t_2)) + (n_1 - n_2)}{\langle \sum T_i \rangle}. \tag{6.2}$$

Where the term $\langle \sum T_i \rangle$ is the median value of all the apertures and is used to remove the T_b dependence in D. The randomly generating D using different pairs of data results in a distribution that will have a mean of $\langle \delta(t_1) - \delta(t_2) \rangle$, which can be used to describe the mean MFI relative calibration uncertainty.

Table 6.3 shows the mean calibration uncertainties derived from the jack-knifes of the daily wide-survey maps. The typical uncertainties shown in the table are higher than those reported in Chapter 3, especially the uncertainties derived from different observing days. This implies that there are either unknown sources of calibration uncertainty or the uncertainties reported in Chapter 3 were underestimated. This is especially true of the high frequency 17 and 19 GHz MFI horns, which have almost twice the calibration uncertainty reported in Chapter 3. This Chapter will adopt the calibration uncertainties reported in Table 6.3.

This Section has re-evaluated the relative calibration uncertainty associated with each MFI horn. The MFI 17 and 19 GHz horns have been shown to have a 6 to 8 %

Table 6.3: Percentage calibration uncertainties in the MFI wide-survey derived by jack-knifing difference maps of individual wide-survey observations. The first column shows the calibration uncertainty derived when measuring residual flux densities of bright regions over different days. The second column shows the calibration uncertainty when measuring residual flux densities between horns for a set of maps derived from the same days.

	Days (%)	Horns (%)
Horn 1	2.7	2.2
Horn 3	2.5	
Horn 2	6.2	4.8
Horn 4	8.7	

calibration uncertainty in this Section and a factor two to three higher noise than the 11 and 13 GHz horns in the last Section. For these reasons the high frequency MFI wide-survey maps are not used in any of the proceeding scientific analysis of the wide-survey data. In Section 6.4 the high frequency flux densities of specific Galactic regions are only reported for completeness. The MFI 11 and 13 GHz wide-survey maps and horns have been found to have acceptably low calibration and noise uncertainties, especially when combined with ancillary multi-frequency data from other surveys and instruments.

6.3 Multi-Frequency Data

In Section 6.5 the MFI wide-survey is used to derive spectral index maps of the Galactic plane. Section 6.4 investigates the SEDs of specific Galactic regions in search of spinning dust emission. However, the MFI 11 and 13 GHz maps alone do not have the frequency resolution to derive these scientific products. For that reason it is crucial to use multifrequency ancillary datasets from other surveys. These include:

- A composite all-sky map at 408 MHz.
- *WMAP* 9-year maps at 23, 33, 41, 61 and 94 GHz.
- *Planck* LFI/HFI maps at 28.5, 44, 70, 100, 143, 217, 353, 545 and 857 GHz.

- *COBE*-DIRBE maps at 1249, 2141 and 2997 GHz.

The survey maps and references used in this Chapter, including the MFI wide-survey data are summarised in Table 6.4. All maps are gridded using the `HEALPix` pixelisation scheme (Górski et al., 2005) and are smoothed to a common angular resolution of 1 degree. All map units were converted to Rayleigh-Jeans (RJ) brightness temperature units in mK.

6.3.1 408 MHz Map

The Haslam et al. (1982) 408 MHz all-sky map is a composite of observations by the Jodrell Bank MkI and MkIA telescopes, the Effelsberg 100 m telescope and the Parkes 64 m telescope. The map is in units of RJ brightness temperature units (K). The version of the 408 MHz map used in this Chapter has been reprocessed by Remazeilles et al. (2015) to remove the striping effects in the original image. There are known to be significant baseline uncertainties in the 408 MHz, quoted as ± 3 K in Haslam et al. (1982). However, these should have only a minor effect on the results in Section 6.4 as only small regions are being studied. The baseline uncertainties in the 408 MHz map could potentially affect the results of the low frequency spectral index map in Section 6.5, but as only the bright Galactic plane regions are being measured, this will be negligible. The calibration uncertainty of 408 MHz map is quoted in Haslam et al. (1982) as $\approx$ 10 per cent. However, this was derived using an older, absolutely calibrated 404 MHz (Pauliny-Toth and Shakeshaft, 1962). Note also that in Remazeilles et al. (2015) questions are raised regarding the reliability of the full-beam to main-beam ratio quoted in Haslam et al. (1982). If unreliable, this could translate into a larger uncertainty in the absolute calibration of the 408 MHz map. In this Chapter a 10 per cent calibration uncertainty will be assumed, and a baseline uncertainty of ± 3 K.

6.3.2 *WMAP* 9-year Maps

The *WMAP* 9-year observations span a frequency range of 22.8 to 93.5 GHz. The *WMAP* data are in units of brightness temperature units relative to the CMB. To convert the *WMAP* maps into RJ brightness temperature units the following relationship was used,

$$T_{\rm b} = T_{\rm c} \frac{(e^x - 1)^2}{x^2 e^x}, \tag{6.3}$$

where $T_{\rm b}$ is the RJ brightness temperature, $T_{\rm c}$ is the CMB relative brightness temperature, and $x = h\nu/kT_{\rm cmb}$, where $T_{\rm cmb}$ is the black-body temperature of the CMB. All *WMAP* maps are smoothed to a common resolution of 1 degree assuming the mean beam FWHM quoted in Page et al. (2003). In Section 6.4 the original *WMAP* maps are used and in Section 6.5 the beam deconvolved *WMAP* maps are used. Colour corrections are applied using the method described in Jarosik et al. (2003). The absolute calibration of the *WMAP* maps is based on measurements of Jupiter and typical uncertainty is expected to be much less than 1 per cent (e.g., Weiland et al., 2011). This Chapter will assume a 1 per cent uncertainty in the *WMAP* data. All *WMAP* data is taken from the NASA LAMBDA website[1].

6.3.3 *Planck* LFI/HFI Maps

The latest *Planck* LFI and HFI all-sky maps were taken from the *Planck* Legacy Archive website[2]. Both *Planck* instruments together cover a frequency range of 30 to 857 GHz. The *Planck* LFI maps are in units of CMB brightness temperature and were converted to RJ brightness temperature using Equation 6.3. The *Planck* HFI maps are in units of MJy sr^{-1} and were converted to RJ brightness temperature in mK using,

$$T_{\rm b} = \frac{S_\nu c^2}{2k\nu^2} \times 10^9, \tag{6.4}$$

where S_ν is flux density, and ν is frequency. All the maps were smoothed to a common resolution of 1 degree. The *Planck* LFI colour corrections are performed using polynomial fits to values in table 1 of Planck Collaboration et al. (2014h). A calibration uncertainty of 1 per cent was assumed for the LFI maps (table 8 Planck Collaboration et al., 2014h) and a calibration uncertainty of 1 per cent was assumed for the HFI maps (table 6 Planck Collaboration et al., 2014f). HFI 100 and 217 GHz maps are ignored during the SED fitting procedure due to the contamination of the 115 GHz $J = 0 \rightarrow 1$ CO transition. Similarly, the 217 GHz channel is ignored because of the 231 GHz $J = 1 \rightarrow 2$ CO transition.

[1] http://lambda.gsfc.nasa.gov
[2] http://pla.esac.esa.int/pla/

6.3.4 *COBE*-DIRBE Maps

To measure the peak of the thermal dust modified black-body curve the Zodi-Subtracted Mission Average DIRBE 240 μm (1249 GHz), 140 μm (2141 GHz) and 100 μm (2997 GHz) maps were used (Hauser et al., 1998). The DIRBE maps were in units of MJy sr^{-1}, and were converted to RJ brightness temperature units in mK using Equation 6.4. Each map was gridded into the `HEALPix` pixelisation scheme and smoothed to 1 degree resolution. Higher frequency DIRBE bands were not used as these bands can be contaminated by transiently heated, small grain emission. Note that in regions of high dust temperatures, even the 100 μm map will be affected. Calibration uncertainties for the three DIRBE bands used are taken from table 2 in Hauser et al. (1998) and range from 10 to 14 per cent.

6.4 Regions of Spinning Dust Emission

In this Section, known and tentative spinning dust emission sources are reanalysed with the inclusion of the MFI wide-survey maps. The regions include: the Perseus molecular cloud (e.g., Watson et al., 2005; Planck Collaboration Early XX, 2011), Lynds dark cloud LDN 1622 (Casassus et al., 2006), and HII complex W40 (Demetroullas et al., 2015). A fourth source LDN 1582/84, will also be investigated as it was identified in Planck Collaboration Int. XV (2014) as a potential spinning dust emission source.

Models of each source SED are determined using a multi-component parametric fitting method that is used by numerous other studies (e.g., Planck Collaboration Early XX, 2011; Planck Collaboration Int. XV, 2014). The integrated flux density ($S(\nu)$) of a source can be decomposed into:

$$S(\nu) = S_{\rm ff} + S_{\rm dust} + S_{\rm cmb} + S_{\rm sync} + S_{\sf SpDust}, \tag{6.5}$$

$S_{\rm ff}$ is the free-free contribution, $S_{\rm dust}$ is the thermal dust contribution, $S_{\rm cmb}$ is CMB contribution, $S_{\rm sync}$ is the synchrotron contribution and $S_{\sf SpDust}$ is the spinning dust emission contribution.

Details of each emission have been discussed at length in Chapter 1 but a brief summary of each is given here. The free-free flux density component is derived from the free-free brightness temperature ($T_{\rm ff}$) as,

$$S_{\rm ff} = \frac{2kT_{\rm ff}\nu^2\Omega}{c^2}, \tag{6.6}$$

Table 6.4: Compilation of all the multi-frequency all-sky survey data used in this Chapter. See text for details.

ν (GHz)	Telescope/ Survey	Angular Resolution (arcmin)	Units	Notes
0.408	Haslam et al. (1982)	51	K	Remazeilles et al. (2015) destriped version.
11	MFI	56.4	K	
13	MFI	56.4	K	
17	MFI	38.4	K	Ignored due to high uncertainties.
19	MFI	38.4	K	Ignored due to high uncertainties.
22.8	*WMAP* 9-year	49.2	$\mathrm{mK_{cmb}}$	1 degree smoothed version.
28.5	*Planck* LFI	32.65	$\mathrm{K_{cmb}}$	
33.0	*WMAP* 9-year	37.2	$\mathrm{mK_{cmb}}$	1 degree smoothed version.
40.7	*WMAP* 9-year	29.4	$\mathrm{mK_{cmb}}$	1 degree smoothed version.
44.1	*Planck* LFI	27.92	$\mathrm{K_{cmb}}$	
60.7	*WMAP* 9-year	19.8	$\mathrm{mK_{cmb}}$	1 degree smoothed version.
70.3	*Planck* LFI	13.01	$\mathrm{K_{cmb}}$	
93.5	*WMAP* 9-year	12.6	$\mathrm{mK_{cmb}}$	1 degree smoothed version.
100	*Planck* HFI	9.37	$\mathrm{MJy\,sr^{-1}}$	Ignored due to CO $J = 0 \rightarrow 1$ contamination.
143	*Planck* HFI	7.04	$\mathrm{MJy\,sr^{-1}}$	
217	*Planck* HFI	4.68	$\mathrm{MJy\,sr^{-1}}$	Ignored due to CO $J = 1 \rightarrow 2$ contamination.
353	*Planck* HFI	4.43	$\mathrm{MJy\,sr^{-1}}$	
545	*Planck* HFI	3.80	$\mathrm{MJy\,sr^{-1}}$	
857	*Planck* HFI	3.67	$\mathrm{MJy\,sr^{-1}}$	
1249	*COBE*-DIRBE	37.1	$\mathrm{MJy\,sr^{-1}}$	
2141	*COBE*-DIRBE	38.0	$\mathrm{MJy\,sr^{-1}}$	
2997	*COBE*-DIRBE	38.6	$\mathrm{MJy\,sr^{-1}}$	

where ν is frequency, and Ω is the solid angle of the aperture. The free-free brightness temperature for an optically thin region is defined as

$$T_{\rm ff} = T_{\rm e}\tau_{\rm ff}, \tag{6.7}$$

where $\tau_{\rm ff}$ is the free-free optical depth and $T_{\rm e}$ is the electron temperature. The free-free optical depth is given by

$$\tau_{\rm ff} = 5.468 \times 10^{-2} T_{\rm e}^{-1.5} \nu^{-2} {\rm EM} g_{\rm ff}, \tag{6.8}$$

where the emission measure EM $= \int n_{\rm e}^2 {\rm d}s$, which is the integral of the square of the electron density ($n_{\rm e}$) along a line-of-sight (s), and $g_{\rm ff}$ is the gaunt factor. The free-free gaunt factor is defined in Draine (2011) as

$$g_{\rm ff} = \ln\left(e^{\left[5.960 - \frac{\sqrt{3}}{\pi}\ln\left(\frac{\nu}{\rm GHz}\frac{T_{\rm e}}{10^4{\rm K}}\right)\right]} + 2.71827\right). \tag{6.9}$$

The resulting free-free SED has an almost flat spectral index with some curvature due to the gaunt factor.

Thermal dust emission can be described by a modified black-body of the form

$$S_{\rm dust} = \frac{2h\nu^3}{c^2}\frac{1}{e^{h\nu/kT_d} - 1}\tau_{250}\left(\frac{\nu}{1.2\,{\rm GHz}}\right)^{\beta}\Omega, \tag{6.10}$$

where T_d is the dust temperature, τ_{250} is the dust optical depth at 250 μm and β is the dust emissivity. The CMB contribution is modelled as the differential of a blackbody at $T_{\rm cmb}$ at 2.7255 K (Fixsen, 2009),

$$S_{\rm cmb} = \left(\frac{2k\Omega\nu^2}{c^2}\right)\Delta T_{\rm cmb}\frac{x^2e^x}{(e^x-1)^2} \tag{6.11}$$

where $\Delta T_{\rm cmb}$ is the amplitude of a background CMB perturbation in RJ brightness temperature, and $x = h\nu/kT_{\rm cmb}$. Finally, the contribution of synchrotron emission to the SED of a source is modelled as a powerlaw of the form

$$S_{\rm sync} = A\left(\frac{\nu}{\rm GHz}\right)^{\alpha}, \tag{6.12}$$

where A is the amplitude of the source at 1 GHz, and α is the spectral index.

Spinning dust emission is modelled using an SED derived using SpDust (Ali-Haïmoud et al., 2009; Silsbee et al., 2011) using environmental parameters of the cold neutral medium (CNM) taken from table 1 in Draine and Lazarian (1998b). The peak brightness of the SpDust model SED was normalised to unity and the peak frequency was

set to zero. Linear interpolation was used to determine the flux density of the spinning dust emission given

$$S_{\rm sp} = A_{\rm sp} s(\nu - \nu_{\rm sp}), \tag{6.13}$$

where $A_{\rm sp}$ is the spinning dust emission amplitude, $\nu_{\rm sp}$ is the peak frequency and $s(\nu - \nu_{\rm sp})$ is the flux density of the model SED at frequency $\nu - \nu_{\rm sp}$. Note that the morphology of SpDust models does not vary significantly with environment, only the peak amplitude and peak frequency.

6.4.1 Aperture Photometry and Model Fitting

The SED of four sources: Perseus, LDN 1622, W40, and LDN 1582 were measured using aperture photometry and a SED model described by Equation 6.5 was fitted to the measurement using the least-squares method. The aperture photometry was performed by converting each map into units of Jy pixel^{-1}, then summing all the pixels within a given aperture as described by

$$S_\nu = \sum_{\rm pixels} \left[S_{\rm aper} - \langle S_{\rm bkgd} \rangle \right]. \tag{6.14}$$

As only the flux density S_ν of any given source is of interest, an estimate must be made of the mean background emission ($\langle S_{\rm bkgd} \rangle$), which is then subtracted from the flux density of each pixel within the aperture (S_{aper}).

The mean background emission within the aperture was estimated by comparing the mean value of several 1 degree diameter apertures equally distributed 0.75 degrees from the perimeter of the main aperture. For examples of how these small apertures are distributed see Figures 6.7, 6.9, 6.11 and 6.14 in the proceeding subsections. The aperture containing the lowest mean value across all frequencies was used to determine the mean background offset.

The uncertainty in the measured flux density has three contributions. The uncertainty from the pixel noise in the map, the known calibration uncertainty in the data, and the uncertainty in the background variations. The pixel noise in the map was estimated by taking the mean value of the standard deviation across all the small 1 degree diameter apertures, this essentially acts as a spatial filter, removing large-scale variations due to Galactic emission or correlated noise.

The background uncertainty was measured by taking the mean temperature value

of each aperture ($\langle T \rangle_i$), and generating a set of unique differences in the mean values:

$$\Delta T_{ij} = \langle T \rangle_i - \langle T \rangle_j \,, \tag{6.15}$$

where ΔT_{ij} is the difference in the means between the ith and jth apertures. For a set of N apertures, it is possible to generate $N(N-1)/2$ unique pairings. The resulting variance of all the ΔT_{ij} values is the sum of the variance in the differenced mean due to the pixel noise and the variance due to the background variations. The resulting standard deviation in the background signal can be estimated as

$$\sigma_{\rm bkgd} = \sqrt{{\rm Var}(\Delta T_{ij}) - \frac{\sigma^2_{\rm pix}}{N(N-1)/2}}, \tag{6.16}$$

where ${\rm Var}(\Delta T_{ij})$ is the variance in the difference means of the background apertures and $\sigma_{\rm pix}$ is the pixel noise uncertainty calculated in the previous paragraph.

The SED model was fitted to the flux densities using the `SciPy` least-squares fitting routine. The least-squares fitter uses the Levenberd-Marquardt algorithm. Least-squares optimisation is known to sometimes converge to local-minima within the parameter space of a model. To test whether local-minima were biasing the the SED fitting, each fit was repeated 100 times with different, randomly selected starting values between a pair of pre-determined lower and upper boundary conditions. Table 6.5 lists the limits on each parameter and the mean fitting uncertainty associated with each parameter. The least constrained and most variable parameters are the local variation in the CMB brightness and the parameters τ_{250} and β that modify the the thermal dust black-body curve. The differences in the uncertainties for each source is caused by the variations in the morphology of the source, the source background and the source SED that is being measured.

The final uncertainty associated with each flux density was estimated as

$$\sigma^2 = \sum \sigma^2_{\rm pix} + \sigma^2_{\rm cal} + \sigma^2_{\rm bkgd} + \sigma^2_{\rm fit}, \tag{6.17}$$

where $\sigma_{\rm pix}$ is the pixel noise uncertainty, $\sigma_{\rm cal}$ is the calibration uncertainty, $\sigma_{\rm bkgd}$ is the background uncertainty, and $\sigma_{\rm fit}$ is the fit uncertainty. The fit uncertainty in the fluxes is typically quite small, never exceeding more than a few per cent. The uncertainty in each parameter is determined from a combination of the estimated covariance matrix of the least-squares fit and the uncertainties reported in Table 6.5. The quality of a fit

Table 6.5: Fitting limits and mean fitting uncertainties associated with each fitted SED parameter for each observed source. The values listed under each source are the percentage uncertainties in the least-squares fit per parameter. As no source was fitted for synchrotron emission, the parameters A and α have been omitted.

	Limits		Fit Uncertainties (%)			
Parameter	Lower	Upper	Perseus	LDN 1622	W40	LDN 1582/84
$A_{\rm sp}$ (Jy)	0	100	0.3	1.1	17.2	15.8
$\nu_{\rm sp}$ (GHz)	10	60	0.5	1.6	8.4	8.2
EM ($\rm cm^{-6}\,pc^{-1}$)	1	1000	2.5	5.2	2.9	5.1
$\Delta T_{\rm cmb}$ (mK)	-10	10	8.4	15.7	30.3	8.1
$T_{\rm dust}$ (K)	-2	150	5.7	9.5	8.4	9.2
τ_{250}	10^{-5}	10^{-2}	23.1	36.6	30.1	23.3
β	0.5	3	6.1	17.7	8.1	10.8

was determined using the reduced $\chi^2/(\text{d.o.f.})$, which is defined as

$$\frac{\chi^2}{\text{d.o.f.}} = \frac{1}{N-\lambda}\sum\left(\frac{S_\nu - m_\nu}{\sigma_\nu}\right)^2, \tag{6.18}$$

where S_ν is the measured flux density at a given frequency with uncertainty σ_ν, m_i is the predicted flux density given the model, N is the number of measurements and λ is the number of parameters used in the fit. Note however, that χ^2 in this situation can only be used to guide the quality of a fit, as it requires the condition that the noise on each parameter is gaussian and uncorrelated, which in this situation will not be the case.

6.4.2 Perseus Molecular Cloud

The Perseus molecular cloud is a nearby low-to-medium mass star formation region with an angular extent of approximately 6 degrees. It is currently the most studied and brightest spinning dust emitting source currently identified (Watson et al., 2005; Planck Collaboration Early XX, 2011; López-Caraballo et al., 2011; Tibbs et al., 2013a; Planck Collaboration Int. XV, 2014). Support for spinning dust emission within the Perseus molecular cloud comes from the observed correlations between radio emission at 30 GHz with 12 μm infrared emission (Watson et al., 2006), and the observed presence of emission lines from PAH molecules (Iglesias-Groth et al., 2008), which are considered to be likely carriers for spinning dust emission. The primary source

of spinning dust emission originates from a small ring-like structure embedded within the Perseus molecular cloud as identified by VSA observations (Tibbs et al., 2010). The ring-like structure has formed at the edge of an expanding shell of HII gas driven by the O9.5-B0V binary HD 278942 (Andersson et al., 2000). Figure 6.6 shows the Perseus molecular cloud and surrounding region at 100 μm taken from the reprocessed *IRAS* data, IRIS (Miville-Deschênes and Lagache, 2005). A red-dashed ring marks the location of the ring structure in the figure, which is clearly visible at 100 μm. A cross marks the location of the star HD 278942. The open cluster IC348 is marked too as this was also identified as a source of spinning dust emission by Tibbs et al. (2010). The Perseus molecular cloud was the focus of the first QUIJOTE MFI scientific release (Génova-Santos et al., 2015). The previous QUIJOTE MFI measurements of Perseus were taken using only raster scan observations, and the maps were calibrated using the IAC pipeline. Therefore the results presented in this Section on Perseus are almost entirely independent of those reported in Génova-Santos et al. (2015).

Figure 6.7 shows a subset of the maps used to fit the SED of the extended Perseus molecular cloud emission. At 408 MHz very little emission can be seen. The emission at 13 and 30 GHz can be seen to peak around the marked purple dot-dashed ring marking G160.26-18.62 in the figures and around IC348. The emission in the 13 and 30 GHz images also correlates with the thermal dust emission seen at 143 GHz and with the 100 μm emission, as seen in Figure 6.6. Dust-radio correlations have also been seen on much smaller scales of 2 arcmin at 15 GHz by the Arcminute Imager (AMI) and cannot be attributed to free-free emission from diffuse or UCHII regions within the cloud (Tibbs et al., 2013b,a).

The source flux density was measured using the elliptical aperture marked with the yellow line in Figure 6.7, The ellipse position and dimensions were chosen by visually inspecting the data. The criteria for the selected region was to ensure that the bright core of the Perseus molecular cloud was enclosed with the elliptical aperture. The background signal and noise was estimated from the ring of 1 degree diameter apertures as described in subsection 6.4.1, marked in the figure as dash black circles. Table 6.6 summarises the attributes of the aperture ellipse.

The spectrum of the Perseus molecular cloud is shown in Figure 6.8. The model fit is a combination of free-free, spinning dust, thermal dust and CMB emission. CO contamination can be seen in the *Planck* HFI 100 GHz and 217 GHz bands, and as such were omitted from the fit but are shown for completeness.

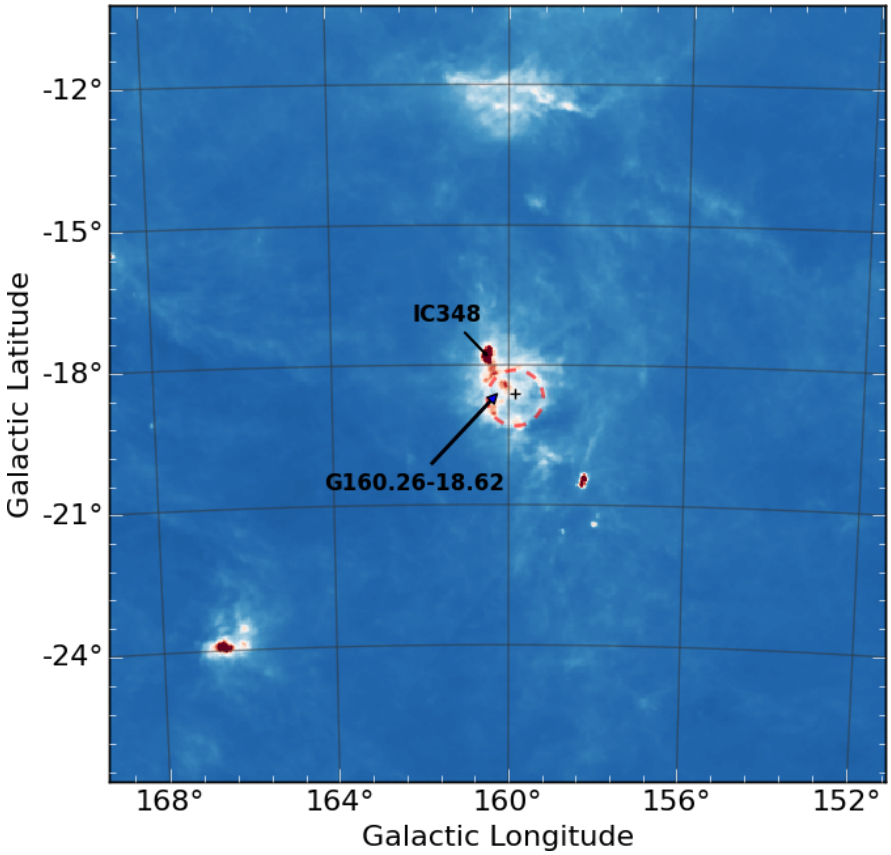

Figure 6.6: IRAS 100 μm Image of the Perseus Molecular Cloud (Galactic coordinates). The red-dashed ring structure marked in the figure is the spinning dust emitting shell referred to as G160.26-18.62. The cross in the centre of the ring is the O9.5-B0V binary, HD 278942, which is driving an expanding shell of HII gas encapsulated by G160.26-18.62. Blue is low emission, red is high emission.

Table 6.6: Parameters defining the aperture used to measure the flux density at each frequency for the Perseus molecular cloud. The parameters l and b mark the central Galactic coordinates of the aperture. a_1 and a_2 are the semi-major and semi-minor axes respectively. The position angle of the aperture is $\theta_{\rm p}$ measured anti-clockwise from the latitude axis.

Parameter	Value (degrees)
l	160.35
b	-18.5
a_1	1.5
a_2	1.0
$\theta_{\rm p}$	12

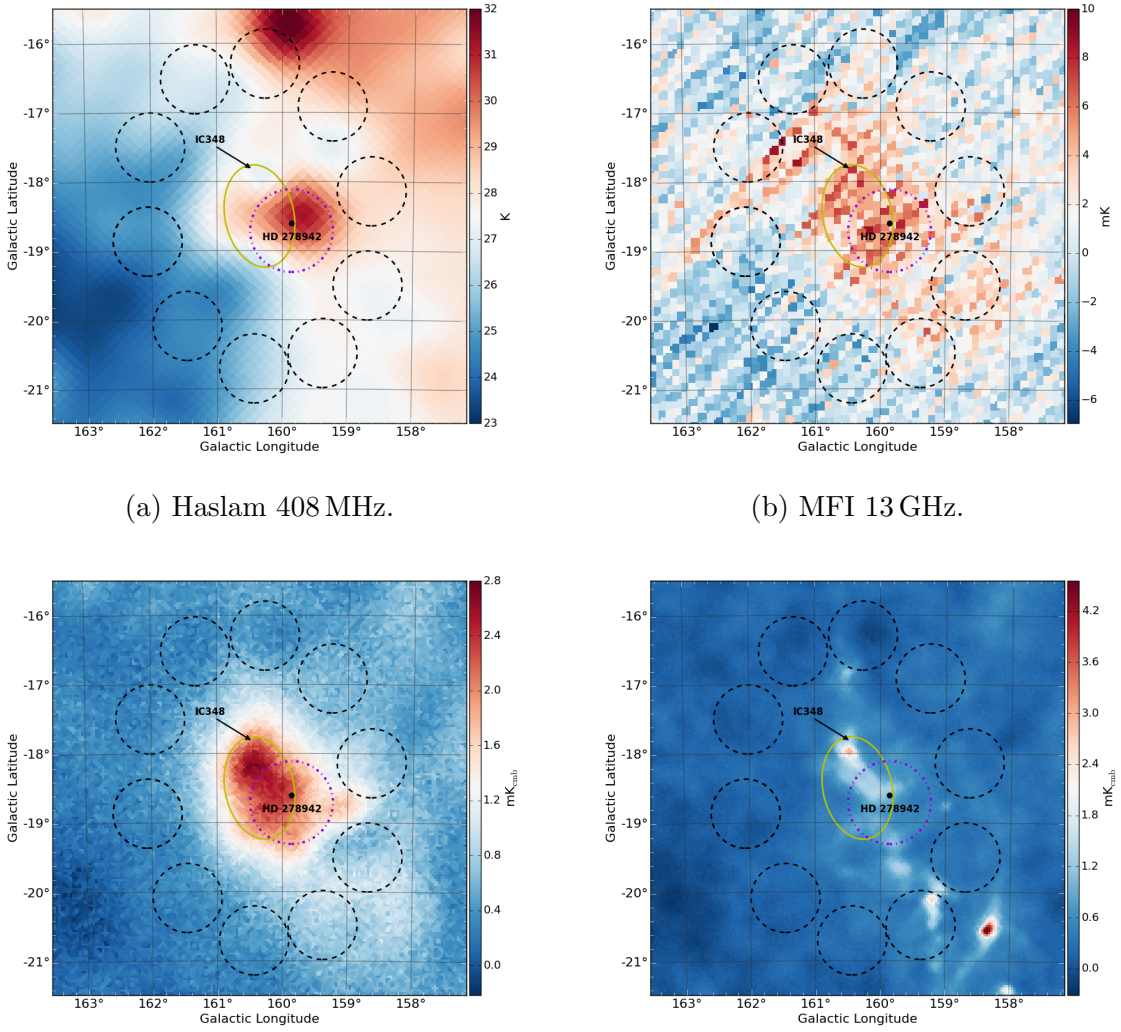

(a) Haslam 408 MHz.

(b) MFI 13 GHz.

(c) *Planck* LFI 30 GHz.

(d) *Planck* HFI 143 GHz.

Figure 6.7: Images of the Perseus molecular cloud as seen at frequencies between 408 MHz to 143 GHz in Galactic coordinates. The source of the spinning dust emission within Perseus is a small ring-like substructure labelled in the images as G160.26-18.62 and marked by a purple dot-dashed ring. Note that the bright core in 143 GHz is slightly offset from the core associated with IC348 seen in the IRAS data. This may be explained by a strong separation in the morphology of the local grain populations. Blue is low emission, red is high emission. Units are in brightness temperature and the images are presented at the native resolutions of the datasets.

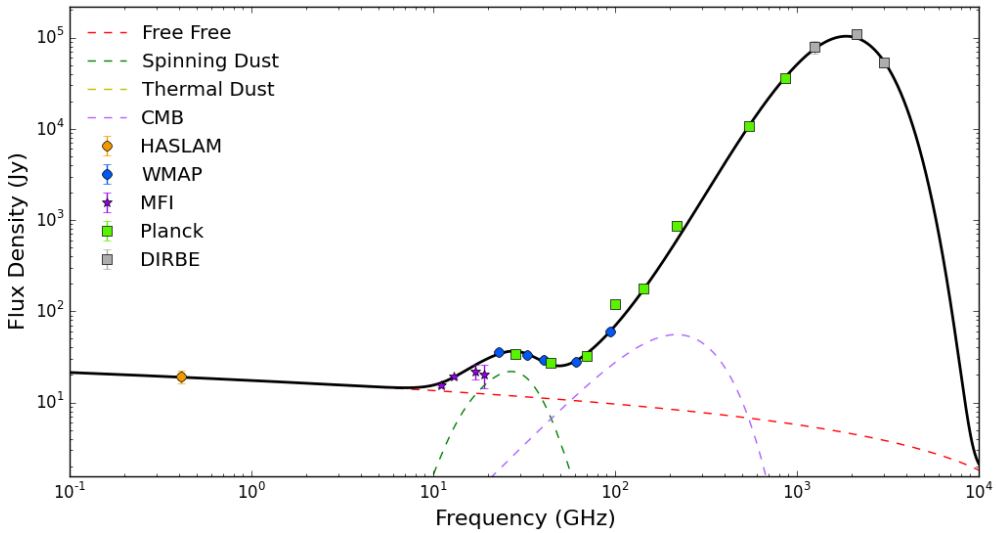

Figure 6.8: Model best fit to the SED of the Perseus molecular cloud. Data points are: MFI (purple stars), *Planck* (green squares), *WMAP* (blue circles), and DIRBE (grey squares). Fitted for free-free, thermal dust, spinning dust and CMB emissions.

The MFI data plus *WMAP* and *Planck* measurements between 10 and 60 GHz show a clear peak spectrum that can not be described by a free-free spectrum. The peak of the spectrum is 26.7 ± 0.8 GHz, and has a detection significance for spinning dust of $10.5\,\sigma$. The fraction of spinning dust emission at the peak is approximately 60 per cent, which is lower than the ≈ 80 per cent value reported in Planck Collaboration et al. (2014d) and the previous QUIJOTE MFI results (Génova-Santos et al., 2015). The discrepancy between these measurements and previous measurements is due to differences in the estimation of the background free-free emission. The colour corrected flux densities at each frequency can be found in Table 6.7 and the best fit parameters are reported in Table 6.8.

6.4.3 LDN 1622

Lynds dark cloud LDN 1622 is a starless cometary cloud within Orion seen *North-East* of Barnard's Loop (Maddalena et al., 1986). The cloud is embedded in a moderately bright, diffuse HII background and has an angular extent of approximately 10 arcmin. LDN 1622 and the nearby neighbouring cloud LDN 1621 have been the focus of several

Table 6.7: Flux densities of the Perseus molecular cloud measured within the aperture described by Table 6.6. Uncertainties have contributions from the pixel noise, calibration at each frequency, background signal, and fitting uncertainty.

Frequency (GHz)	Flux Density (Jy)
0.408	19.0 ± 3.0
11.0	15.5 ± 0.7
13.0	19.2 ± 0.6
17.0	22.0 ± 4.0
19.0	20.0 ± 6.0
22.8	35.7 ± 0.8
28.4	34.3 ± 0.8
33.0	33.4 ± 0.8
40.7	29.0 ± 0.8
44.0	27.3 ± 0.8
60.7	28.0 ± 1.0
70.0	32.0 ± 1.0
93.6	60.0 ± 3.0
100.0	118.0 ± 8.0
143.0	177.0 ± 10.0
217.0	855.0 ± 71.0
545.0	10676.0 ± 1015.0
857.0	35651.0 ± 3298.0
1249.0	78468.0 ± 12344.0
2141.0	108913.0 ± 12442.0
2997.0	53037.0 ± 6456.0

Table 6.8: Best fit parameters for the SED model using least-squares fitting to the flux densities derived for Perseus molecular cloud between 0.408 and 4000 GHz. Uncertainties are a combination of the uncertainties derived from the covariance matrix of the least-squares fit and the percentage fitting uncertainties in Table 6.5.

Parameter	Best Fit Value
$A_{\rm sp}$ (Jy)	21 ± 2
$\nu_{\rm sp}$ (GHz)	26.7 ± 0.8
EM ($\rm cm^{-6}\,pc^{-1}$)	411 ± 61
$\Delta T_{\rm cmb}$ (μK)	35 ± 9
$T_{\rm dust}$ (K)	18.4 ± 1.3
τ_{250} (10^-3)	2.0 ± 0.6
β	1.9 ± 0.2
χ^2/(d.o.f.)	1.66

observations using the 140 ft Green Bank Telescope and the Cosmic Background Interferometer (CBI) (Finkbeiner et al., 2002; Casassus et al., 2006; Mason et al., 2009; Dickinson et al., 2010). LDN 1622 was one of the first spinning dust emission sources identified, however the nature and origin of the emission is still in question. LDN 1622 will be discussed in detail in Chapter 7.

Figure 6.9 shows the region surrounding LDN 1622 at 408 MHz to 143 GHz. The figures mark the location of the nearby bright HII feature of Barnard's loop, which is clearly visible in all the image apart from the 143 GHz map. White arrows also mark the approximate direction of the radiation field generated by the Orion B stellar association. The radiation field from Orion B is illuminating the photo-dissociation region that is thought be the source of the spinning dust emission within LDN 1622 (Casassus et al., 2006). In the 13 and 30 GHz images a second feature can be seen protruding from Barnard's loop towards the Galactic plane, passing through the region containing LDN 1622. At 30 GHz a discrete source can be seen to correlate with the dust emission from LDN 1622 that is seen in the 143 GHz image. Note that the data on the left-side of the 13 GHz image has a large amount of noise due to much of the TOD within this region being contaminated by GSO satellite emission. Background apertures within this region are not used to estimate the pixel noise or background emission contribution.

The parameters that describe the elliptical aperture shown in Figure 6.9 are given

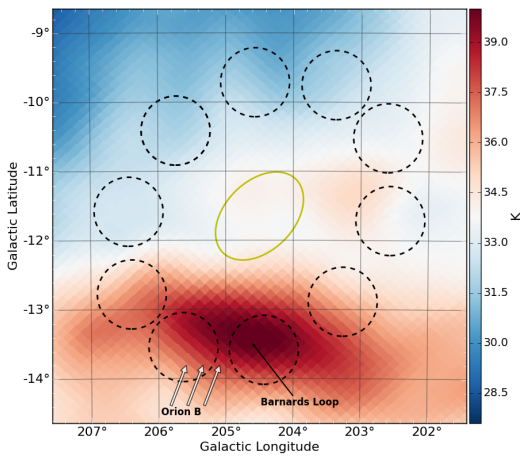

(a) Haslam 408 MHz.

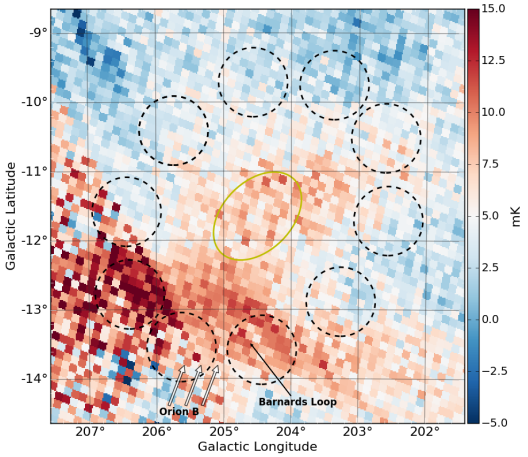

(b) MFI 13 GHz.

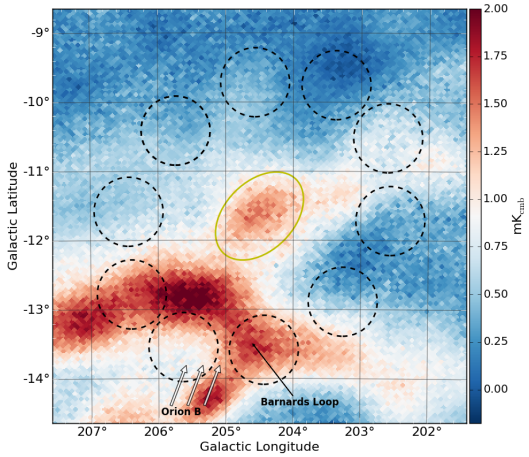

(c) *Planck* LFI 30 GHz.

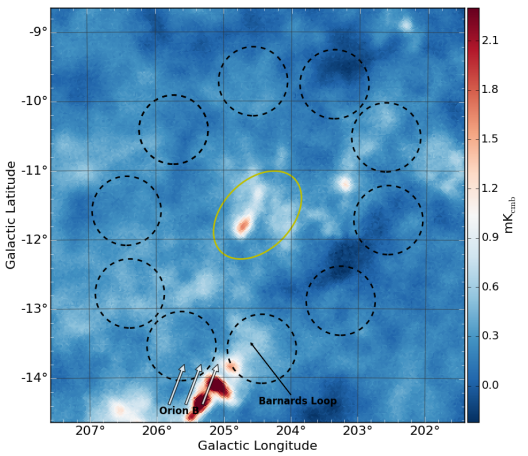

(d) *Planck* HFI 143 GHz.

Figure 6.9: Images of LDN 1622 as seen at frequencies between 408 MHz to 143 GHz in Galactic coordinates. LDN 1622 is too small to be resolved in these images, except at 143 GHz. At 408 MHz and 13 GHz most of the emission is smooth continuum free-free emission. However, the 30 GHz map shows a structure appearing above the free-free background that is coincident with the thermal dust emission of LDN 1622. The white-arrows labelled Orion B illustrate the approximate direction of the local radiation field. Units are in brightness temperature and the maps are presented at the native resolutions of each dataset.

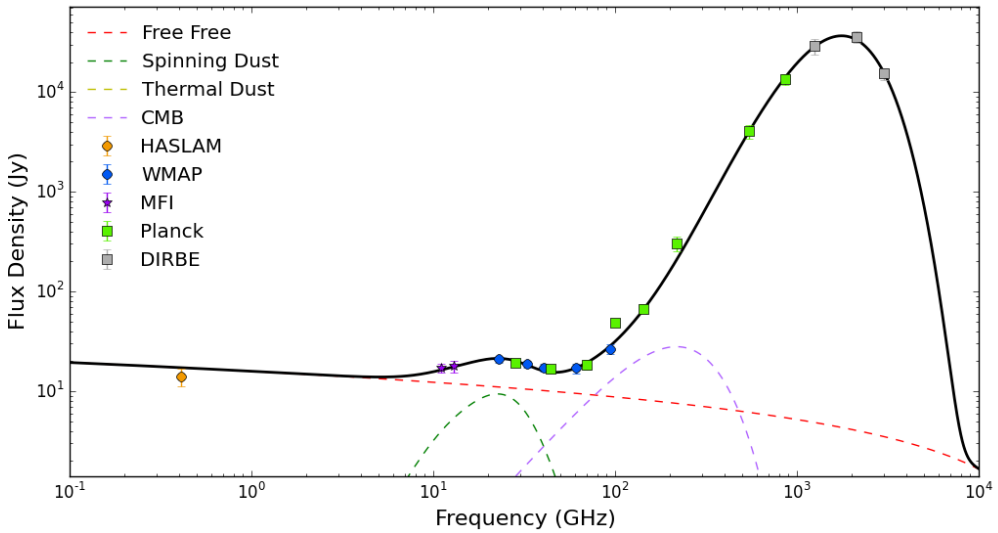

Figure 6.10: Model best fit to the SED of LDN 1622. Data points are: MFI (purple stars), *Planck* (green squares), *WMAP* (blue circles), and DIRBE (grey squares). Components fitted were free-free, thermal dust, spinning dust and CMB emissions.

in Table 6.9. The aperture location and size was chosen such that to carefully avoid Barnard's loop, but contain the whole of LDN 1622 and the nearby more diffuse LDN 1621 region. The background apertures that are within the noisy regions seen in the MFI 13 GHz image were ignored.

The parametric model fit to the spectrum of LDN 1622 is shown in Figure 6.10 and Table 6.10 lists all the colour corrected flux densities. Measurements at 100 GHz and 217 GHz were ignored due to CO line contamination. The fit is contains contributions from free-free, thermal dust, spinning dust and CMB emissions. The fit has a $\chi^2/(\text{d.o.f.}) = 0.35$, implying the fit is slightly over constrained for the given uncertainty estimates. The uncertainties in the region of LDN 1622 are typically dominated by the background uncertainty, which strongly varies as seen in Figure 6.9.

The fit reports a $9\,\sigma$ detection significance on spinning dust emission, with a peak frequency of 22 ± 1.2 GHz, which is significantly lower than the peak frequency of 30.1 ± 1.9 GHz reported in Planck Collaboration et al. (2014d). The difference in the peak frequency demonstrates the importance of observations between 10 and 20 GHz, such as the MFI data, when studying spinning dust emission regions especially when trying to understand the grain carrier populations behind the spinning dust emission. Table 6.11 lists the rest of the best fit parameters and uncertainties.

Table 6.9: Parameters defining the aperture used to measure the flux density at each frequency of LDN 1622. The parameters l and b mark the central Galactic coordinates of the aperture. a_1 and a_2 are the semi-major and semi-minor axes respectively. The position angle of the aperture is $\theta_{\rm p}$ measured anti-clockwise from the latitude axis.

Parameter	Value (degrees)
l	204.5
b	11.65
a_1	1.5
a_2	1.0
$\theta_{\rm p}$	-45

Table 6.10: Flux densities of LDN 1622 measured within the aperture described by Table 6.9. Uncertainties have contributions from the pixel noise, calibration at each frequency, background signal, and fitting uncertainty.

Frequency (GHz)	Flux Density (Jy)
0.408	14.0 ± 3.0
11.0	17.0 ± 2.0
13.0	18.0 ± 2.0
17.0	-4.0 ± 2.0
19.0	-15.0 ± 5.0
22.8	21.0 ± 1.0
28.4	19.0 ± 1.0
33.0	19.0 ± 2.0
40.7	17.0 ± 2.0
44.0	17.0 ± 2.0
60.7	17.0 ± 2.0
70.0	18.0 ± 2.0
93.6	27.0 ± 3.0
100.0	49.0 ± 5.0
143.0	67.0 ± 7.0
217.0	306.0 ± 52.0
545.0	4046.0 ± 657.0
857.0	13538.0 ± 1732.0
1249.0	28894.0 ± 4989.0
2141.0	35909.0 ± 4752.0
2997.0	15278.0 ± 2117.0

Table 6.11: Best fit parameters for the SED model using least-squares fitting to the flux densities derived for the Lynds dark cloud LDN 1622 between 0.408 and 3000 GHz. Uncertainties are a combination of the uncertainties derived from the covariance matrix of the least-squares fit and the percentage fitting uncertainties in Table 6.5.

Parameter	Best Fit Value
$A_{\rm sp}$ (Jy)	9 ± 1
$\nu_{\rm sp}$ (GHz)	22 ± 1.2
EM ($\rm cm^{-6}\,pc^{-1}$)	374 ± 34
$\Delta T_{\rm cmb}$ (μK)	16 ± 4
$T_{\rm dust}$ (K)	17.0 ± 1.7
τ_{250} (10^-3)	0.9 ± 0.2
β	2.0 ± 0.2
χ^2/(d.o.f.)	0.35

6.4.4 HII Complex W40

The HII complex W40 is situated just off the Galactic plane at $l = 28.8^\circ$ and $b = 3.4^\circ$. The angular extent of the complex is approximately 8.5 arcmin (Quireza et al., 2006). W40 was first tentatively identified by Finkbeiner et al. (2004) in a GBT survey of the Galactic plane. Later observations by CBI ruled out UCHII contamination and provided a tentative $2\,\sigma$ upper limit on the presence of spinning dust emission (Demetroullas et al., 2015). Similarly, *Planck* observations of W40 also suggest the presence of spinning dust (Planck Collaboration Int. XV, 2014). The limitations of these observations stem principally from the lack of low frequency constraints on the bright diffuse free-free emission that dominates the W40 SED.

The 408 MHz image of W40 shown in Figure 6.11 reveals that the complex, on 1 degree scales, is merged with the extended synchrotron structure of the Galaxy. However, as discussed in Demetroullas et al. (2015), little or no synchrotron emission is expected to originate from the complex. The mixing of W40 with the extended Galactic plane emission means that the 408 MHz map is considered unreliable and is therefore not included in the spectral fit. At 11 GHz and above the W40 complex is a distinct feature separate from the Galactic plane. The 100 GHz and 217 GHz HFI data are also ignored due to CO contamination

The model fit to the spectrum of W40 shown in Figure 6.12, reveals that the source is dominated by free-free emission at frequencies less than 100 GHz. A full list of flux

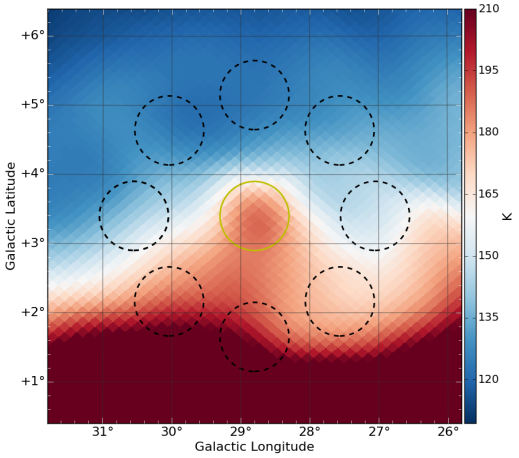

(a) Haslam 408 MHz.

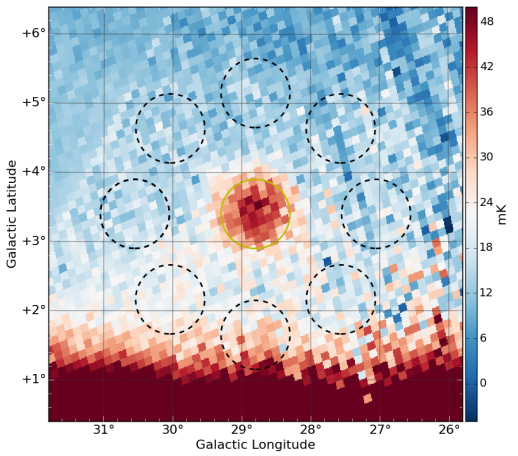

(b) MFI 13 GHz.

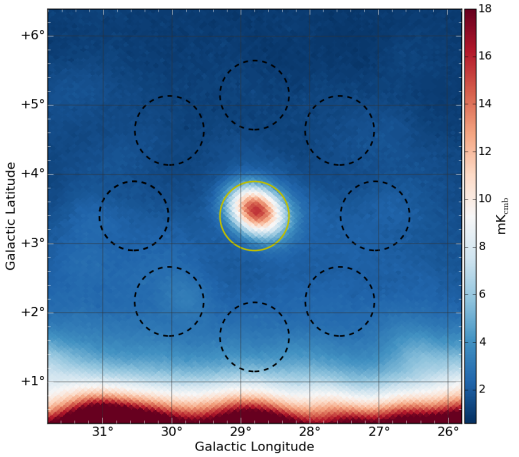

(c) *Planck* LFI 30 GHz.

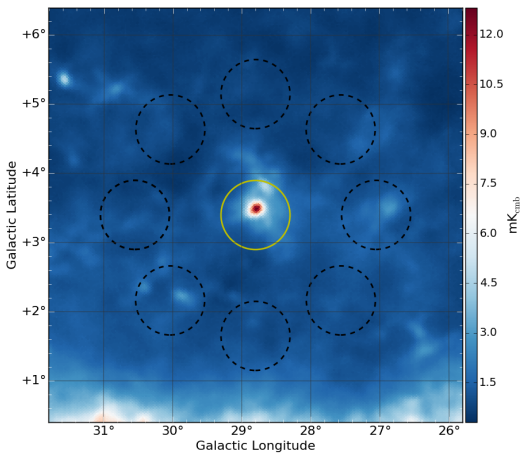

(d) *Planck* HFI 143 GHz.

Figure 6.11: Images of W40 as seen at frequencies between 408 MHz to 143 GHz in Galactic coordinates. The high background noise seen at 13 GHz is due to this region being highly contaminated by GSO satellite emission. At 408 MHz W40 is seen to be mixing with extended synchrotron emission from the Galactic plane. Units are in brightness temperature and the maps are presented at the native resolutions of each dataset.

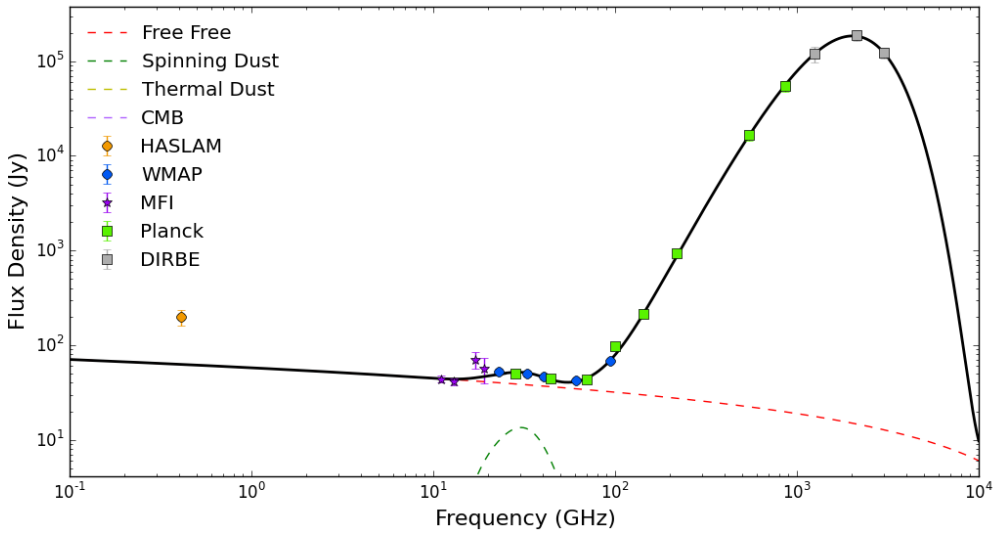

Figure 6.12: Model best fit to the SED of W40. The spectrum shows that on 1 degree scales W40 is dominated by free-free emission at spinning dust frequencies. Data points are: MFI (purple stars), *Planck* (green squares), *WMAP* (blue circles), and DIRBE (grey squares). The Haslam 408 MHz point was not included in the fit. Components fitted for were free-free, thermal dust, spinning dust and CMB emissions.

densities can be found in Table 6.12. The aperture for W40 was chosen to be circular as the source is unresolved at 1 degree scales, Table 6.13 lists the aperture parameters.

The fit appears to be clearly constraining a free-free spectrum with a fit quality of χ^2/d.o.f. = 1.30. A tentative hint of a peak spectrum indicative of spinning dust emission can be seen between 22 and 40 GHz but with a very low significance of 2.3 σ. This agrees with the findings in Demetroullas et al. (2015), which also demonstrated that on large-scales free-free dominates the spectrum of W40 and the spinning dust emission is originating from small substructures within the complex. Table 6.14 lists all the best fit parameters for the W40 SED model.

6.4.5 LDN 1582/84

Lynds dark cloud LDN 1582 and its neighbouring cloud LDN 1584 have a combined angular extent of between 20 and 40 arcmin. The clouds are part of a complete ring structure of approximately 8 degrees in diameter that has been swept out by a spherical region of HII, powered by the O-type star λ-Orionis (e.g., Zhang et al., 1989). In Figure 6.13, the ring-like structure has been marked as a red-dashed line overlaid onto a cutout

Table 6.12: Flux densities of W40 measured within the aperture described by Table 6.13. Uncertainties have contributions from the pixel noise, calibration at each frequency, background signal, and fitting uncertainty.

Frequency (GHz)	Flux Density (Jy)
0.408	198.0 ± 37.0
11.0	44.0 ± 4.0
13.0	41.0 ± 3.0
17.0	70.0 ± 13.0
19.0	56.0 ± 16.0
22.8	53.0 ± 3.0
28.4	50.0 ± 3.0
33.0	50.0 ± 3.0
40.7	46.0 ± 3.0
44.0	44.0 ± 2.0
60.7	42.0 ± 2.0
70.0	44.0 ± 2.0
93.6	69.0 ± 3.0
100.0	98.0 ± 5.0
143.0	214.0 ± 11.0
217.0	932.0 ± 68.0
545.0	16461.0 ± 1996.0
857.0	54490.0 ± 7398.0
1249.0	119971.0 ± 22560.0
2141.0	188235.0 ± 25264.0
2997.0	122713.0 ± 16324.0

Table 6.13: Parameters defining the aperture used to measure the flux density at each frequency for W40. The parameters l and b mark the central Galactic coordinates of the aperture. a_1 and a_2 are the semi-major and semi-minor axes respectively. The position angle of the aperture is $\theta_{\rm p}$ measured anti-clockwise from the latitude axis.

Parameter	Value (degrees)
l	28.8
b	3.4
a_1	1.0
a_2	1.0
$\theta_{\rm p}$	0

Table 6.14: Best fit parameters for the SED model using least-squares fitting to the flux densities derived for the Galactic HII complex W40 between 0.408 and 3000 GHz. Uncertainties are a combination of the uncertainties derived from the covariance matrix of the least-squares fit and the percentage fitting uncertainties in Table 6.5.

Parameter	Best Fit Value
$A_{\rm sp}$ (Jy)	14 ± 6
$\nu_{\rm sp}$ (GHz)	30 ± 4
EM ($\rm cm^{-6}\,pc^{-1}$)	1362 ± 104
$\Delta T_{\rm cmb}$ (μK)	-10.5 ± 12
$T_{\rm dust}$ (K)	28 ± 2
τ_{250} (10^-3)	1.9 ± 0.5
β	1.7 ± 0.2
χ^2/(d.o.f.)	1.30

from the *Planck* derived AME all-sky map (Planck Collaboration et al., 2015d), and 100 μm IRIS data. The cross in the figure marks the location of λ-Orionis. Originally, LDN 1582/84 was identified in Planck Collaboration Int. XV (2014) as a tentative spinning dust emitting region. Within the AME map in Figure 6.13, spinning dust emission should be seen originating from all the clouds in the ring. Interestingly, a comparison of the IRIS 100 μm with the AME model map seems to demonstrate that the actual source of spinning dust emission is not coming from the dense region of LDN 1582/84 but from the less dense dust region seen to the right side of the cloud.

As with the Perseus molecular cloud and LDN 1622, the region around LDN 1582/84 has very little emission in the 408 MHz map as shown in Figure 6.14. However, a small core of emission can be seen surrounding the λ-Orionis star. At 13 GHz, the region around λ-Orionis is dominated by free-free emission forming a HII shell that can be seen to lie within the 8 degree diameter ring of dust. Visual inspection of the figure shows that LDN 1582/84 at 13 GHz cannot be readily separated from the surrounding HII emission. However, at 30 GHz a weak snaking structure can be seen, which peaks in the vicinity of LDN 1582/84. Immediately it is clear that the peak at 30 GHz is coincident with the dense, dusty core seen at 143 GHz. Careful visual inspection of the 143 GHz map reveals the same snaking structure seen at 30 GHz. Of course, this does not immediately imply that the dust seen at 143 GHz is the source of the 30 GHz emission, after all it was stated at the beginning of this thesis that "*stuff traces stuff*".

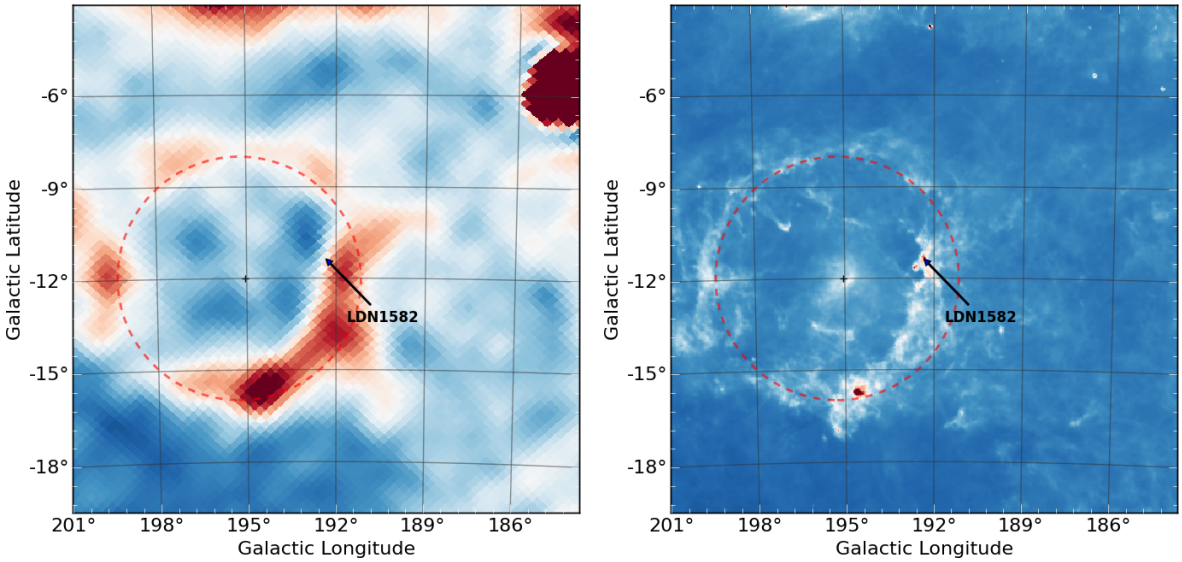

(a) *Planck* AME Model. (b) IRIS 100 μm.

Figure 6.13: Cutout from the *Planck* derived AME all-sky map and IRIS 100 μm data in Galactic coordinates. The red-dashed ring marks the 8 degree extent of a ring of dust that encloses an extended HII region. The HII and PDRs on the inner edge of the dust clouds are illuminated by the central O-type star λ-Orionis (marked by a black cross).

Another interesting feature of the 30 GHz image is that the bright peak seen, is not coincident with the peak of the AME emission shown in Figure 6.13. However, this could simply be a problem with the *Planck* model, as at 1 degree resolution the HII and dust-correlated radio emission around LDN 1582 will be difficult to separate.

A spectrum and best fit SED model for LDN 1582/84 is shown in Figure 6.15 and the associated colour-corrected flux densities are reported in Table 6.15. Flux densities measured at 100 GHz and 217 GHz were ignored due to CO contamination.The parameters of the aperture ellipse are given in Table 6.16, the extent of the aperture was chosen to completely contain the emission visible at 30 GHz and include as little of this HII emission seen at 13 GHz. Note that the Haslam 408 MHz map was not included in the fit as very little emission is visible and therefore would not reliably constrain the free-free spectrum.

The $\chi^2/(\text{d.o.f.}) = 0.26$ implies the fit is overly constrained. As with LDN 1622, LDN 1582 has very large uncertainties associated with the variations in the background emission that must be accounted for. Even with these large uncertainties the spinning dust emission peak is tentatively constrained at the $5\,\sigma$ level, this is similar to the result found in Planck Collaboration Int. XV (2014). Due to the large-scale, bright HII region nearby separating the spinning dust emission may require future higher resolution observations that can resolve the photo-dissociation region of LDN 1582. The rest of the fitted parameters can be found in Table 6.17. Also note that the detection significance of the spinning dust will be highly dependent on the background emission of the source.

6.4.6 Discussion

In this Section, four individual spinning dust regions have been investigated using previously available surveys and the MFI 11 and 13 GHz wide-survey maps. To test the reliability of this analysis the parameters derived from the fitted SED models can be compared with the results found in another analysis by Planck Collaboration et al. (2014d), which differs from this analysis only by the lack of the MFI maps.

Figure 6.16 shows plots comparing $T_{\rm dust}$ and dust emissivity β, $T_{\rm dust}$ and peak spinning dust frequency $\nu_{\rm sp}$, and τ_{250} with the ratio $A_{\rm sp}/\tau_{250}$. These parameters should be largely independent on the absolute scaling in flux density, meaning these can be compared with the parameters found in Planck Collaboration et al. (2014d) directly.

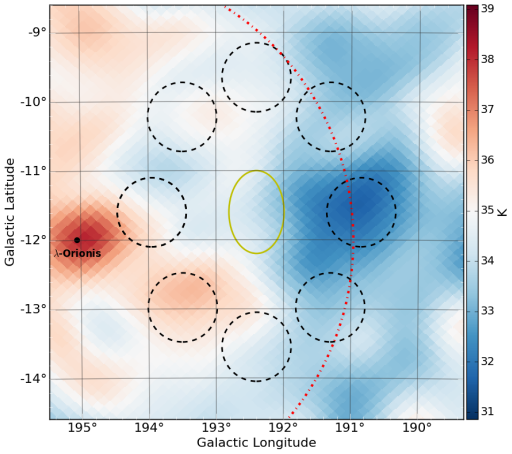

(a) Haslam 408 MHz.

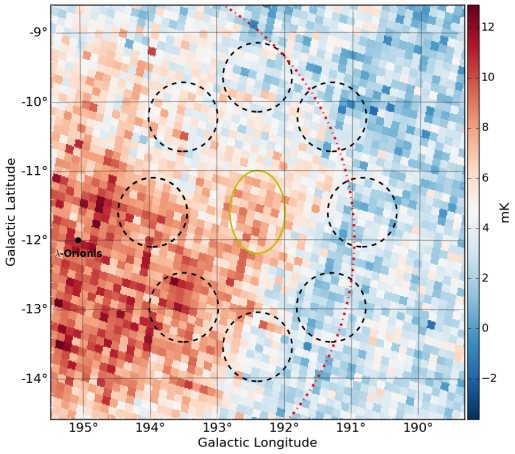

(b) MFI 13 GHz.

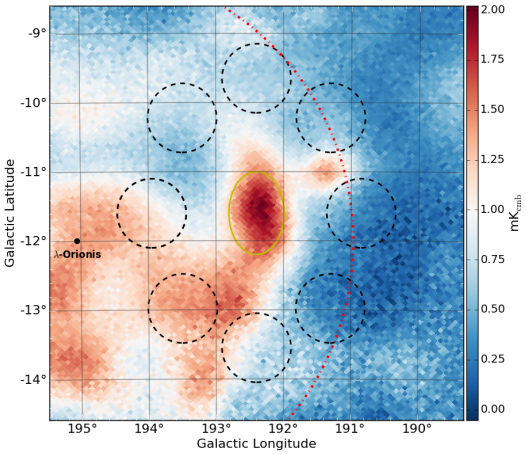

(c) *Planck* LFI 30 GHz.

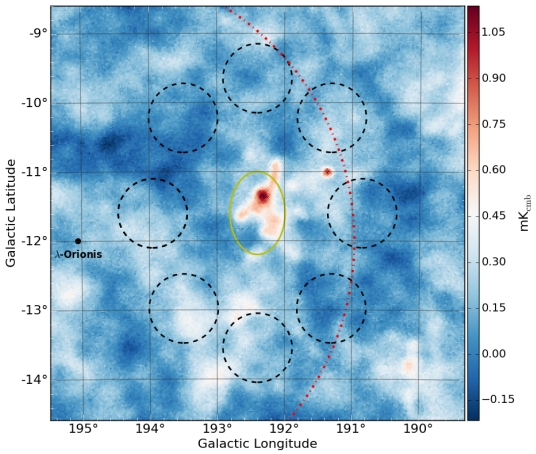

(d) *Planck* HFI 143 GHz.

Figure 6.14: Images of LDN 1582/84 as seen at frequencies between 408 MHz to 143 GHz in Galactic coordinates. The location of LDN 1582 has been indicated. The red-dashed line marks the ring of dust enclosing the bright HII region swept out by the O-type star λ-Orionis. The location of λ-Orionis is marked by a cross. Units are in brightness temperature and the maps are presented at the native resolutions of each dataset.

Table 6.15: Flux densities of LDN 1582 measured within the aperture described by Table 6.16. Uncertainties have contributions from the pixel noise, calibration at each frequency, background signal, and fitting uncertainty.

Frequency (GHz)	Flux Density (Jy)
0.408	4.0 ± 1.0
11.0	9.0 ± 1.0
13.0	8.0 ± 1.0
17.0	16.0 ± 3.0
19.0	15.0 ± 4.0
22.8	12.2 ± 1.0
28.4	13.0 ± 1.0
33.0	13.0 ± 1.0
40.7	14.0 ± 1.0
44.0	13.0 ± 1.0
60.7	13.0 ± 2.0
70.0	14.0 ± 2.0
93.6	15.0 ± 2.0
100.0	27.0 ± 2.0
143.0	26.0 ± 3.0
217.0	109.0 ± 18.0
545.0	942.0 ± 277.0
857.0	3447.0 ± 785.0
1249.0	8841.0 ± 1908.0
2141.0	12606.0 ± 1980.0
2997.0	5638.0 ± 940.0

Table 6.16: Parameters defining the aperture used to measure the flux density at each frequency for LDN 1582. The parameters l and b mark the central Galactic coordinates of the aperture. a_1 and a_2 are the semi-major and semi-minor axes respectively. The position angle of the aperture is $\theta_{\rm p}$ measured anti-clockwise from the latitude axis.

Parameter	Value (degrees)
l	192.4
b	-11.6
a_1	1.2
a_2	0.8
$\theta_{\rm p}$	0

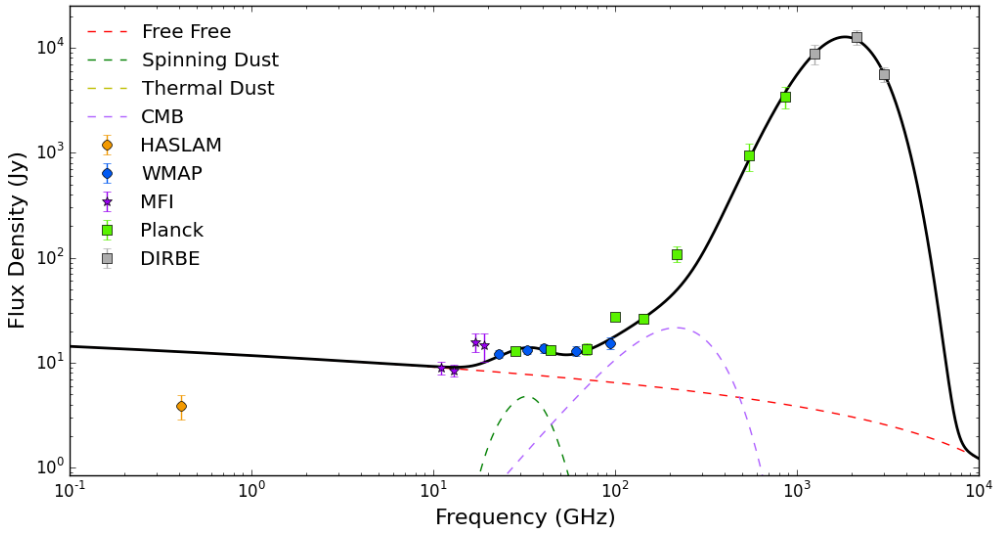

Figure 6.15: Model best fit to the SED of LDN 1582/84. Data points are: MFI (purple stars), *Planck* (green squares), *WMAP* (blue circles), and DIRBE (grey squares). The Haslam 408 MHz point was not included in the fit. Fitted emission components were free-free, thermal dust, spinning dust and the CMB.

Table 6.17: Best fit parameters for the SED model using least-squares fitting to the flux densities derived for the Lynds dark cloud LDN 1582 between 0.408 and 3000 GHz. Uncertainties are a combination of the uncertainties derived from the covariance matrix of the least-squares fit and the percentage fitting uncertainties in Table 6.5.

Parameter	Best Fit Value
$A_{\rm sp}$ (Jy)	5 ± 1
$\nu_{\rm sp}$ (GHz)	33 ± 3
EM ($\rm cm^{-6}\,pc^{-1}$)	276 ± 21
$\Delta T_{\rm cmb}$ (μK)	13 ± 2
$T_{\rm dust}$ (K)	16 ± 2
τ_{250} (10^-3)	0.3 ± 0.2
β	2.6 ± 0.4
χ^2/(d.o.f.)	0.26

The figure shows that the parameters derived from this analysis largely agree with the values found in Planck Collaboration et al. (2014d). With the exception of a slightly large value for dust emissivity for LDN 1582 seen in Figure 6.16a but the uncertainties are large enough to still be consistent with other measurements.

Figure 6.16c shows that the measurements of $A_{\rm sp}/\tau_{250}$ against τ_{250} are consistent with those from *Planck*, which identified $A_{\rm sp}/\tau_{250}$ as a promising method of identifying spinning dust emission sources. For Perseus, LDN 1622 and LDN 1582 the mean value for the ratio of the peak flux density of the spinning dust SED and the dust opacity at 250 μm is $\langle A_{\rm sp}/\tau_{250}\rangle = 1.24 \pm 0.18 \times 10^4\,{\rm Jy}/\tau_{250}$. The mean peak frequency of the spinning dust SED is $\langle \nu_{\rm sp}\rangle = 27.2 \pm 0.7\,{\rm GHz}$. However, these values can only guide the understanding of spinning dust emission because, as seen in Figures 6.16b and 6.16c, both these parameters vary considerably from source to source.

An interesting point to note in this Section is the environmental similarities between the source of spinning dust emission within the Perseus molecular cloud and the region around LDN 1582/84. Both regions are HII shells that have swept out a ring of dust, illuminated by a central O-type star. Inside the Perseus molecular cloud, the spinning dust emission is seen to be tracing the photo-dissociation regions along the edge of the HII shell (Tibbs et al., 2010, 2013b). In principal, the same environment is occurring around the edge of the HII shell swept out by λ-Orionis. From the spectrum shown in Figure 6.15, it seems fairly clear that spinning dust emission is contributing to the total emission of the region. The large angular extent of λ-Orionis, coupled with the extensive ancillary data available for the Orion region, means that this region will be ideal for further investigations into, and the modelling of, spinning dust emission.

The analysis in the Section shows that a model spinning dust emission SED can be used to explain excess emission above background free-free or synchrotron emission within compact sources. The inclusion of the MFI data points helps to constrain parameters such as the peak frequency of the spinning dust emission and also confirms that the spectrum between 10 and 30 GHz is rising. However, correlations between the source and background emissions, tension between parameters in the fitted SED models, and a dependence on well chosen starting conditions limits this analysis. Ideally, the spinning dust emission SED could give an independent method of studying dust grain populations, measuring column densities along lines-of-sight and constrain environmental information within a region. To improve the analysis will require observations that can constrain the free-free emission, such as the C-BASS 5 GHz observations

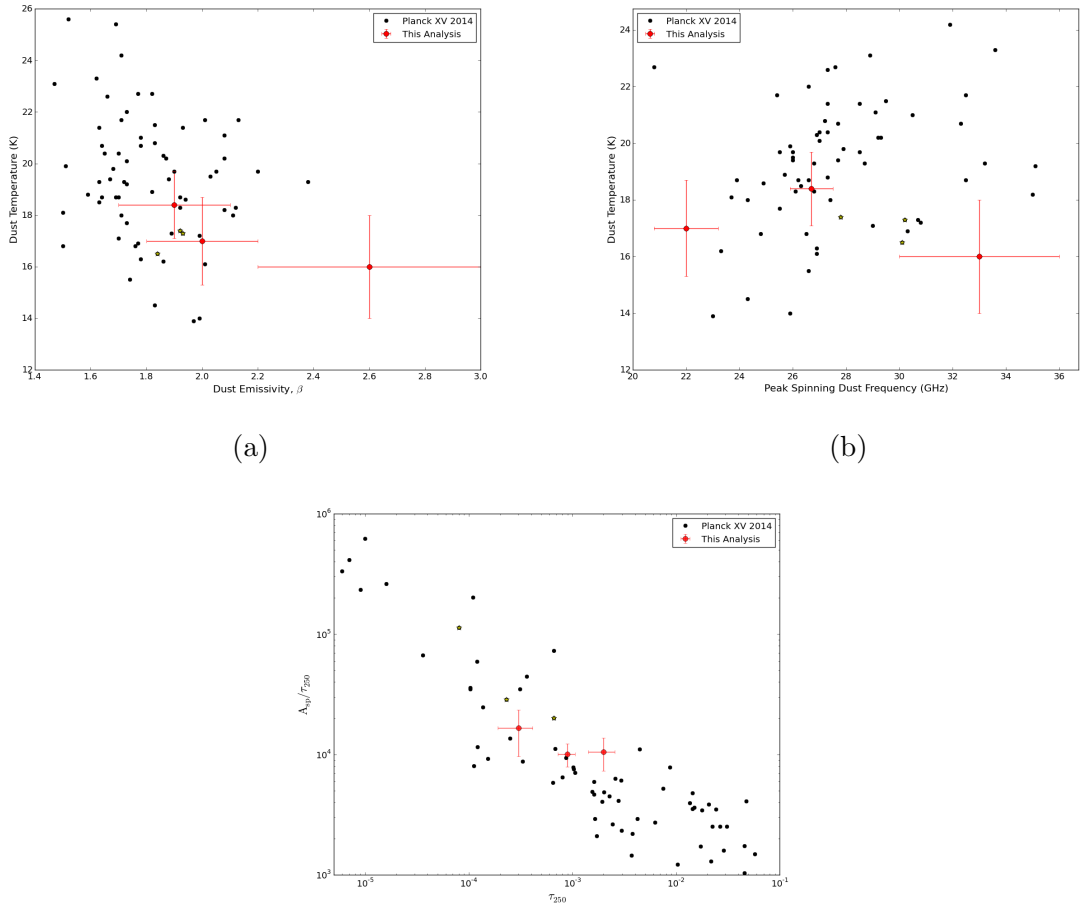

(a) (b)

(c)

Figure 6.16: Plots comparing the values of $A_{\rm sp}$, $T_{\rm dust}$, $\nu_{\rm sp}$ and τ_{250} derived from this analysis for Perseus, LDN 1622 and LDN 1582 (Red Points) with those derived by *Planck* in Planck Collaboration et al. (2014d) (Black Points). The yellow stars indicate the values for Perseus, LDN 1622 and LDN 1582 found in the *Planck* paper.

(King et al., 2014). Also the analysis technique would benefit from a full Monte-Carlo, maximum-likelihood approach, which would help to describe the correlations between the background emission, source emission and fitted parameters.

6.5 Spectral Index Maps

Flux density spectral index is defined, in full, as

$$\frac{S(\nu_1)}{S(\nu_2)} = \frac{T(\nu_1)}{T(\nu_2)} \left(\frac{\nu_1}{\nu_2}\right)^2 = \left(\frac{\nu_1}{\nu_2}\right)^\alpha, \tag{6.19}$$

where S and T are the source flux density and brightness temperature respectively for the observing frequencies ν_1 and ν_2. The spectral index, α in Equation 6.19, can be used to describe the *colour* of a source. For example if a spectral index is negative, the low frequency emission is brighter than the high frequency emission (e.g., the source is *redder*). If the spectral index is positive, then the reverse is true (e.g., the source is *bluer*). The spectral indices of a source can provide model independent insight into its nature, even when the SED of the source has poor frequency sampling. The key points (which can also be inferred from Figure 1.2) are:

- Between 408 MHz and 10 GHz spectral indices are typically negative due to synchrotron and free-free emissions (therefore these sources are *red*).
- Above 60 GHz, spectral indices are typically positive due to thermal dust emission (therefore these sources are *blue*).
- From 10 to 60 GHz, there is a mixture of synchrotron, free-free and spinning dust emissions. If the spectral index is negative (red) then synchrotron and free-free dominate. If the spectrum is flat (white) or rising (blue) then the SED has some contribution from spinning dust emission or possibly the integrated emission from bright ultra compact HII regions (UCHII).

To derive a spectral index with low uncertainties requires using two datasets with sufficient separation in frequency space, high signal-to-noise ratios and low calibration uncertainties. These criteria can be summarised by:

$$\sigma_\alpha = \frac{1}{\ln(\nu_1/\nu_2)} \sqrt{c_{\nu_1}^2 + c_{\nu_2}^2}, \tag{6.20}$$

where σ_α is the spectral index uncertainty assuming Gaussian noise, and c_{ν_1} and c_{ν_2} are the combined fractional calibration and noise uncertainties of each dataset. To maximise the signal-to-noise ratio of the MFI wide-survey observations, the 11 and 13 GHz images are combined into a single map, which will be referred to in this Section as the MFI wide-survey 12 GHz map.

In this Section, two maps of spectral indices will be derived for regions at low Galactic latitudes and between the Galactic longitudes $0^\circ < l < 180^\circ$. The region being investigated is shown in Figure 6.17 at 408 MHz, 12 GHz and 22.8 GHz. Key features such as the strong synchrotron sources Cas A and Cyg A are marked as well as the Perseus molecular cloud, which is a known bright spinning dust emission source (e.g., Planck Collaboration Early XX, 2011). One spectral index map is between the Haslam et al. (1982) 408 MHz survey and the MFI 12 GHz map. This is predicted to be dominated by free-free and synchrotron emission. The second spectral index map is between the MFI 12 GHz map and the *WMAP* 9-year beam deconvolved map, smoothed to a 1 degree resolution. The colour of this spectral index map could be either blue or red depending on the prevalence of spinning dust emission along any given line-of-sight.

The spectral index map has a `HEALPix` resolution of $N_{\rm side} = 128$ (pixel size $\sim$ 27.48 arcmin). The 408 MHz, 12 GHz and *WMAP* 22.8 GHz data maps all have `HEALPix` resolutions of $N_{\rm side} = 512$ (pixel size $\sim$ 6.87 arcmin). For each pixel in the spectral index map the spectral index was derived from the gradient between common pixels in the higher resolution pairs of data maps. An aperture of 0.5 degrees diameter centred on the central coordinate of the pixel within the spectral index map defined the common pixels compared in the data maps. As the data maps are in common brightness temperature units, the spectral index derived from the gradient (A) of the common pixels is defined as:

$$\alpha = \frac{\ln(A)}{\ln(\nu_1/\nu_2)} - 2. \tag{6.21}$$

To minimise the uncertainty of the spectral index map, spectral index pixels associated with apertures that have a mean signal-to-noise ratio less than 5σ in the 12 GHz MFI map were ignored. The MFI 12 GHz map is in units of main beam brightness temperature, and extended emission is being measured in this Section, the MFI wide-survey pixel values were reduced by the beam efficiency factor ($\nu_{\rm mb}$ from Section 3.4). As the aperture size used to compare the pixels is less than a single beam, all the pixel

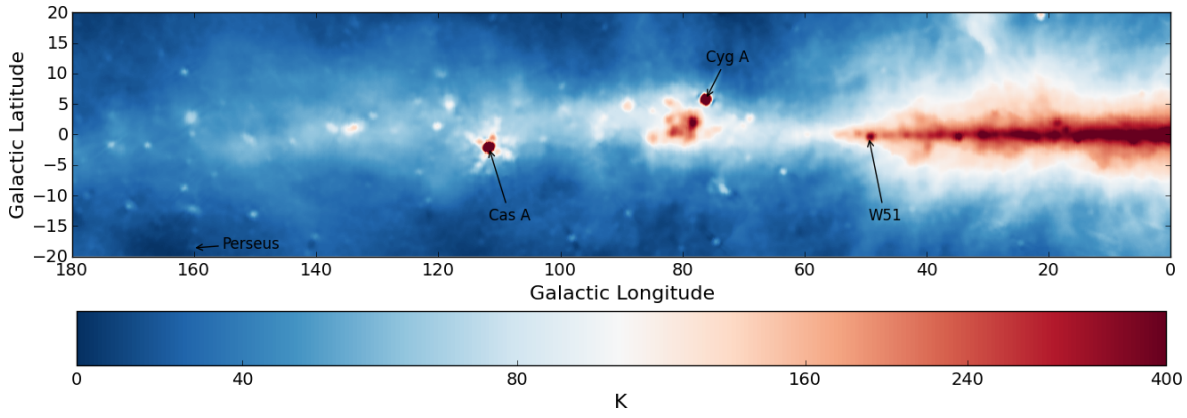

(a)

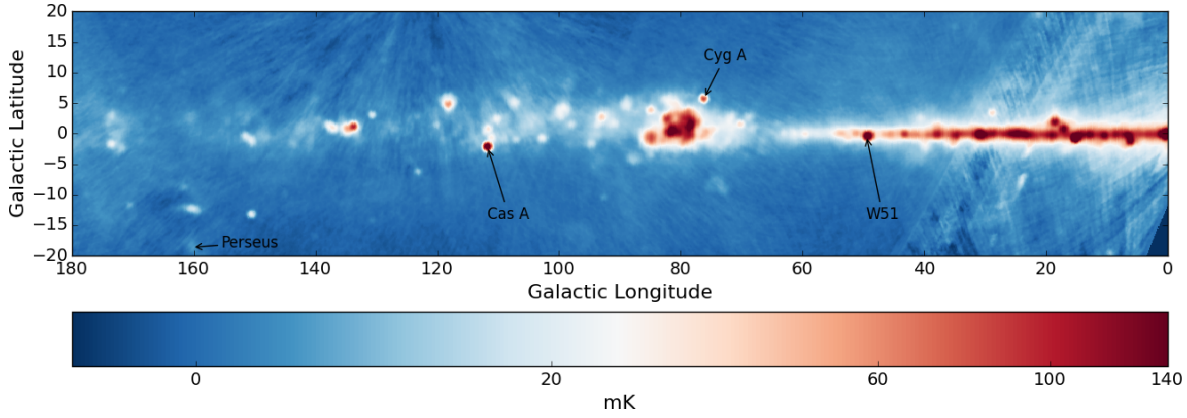

(b)

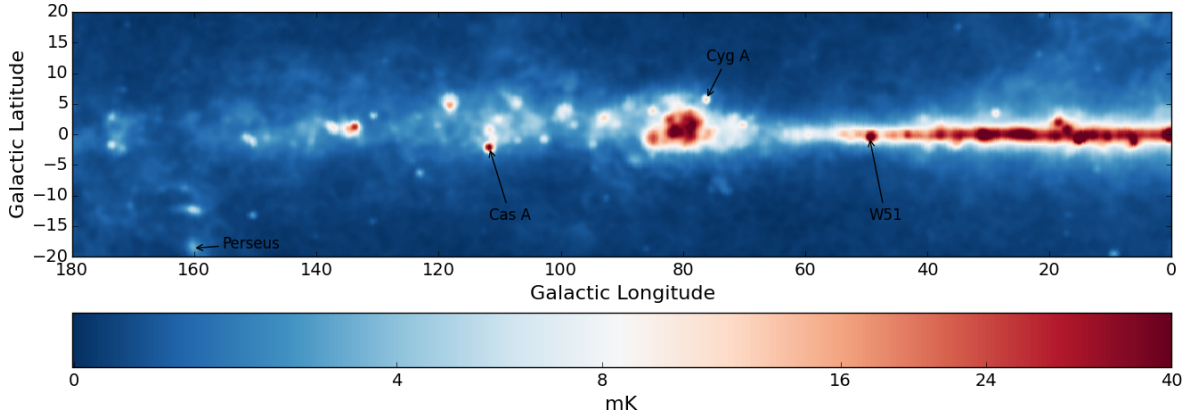

(c)

Figure 6.17: Multi-frequency Cartesian projections of the Galaxy between $0^\circ < l < 180^\circ$ and $|b| < 20^\circ$. Key features such as the Cas A SNR, the Cyg A galaxy, the Perseus molecular cloud and the W51 complex are marked. *Top*: 408 MHz map. *Centre*: 12 GHz MFI map. *Bottom*: *WMAP* 22.8 GHz map.

information will be correlated. In effect, this means that the analysis performed here should give a similar result to simply comparing the spectral indices derived from the ratio of pseudo-independent pixels.

Calibration of the spectral index maps between both frequencies was based upon Tau A ($\alpha \approx -0.3$). Once the maps are calibrated using Tau A, the spectral indices of Cas A and Cyg A were measured as a secondary check of the reliability of the maps. The spectral indices for Cas A and Cyg A in the 408 MHz to 12 GHz spectral index map are -0.85 ± 0.03 and -1.06 ± 0.03 respectively, and in the 12 to 23 GHz spectral map are -0.66 ± 0.07 and -1.07 ± 0.07 respectively. The nominal values for the spectral indices of Cas A and Cyg A are ≈ -0.7 and ≈ -1.2 respectively, which are consistent with those measured in this analysis. Note that due to the correlations between pixels, there is potentially a baseline offset uncertainty that has not been accounted for in this analysis but the effect should be negligible.

The pixels used to generate the spectral index map were chosen such that the signal within a given pixel was $10\,\sigma$ above the background pixel noise level of the maps. Assuming calibration uncertainties of 3 %, 3.7 % and 10 % for the MFI, *WMAP* and Haslam maps respectively, and a maximum of 10 % uncertainty on the mean value within a given pixel, the maximum uncertainty in both spectral index maps can be derived using Equation 6.20. For the Haslam 408 MHz to 12 GHz MFI map the maximum uncertainty is ± 0.009, and for the MFI 12 GHz to 22.8 GHz *WMAP* map the maximum uncertainty is ± 0.018. However, this does not take into account local background variations in either map caused by non-celestial sources. This is especially problematic for the ground-based measurements from MFI and Haslam.

6.5.1 Spectral Index Map: 408 MHz to 12 GHz

Figure 6.18 shows the spectral index map derived from the Haslam et al. (1982) 408 MHz and combined 12 GHz MFI wide-survey maps. The map is dominated by negative (red) spectral indices meaning that the emission at 408 MHz is brighter than the emission at 12 GHz. Along the low Galactic latitudes ($|b| < 1^\circ$), and within the Cygnus region (at longitude $\approx 80^\circ$), the majority of the spectral indices are consistent with diffuse free-free emission illuminated by OB-type stars in star-forming regions (Alves et al., 2012; Planck Collaboration et al., 2015c). For $|b| > 1^\circ$, especially within the inner Galactic disk ($l < 60^\circ$), the spectral indices steepen implying that these

regions are dominated by synchrotron emission and merging, ancient SNRs.

Figure 6.19 shows a histogram of the spectral index distribution for two regions with Galactic latitudes of $|b| < 2^\circ$. One region spans a subsection of the inner Galactic disk between $20^\circ < l < 40^\circ$, and the other spans the entire Galactic plane between $0^\circ < l < 180^\circ$. The distribution of the spectral indices show that the SED of the Galaxy between 408 MHz and 12 GHz is predominantly falling. The median spectral indices within the disk and the whole plane are -0.24 ± 0.03 and -0.15 ± 0.03 respectively. The uncertainties are estimated from Equation 6.20, assuming a total uncertainty of 3.7 % for the MFI and 10 % for the 408 MHz map. The MFI 3.7 % uncertainty includes the calibration uncertainty and colour correction uncertainty.

6.5.2 Spectral Index Map: 12 to 23 GHz

The second spectral index map was derived from the MFI 12 GHz survey and the *WMAP* 22.8 GHz image. A classical view of the Galactic emission over this frequency range would predict that the spectral indices should be negative (red) and that the Galactic plane will still be dominated by free-free and synchrotron emission. Certainly, for the point sources Cas A and Cyg A in Figure 6.20 this is true. However, the spectral index map reveals that within the inner Galactic disk ($l < 60^\circ$), the spectral indices are rising (blue) and only complex star-forming regions such as W51, which contains SNRs, have flat or negative indices. Previous results from C-BASS (Irfan et al., 2015) and *Planck* (Planck Collaboration et al., 2011, 2015c) have already suggested that spinning dust emission contributes between 10 and 50 per cent of the total emission within the inner Galaxy. However, as Figure 6.20 is derived from the direct measurement of the rising spectrum between 12 and 22.8 GHz, it provides definitive evidence for the ubiquity of spinning dust emission throughout the diffuse structures of the inner Galaxy.

The histograms in Figure 6.21 show the distribution of the derived spectral indices for several cuts through the Galactic plane. The top histogram shows a comparison between the distribution of spectral indices between the inner and outer Galactic plane over $0^\circ < l < 180^\circ$ (yellow line) and a region of the inner disk over $20^\circ < l < 40^\circ$ (blue line) for $|b| < 0.5^\circ$. The lines-of-sight associated with the blue line in the top histogram will be referred to as *Region 1*. The median spectral index of Region 1 is found to be 0.17 ± 0.07, whereas the whole plane is consistent with a flat spectral index of 0.01 ± 0.07. The uncertainties assumed are a 3.7 % MFI total uncertainty, and a 3 %

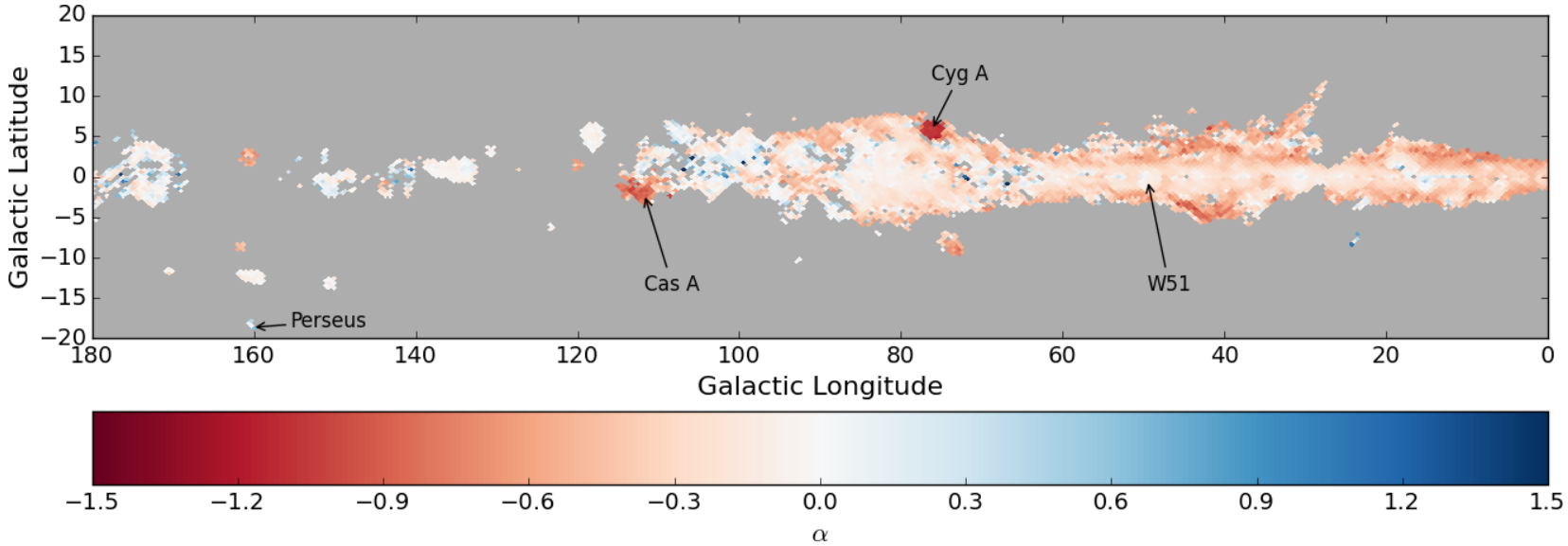

Figure 6.18: Spectral index map between the Haslam et al. (1982) 408 MHz map and the combined 12 GHz MFI wide-survey map. The colour scale shows flux density spectral indices, where red regions are dominated by low frequency synchrotron emission. White regions indicate that the emission between 408 MHz and 12 GHz is flat and blue regions means that the 12 GHz emission dominates. Most regions with rising spectra in this map are also regions with a low signal-to-noise ratio in one of the maps and are considered unreliable.

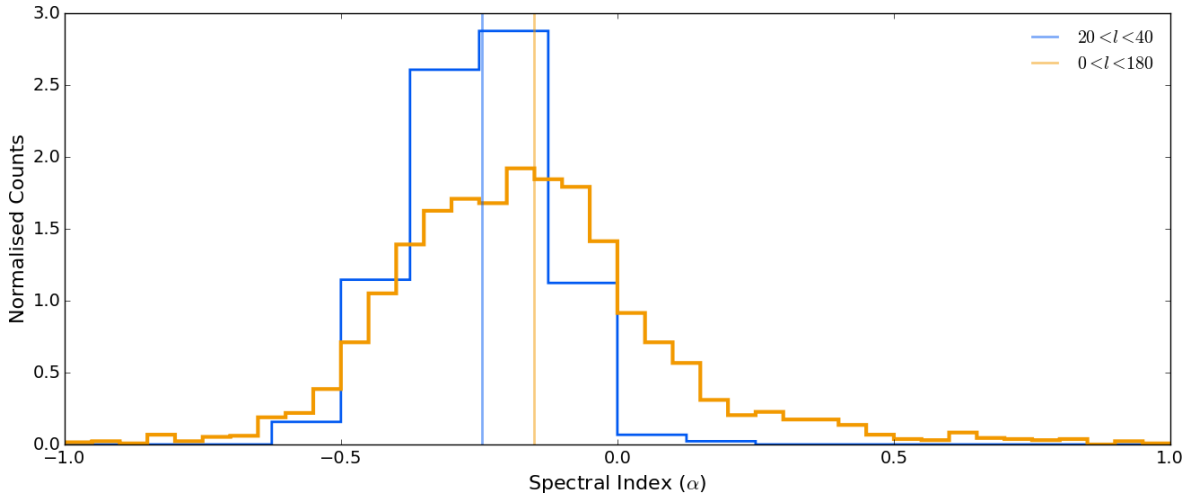

Figure 6.19: Histogram distribution of spectral indices between 408 MHz to 12 GHz for two regions with $|b| < 2°$. The blue histogram is a region of the inner Galactic disk between $20° < l < 40°$. The yellow histogram spans the Galactic plane between $0° < l < 180°$.

total uncertainty in the *WMAP* map. The bottom histogram covers the longitudes $0° < l < 180°$ (yellow line) and $36° < l < 39°$ (the blue line, *Region 2*) for latitudes $|b| < 2°$. The median spectral index in Region 2 is found to be slightly steeper than in Region 1 at 0.24 ± 0.07.

The spinning dust emission fraction at 22.8 and 28.4 GHz have recently been estimated for Region 1 (Planck Collaboration et al., 2015c) and Region 2 (Irfan et al., 2015) described above. The lower limit of the spinning dust fraction in a region can be estimated as

$$\frac{S_{\mathsf{SpDust}}}{S_{\mathrm{Total}}} = 1 - \frac{(\nu_1/\nu_2)^{\alpha_{\mathrm{ff}}}}{(\nu_1/\nu_2)^{\alpha_{\mathrm{tot}}}}, \tag{6.22}$$

where α_{tot} is the measured spectral index of a region and α_{ff} is the spectral index of free-free emission (-0.1). This simple estimate assumes that the contribution from synchrotron emission between ν_1 and ν_2 is negligible. For Region 1, Planck Collaboration et al. (2015c) estimated the fractional spinning dust emission contribution at 28.4 GHz using SED model fitting, as 0.47. Using Equation 6.22 and the measured median spectral index of Region 1, the spinning dust emission fraction is found to be 0.21 ± 0.02 at 23 GHz. For Region 2, Irfan et al. (2015) found a fractional contribution of 0.38 and the MFI found a fraction of 0.25 ± 0.03 at 23 GHz. For comparison, Planck Collaboration et al. (2011) estimated a contribution fraction of 0.25 ± 0.05 for the entire Galactic plane.

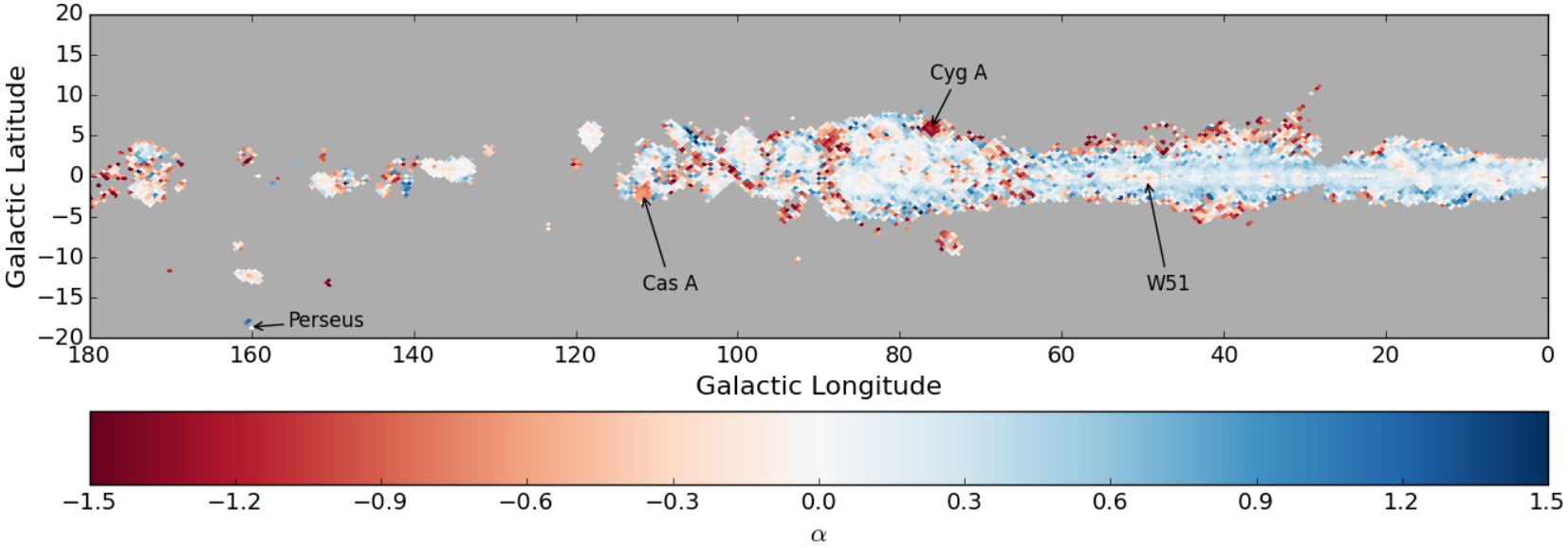

Figure 6.20: Spectral index map between the *WMAP* 22.8 GHz map and the combined 12 GHz MFI wide-survey map. The colour scale shows flux density spectral indices, where red regions are dominated by free-free or synchrotron emission. Whilst blue and white regions indicate that another emission is increasing the spectral index. This positive spectral emission mechanism is expected to be due to diffuse spinning dust emission in the ISM.

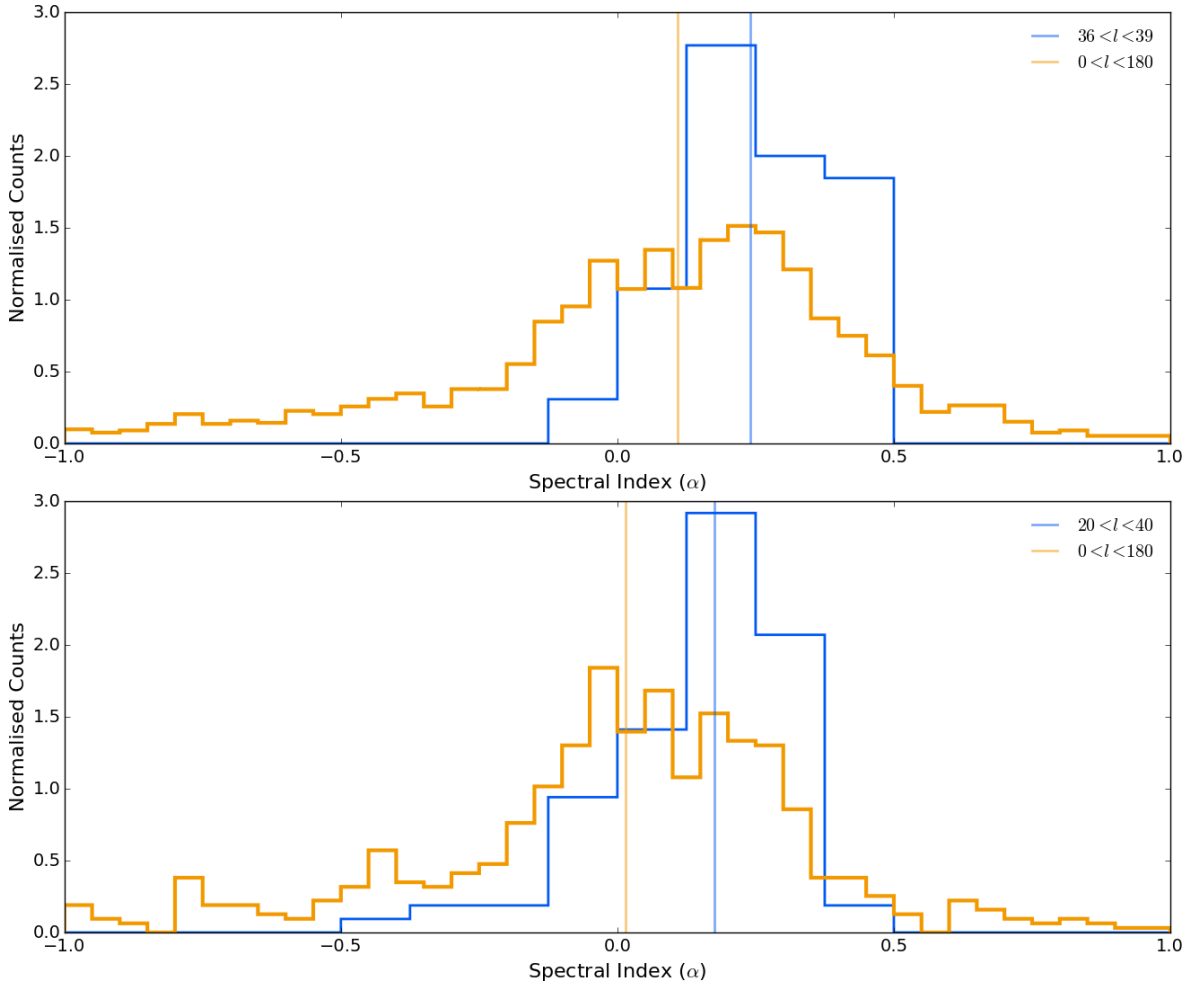

Figure 6.21: Histograms of spectral indices for four regions of the Galactic plane. *Top*: Galactic latitudes of $|b| < 0.5^\circ$, for $0^\circ < l < 180^\circ$ (the yellow line) and $20^\circ < l < 40^\circ$ (the blue line, *Region 1*). *Bottom*: Galactic latitudes of $|b| < 2^\circ$, for $0^\circ < l < 180^\circ$ (the yellow line) and $36^\circ < l < 39^\circ$ (the blue line, *Region 2*).

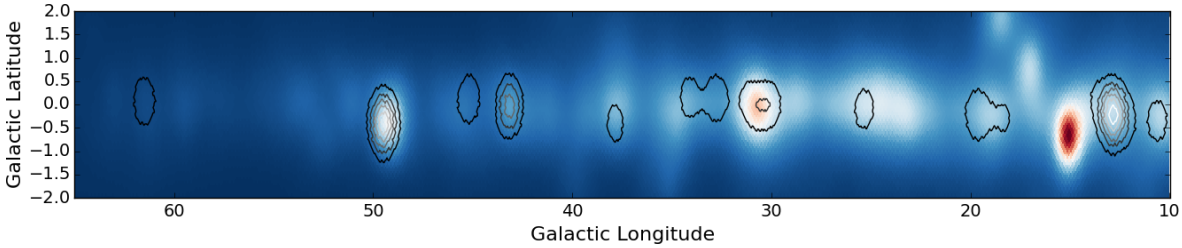

Figure 6.22: Cutout of the Galactic plane over the range $10^\circ < l < 65^\circ$ and $|b| < 5^\circ$. The image is 22.8 GHz *WMAP* data and the contours are the integrated UCHII emission measured at 5 GHz by the VLA in the CORNISH survey convolved to 1 degree.

6.5.3 UCHII Regions

The CORNISH (Co-ordinated Radio 'N' Infrared Survey for High Mass Star Formation) VLA 5 GHz source catalogue was used to estimate the integrated flux density contribution of the UCHII regions (Hoare et al., 2012; Purcell et al., 2013). The CORNISH survey covers $10^\circ < l < 65^\circ$ degrees and $|b| < 1^\circ$ degree. The CORNISH survey is ideal for estimating the flux density contribution of UCHII regions because it has a very high angular resolution compared to the survey maps used in this Section. This means that the CORNISH survey can isolate individual UCHII regions from the extended diffuse emission of the Galaxy. The flux density of each UCHII region was binned into a `HEALPix` map and smoothed with a 1 degree beam. The smoothed UCHII map was then extrapolated with an unrealistically pessimistic model that assumed that the UCHII regions remained optically thick with a rising power spectrum of +2 up to 23 GHz. In reality, most UCHII regions are optically thin (have a flat spectrum) at 15 GHz or above (Kurtz et al., 1994). Figure 6.22 shows the smoothed UCHII map overlaid onto the *WMAP* 22.8 GHz image for the area covered by the CORNISH survey. The UCHII contribution when using a very pessimistic model was found to be less than 50 % of the emission even for regions with dense UCHII clustering, as for W51 seen at $l \approx 30^\circ$ and $b \approx 0^\circ$. For most of the diffuse Galactic emission, UCHII regions were considered to provide a negligible contribution to the total integrated emission within the uncertainties of this analysis and could be safely ignored.

6.5.4 Discussion

This Section has shown the distribution of the spectral indices within the Galactic plane. Before these observations, the prevalence of spinning dust emission within the

inner Galactic disk relied upon inference from parametric SED fitting (Planck Collaboration et al., 2015d) or simple extrapolation of the free-free continuum emission to higher frequencies (e.g., Irfan et al., 2015). However, this Section has shown through direct measurements that the emission between 13 and 23 GHz is rising, a finding that cannot be explained by the integration of UCHII regions. The median spectral index within the disk was found to be 0.24 ± 0.07 for latitudes $|b| < 2^\circ$, which corresponds to a spinning dust emission contributing of 25 ± 3 per cent of the total emission within the inner Galaxy. Interestingly, a gradient in spectral index is seen, with spinning dust contributing more at higher Galactic latitudes, away from the narrow Galactic disk at $|b| < 1^\circ$.

The Cygnus region ($l \approx 80$) is also a particularly interesting feature in Figure 6.20. Careful visual inspection of the figure reveals that there are structures with decreasing spectral indices within the region. These regions are found to correspond to known star forming regions, or SNRs, within Cygnus. The figure shows that the diffuse emission between these structures have rising spectral indices, implying that significant spinning dust emission may be occurring in the intervening medium.

6.6 Summary

In this Chapter, the MFI wide-survey total intensity maps have been presented for the first time. A simple analysis of the data efficiency and data integrity of the maps was performed. The high frequency MFI wide-survey maps were found to be contaminated significantly by both unidentified calibration uncertainties and high levels of *1/f* noise, therefore limiting the applicability of the 17 and 19 GHz wide-survey maps. However, the low frequency MFI wide-survey maps were found to have calibration uncertainties between 2 and 3 per cent, which is sufficient for comparison with existing multifrequency observations of Galactic continuum emission.

The MFI was used in combination with *Planck*, *WMAP*, *COBE* and 408 MHz data to investigate four spinning dust emission regions. The first region to be investigated was the Perseus molecular cloud, which is a very well known spinning dust emission source. The MFI wide-survey observations at 11 and 13 GHz, along with the fitted spinning dust model parameters were found to be consistent with those already found in the literature. This was an important test of both the MFI wide-survey maps and the SED fitting method. Other regions investigated included the HII complex

W40, LDN 1622 and LDN 1582/84. Of these LDN 1622 and LDN 1582 had $9\,\sigma$ and $5\,\sigma$ detections of spinning dust emission within each region. W40 however appears to be too dominated by free-free emission on large-scales within the complex to be able to reliably measure the spinning dust component. Comparisons were made between LDN 1582/84 and the ring-like structure within the Perseus molecular cloud. This indicated that LDN 1582/84 and the ring of dust that surrounding λ-Orionis may be an ideal environment for the study of spinning dust emission. From the three brightest spinning dust regions (Perseus, LDN 1622 and LDN 1582/84), the weighted mean of the spinning dust peak frequency was found to be $\langle \nu_{\rm sp} \rangle = 27.2 \pm 0.7\,{\rm GHz}$. The weighted mean of the ratio of the spinning dust peak brightness over the $250\,\mu$m dust opacity was $\langle A_{\rm sp}/\tau_{250} \rangle = 1.24 \pm 0.18 \times 10^4\,{\rm Jy}/\tau_{250}$.

In the final Section of this Chapter the large-scale structure of spinning dust within the Galaxy at low latitudes was investigated. From the direct measurement of the rising spectral index between 12 and 23 GHz it was inferred that the inner Galactic disk has a 25 ± 3 per cent contribution to the total integrated flux density from spinning dust emission at 22.8 GHz. This result is consistent with, and thus confirms, previous estimates of 10 and 50 per cent of the integrated flux density of inner Galaxy is due to spinning dust emission.

Chapter 7

GBT Observations of LDN 1622

> "To my surprise these pictures showed an enormous curved nebulosity encircling the belt and the great nebula of Orion, and covering a large portion of the body of the giant."
>
> Barnard (1894)

The *enormous curved nebulosity* that is being remarked upon by Barnard can be seen in optical images of the Orion region as shown in Figure 7.1. The snaking red arc protruding from the *South* of the image up towards the *West* is a region of warm plasma, illuminated by the Orion B OB1b-stellar association (Kun et al., 2008). Today the curved nebulosity bares the name Barnard's loop. *North-East* of Barnard's Loop is a small dark, structure with an angular extent of ≈ 10 arcmin. This structure is the focus of this Chapter and is known as Lynds dark cloud LDN 1622.

The 100 m Robert C. Byrd Green Bank Telescope (GBT) was used to observe LDN 1622 at 5 and 13.7 GHz with arcminute resolution. The general structure of this Chapter will be presented in a similar way to this thesis as a whole. Beginning with a discussion of the GBT observations and calibration procedures. Followed by a presentation of the GBT maps, discussion of ancillary datasets and finally interpretation of the observations in regards to spinning dust emission within LDN 1622.

7.1 Overview of LDN 1622

In the previous Chapter, the integrated flux density SED of LDN 1622 and surrounding ISM was parametrically-fitted using the 1 degree resolution maps of the QUIJOTE MFI

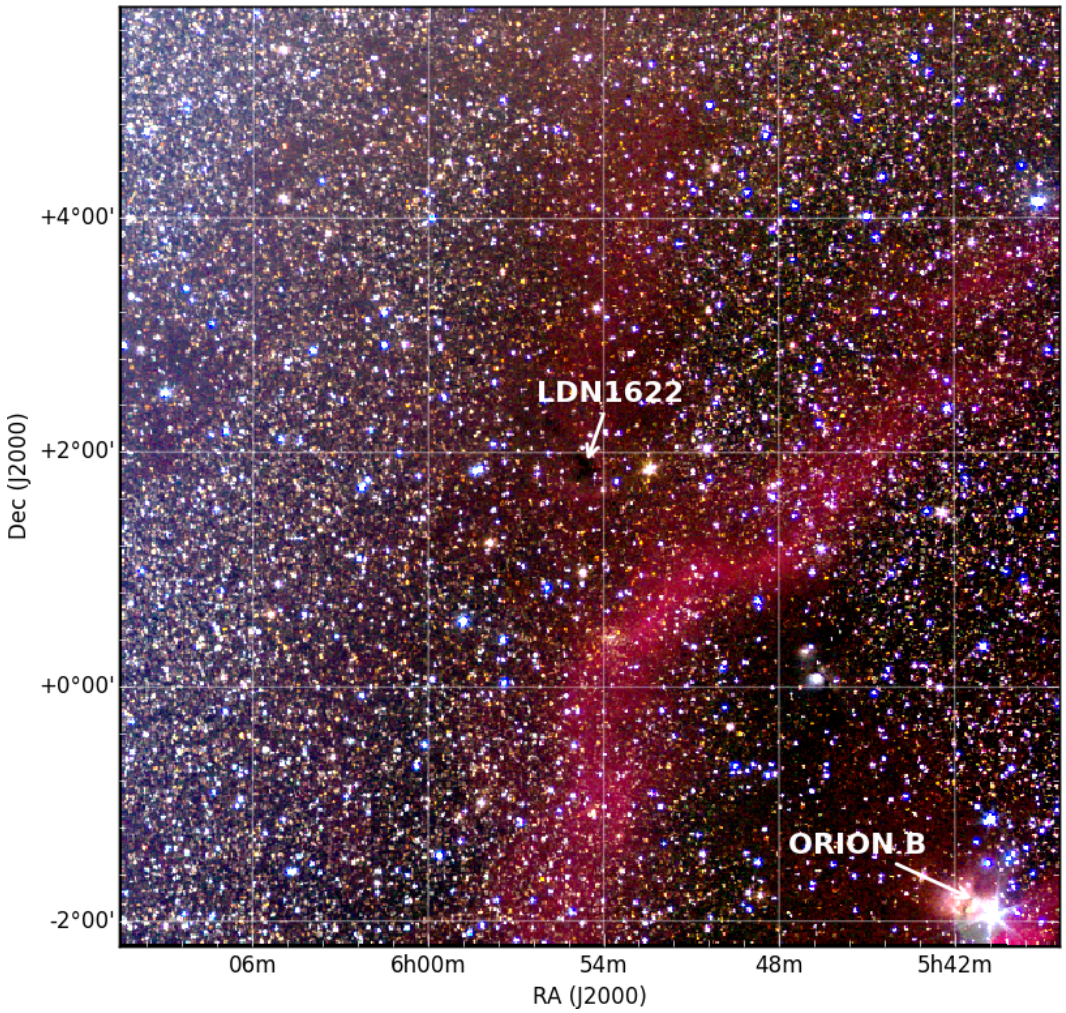

Figure 7.1: A composite *RGB* optical image of the Orion region centred on LDN 1622 taken from the all-sky panorama by Mellinger (2009). The reddish hue of the warm, ionised plasma in Barnard's loop can be seen arching from the *South* of the image. A second, fainter region of diffuse HII can be also be seen filling the background behind LDN 1622.

11 and 13 GHz wide-survey and all-sky, multi-frequencies surveys by *Planck*, *WMAP* and *COBE*. The results of the last Chapter imply that there may some spinning dust emission in LDN 1622 but the bright free-free emission behind LDN 1622 (seen as the faint red haze in Figure 7.1) makes isolating the spinning dust emission challenging. This agrees with Planck Collaboration Int. XV (2014) that found an 8σ detection of spinning dust emission on scales of ≈ 2 degrees around LDN 1622. The first tentative indication that LDN 1622 may be a spinning dust emission source came from half a degree resolution observations at 5 to 10 GHz with the 140 ft Green Bank Telescope (GB6) by Finkbeiner et al. (2002). Later $\sim$ 8 arcmin resolution CBI observations by Casassus et al. (2006) found tight correlations between the 12 μm dust emission originating from the *photodissociation region* (PDR) that surrounds the *South* and *West* sides of LDN 1622, and the observed emission at 31 GHz. This was highly suggestive that the spinning dust carriers are PAH molecules.

This Chapter presents the first arcminute-resolution, single-dish radio telescope, extended-mapping observations of a Lynds dark cloud. The goal of this Chapter is to quantify the free-free emission within the PDR of LDN 1622 at 5 GHz and ascertain the origin of the radio-infrared correlations seen by Casassus et al. (2006).

7.2 GBT 100 m Observations

The GBT is a 100 m diameter fully-steerable single-dish radio telescope that operates at frequencies less than 100 GHz. The observations were taken over several days in January 2007 and one extra observation was made the following year in January 2008. Both sets of observations were proposed and observed by Clive Dickinson and Kieron Cleary. The observed time on source at 5 GHz was 5 hours, and 7.5 hours at 13.7 GHz.

Observations were made at two frequencies: 4.85 GHz (C-band) and 13.7 GHz (Ku-band). Both C-band and Ku-band observations used the Digital Continuum Receiver (DCR) on the GBT. The observations used all the 16 frequency channels available to the DCR for each frequency, providing a bandwidth of 1.28 GHz at C-band and 3.5 GHz at Ku-band. The sample integration time was 0.2 seconds. The C-band receiver has a single beam with a Full-Width Half-Max (FWHM) resolution of 2.6 arcmin at 4.85 GHz. At Ku-band the GBT has two receivers with independent beams, both with a FWHM resolution at 13.7 GHz of 55 arcsec. One receiver is located in the central focal position

of the GBT and will be referred to hereafter as the central beam. The other Ku-band receiver is displaced by 330 arcsec in the positive azimuth direction and will be referred to as the off-centre beam. Both C-band and Ku-band operated in dual polarisation mode, measuring left (LL) and right (RR) circularly polarised radiation simultaneously. It was assumed that the emission from LDN 1622 would have negligible circular polarisation, therefore total intensity could be obtained by averaging together the LL and RR data.

On-The-Fly (OTF) mapping was used to scan across the regions in Right Ascension and Declination, at a speed on the sky of $1\,\mathrm{arcmin\,s^{-1}}$. This resulted in a series of nested scans across both regions. The C-band observations mapped a region of 35 arcmin × 35 arcmin centred on LDN 1622 at Right Ascension = $5^{\mathrm{h}}54^{\mathrm{m}}29^{\mathrm{s}}$, Declination = $1^{\circ}45'36''$. The Ku-band observations mapped a 12 arcmin × 12 arcmin sub-region of LDN 1622 centred on Right Ascension = $5^{\mathrm{h}}54^{\mathrm{m}}16^{\mathrm{s}}$ and Declination = $1^{\circ}49'52''$. To obtain the desired total integration time per beam in the final map, multiple scans of the same region were made. By observing in this way using OTF mapping, instead of integrating each beam using a pointed observation, the effect of long timescale correlated *1/f* noise caused by the atmosphere or receivers were minimised.

The theoretical thermal noise of the receiver is given by (GBT Proposers Guide, 2015):

$$\left(\frac{\sigma}{\mathrm{mK}}\right) = \frac{44.2}{\mu} \frac{\left(\frac{T_{\mathrm{sys}}}{\mathrm{K}}\right)}{\sqrt{\left(\frac{\Delta\nu}{\mathrm{GHz}}\right)\left(\frac{\tau}{\mathrm{sec}}\right)}}, \tag{7.1}$$

where T_{sys} is the measured system temperature, $\Delta\nu$ is the bandwidth of the receiver, τ is the sample integration time and μ is the aperture efficiency. The aperture efficiency for C-band was 75 % and for Ku-band 72 %. The theoretical noise levels were 2.34 mK and 2.1 mK for C-band and Ku-band respectively. The median measured noise level in the TOD for C-Band was 16.8 mK and for Ku-band was 13.0 mK.

7.3 GBT Calibration

The internal noise diode of the receiver, with a known equivalent antenna temperature for each receiver (T_{cal}), was used to calibrate the TOD into units of brightness temperature using the following equation:

$$T_b = \frac{T_{\mathrm{cal}}}{2} \frac{V_{\mathrm{on}} + V_{\mathrm{off}}}{\langle V_{\mathrm{on}} - V_{\mathrm{off}} \rangle} - \frac{T_{\mathrm{cal}}}{2}. \tag{7.2}$$

The angular brackets here indicate a time average over each scan. The noise calibration diode was injected into every other sample in the TOD at a frequency of 5 Hz. $V_{\rm on}$ describes the receiver voltage when the noise diode was on and $V_{\rm off}$ describes the receiver voltage when the noise diode was off.

To check the diode calibration, the flux densities of 3C161, 3C48 and 3C147 were measured at the beginning and half-way through each observing session. The measured flux densities based on the diode calibration were then compared to the predicted flux densities from the source models described in Ott et al. (1994). The flux densities of 3C161, 3C48 and 3C147 measured at C-band and Ku-band after calibrating with the diode were all found to be within 5 % of the predicted flux densities.

The opacity of the atmosphere at radio wavelengths is dependent on the water vapour content of the air and the elevation of the observation. Over the several days of observing the relative humidity varied considerably, between 0 % and 90 %, and the elevation of the observations varied by 10 degrees. Measurements of zenith opacity from weather stations near to the GBT were used to estimate the effect of atmospheric opacity on the data. The maximum attenuation was estimated to be <0.05 % and <2.6 % for C-band and Ku-band. As these corrections are much less than the flux density calibration accuracy, no atmospheric absorption corrections were applied to either C-band or Ku-band.

As discussed in Section 4.3 RFI from GSO satellites is a serious problem at Ku-band frequencies. At C-band frequencies a significant RFI contamination can be ground-based radar antennas. Both of these sources of RFI are far brighter than any astronomical sources and therefore contaminated scans had to be carefully identified and removed. The criteria for a scan to be considered RFI contaminated was that it contained a source more than 20 times brighter than the receiver thermal noise level.

As with the QUIJOTE MFI observations, the GBT observations also suffered from correlated baseline instabilities known as *1/f* noise (see Section 3.2 for more discussion on *1/f* noise). The effect of *1/f* noise on astronomical signal was reduced in two ways. First, by slewing the telescope as fast as possible, this shifts the astronomical signal to higher temporal frequencies below the receiver *1/f* knee frequency. Second, the maximum-likelihood (ML) map-maker described in Chapter 5 was used to minimise any remaining *1/f* contamination.

For some scans the *1/f* noise contamination was considered too high for the TOD to be useful. These scans were identified during data processing and removed. The

ratio between the variance of pairs of data separated by two different lags was used as the metric to determine the *1/f* contamination of a scan. The variance σ_τ^2 of a scan can be estimated from the variance of differenced sample pairs separated by a timescale of τ using,

$$\sigma_\tau^2 = \frac{1}{2}\frac{\sum_{i=0}^{N-\tau}(d_{i+\tau} - d_i)^2}{N-\tau}, \tag{7.3}$$

where d_i and $d_{i+\tau}$ are the sample TOD at time i and time $i+\tau$, respectively. N is the length of the TOD. The median knee frequency of the data was found to be $\approx 0.7\,\mathrm{Hz}$, which corresponds to a timescale of $\tau = 1.4\,\mathrm{seconds}$. Differencing the TOD on shorter timescales reduces the *1/f* noise contribution to the total noise of the TOD. The estimate of the thermal white-noise level of the TOD was determined from the variance of pairs differenced by $\tau = 0.2\,\mathrm{seconds}$ (1 sample). An estimator for the TOD *1/f* contribution was determined from a differenced TOD with a lag of $\tau = 1.0\,\mathrm{seconds}$, which is slightly shorter than the median *1/f* timescale. Therefore the variance of the lagged differenced TOD would only deviate from the white-noise variance for scans with a high *1/f* contribution. The ratio between the lagged differenced, TOD standard deviation and the white-noise limit was measured for each scan as

$$R = \frac{\sigma_\tau}{\sigma_W}. \tag{7.4}$$

The metric R defines the ratio of the lagged, differenced TOD standard deviation (σ_τ) and the white noise limit (σ_W). If a scan exceeded a cut-off value for R it was discarded. Many different cut-off values for R were used to generate difference maps of the data. The optimal cut-off for R was determined when the noise in the difference maps was at a minimum. A value of $R = 2.3$ minimised the noise in the difference maps at both frequencies. For C-band and Ku-band, 50 % and 14 % of the scans exceeded the $R = 2.3$ maximum cut-off noise variance ratio and were removed.

A summary of the observations and map noise limits is given in Table 7.1.

7.4 Description of Ancillary Data

This Section will discuss all the existing ancillary data at radio, IR and optical frequencies used in conjunction with the GBT C-band and Ku-band data. These datasets will be used in Sections 7.6, 7.6.1 and 7.6.2 to analyse LDN 1622.

Table 7.1: Receiver and observational properties of the 4.85 GHz (C-band) and 13.7 GHz (Ku-band) datasets.

Central Frequency (GHz)	4.85	13.7
Bandwidth (GHz)	1.28	3.5
No. Beams	1	2
Back end	DCR	DCR
Observing mode	On-The-Fly	On-The-Fly
Hours Observed (Hours)	5	7.5
Beam (FWHM)	2.6 arcmin	55 arcsec
Smoothed Beam (FWHM)	3 arcmin	1.2 arcmin
Sky scan speed (arcmin s^{-1})	1	0.5
Data Flagged (percent)	50	14
Map Noise (mJy $beam^{-1}$)	4.3	5.5
Confusion limit (mJy $beam^{-1}$)	≈ 0.45	≈ 0.03
Map Noise (mK)	2.5	2.5
Confusion limit (mK)	≈ 0.9	≈ 0.05
Field Width (arcmin)	35	12

Ancillary interferometric radio data at 15.7 GHz was provided by the Arcminute Microkelvin Imager (Yvette Perrot, private communication; Zwart et al., 2008, AMI). The AMI Small Array (SA) consists of 10 3.7 m diameter dishes. The AMI SA has baseline spacings between $5 - 20$ m and a synthesised beam of 3 arcmin.

FIR observations were obtained from publicly available archival ESA *Herschel* Space Observatory (Pilbratt et al., 2010) data. The archival data were SPIRE (Griffin et al., 2010) and PACS (Poglitsch et al., 2010) photometry of Orion B at 500 μm, 350 μm, 250 μm and 160 μm. The FWHM resolutions of each band were approximately: 35.2 arcsec, 23.9 arcsec, 17.6 arcsec and 11.7 arcsec. The SPIRE and PACS observations were made in parallel mode with observation identification numbers OBSID: 1342205074 and OBSID: 1342205075. The *Herschel* maps were reduced using the `SPG` v11.1.0 pipeline. For the PACS data, the level 2.5 `MadMap` products were used. The SPIRE level 2 products with an absolute background correction applied from *Planck* data were used. PACS 70 μm data were also available but were not used because of poor signal-to-noise.

MIR data were provided by the Wide-field Infrared Sky Explorer (Wright et al., 2010, *WISE*). This Chapter only uses the 22 μm and 12 μm observations and not the

higher frequency bands in order to reduce the number of point sources contaminating the field. The FWHM resolution of the *WISE* 22 μm map is 12 arcsec and the *WISE* 12 μm map is 7.4 arcsec.

An archival Spitzer IRAC (Fazio et al., 2004) map of LDN 1622 at 8 μm was used to supplement the *WISE* MIR data. Point sources from the *Spitzer* map were subtracted. The IRAC 8 μm map has a FWHM resolution of $\approx$1.98 arcsec.

Optical Hα data of LDN 1622 were taken from the Southern H-Alpha Sky Survey Atlas (Gaustad et al., 2001, SHASSA). The SHASSA Hα data serves as a tracer for the free-free emission seen at C-band (e.g., Dickinson et al., 2003). The SHASSA map has a FWHM resolution of 0.8 arcmin and can detect sources down to the level of $\approx$2 Rayleigh. The SHASSA continuum-subtracted maps contain numerous stellar artefacts around poorly subtracted bright sources. However, no significant stellar artefact contamination of the Hα emission observed around LDN 1622 was visible.

7.5 GBT Maps

The GBT maps at both frequencies were processed using the ML map-making method and implementation outlined in Chapter 5.

Figure 7.2 presents the final C-band and Ku-band ML maps, both unsmoothed and smoothed. The unsmoothed C-band map has a FWHM resolution of 2.6 arcmin. The map pixel size for the C-band map is 57.6 arcsec, ensuring 2.7 pixels across a beam. The pixel size was chosen to maintain Nyquist sampling across the field. The noise in the C-band map was estimated from differencing the RR and LL polarisation maps. The difference map should contain only the white noise and residual receiver *1/f* noise. To avoid the higher noise towards the edge of the C-band map, the noise was estimated from a 20 arcmin diameter aperture in the centre of the difference map. The pixel noise within the aperture was measured to be 2.5 mK (i.e. 4.3 mJy beam^{-1}).

The Ku-band map is shown alongside the C-band map in Figure 7.2. The original resolution of the Ku-band map was 55 arcsec FWHM and the map has 2.7 pixels per beam FWHM with a pixel size of 20.5 arcsec. As with the C-band map, the pixel size was chosen to ensure Nyquist sampling across the map. The Ku-band map combines data from a central beam and an off-centre beam. The off-centre beam, which is displaced by 330 arcsec in azimuth from focal centre, observed a larger region than the central beam as the observations were made at several different Hour Angles. The

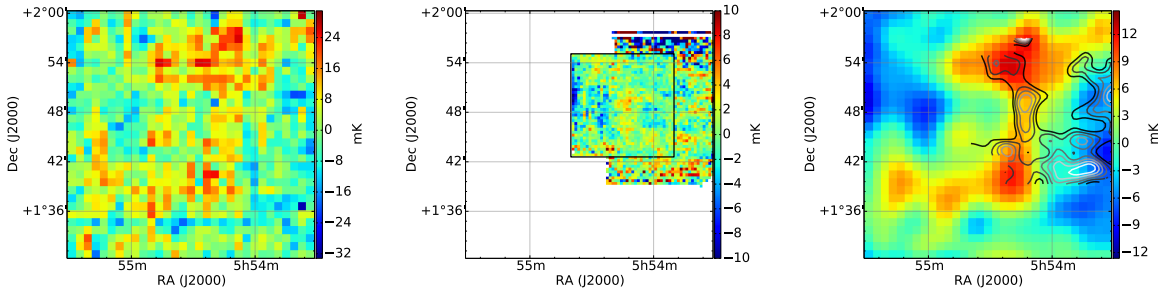

Figure 7.2: Final C-band and Ku-band maps as generated by the ML map-making method. The images are centred at Right Ascension = $5^{\mathrm{h}}54^{\mathrm{m}}29^{\mathrm{s}}$, Declination = $1^{\circ}45'36''$ with dimensions 30 arcmin × 30 arcmin. *Left*: C-band map at the original 2.6 arcmin FWHM resolution. *Centre*: Ku-band map at the original 55 arcsec FWHM resolution. The black box marks the extent of the area observed by the central beam. *Right*: Overlay of smoothed Ku-band map contours on the smoothed C-band map. The contour levels are 0.1, 0.45, 0.8, 1.15, 1.5 and 1.85 mJy beam^{-1} for a 1.2 arcmin beam.

region observed by both beams is marked in Figures 7.2 and 7.3 with a box. For this reason the area outside the marked box has far lower sampling and higher noise than the region of the map enclosed within the box, which was observed by both beams. To avoid the regions of high noise within the Ku-band map the noise in the map was measured from a RR and LL difference map inside an aperture of 6 arcmin diameter centred on the Ku-band source marked in Figure 7.3. The noise was found to be 2.5 mK (i.e. 5.5 mJy beam^{-1}).

The right panel of Figure 7.2 also shows smoothed contours of the Ku-band map overlaid onto a smoothed C-band map. The Ku-band map was smoothed to 1.2 arcmin FWHM resolution and the C-band map was smoothed to 3 arcmin FWHM resolution. The smoothing kernel for both GBT maps was chosen to increase signal-to-noise while retaining the structure of the emission within the field. The noise level of the smoothed C-band map is 1.7 mK (i.e. 2.9 mJy beam^{-1}) and the noise level of the smoothed Ku-band map is 0.8 mK (i.e. 1.8 mJy beam^{-1}).

7.6 Comparison with Multi-Frequency Data

In Figure 7.3 the smoothed C-band and Ku-band maps are shown alongside ancillary maps of LDN 1622.

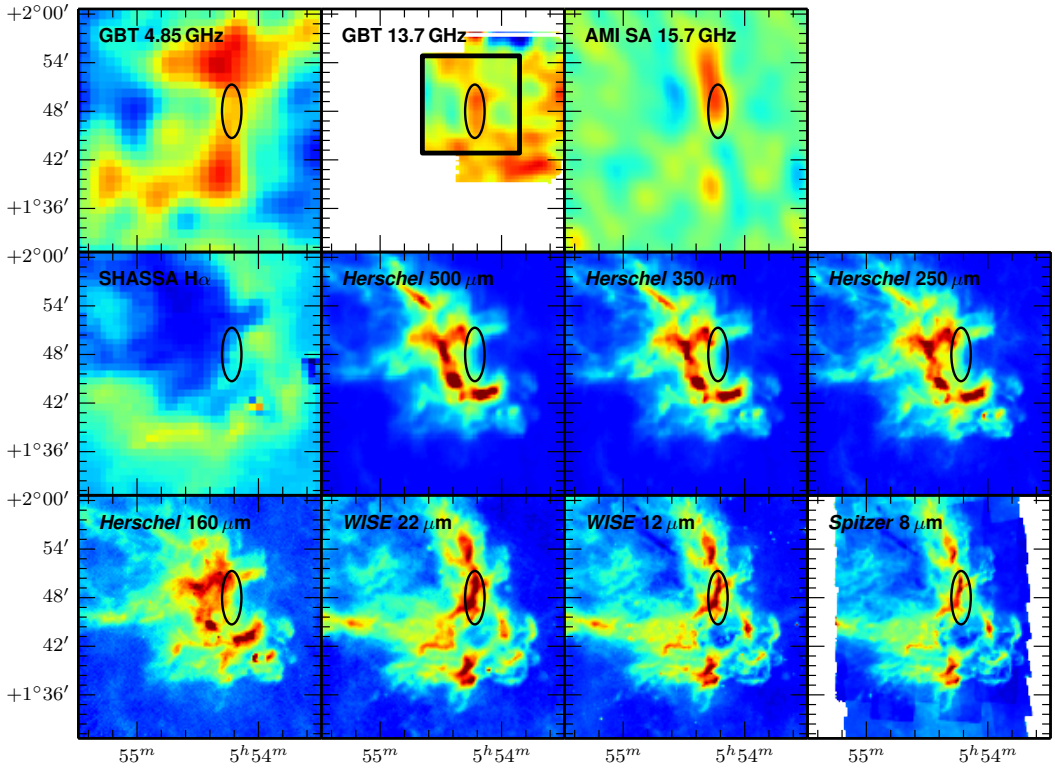

Figure 7.3: Maps of LDN 1622 from GBT C-band and Ku-band observations and ancillary data. Each image is centred at Right Ascension = $5^{\rm h}54^{\rm m}29^{\rm s}$, Declination = $1°45'36''$ with dimensions of 30 arcmin×30 arcmin. The elliptical aperture in each map marks the peak in Ku-band emission. A box surrounds the region observed by the central Ku-band beam in the Ku-band map. From the *top left* to the *bottom right* the images are: GBT C-band 4.85 GHz smoothed to a 3 arcmin beam and Ku-band 13.7 GHz smoothed to a 1.2 arcmin beam; AMI 15.7 GHz Small Array; SHASSA Hα; *Herschel* SPIRE 500 μm, 350 μm and 250 μm; *Herschel* PACS 160 μm; *WISE* 22 μm and 12 μm; *Spitzer* IRAC 8 μm.

A corona of C-band free-free emission in Figure 7.3 encloses LDN 1622, which spans from the *South-East* to the *North-West*, and arches towards the *South-West* corner of the map. Hα emission, a known tracer of free-free (e.g., Dickinson et al., 2003), is also present as a corona of emission that traces the morphology of the similar corona seen at C-band. A key feature in the C-band and Hα maps is the Southern bar that spans the cloud *East* to *West*. This feature correlates quite well between the C-band and Hα maps. The rest of the corona shows significant differences in morphology between the Hα and C-band emission, which can be mostly attributed to dust absorption of the Hα emission. Corrections for dust absorption are discussed in more detail in Section 7.6.1.

The corona, seen as both free-free and Hα emission, is likely associated with warm HII gas within the PDR around LDN 1622. The PDR around LDN 1622 is a transitional region, where on the Western side, gas and dust are heated and ionised by far ultraviolet (FUV) radiation. Progressing Eastward the FUV flux is absorbed and the gas and dust eventually cool into the atomic and molecular phases (Hollenbach and Tielens, 1999). The FIR and MIR structures shown in the *Herschel*, *WISE* and *Spitzer* maps around the aperture marked in Figure 7.3 clearly show the separate stages occurring within the PDR. The MIR maps are tracing the emission from the warm VSGs, which are mixed with the ionised HII gas, as shown by the C-band data, and are exposed to the ionising interstellar radiation field. PDRs are environments rich in PAH molecules that have emission lines which lie within the passbands of the *WISE* 12 μm and *Spitzer* 8 μm maps (Tielens, 2008). At longer wavelengths, such as in the FIR *Herschel* maps, the maps trace the location of cooler dust. Cooler dust is located in clumps near the core of LDN 1622 where it is shielded from the interstellar radiation field and is in thermal equilibrium with the environment.

In the smoothed Ku-band map, an elongated structure can be seen running *North-South* through the marked aperture in Figure 7.3. The location of this aperture coincides with the peak in emission seen at 31 GHz by CBI (Casassus et al., 2006). The weak emission from the elongated structure at Ku-band is also clearly visible in the AMI 15.7 GHz SA map, also shown in Figure 7.3. Comparing the Ku-band map with the MIR maps reveals a shared morphology in the region of the aperture. The correlations between the MIR and Ku-band maps implies a possible common source. The spinning dust model provides a possible explanation for the shared MIR and Ku-band morphology as it provides a mechanism for PAH molecules to emit at the Ku-band frequency (Ali-Haïmoud et al., 2009; Ysard et al., 2010). A more detailed discussion

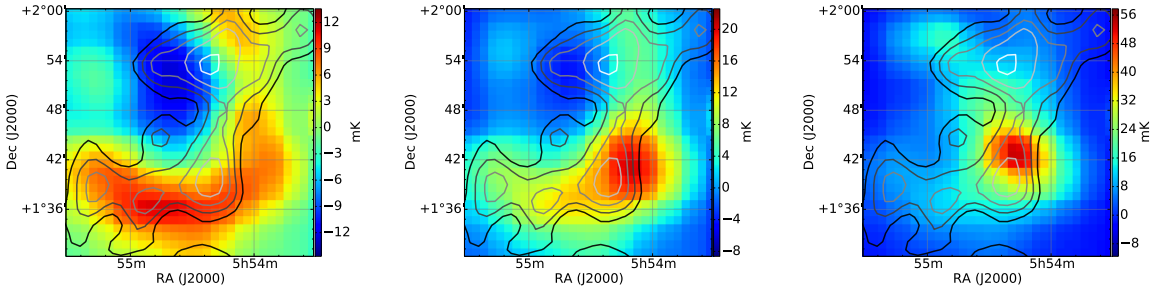

Figure 7.4: Overlay of smoothed C-band contours on Hα derived free-free maps assuming an electron temperature of 7000 K. The contour levels are 1, 3.75, 6.5, 9.25 and 12 in units of mK. The dust mixing fraction for each map from *left* to *right* is: f =0.1, 0.5 and 1.0.

of the Ku-band emission and its correlations with IR and radio emission can be found in Section 7.6.2.

Note that a bright young stellar object (YSO) at Right Ascension = $5^{\rm h}54^{\rm m}24.3^{\rm s}$ and Declination = $1^{\circ}44'19''$ was removed from the FIR and MIR maps. The YSO has been briefly discussed in Bally et al. (2009) and is associated with the proto-stellar outflow HH 962.

7.6.1 C-band Emission

Ionised regions of HII gas generate both Hα and free-free continuum emission. The brightness of Hα emission is directly proportional to the density of the ionised hydrogen (n_H) and the rate at which recombination occurs within the cloud. The brightness of free-free emission depends on the density of free electrons (n_e) and ions within a region. In HII regions the free electrons are generated via ionisation therefore it is expected that $n_e \approx n_H$. Both emissions also depend on the electron temperature of the region, which is typically $T_e \approx 10^4$ K. As both free-free and Hα emissions share a common source, it is possible to directly relate the brightness of one emission to the brightness of the other (e.g., Dickinson et al., 2003).

In Figure 7.3 both the C-band and SHASSA maps show the same corona of HII tracing the *South* and *West* edges of LDN 1622. The differences in the morphology of the radio free-free and SHASSA Hα emissions around LDN 1622 are primarily due to optical dust absorption of the Hα emission. Correcting for Hα dust absorption is complicated as the distribution of dust and HII gas is unknown. In this Section the

radio free-free emission is estimated from the SHASSA map using the method outlined in Dickinson et al. (2003) and compared with the observed C-band free-free emission. The extinction of the Hα by dust is estimated using a simple radiative transfer model and optical depths measured from the *Herschel* FIR maps.

FIR *Herschel* data of LDN 1622 were used to estimate Hα absorption, A(Hα). The first step in deriving A(Hα) was to smooth all the *Herschel* maps to a common resolution. The 353 GHz optical depth (τ_{353}) was fitted for, pixel-by-pixel, over four *Herschel* bands. Each pixel was fitted with the modified black-body curve:

$$S_\nu = B_\nu(T_\mathrm{d})\tau_{353}\left(\frac{\nu}{353\,\mathrm{GHz}}\right)^\beta, \tag{7.5}$$

where the emissivity index β, the dust temperature T_d, and the dust opacity τ_{353} were all free parameters. B_ν is a black-body curve dependent on the dust temperature.

IR optical depth was converted to hydrogen column density (N_H) using:

$$\tau_{353} = \sigma_{e\,353} N_\mathrm{H}, \tag{7.6}$$

where $\sigma_{e\,353}$ is the mean whole sky dust opacity derived by *Planck* (Planck Collaboration Int. XI, 2013). The hydrogen column density was then related to extinction, $E(B-V)$, by assuming the relationship $N_\mathrm{H}/E(B-V) \approx 6.94 \times 10^{21}\,\mathrm{cm}^{-2}$ (Planck Collaboration Int. XI, 2013). The Hα absorption factor was related to the measured extinction with,

$$A(\mathrm{H}\alpha) = 0.81 R(V) E(B-V) \tag{7.7}$$

The reddening value ($R(V)$) for the ISM is typically ≈ 3.1 (Schultz and Wiemer, 1975; Sneden et al., 1978). However, $R(V)$ is observed to increase in denser regions of the ISM and even vary significantly between the edge of a dark cloud and its interior with a range of $3.5 < R(V) < 5.5$ (Vrba and Rydgren, 1984, 1985). Considering the typical reddening values of other dark clouds and that LDN 1622 is quite a translucent cloud, a nominal reddening value of $R(V) = 4$ was assumed.

The expected Hα emission (I_em) was estimated from the observed Hα emission (I_obs) by applying the following Hα absorption model pixel-by-pixel to the SHASSA map:

$$I_\mathrm{obs} = \frac{I_\mathrm{em}}{\tau}\int_0^{f\tau} e^{\tau'-\tau} d\tau' + (1-f) I_\mathrm{em} \tag{7.8}$$

The Hα optical depth (τ) is related to Hα absorption by $\tau = A(\mathrm{H}\alpha)/(2.5\log_{10}(e))$. The H$\alpha$ absorption model assumed that a certain fraction (f) of the HII gas and dust

were mixed and in thermal equilibrium, while the remaining fraction of HII gas was in front of the dust and its Hα emission unabsorbed. The model does not consider HII gas completely behind the dust within LDN 1622 because the Hα emission in that case would be mostly absorbed resulting in large uncertainties in the estimated radio free-free. However, it is possible that some fraction of HII gas is completely obscured by dust behind LDN 1622.

After correcting for Hα absorption, the Hα brightness was converted to the equivalent radio free-free brightness using the method described in Dickinson et al. (2003). The derived Hα to radio free-free conversion factor, assuming an electron temperature of $T_e = 7000\,\mathrm{K}$, was $0.28\,\mathrm{mK\,R^{-1}}$ at 4.85 GHz. The final simulated free-free map was smoothed to a FWHM of 3 arcmin to match the smoothed C-band resolution. The median background of the simulated free-free map was subtracted to represent the effect of the map-making process, which removes the zero-level of the C-band data.

Three examples of simulated free-free maps with dust-gas mixing fractions of $f = 0.1$, 0.5 and 1.0 are shown in Figure 7.4, with C-band contours overlaid. At low mixing fractions, the morphology and brightness of the Southern bar of the corona is reasonably well reconstructed by the simulated free-free map. At higher mixing fractions, a bright core of emission forms in the *West* of the simulated LDN 1622 corona that is completely unrepresentative of the observed C-band emission. This implies that there is very little dust-gas mixing occurring in the *South* of LDN 1622. The morphology and brightness of the *North-West* region of the corona appears significantly different in the predicted free-free maps to the observed C-band emission. The brightest region of the C-band emission in the *North-West* region of the corona is offset towards the *East* of the predicted free-free emission. An explanation for this is that much of the HII gas generating the free-free emission is behind the dust in LDN 1622, therefore the Hα emission has been completely absorbed along that line-of-sight.

Discrepancies between the observed C-band emission and simulated free-free emission could be explained by the dust-gas mixing fraction (f) varying across the cloud. However, changes in the dust-gas mixing fraction is not the only explanation. The model assumed that both the 353 GHz dust opacity ($\sigma_{e\,353}$) and optical reddening value ($R(V)$) were both constant across LDN 1622. However, IR dust opacity and reddening are both linked to grain size distributions, which could be changing from the edge of LDN 1622 towards the core (Weingartner and Draine, 2001).

Figure 7.5 shows the comparison between the SHASSA Hα and CBI 31 GHz maps

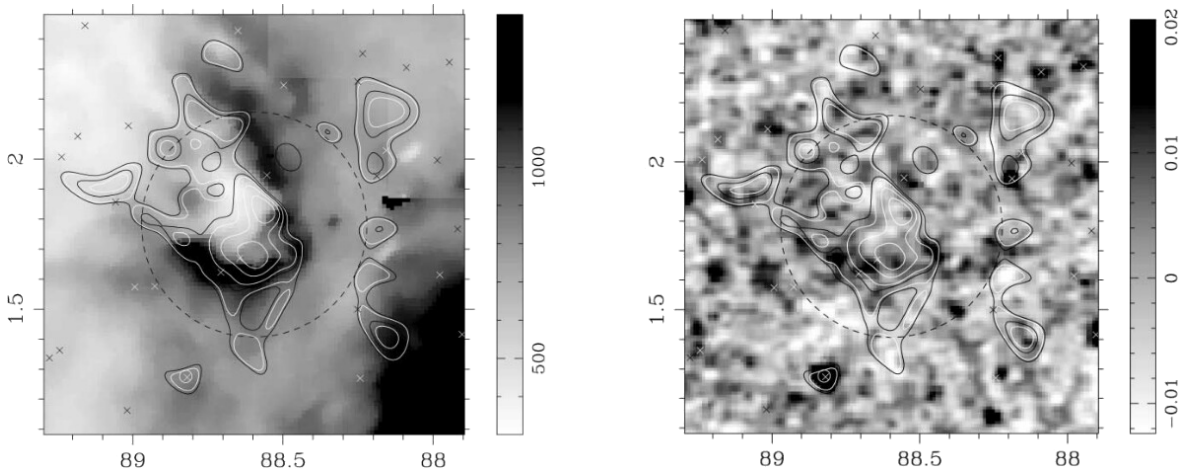

Figure 7.5: *Left*: 31 GHz CBI contours overlaid onto the SHASSA Hα map, the grey scale is in dR. White contour levels are 0.010, 0.020, 0.031, and 0.042 MJy sr^{-1}. *Right*: 31 GHz CBI contours overlaid on to the PWM 5 GHz map (Griffith and Wright, 1993), in units of Jy beam^{-1}.

of LDN 1622 taken from Casassus et al. (2006). The figure shows that the CBI 31 GHz observations do not detect any emission originating from the North-Western region of the Hα corona. Therefore, using the lowest contour level in the CBI map, an estimated upper limit on the free-free emission in the region is found to be 16.7 mK at 5 GHz. This agrees with the measured brightness temperature from the C-band data that ranged between 6 to 11 mK across the corona.

To summarise, the emission detected at C-band traces the HII corona of LDN 1622 and broadly agrees with the morphology of the SHASSA Hα map. The peak free-free brightness predicted by the Hα emission agrees within $\approx$10 % of the peak observed C-band free-free emission for the bright Hα ridge in the *South* of LDN 1622 for dust mixing fractions of $f \lesssim 0.1$. From these C-band observations the precise cause for the differences in morphology and brightness between the expected and observed free-free emission remains unknown. Possible explanations are variations in the local dust-gas mixing fraction, reddening value or IR dust opacity over LDN 1622. These explanations can not satisfactorily explain the emergence of the bright core in the expected free-free emission at high mixing fractions, as seen in Fig. 7.4. The high noise level in the C-band maps will also be a significant contribution to the differences in expected and observed free-free morphology and brightness across the LDN 1622 corona.

7.6.2 Ku-band Emission

In the smoothed 13.7 GHz Ku-band GBT map in Figure 7.3, the aperture is centred on the peak in Ku-band emission at Right Ascension = $5^{\rm h}54^{\rm m}13^{\rm s}$, Declination = $1^{\circ}47'49''$. The aperture has a semi-major axis of 3 arcmin and a semi-minor axis of 1.25 arcmin.

Visual inspection of Figure 7.3 shows that there is some contribution of free-free emission from HII gas as well as MIR emission from dust grains within the aperture. This Section will determine whether the emission at Ku-band is from spinning dust or just free-free emission. This requires calculating the expected free-free emission flux at Ku-band and assessing whether there is any significant morphological similarities between the emissions at Ku-band and the MIR.

Aperture photometry was used to measure the flux within the Ku-band aperture shown in Figure 7.3. The aperture size of 3 arcmin by 1.25 arcmin was chosen by expanding the aperture axes from zero until the signal-to-noise ratio within the aperture was maximised. The uncertainty and background within the Ku-band aperture was estimated from an elliptical annulus around the aperture. The annulus had inner and outer semi-minor axes of $2.17 - 4.68$ arcmin, and inner and outer semi-major axes of $5.2 - 11.2$ arcmin. These were chosen to enclose a sufficiently large sample of the C-band and Ku-band maps. Due to the Ku-band source being in close proximity to a number of diffuse sources, the estimated uncertainty on the flux density was measured from a residual map generated by differencing maps made for each observing day. By differencing different days, the residual map would contain statistically similar *1/f* noise from the atmosphere and receivers as the original Ku-band map. A five percent systematic uncertainties from the calibration of the data were added in quadrature to the measured uncertainties of the C-band and Ku-band flux densities.

The flux density within the Ku-band aperture shown in Figure 7.3 is 7.0 ± 1.4 mJy. The flux density within the same aperture at C-band is 5.8 ± 2.4 mJy, which corresponds to an expected free-free flux density at 13.7 GHz of 5.0 ± 2.0 mJy assuming a free-free spectral index of -0.15. The corresponding fractional excess at 13.7 GHz of 0.29 ± 0.13.

The measured fluxes from LDN 1622 were compared to the expected spinning dust emission flux densities predicted by the spinning dust model and Interactive Data Language (IDL) code SpDust (Ali-Haïmoud et al., 2009; Silsbee et al., 2011). The SpDust model expects nine environment parameters in order to estimate the expected

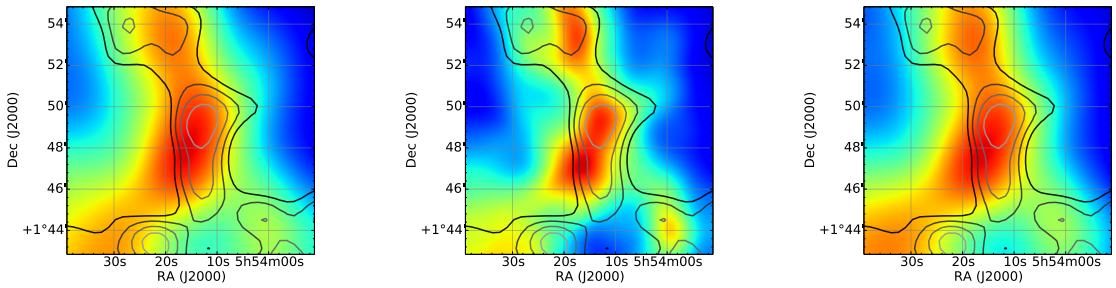

Figure 7.6: Overlay of smoothed Ku-band contours on the smoothed, point source removed MIR maps. *Left WISE* 22 μm, *centre WISE* 12 μm, *right Spitzer* IRAC 8 μm. The contour levels are 0.1, 0.45, 0.8 and 1.15 mJy beam^{-1} for a 1.2 arcmin beam.

spinning dust emission flux density from a region. The following is a brief description of each environment parameter and its value: the hydrogen number density (n_H = 10^4 H cm^{-3}), the gas temperature (T = 22 K), relative intensity of interstellar radiation field ($\chi = 10^{-4}$), hydrogen ionisation fraction (x_H = 1 ppm), carbon ionisation fraction (x_C = 1 ppm), fractional abundance of molecular hydrogen (y = 0), H_2 formation rate (γ = 0), RMS of the dipole moment for dust grains (β = 9.3), and the grain size distribution parameters corresponding to line 7 in Weingartner and Draine (Table 1 2001). A more detailed discussion of the SpDust environment parameters is given in Ali-Haïmoud et al. (2009).

The dark cloud environment parameters from Draine and Lazarian (1998b) are used as inputs for the SpDust model. The expected hydrogen number density for a dark cloud was checked against a calculated estimate of the true hydrogen number density for LDN 1622. The distance to LDN 1622 is typically considered to be similar to the Orion molecular clouds (≈400 pc) and it has an approximate angular size of 13 arcmin. Assuming the cloud is spherical and using the measured mean column density from *Herschel* FIR data ($\approx 1.5 \times 10^{22}$ H cm^{-2}), the estimated hydrogen number density was found to be ≈3000 H cm^{-3}, implying that the typical dark cloud $n_H = 10^4$ H cm^{-3} is a reasonable order of magnitude estimate for LDN 1622. The gas temperature parameter was matched to the mean dust temperature (T_d) within the Ku-band aperture derived from the *Herschel* FIR data, $T = T_\mathrm{d} = 22 \pm 2$ K. Figure 7.7 shows the *Herschel* derived dust temperature and hydrogen column density maps of LDN 1622. From these maps it can be seen that the outer PDR regions of LDN 1622 are both several Kelvin warmer and 25 % less dense than the inner regions of cloud.

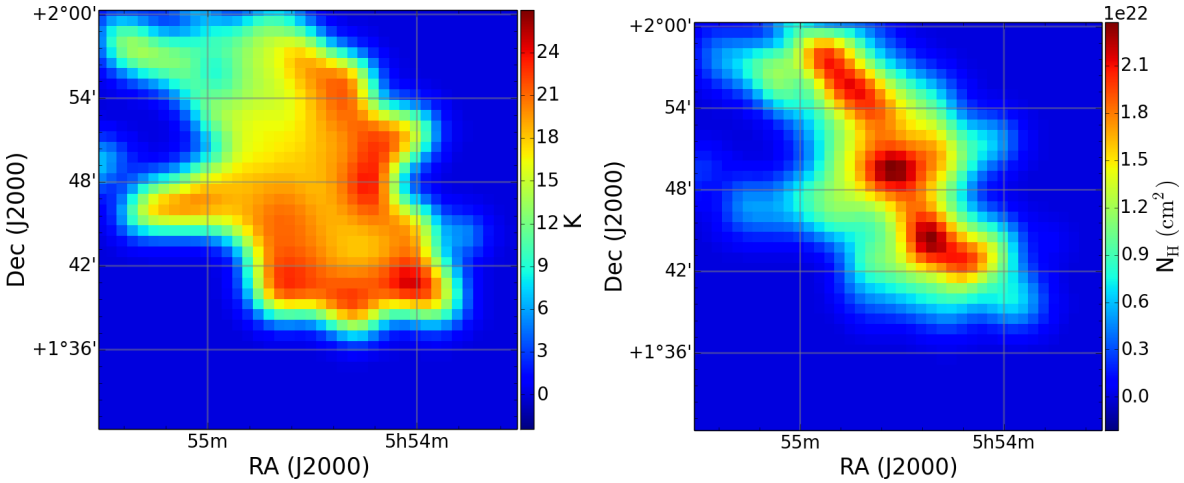

Figure 7.7: Dust temperatures and hydrogen column densities derived from *Herschel* data. *Left*: Dust temperatures. *Right*: Hydrogen column densities.

A key indication of spinning dust is a rising spectrum between $\approx 10 - 30\,\mathrm{GHz}$. The expected flux density within the Ku-band aperture at 31 GHz was estimated using the CBI contours shown in Casassus et al. (2006) and scaling the flux density, assuming a smooth source, to the expected flux within just the Ku-band aperture. The spectral index between 13.7 GHz and 31 GHz was found to be 2.3 ± 0.2, where the spectral index is defined by the simple power-law relationship,

$$S_2 = S_1 \left(\frac{\nu_2}{\nu_1}\right)^{\alpha}. \tag{7.9}$$

Here S_1 and ν_1 are the Ku-band flux density and frequency of $7.0 \pm 1.4\,\mathrm{mJy}$ and 13.7 GHz respectively, S_2 and ν_2 are the derived CBI flux density and frequency of $44.3 \pm 1.4\,\mathrm{mJy}$ and 31 GHz, and α is the spectral index. The uncertainty in the spectral index was estimated using,

$$\sigma_\alpha = \frac{1}{\log(\frac{\nu_2}{\nu_1})} \sqrt{\left(\frac{\sigma_1}{S_1}\right)^2 + \left(\frac{\sigma_2}{S_2}\right)^2}, \tag{7.10}$$

where ν is a given frequency, S is the flux density at a given frequency and σ is the measured flux density uncertainty. The spectral index derived from SpDust between the same frequencies is 1.84, which is $2.6\,\sigma$ from the measured spectral index. The strong confirmation that the spectral flux density spectrum is rising between 13.7 GHz and 31 GHz, and the agreement with the rising spectral index predicted by SpDust is a good indication that spinning dust is present within LDN 1622 in the region of the Ku-band aperture.

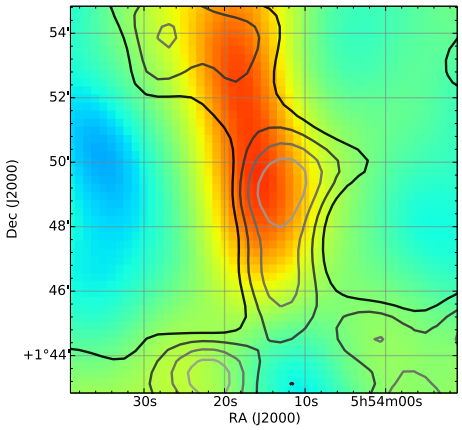

Figure 7.8: Overlay of smoothed GBT Ku-band contours on AMI SA colourscale. The contours are in units of mJy beam^{-1}, with a beam FWHM of 1.2 arcmin. The contour levels are 0.1, 0.45, 0.8 and 1.15 mJy beam^{-1}.

A map of LDN 1622 using the AMI SA at 15.7 GHz is provided for the purposes of visual comparison with the Ku-band map. Figure 7.8 shows the AMI SA data overlaid with Ku-band contours. As both observations are at similar frequencies, and are sensitive to similar large scale structures there should be significant correlations between the AMI SA and Ku-band maps. Both the AMI SA color scale and Ku-band contours in Figure 7.8 share the same large-scale elongated *North-South* structure. The most significant difference between the image and contours in Figure 7.8 is the small displacement of the Ku-band GBT data towards the *West*.

It was shown in the previous discussion that the flux at Ku-band can be naturally accounted for by the spinning dust model and that there is a clear rising spectrum between 13.7 GHz and 31 GHz indicative of spinning dust emission. However, if spinning dust is the origin of the Ku-band emission there should be significant correlations between Ku-band and MIR emission. The spinning dust model predicts that PAH molecules, VSGs or a combination of both are the source of spinning dust emission. VSGs generate MIR continuum emission and PAH molecules emit bright MIR emission lines at 12.7 μm, 11.3 μm, 8.6 μm and 7.7 μm (Tielens, 2008). The *WISE* 12 μm and *Spitzer* 8 μm passbands encompass these four PAH emission lines. The *WISE* 22 μm passband only contains MIR continuum emission from the VSGs. Therefore, if PAH molecules contribute to the generation of spinning dust emission, there should be a larger morphological correlation between the Ku-band and the 12 μm and 8 μm

maps than with the 22 μm map. It should be noted that it has been suggested that MIR emission in some HII regions and PDRs could be due to the formation of second-generation BGs in these environments (Everett and Churchwell, 2010; Draine, 2011; Paladini et al., 2012). There is a possibility that second-generation BGs are contributing to the MIR emission inside the PDR around LDN 1622, especially as the measured dust temperature within the PDR is quite warm, $T_{\rm d} = 22$ K. It is assumed here that the BGs are not significantly contributing to the observed MIR emission.

In order to determine the correlation between the diffuse emission at Ku-band with the diffuse emission in the MIR, the MIR maps had to first be filtered of point sources. For both the *WISE* and *Spitzer* maps a number of point sources near to the elongated *North-South* structure were patched out. The patching process involved replacing the source with a 2nd-order polynomial and noise estimated from the background around the source. Due to the shorter wavelength and higher resolution of the *Spitzer* map there were a much larger number of weaker visible point sources, which were then removed using a median filter.

The patching and median filtering of the point sources left a number of artefacts in the diffuse structure of the MIR maps at scales comparable to the FWHM resolutions of the MIR maps. However, it is reasonable to assume that these artefacts had minimal effect on this analysis as all the MIR maps were smoothed considerably to match the 1.2 arcmin FWHM resolution of the smoothed Ku-band map.

The 1.2 arcmin FHWM, point source filtered *WISE* and *Spitzer* maps are shown in Figure 7.6 with Ku-band contours overlaid. All three maps and contours share the similar elongated *North-South* morphology. All the maps in Figure 7.6 reveal that the peak in MIR emission coincides with the location of the peak Ku-band emission. From visual inspection of the MIR maps with the Ku-band contours there is no clear indication that either the *Spitzer* 8 μm or *WISE* 12 μm maps, which contain the PAH emission lines, have stronger correlations with the Ku-band contours than the MIR continuum emission seen in the *WISE* 22 μm map.

The Pearson's correlation coefficient, r, between the Ku-band map and each MIR map was measured to quantify any morphological correlations between the maps. The pixels in the maps were made quasi-independent by matching the pixel size to the FWHM of the maps. The Pearson correlations for each MIR map with the Ku-band map were found to be: $r(22\,\mu{\rm m}) = 0.54\pm0.13$, $r(12\,\mu{\rm m}) = 0.59\pm0.13$ and $r(8\,\mu{\rm m}) = 0.49\pm0.13$. The uncertainties in r were estimated by bootstrapping the data and using

the Fisher's r to z transform (Fisher, 1915). The Pearson correlation measurements imply that there is a slightly higher correlation between the Ku-band and the MIR maps containing PAH emission lines. However, the uncertainties on the correlation coefficients reveal there is no significantly higher correlation between the Ku-band map and any one MIR map.

In summary, this Section supports that spinning dust in the form of either VSGs or PAHs is being generated within the PDR of LDN 1622. Comparing the C-band and Ku-band data alone finds a small excess of emission at Ku-band at the $2\,\sigma$ level. However, a rising spectrum indicative of spinning dust emission, was found when comparing the flux densities at 13.7 GHz and 31 GHz. Finally, morphological correlations between the Ku-band and MIR emissions lends further support to the presence of spinning dust emission within LDN 1622.

7.7 Summary

This Chapter presented arcminute observations of Lynds dark cloud LDN 1622 by the GBT at 5 and 13.7 GHz. The aim of these observations was to quantify the level of free-free and spinning dust emission within LDN 1622 and compare these results with other, multi-frequency data.

A free-free corona associated with the PDR of LDN 1622 that is clearly visible in the SHASSA Hα image was found to moderately correlate with similar structures observed at C-band. The expected free-free brightness temperatures at C-band derived from the SHASSA Hα map were compared with those measured at C-band and agree within 10 % at peak brightness. However, simple modelling of the dust absorption clearly visible in the SHASSA Hα map was insufficient to replicate the emission seen at C-band.

The Ku-band observations show a weak *North-South* elongated source inside the PDR of LDN 1622. The diffuse nature of the Ku-band emission made measurements of the flux density difficult. However, a weak source at the core of an elongated structure was identified, with a flux density of 7.0 ± 1.4 mJy. Using the C-band map, the estimated free-free background flux density at 13.7 GHz is 5.0 ± 2.0 mJy. The resulting fractional excess in emission at Ku-band was therefore 0.29 ± 0.13, which is a tentative indication of spinning dust emission within LDN 1622.

In the previous Chapter, the MFI measured the integrated flux density of LDN 1622

and surrounding region with an aperture of 2 degrees diameter. The flux density at 13 GHz was 4.4 ± 1.5 Jy. At 13 GHz the SED of LDN 1622 is dominated by free-free emission that has a large smooth large-scale structure, evident from the surrounding diffuse red haze in Figure 7.1. Therefore, it is a reasonable assumption that the flux density in the large MFI aperture can be scaled down to the smaller Ku-band aperture. The flux density predicted by the MFI within the Ku-band aperture is 4.4 ± 1.5 mJy. This is close to the GBT C-band estimated flux density at 13.7 GHz. The remarkable agreement between the GBT C-band and MFI data lend greater credibility to the measured 13.7 GHz spinning dust emission excess in the above paragraph. Combining this evidence with the correlation between the 13.7 GHz and MIR data, gives reasonable confidence that the observed 13.7 GHz emission from LDN 1622 is partially driven by the spinning dust mechanism.

Chapter 8

Conclusions and Future Work

In this concluding chapter, the major results of each topic discussed in this thesis will be summarised. This is followed by a brief discussion of how the author's work may be expanded upon in the future.

8.1 Manchester QUIJOTE MFI Pipeline

A major portion of the work in this thesis has been in the development of tools for a Manchester QUIJOTE MFI pipeline that calibrates the raw voltage TOD from the receivers onto an absolute flux density scale. The principal difficulty associated with the calibration procedure is identifying sources of uncertainty and devising methods of quantifying that uncertainty.

The MFI `CST` beam model was used to determine key calibration parameters, such as the excellent main beam efficiency of 97 per cent and nearly symmetric main beam shapes of QT1. The observed main beam response was found to agree with the main beam model down to a level of -20 dB. However, the beam models could not reliably replicate the observed near or far sidelobe pattern. The high beam efficiency and main beam symmetry of the MFI were crucial to the reliability of the measurements of Galactic extended structures as discussed in Chapter 6.

The *1/f* noise contaminating the intensity TOD was measured to have a knee frequency between 10 to 100 Hz that appeared as baseline instabilities. The calibration diode was used to control *1/f* noise fluctuations in the system gain on timescales greater than 24 minutes. To use the calibration diode reliably requires the identification of key systematic effects, such as the apparent diode polarisation and the Gibbs ringing

artefacts seen when turning the diode on and off.

Variations in the absolute flux scale of the TOD were tracked using measurements of two astronomical sources. Tracking the absolute flux scale also required a model of the change in the relative gain modulation (*r-factor*) over time and applying bandpass colour corrections to the apparent source flux densities.

The total uncertainty in the calibration was estimated assuming contributions from the *r-factors*, the absolute flux scale model, and the atmosphere. The total uncertainty was estimated to be 1.6 per cent at 11 and 13 GHz, and 3 to 6 per cent at 17 and 19 GHz. These analytically derived absolute calibration uncertainties were then compared with the relative calibration uncertainties derived using day-to-day jack-knives of MFI wide-survey observations. The jack-knife relative uncertainties were found to be 2 to 3 per cent at 11 and 13 GHz, and 6 to 8 per cent at 17 and 19 GHz. These higher values imply that the analytical absolute uncertainties are either underestimated or some unknown sources of uncertainty have not been accounted for.

8.2 Map-Making

Chapter 5 discussed at length the author's implementation of the Destriping and maximum-likelihood map-making algorithms. These two map-making methods were applied to the MFI large-scale wide-survey observations, and also to the arcminute scale GBT raster observations. The framework and MPI implementation of the map-making codes were designed so that the map-makers could be applied to other current and future multi-feed array single-dish instruments.

Simulations were used to demonstrate the integrity of the map-making methods to suppressing the *1/f* noise, whilst simultaneously avoiding compromising the astronomical signal of interest. The simulations also indicated that a critical limitation of map-making is that the thermal noise limit of the TOD cannot be recovered once the TOD is contaminated by *1/f* noise. This is an important point because it indicates that it is preferable, where possible, to try and suppress *1/f* noise in hardware, such as with the MFI correlated channels, than to rely entirely on post-processing in software.

The map-making simulations were also used to inform the map-making strategy for both the MFI wide-survey and GBT observations. For the wide-survey, a ten second Destriping baseline was found to be the optimal solution, achieving an effective noise level in the maps only 10 per cent higher than the maximum-likelihood solution. For the

GBT, the observations were sufficiently small in size so that the maximum-likelihood method could be applied directly.

8.3 Galactic Spinning Dust Emission

This thesis has presented several investigations into spinning dust emission within the Galaxy. On large-scales, within the inner Galactic disk, spectral indices measured between 12 and 23 GHz were found to be rising with a median spectral index between 0.17 to 0.24 depending on the region. The contribution of spinning dust emission to the total emission within the inner Galactic disk was estimated to be approximately 25 ± 3 per cent at 23 GHz. This agrees with estimates from models and other instruments that place the integrated contribution of spinning dust within the plane of the Galaxy to be between 10 and 50 per cent with large uncertainties.

Parametric model fitting to the SEDs of four known spinning dust emitting regions of the Galaxy was performed using a combination of the MFI wide-survey maps and other multifrequency ancillary data. Key parameters describing the spinning dust emission spectrum were derived and found to be consistent with the literature. For example, Planck Collaboration et al. (2014d) found, from a sample of 42 spinning dust emission sources, the weighted mean spinning dust peak frequency to be 27.9 GHz. The work in this thesis finds the weighted mean to be 27.2 ± 0.7 GHz. One particular region, LDN 1582/84, tentatively identified as a spinning dust source in Planck Collaboration et al. (2014d), was found to have a 5σ significance. Critically, the MFI 11 and 13 GHz wide-survey maps have helped to constrain the bright free-free background of LDN 1582/84, confirming that this region has up to a 38 ± 8 per cent total contribution from spinning dust emission at 30 ± 3 GHz.

On arcminute scales, the photo-dissociation region around LDN 1622 was measured to have up to a 7.0 ± 1.4 mJy emission excess over the free-free background at 13.7 GHz, an indication of spinning dust emission. This agrees with the MFI large-scale integrated measurement of LDN 1622 and the surrounding diffuse free-free emission, which was found to have a tentative 3σ measurement of spinning dust emission. The GBT C-band measurements predicted a 5.0 ± 2.0 mJy free-free background to the source seen at 13.7 GHz. The 13 GHz MFI predicted a free-free background of 4.4 ± 1.5 mJy, agreeing with the C-band GBT measurements to within 1σ. The close agreement of the GBT C-band and MFI 13 GHz data lends greater credibility to the estimated 29 ± 13 per cent

spinning dust contribution at 13.7 GHz within the PDR of LDN 1622.

8.4 Future Work

This thesis has discussed the technical aspects of reducing single-dish radio TOD, and the scientific applications of the reduced data to study phenomena within the interstellar medium. There are many areas of future work available to expand upon the topics discussed.

Currently, the Manchester QUIJOTE MFI pipeline has been used to fully reduce the wide-survey observations and in the future will also be applied to the MFI deep-survey raster observations. Direct comparisons should be made between the integrity of the author's absolute and relative calibration uncertainty, and the calibration uncertainty associated with the pipeline developed at the IAC. This is important as it could shed light upon the sources of unknown calibration uncertainty mentioned earlier. The pipeline should also be expanded to include characterisation of the polarisation properties, as this to date has been the focus of QUIJOTE collaborators at the IAC alone.

In Section 4.3, the integrated far sidelobe pickup from GSO satellites was discussed at length. As evident from the MFI wide-survey maps, the GSO satellites are a significant source of RFI. The GSO satellite emission is also the reason why the performance of the map-makers in removing correlated noise in the simulations is not replicated in the final MFI wide-survey maps to the same extent. In principle, the methods discussed in this thesis could be expanded upon if an accurate beam model of QT1 was available, allowing for the extended RFI emission to be subtracted directly from the TOD.

There are a number of possible additions that could be implemented into the author's map-making codes. The most obvious is to incorporate polarisation map-making, which was beyond the remit of this thesis. Another addition could be to incorporate the MPI routines used in the Destriping map-making codes into the maximum-likelihood map-making codes. This would require implementing a method for sharing the *1/f* noise information between computer cluster nodes. A significant bottle-neck in the current `MPI` implementation is that for every CGM iteration, the entire sky information is shared. Instead, nodes could process a small subset of pixels, optimised for the network connecting the computer cluster. This would dramatically increase the

computational speed of the Destriping map-making code.

Finally, there still remain many open scientific questions about spinning dust emission. Understanding the nature of spinning dust emission will require further follow up high resolution observations of sources identified at 1 degree scales. In particular, new observations of the boundary between LDN 1582/84 and its neighbouring HII region would be useful for determining whether the spinning dust emission is originating from the PDR. These observations would be ideal to perform using instruments on the GBT, such as the K-band Focal Plane Array, coupled with lower frequency C-band or X-band observations to constrain the free-free component.

In the future, the C-BASS 5 GHz maps of the Northern sky will be a perfect compliment to the MFI wide-survey data, as well as other existing surveys. The C-BASS data will be ideal for constraining the free-free component of the Galactic continuum.

The major finding in this thesis is that the inner Galactic disk at 23 GHz has a 25 ± 3 per cent contribution from spinning dust emission. If the Milky Way can be considered a typical star forming Galaxy, then this raises a serious question about the reliability of star-formation rate estimates based on observations of other galaxies using Ka-band or K-band data (Murphy et al., 2010). This could also be a problem for high redshift surveys such as the 1.42 and 5 GHz *e*-MERGE survey (Muxlow, 2015). If a source at $z = 4$ to 5 emits at a rest frequency of 25 to 30 GHz, the emission will be detected at 5 GHz.

Bibliography

Station-keeping in longitude of geostationary satellites in the fixed-satellite service . Technical Report S.484-3 (03/92), ITU, https://www.itu.int/rec/R-REC-S.484/en, March 1992.

Pointing accuracy as a design objective for earthward antennas on board geostationary satellites in the fixed-satellite service. Technical Report S.1064-1 (10/95), ITU, https://www.itu.int/rec/R-REC-S.1064/en, October 1995.

Abdo, A.A. et al. Measurement of the Cosmic Ray e^++e^- Spectrum from 20GeV to 1TeV with the Fermi Large Area Telescope. *Physical Review Letters*, 102(18):181101, May 2009. doi: 10.1103/PhysRevLett.102.181101.

Ackermann, M. et al. Fermi LAT observations of cosmic-ray electrons from 7 GeV to 1 TeV. Phys.Rev.D, 82(9):092004, November 2010. doi: 10.1103/PhysRevD.82.092004.

Ackermann, M. et al. Measurement of Separate Cosmic-Ray Electron and Positron Spectra with the Fermi Large Area Telescope. *Physical Review Letters*, 108(1): 011103, January 2012. doi: 10.1103/PhysRevLett.108.011103.

Adriani, O. et al. The PAMELA space mission. *Nuclear Physics B Proceedings Supplements*, 188:296–298, March 2009. doi: 10.1016/j.nuclphysbps.2009.02.070.

Adriani, O. et al. Cosmic-Ray Electron Flux Measured by the PAMELA Experiment between 1 and 625 GeV. *Physical Review Letters*, 106(20):201101, May 2011. doi: 10.1103/PhysRevLett.106.201101.

Agladze, N.I. et al. Laboratory Results on Millimeter-Wave Absorption in Silicate Grain Materials at Cryogenic Temperatures. ApJ, 462:1026, May 1996. doi: 10.1086/177217.

Aguilar, M. et al. The alpha magnetic spectrometer (ams) on the international space station: Part i results from the test flight on the space shuttle. *Physics Reports*, 366(6):331 – 405, 2002. ISSN 0370-1573. doi: http://dx.doi.org/10.1016/S0370-1573(02)00013-3. URL `http://www.sciencedirect.com/science/article/pii/S0370157302000133`.

Ali-Haïmoud, Y., Hirata, C.M. and Dickinson, C. A refined model for spinning dust radiation. MNRAS, 395:1055–1078, May 2009. doi: 10.1111/j.1365-2966.2009.14599.x.

Aller, H.D. and Reynolds, S.P. The decrease with time of the radio flux of the Crab Nebula. ApJ, 293:L73–L75, June 1985. doi: 10.1086/184494.

Alves, M.I.R. et al. A derivation of the free-free emission on the Galactic plane between l= 20 and 44. MNRAS, 422:2429–2443, May 2012. doi: 10.1111/j.1365-2966.2012.20796.x.

Alves, M.I.R. et al. The HIPASS survey of the Galactic plane in radio recombination lines. MNRAS, 450:2025–2042, June 2015. doi: 10.1093/mnras/stv751.

AMI Consortium et al. AMI observations of Lynds dark nebulae: further evidence for anomalous cm-wave emission. MNRAS, 400:1394–1412, December 2009. doi: 10.1111/j.1365-2966.2009.15542.x.

Anderson, M.C. and Rudnick, L. Sites of Relativistic Particle Acceleration in Supernova Remnant Cassiopeia A. ApJ, 456:234, January 1996. doi: 10.1086/176644.

Andersson, B.G. et al. The Nature of the IRAS Ring G159.6-18.5 in Perseus and Its Exciting Star HD 278942. AJ, 119:1325–1338, March 2000. doi: 10.1086/301258.

Atoyan, A.M., Aharonian, F.A. and Völk, H.J. Electrons and positrons in the galactic cosmic rays. Phys.Rev.D, 52:3265–3275, September 1995. doi: 10.1103/PhysRevD.52.3265.

Atwood, W.B. et al. The Large Area Telescope on the Fermi Gamma-Ray Space Telescope Mission. ApJ, 697:1071–1102, June 2009. doi: 10.1088/0004-637X/697/2/1071.

Baars, J.W.M. et al. The absolute spectrum of CAS A - an accurate flux density scale and a set of secondary calibrators. A&A, 61:99–106, October 1977.

Bally, J. et al. Outflows and Young Stars in Orion's Large Cometary Clouds L1622 and L1634. AJ, 137:3843–3858, April 2009. doi: 10.1088/0004-6256/137/4/3843.

Barnard, E.E. The great photographic nebula of Orion, encircling the belt and theta nebula. *Popular Astronomy*, 2:151–154, 1894.

Bate, R.R., Mueller, D.D. and White, J.E. *Fundamentals of astrodynamics.* 1971.

Battistelli, E.S. et al. Polarization Observations of the Anomalous Microwave Emission in the Perseus Molecular Complex with the COSMOSOMAS Experiment. ApJ, 645: L141–L144, July 2006. doi: 10.1086/506254.

Battistelli, E.S. et al. New Radio Observations of Anomalous Microwave Emission in the H II Region RCW175. ApJ, 801:111, March 2015. doi: 10.1088/0004-637X/801/2/111.

Bell, A.R. Proper motions and temporal flux changes of compact features in Cassiopeia A at 5 GHz. MNRAS, 179:573, June 1977.

Bennett, C.L. et al. First-Year Wilkinson Microwave Anisotropy Probe (WMAP) Observations: Foreground Emission. ApJS, 148:97–117, September 2003. doi: 10.1086/377252.

Bennett, C.L. et al. Nine-year Wilkinson Microwave Anisotropy Probe (WMAP) Observations: Final Maps and Results. ApJS, 208:20, October 2013. doi: 10.1088/0067-0049/208/2/20.

Betoule, M. et al. Improved cosmological constraints from a joint analysis of the SDSS-II and SNLS supernova samples. A&A, 568:A22, August 2014. doi: 10.1051/0004-6361/201423413.

BICEP2/Keck and Planck Collaborations et al. Joint Analysis of BICEP2/Keck Array and Planck Data. *Physical Review Letters*, 114(10):101301, March 2015a. doi: 10.1103/PhysRevLett.114.101301.

BICEP2/Keck and Planck Collaborations et al. Joint Analysis of BICEP2/Keck Array and Planck Data. *Physical Review Letters*, 114(10):101301, March 2015b. doi: 10.1103/PhysRevLett.114.101301.

Boland, J.W. et al. Polarization of Cygnus A, Taurus A, and Cassiopeia A at 2.07 Centimeters. ApJ, 144:437, April 1966. doi: 10.1086/148625.

Breen, A. and McCarthy, D. A Re-evaluation of the Eastern and Western Records of the Supernova of 1054. *Vistas in Astronomy*, 39:363–379, 1995. doi: 10.1016/0083-6656(95)96619-S.

Burke, B.F. and Graham-Smith, F. *An Introduction to Radio Astronomy*. 1996.

Cano, J.L. et al. Full band waveguide turnstile junction orthomode transducer with phase matched outputs. *International Journal of RF and Microwave Computer-Aided Engineering*, 20:8, 2010.

Cantalupo, C.M. et al. MADmap: A Massively Parallel Maximum Likelihood Cosmic Microwave Background Map-maker. ApJS, 187:212–227, March 2010. doi: 10.1088/0067-0049/187/1/212.

Casassus, S. et al. Anomalous Radio Emission from Dust in the Helix. ApJ, 603:599–610, March 2004. doi: 10.1086/381667.

Casassus, S. et al. Morphological Analysis of the Centimeter-Wave Continuum in the Dark Cloud LDN 1622. ApJ, 639:951–964, March 2006. doi: 10.1086/499517.

Casassus, S. et al. Centimetre-wave continuum radiation from the ρ Ophiuchi molecular cloud. MNRAS, 391:1075–1090, December 2008. doi: 10.1111/j.1365-2966.2008.13954.x.

Dalcin, L., Paz, R. and Storti, M. {MPI} for python. *Journal of Parallel and Distributed Computing*, 65(9):1108–1115, 2005.

Das, S. et al. The Atacama Cosmology Telescope: temperature and gravitational lensing power spectrum measurements from three seasons of data. , 4:014, April 2014. doi: 10.1088/1475-7516/2014/04/014.

Davies, R.D. et al. A determination of the spectra of Galactic components observed by the Wilkinson Microwave Anisotropy Probe. MNRAS, 370:1125–1139, August 2006. doi: 10.1111/j.1365-2966.2006.10572.x.

de Oliveira-Costa, A. et al. Galactic Emission at 19 GHZ. ApJ, 509:L9–L12, December 1998. doi: 10.1086/311754.

de Oliveira-Costa, A. et al. A model of diffuse Galactic radio emission from 10 MHz to 100 GHz. MNRAS, 388:247–260, July 2008a. doi: 10.1111/j.1365-2966.2008.13376.x.

de Oliveira-Costa, A. et al. A model of diffuse Galactic radio emission from 10 MHz to 100 GHz. MNRAS, 388:247–260, July 2008b. doi: 10.1111/j.1365-2966.2008.13376.x.

Delabrouille, J. Analysis of the accuracy of a destriping method for future cosmic microwave background mapping with the PLANCK SURVEYOR satellite. A&AS, 127:555–567, February 1998. doi: 10.1051/aas:1998119.

Demetroullas, C. et al. Observations of Galactic star-forming regions with the Cosmic Background Imager at 31 GHz. MNRAS, 453:2082–2093, October 2015. doi: 10.1093/mnras/stv1793.

Dent, W.A., Aller, H.D. and Olsen, E.T. The Evolution of the Radio Spectrum of Cassiopeia a. ApJ, 188:L11, February 1974. doi: 10.1086/181418.

Desert, F.X., Boulanger, F. and Puget, J.L. Interstellar dust models for extinction and emission. A&A, 237:215–236, October 1990.

Dicke, R.H. et al. Cosmic Black-Body Radiation. ApJ, 142:414–419, July 1965. doi: 10.1086/148306.

Dickinson, C., Davies, R.D. and Davis, R.J. Towards a free-free template for CMB foregrounds. MNRAS, 341:369–384, May 2003. doi: 10.1046/j.1365-8711.2003.06439.x.

Dickinson, C. et al. An Upper Limit on Anomalous Dust Emission at 31 GHz in the Diffuse Cloud [LPH96] 201.663+1.643. ApJ, 643:L111–L114, June 2006. doi: 10.1086/505299.

Dickinson, C. et al. CBI limits on 31GHz excess emission in southern HII regions. MNRAS, 379:297–307, July 2007. doi: 10.1111/j.1365-2966.2007.11967.x.

Dickinson, C. et al. Anomalous Microwave Emission from the H II Region RCW175. ApJ, 690:1585–1589, January 2009. doi: 10.1088/0004-637X/690/2/1585.

Dickinson, C. et al. Infrared-correlated 31-GHz radio emission from Orion East. MNRAS, 407:2223–2229, October 2010. doi: 10.1111/j.1365-2966.2010.17079.x.

Dickinson, C., Peel, M. and Vidal, M. New constraints on the polarization of anomalous microwave emission in nearby molecular clouds. MNRAS, 418:L35–L39, November 2011. doi: 10.1111/j.1745-3933.2011.01138.x.

Dmitrenko, D. et al. Absolute measurements of the intensity of radio emission from cassiopeia-a, cygnus-a, and taurus-a in the 315 cm range of wavelength s. *Radiophysics and Quantum Electronics*, 13(6):649–654, 1970. ISSN 0033-8443. doi: 10.1007/BF01030765. URL `http://dx.doi.org/10.1007/BF01030765`.

Dodelson, S. *Modern Cosmology*. Elsevier Science, 2003. ISBN 9780080511979.

Dodelson, S. et al. The Origin of the Universe as Revealed Through the Polarization of the Cosmic Microwave Background. In *astro2010: The Astronomy and Astrophysics Decadal Survey*, volume 2010 of *ArXiv Astrophysics e-prints*, page 67, 2009.

Doré, O. et al. MAPCUMBA: A fast iterative multi-grid map-making algorithm for CMB experiments. A&A, 374:358–370, July 2001. doi: 10.1051/0004-6361:20010692.

Draine, B.T. On Radiation Pressure in Static, Dusty H II Regions. ApJ, 732:100, May 2011. doi: 10.1088/0004-637X/732/2/100.

Draine, B.T. and Fraisse, A.A. Polarized Far-Infrared and Submillimeter Emission from Interstellar Dust. ApJ, 696:1, May 2009. doi: 10.1088/0004-637X/696/1/1.

Draine, B.T. and Lazarian, A. Diffuse Galactic Emission from Spinning Dust Grains. ApJ, 494:L19, February 1998a. doi: 10.1086/311167.

Draine, B.T. and Lazarian, A. Electric Dipole Radiation from Spinning Dust Grains. ApJ, 508:157–179, November 1998b. doi: 10.1086/306387.

Draine, B.T. and Lazarian, A. Magnetic Dipole Microwave Emission from Dust Grains. ApJ, 512:740–754, February 1999. doi: 10.1086/306809.

Draine, B.T. and Li, A. Infrared Emission from Interstellar Dust. I. Stochastic Heating of Small Grains. ApJ, 551:807–824, April 2001. doi: 10.1086/320227.

Dunkley, J. et al. Five-Year Wilkinson Microwave Anisotropy Probe (WMAP) Observations: Bayesian Estimation of Cosmic Microwave Background Polarization Maps. ApJ, 701:1804–1813, August 2009. doi: 10.1088/0004-637X/701/2/1804.

Edge, D.O. et al. A survey of radio sources at a frequency of 159 Mc/s. MmRAS, 68: 37–60, 1959.

Emerson, D.T. and Graeve, R. The reduction of scanning noise in raster scanned data. A&A, 190:353–358, January 1988.

Erickson, W.C. A Mechanism of Non-Thermal Radio-Noise Origin. ApJ, 126:480, November 1957. doi: 10.1086/146421.

Eriksen, H.K. et al. Joint Bayesian Component Separation and CMB Power Spectrum Estimation. ApJ, 676:10–32, March 2008. doi: 10.1086/525277.

Everett, J.E. and Churchwell, E. Dusty Wind-blown Bubbles. ApJ, 713:592–602, April 2010. doi: 10.1088/0004-637X/713/1/592.

Fazio, G.G. et al. The Infrared Array Camera (IRAC) for the Spitzer Space Telescope. ApJS, 154:10–17, September 2004. doi: 10.1086/422843.

Finkbeiner, D.P. A Full-Sky Hα Template for Microwave Foreground Prediction. ApJS, 146:407–415, June 2003. doi: 10.1086/374411.

Finkbeiner, D.P. et al. Tentative Detection of Electric Dipole Emission from Rapidly Rotating Dust Grains. ApJ, 566:898–904, February 2002. doi: 10.1086/338225.

Finkbeiner, D.P., Langston, G.I. and Minter, A.H. Microwave Interstellar Medium Emission in the Green Bank Galactic Plane Survey: Evidence for Spinning Dust. ApJ, 617:350–359, December 2004. doi: 10.1086/425165.

Fisher, R.A. Frequency Distribution of the Values of the Correlation Coefficients in Samples from an Indefinitely Large Population. *Biometrika*, 10:507–521, 1915. doi: 10.1093/biomet.

Fixsen, D.J. The Temperature of the Cosmic Microwave Background. ApJ, 707:916–920, December 2009. doi: 10.1088/0004-637X/707/2/916.

Fridman, P.A. Statistically Stable Estimates of Variance in Radio-Astronomy Observations as Tools for Radio-Frequency Interference Mitigation. AJ, 135:1810–1824, May 2008. doi: 10.1088/0004-6256/135/5/1810.

Garcia-Munoz, M., Mason, G.M. and Simpson, J.A. The age of the galactic cosmic rays derived from the abundance of Be-10. ApJ, 217:859–877, November 1977. doi: 10.1086/155632.

Garny, M., Ibarra, A. and Vogl, S. Antiproton constraints on dark matter annihilations from internal electroweak bremsstrahlung. , 7:028, July 2011. doi: 10.1088/1475-7516/2011/07/028.

Gaustad, J.E. et al. A Robotic Wide-Angle Hα Survey of the Southern Sky. PASP, 113:1326–1348, November 2001. doi: 10.1086/323969.

GBT Proposers Guide. *The Proposers Guide for the Green Bank Telescope*, 2015.

Génova-Santos, R. et al. Measurements of the Intensity and Polarization of the Anomalous Microwave Emission in the Perseus molecular complex with QUIJOTE. *ArXiv e-prints*, January 2015.

Georgelin, Y.M. and Georgelin, Y.P. The spiral structure of our Galaxy determined from H II regions. A&A, 49:57–79, May 1976.

Ghosh, T. et al. Foreground analysis using cross-correlations of external templates on the 7-year Wilkinson Microwave Anisotropy Probe data. MNRAS, 422:3617–3642, June 2012. doi: 10.1111/j.1365-2966.2012.20875.x.

Gold, B. et al. Five-Year Wilkinson Microwave Anisotropy Probe Observations: Galactic Foreground Emission. ApJS, 180:265–282, February 2009. doi: 10.1088/0067-0049/180/2/265.

Gold, T. Polarization of Starlight. Nature, 169:322, February 1952. doi: 10.1038/169322a0.

Gomez, A. et al. QUIJOTE telescope design and fabrication. In *Society of Photo-Optical Instrumentation Engineers (SPIE) Conference Series*, volume 7733 of *Society of Photo-Optical Instrumentation Engineers (SPIE) Conference Series*, page 0, July 2010. doi: 10.1117/12.857286.

Górski, K.M. et al. HEALPix: A Framework for High-Resolution Discretization and Fast Analysis of Data Distributed on the Sphere. ApJ, 622:759–771, April 2005. doi: 10.1086/427976.

Green, A.J., Baker, J.R. and Landecker, T.L. Observations of eight supernova remnants at 15 GHz. A&A, 44:187–194, November 1975.

Green, D.A. A revised Galactic supernova remnant catalogue. *Bulletin of the Astronomical Society of India*, 37:45–61, March 2009.

Griffin, M.J. et al. The Herschel-SPIRE instrument and its in-flight performance. A&A, 518:L3, July 2010. doi: 10.1051/0004-6361/201014519.

Griffith, M.R. and Wright, A.E. The Parkes-MIT-NRAO (PMN) surveys. I - The 4850 MHz surveys and data reduction. AJ, 105:1666–1679, May 1993. doi: 10.1086/116545.

Hafez, Y.A. et al. Radio source calibration for the Very Small Array and other cosmic microwave background instruments at around 30 GHz. MNRAS, 388:1775–1786, August 2008. doi: 10.1111/j.1365-2966.2008.13515.x.

Hanany, S. and Rosenkranz, P. Polarization of the atmosphere as a foreground for cosmic microwave background polarization experiments. NAR, 47:1159–1165, December 2003. doi: 10.1016/j.newar.2003.09.017.

Haslam, C.G.T. et al. A 408 MHz all-sky continuum survey. II - The atlas of contour maps. A&AS, 47:1, January 1982.

Hauser, M.G. et al. The COBE Diffuse Infrared Background Experiment Search for the Cosmic Infrared Background. I. Limits and Detections. ApJ, 508:25–43, November 1998. doi: 10.1086/306379.

Hensley, B.S. and Draine, B.T. A Case Against Spinning PAHs as the Source of the Anomalous Microwave Emission. *ArXiv e-prints*, May 2015.

Hewish, A. et al. Observation of a Rapidly Pulsating Radio Source. Nature, 217: 709–713, February 1968. doi: 10.1038/217709a0.

Hicken, M. et al. Improved Dark Energy Constraints from ˜100 New CfA Supernova Type Ia Light Curves. ApJ, 700:1097–1140, August 2009. doi: 10.1088/0004-637X/700/2/1097.

Hinshaw, G. et al. Nine-year Wilkinson Microwave Anisotropy Probe (WMAP) Observations: Cosmological Parameter Results. ApJS, 208:19, October 2013. doi: 10.1088/0067-0049/208/2/19.

Hoang, T., Draine, B.T. and Lazarian, A. Improving the Model of Emission from Spinning Dust: Effects of Grain Wobbling and Transient Spin-up. ApJ, 715:1462–1485, June 2010. doi: 10.1088/0004-637X/715/2/1462.

Hoang, T., Lazarian, A. and Martin, P.G. Constraint on the Polarization of Electric Dipole Emission from Spinning Dust. ApJ, 779:152, December 2013. doi: 10.1088/0004-637X/779/2/152.

Hoare, M.G. et al. The Coordinated Radio and Infrared Survey for High-Mass Star Formation (The CORNISH Survey). I. Survey Design. PASP, 124:939–955, September 2012. doi: 10.1086/668058.

Hobbs, R.W. and Haddock, F.T. Measurements of the Linearly Polarized Components of Radio Sources at a Wavelength of 3.75 CM. ApJ, 147:908, March 1967. doi: 10.1086/149082.

Hollenbach, D.J. and Tielens, A.G.G.M. Photodissociation regions in the interstellar medium of galaxies. *Reviews of Modern Physics*, 71:173–230, January 1999. doi: 10.1103/RevModPhys.71.173.

Hubble, E.P. Novae or Temporary Stars. *Leaflet of the Astronomical Society of the Pacific*, 1:55, 1928.

Iglesias-Groth, S. et al. Evidence for the Naphthalene Cation in a Region of the Interstellar Medium with Anomalous Microwave Emission. ApJ, 685:L55–L58, September 2008. doi: 10.1086/592349.

Irfan, M.O. et al. C-Band All-Sky Survey: a first look at the Galaxy. MNRAS, 448: 3572–3586, April 2015. doi: 10.1093/mnras/stv212.

Jansky, K.G. Radio Waves from Outside the Solar System. Nature, 132:66, July 1933. doi: 10.1038/132066a0.

Jarosik, N. et al. Design, Implementation, and Testing of the Microwave Anisotropy Probe Radiometers. ApJS, 145:413–436, April 2003. doi: 10.1086/346080.

Jenness, T. and Economou, F. ORAC-DR – SCUBA Pipeline Data Reduction. *Starlink User Note*, 231, 2004.

Jewell, P.R. and Prestage, R.M. The Green Bank Telescope. In Oschmann, Jr., J.M., editor, *Ground-based Telescopes*, volume 5489 of *Society of Photo-Optical Instrumentation Engineers (SPIE) Conference Series*, pages 312–323, October 2004. doi: 10.1117/12.550631.

Johnston, K.J. and Hobbs, R.W. Distribution of Brightness in Polarization of Taurus a and Brightness Distribution of NGC 1976 AT 9.55-MM Wavelength. ApJ, 158: 145, October 1969. doi: 10.1086/150178.

Jonas, J.L., Baart, E.E. and Nicolson, G.D. The Rhodes/HartRAO 2326-MHz radio continuum survey. MNRAS, 297:977–989, July 1998. doi: 10.1046/j.1365-8711.1998.01367.x.

Jones, E. et al. SciPy: Open source scientific tools for Python, 2001–. URL `http://www.scipy.org`.

Kamionkowski, M., Kosowsky, A. and Stebbins, A. A Probe of Primordial Gravity Waves and Vorticity. *Physical Review Letters*, 78:2058–2061, March 1997. doi: 10.1103/PhysRevLett.78.2058.

Keihänen, E. et al. A maximum likelihood approach to the destriping technique. A&A, 428:287–298, December 2004. doi: 10.1051/0004-6361:200400060.

Keihänen, E. et al. Making cosmic microwave background temperature and polarization maps with MADAM. A&A, 510:A57, February 2010. doi: 10.1051/0004-6361/200912813.

King, O.G. et al. The C-Band All-Sky Survey: instrument design, status, and first-look data. In *Society of Photo-Optical Instrumentation Engineers (SPIE) Conference Series*, volume 7741 of *Society of Photo-Optical Instrumentation Engineers (SPIE) Conference Series*, page 1, July 2010. doi: 10.1117/12.858011.

King, O.G. et al. The C-Band All-Sky Survey (C-BASS): design and implementation of the northern receiver. MNRAS, 438:2426–2439, March 2014. doi: 10.1093/mnras/stt2359.

Klein, M.J. and Gulkis, S. Jupiter's atmosphere - Observations and interpretation of the microwave spectrum near 1.25-cm wavelength. , 35:44–60, July 1978. doi: 10.1016/0019-1035(78)90059-3.

Knox, L. and Song, Y.S. Limit on the Detectability of the Energy Scale of Inflation. *Physical Review Letters*, 89(1):011303, July 2002. doi: 10.1103/PhysRevLett.89.011303.

Kogut, A. et al. Microwave Emission at High Galactic Latitudes in the Four-Year DMR Sky Maps. ApJ, 464:L5, June 1996. doi: 10.1086/310072.

Komatsu, E. et al. Seven-year Wilkinson Microwave Anisotropy Probe (WMAP) Observations: Cosmological Interpretation. ApJS, 192:18, February 2011. doi: 10.1088/0067-0049/192/2/18.

Kun, M. et al. Lynds 1622: a nearby star-forming cloud projected on Orion B? MNRAS, 391:84–94, November 2008. doi: 10.1111/j.1365-2966.2008.13898.x.

Kurtz, S., Churchwell, E. and Wood, D.O.S. Ultracompact H II regions. 2: New high-resolution radio images. ApJS, 91:659–712, April 1994. doi: 10.1086/191952.

Lawson, K.D. et al. Variations in the Spectral Index of the Galactic Radio Continuum Emission in the Northern Hemisphere. MNRAS, 225:307, March 1987.

Lazarian, A. and Draine, B.T. Resonance Paramagnetic Relaxation and Alignment of Small Grains. ApJ, 536:L15–L18, June 2000. doi: 10.1086/312720.

Leahy, J.P. et al. Planck pre-launch status: Expected LFI polarisation capability. A&A, 520:A8, September 2010. doi: 10.1051/0004-6361/200912855.

Leitch, E.M. et al. An Anomalous Component of Galactic Emission. ApJ, 486:L23, September 1997. doi: 10.1086/310823.

Lewis, A. and Challinor, A. CAMB: Code for Anisotropies in the Microwave Background. Astrophysics Source Code Library, February 2011.

Longair, M.S. *High Energy Astrophysics*. February 2011.

López-Caraballo, C.H. et al. Constraints on the Polarization of the Anomalous Microwave Emission in the Perseus Molecular Complex from Seven-year WMAP Data. ApJ, 729:25, March 2011. doi: 10.1088/0004-637X/729/1/25.

Macellari, N. et al. Galactic foreground contributions to the 5-year Wilkinson Microwave Anisotropy Probe maps. MNRAS, 418:888–905, December 2011. doi: 10.1111/j.1365-2966.2011.19542.x.

Macías-Pérez, J.F. et al. Global Spectral Energy Distribution of the Crab Nebula in the Prospect of the Planck Satellite Polarization Calibration. ApJ, 711:417–423, March 2010. doi: 10.1088/0004-637X/711/1/417.

Maddalena, R.J. et al. The large system of molecular clouds in Orion and Monoceros. ApJ, 303:375–391, April 1986. doi: 10.1086/164083.

Maino, D. et al. The Planck-LFI instrument: Analysis of the 1/f noise and implications for the scanning strategy. A&AS, 140:383–391, December 1999. doi: 10.1051/aas:1999429.

Mason, B.S. et al. A Limit on the Polarized Anomalous Microwave Emission of Lynds 1622. ApJ, 697:1187–1193, June 2009. doi: 10.1088/0004-637X/697/2/1187.

Mayer, C.H. and Hollinger, J.P. Polarized Brightness Distribution Over Cassiopeia a, the Crab Nebula, and Cygnus a at 1.55 cm Wavelength. ApJ, 151:53, January 1968. doi: 10.1086/149418.

Meinhold, P. et al. Noise properties of the Planck-LFI receivers. *Journal of Instrumentation*, 4:2009, December 2009. doi: 10.1088/1748-0221/4/12/T12009.

Mellinger, A. A Color All-Sky Panorama Image of the Milky Way. PASP, 121:1180–1187, November 2009. doi: 10.1086/648480.

Mennella, A. et al. Offset balancing in pseudo-correlation radiometers for CMB measurements. A&A, 410:1089–1100, November 2003. doi: 10.1051/0004-6361:20031266.

Mennella, A. et al. Planck pre-launch status: Low Frequency Instrument calibration and expected scientific performance. A&A, 520:A5, September 2010. doi: 10.1051/0004-6361/200912849.

Mennella, V. et al. A New Approach to the Puzzle of the Ultraviolet Interstellar Extinction Bump. ApJ, 507:L177–L180, November 1998. doi: 10.1086/311693.

Mezger, P.G. and Henderson, A.P. Galactic H II Regions. I. Observations of Their Continuum Radiation at the Frequency 5 GHz. ApJ, 147:471, February 1967. doi: 10.1086/149030.

Mezger, P.G., Mathis, J.S. and Panagia, N. The origin of the diffuse galactic far infrared and sub-millimeter emission. A&A, 105:372–388, January 1982.

Miville-Deschênes, M.A. and Lagache, G. IRIS: A New Generation of IRAS Maps. ApJS, 157:302–323, April 2005. doi: 10.1086/427938.

Murphy, E.J. et al. The Detection of Anomalous Dust Emission in the Nearby Galaxy NGC 6946. ApJ, 709:L108–L113, February 2010. doi: 10.1088/2041-8205/709/2/L108.

Murphy, E.J. et al. Calibrating Extinction-free Star Formation Rate Diagnostics with 33 GHz Free-free Emission in NGC 6946. ApJ, 737:67, August 2011. doi: 10.1088/0004-637X/737/2/67.

Muxlow, T. The e-MERGE Galaxy Evolution Survey. *IAU General Assembly*, 22: 50816, August 2015.

Natoli, P. et al. A Map-Making algorithm for the Planck Surveyor. A&A, 372:346–356, June 2001. doi: 10.1051/0004-6361:20010393.

Offringa, A.R. et al. Post-correlation radio frequency interference classification methods. MNRAS, 405:155–167, June 2010. doi: 10.1111/j.1365-2966.2010.16471.x.

on Extension to the Standard Atmosphere, U.S.C. et al. *U.S. standard atmosphere, 1976*. National Oceanic and Amospheric [sic] Administration : for sale by the Supt.

of Docs., U.S. Govt. Print. Off., 1976. URL `https://books.google.co.uk/books?id=5WdTAAAAMAAJ`.

Ott, M. et al. An updated list of radio flux density calibrators. A&A, 284:331–339, April 1994.

Page, L. et al. First-Year Wilkinson Microwave Anisotropy Probe (WMAP) Observations: Beam Profiles and Window Functions. ApJS, 148:39–50, September 2003. doi: 10.1086/377223.

Page, L. et al. Three-Year Wilkinson Microwave Anisotropy Probe (WMAP) Observations: Polarization Analysis. ApJS, 170:335–376, June 2007. doi: 10.1086/513699.

Paine, S. The *am* Atmospheric Model. Technical report, 2004. URL `http://sma-www.cfa.harvard.edu/private/memos`.

Paladini, R., Davies, R.D. and De Zotti, G. Spatial distribution of Galactic HII regions. MNRAS, 347:237–245, January 2004. doi: 10.1111/j.1365-2966.2004.07210.x.

Paladini, R. et al. Spitzer and Herschel Multiwavelength Characterization of the Dust Content of Evolved H II Regions. ApJ, 760:149, December 2012. doi: 10.1088/0004-637X/760/2/149.

Paladini, R. et al. Anomalous Microwave Emission in HII Regions: Is it Really Anomalous? The Case of RCW 49. ApJ, 813:24, November 2015. doi: 10.1088/0004-637X/813/1/24.

Pauliny-Toth, I.K. and Shakeshaft, J.R. A survey of the background radiation at a frequency of 404 Mc/s, I. MNRAS, 124:61, 1962.

Peck, L.W. and Fenech, D.M. SERPent: Automated reduction and RFI-mitigation software for e-MERLIN. *Astronomy and Computing*, 2:54–66, August 2013. doi: 10.1016/j.ascom.2013.09.001.

Peebles, P.J.E. and Hauser, M.G. Statistical Analysis of Catalogs of Extragalactic Objects. III. The Shane-Wirtanen and Zwicky Catalogs. ApJS, 28:19, November 1974. doi: 10.1086/190308.

Peel, M.W. et al. Template fitting of WMAP 7-year data: anomalous dust or flattening synchrotron emission? MNRAS, 424:2676–2685, August 2012. doi: 10.1111/j.1365-2966.2012.21358.x.

Penzias, A.A. and Wilson, R.W. A Measurement of Excess Antenna Temperature at 4080 Mc/s. ApJ, 142:419–421, July 1965. doi: 10.1086/148307.

Pérez-de-Taoro, M.R. et al. QUIJOTE-CMB experiment: a technical overview. In *Society of Photo-Optical Instrumentation Engineers (SPIE) Conference Series*, volume 9145 of *Society of Photo-Optical Instrumentation Engineers (SPIE) Conference Series*, page 4, July 2014. doi: 10.1117/12.2055821.

Perryman, M.A.C. et al. The HIPPARCOS Catalogue. A&A, 323:L49–L52, July 1997.

Peterson, P. F2py: a tool for connecting fortran and python programs. *IJCSCN*, 4(4), 2009.

Pilbratt, G.L. et al. Herschel Space Observatory. An ESA facility for far-infrared and submillimetre astronomy. A&A, 518:L1, July 2010. doi: 10.1051/0004-6361/201014759.

Planck Collaboration et al. Planck early results. XXI. Properties of the interstellar medium in the Galactic plane. A&A, 536:A21, December 2011. doi: 10.1051/0004-6361/201116455.

Planck Collaboration et al. Planck 2013 results. XI. All-sky model of thermal dust emission. A&A, 571:A11, November 2014a. doi: 10.1051/0004-6361/201323195.

Planck Collaboration et al. Planck 2013 results. XI. All-sky model of thermal dust emission. A&A, 571:A11, November 2014b. doi: 10.1051/0004-6361/201323195.

Planck Collaboration et al. Planck 2013 results. I. Overview of products and scientific results. A&A, 571:A1, November 2014c. doi: 10.1051/0004-6361/201321529.

Planck Collaboration et al. Planck intermediate results. XV. A study of anomalous microwave emission in Galactic clouds. A&A, 565:A103, May 2014d. doi: 10.1051/0004-6361/201322612.

Planck Collaboration et al. Planck 2013 results. XVI. Cosmological parameters. A&A, 571:A16, November 2014e. doi: 10.1051/0004-6361/201321591.

Planck Collaboration et al. Planck 2013 results. VIII. HFI photometric calibration and mapmaking. A&A, 571:A8, November 2014f. doi: 10.1051/0004-6361/201321538.

Planck Collaboration et al. Planck 2013 results. IV. Low Frequency Instrument beams and window functions. A&A, 571:A4, November 2014g. doi: 10.1051/0004-6361/201321544.

Planck Collaboration et al. Planck 2013 results. V. LFI calibration. A&A, 571:A5, November 2014h. doi: 10.1051/0004-6361/201321527.

Planck Collaboration et al. Planck 2013 results. II. Low Frequency Instrument data processing. A&A, 571:A2, November 2014i. doi: 10.1051/0004-6361/201321550.

Planck Collaboration et al. Planck 2015 results. X. Diffuse component separation: Foreground maps. *ArXiv e-prints*, February 2015a.

Planck Collaboration et al. Planck intermediate results. XIX. An overview of the polarized thermal emission from Galactic dust. A&A, 576:A104, April 2015b. doi: 10.1051/0004-6361/201424082.

Planck Collaboration et al. Planck intermediate results. XXIII. Galactic plane emission components derived from Planck with ancillary data. A&A, 580:A13, August 2015c. doi: 10.1051/0004-6361/201424434.

Planck Collaboration et al. Planck 2015 results. XXV. Diffuse low-frequency Galactic foregrounds. *ArXiv e-prints*, June 2015d.

Planck Collaboration et al. Planck 2015 results. XIII. Cosmological parameters. *ArXiv e-prints*, February 2015e.

Planck Collaboration Early XX. Planck early results. XX. New light on anomalous microwave emission from spinning dust grains. A&A, 536:A20, December 2011. doi: 10.1051/0004-6361/201116470.

Planck Collaboration Int. XI. Planck 2013 results. XI. All-sky model of thermal dust emission. *ArXiv e-prints*, December 2013.

Planck Collaboration Int. XV. Planck intermediate results. XV. A study of anomalous microwave emission in Galactic clouds. A&A, 565:A103, May 2014. doi: 10.1051/0004-6361/201322612.

Platania, P. et al. Full sky study of diffuse Galactic emission at decimeter wavelengths. A&A, 410:847–863, November 2003. doi: 10.1051/0004-6361:20031125.

Poglitsch, A. et al. The Photodetector Array Camera and Spectrometer (PACS) on the Herschel Space Observatory. A&A, 518:L2, July 2010. doi: 10.1051/0004-6361/201014535.

Ponthieu, N. and Archeops Collaboration. First detection of polarization of the submillimeter diffuse Galactic dust emission by Archeops. NAR, 47:1047–1056, December 2003. doi: 10.1016/j.newar.2003.09.032.

Prasad, J. and Chengalur, J. FLAGCAL: a flagging and calibration package for radio interferometric data. *Experimental Astronomy*, 33:157–171, March 2012. doi: 10.1007/s10686-011-9279-5.

Press, W.H. et al. *Numerical recipes in C. The art of scientific computing.* 1992.

Purcell, C.R. et al. The Coordinated Radio and Infrared Survey for High-mass Star Formation. II. Source Catalog. ApJS, 205:1, March 2013. doi: 10.1088/0067-0049/205/1/1.

Quireza, C. et al. The Electron Temperature Gradient in the Galactic Disk. ApJ, 653:1226–1240, December 2006. doi: 10.1086/508803.

Reber, G. Cosmic Static. ApJ, 100:279, November 1944. doi: 10.1086/144668.

Reich, P. and Reich, W. Absolute calibration of the 1420 MHz Stockert survey. *Bulletin d'Information du Centre de Donnees Stellaires*, 28:59, March 1985.

Reich, P. and Reich, W. A radio continuum survey of the northern sky at 1420 MHz. II. A&AS, 63:205–288, February 1986.

Remazeilles, M. et al. An improved source-subtracted and destriped 408-MHz all-sky map. MNRAS, 451:4311–4327, August 2015. doi: 10.1093/mnras/stv1274.

Reynolds, S.P. and Chevalier, R.A. Evolution of pulsar-driven supernova remnants. ApJ, 278:630–648, March 1984. doi: 10.1086/161831.

Rohlfs, K. and Wilson, T.L. *Tools of radio astronomy.* 2004.

Rozo, E. et al. Cosmological Constraints from the Sloan Digital Sky Survey maxBCG Cluster Catalog. ApJ, 708:645–660, January 2010. doi: 10.1088/0004-637X/708/1/645.

Rubiño-Martín, J.A. et al. Observations of the Polarisation of the Anomalous Microwave Emission: A Review. *Advances in Astronomy*, 2012:351836, 2012. doi: 10.1155/2012/351836.

Rybicki, G.B. and Lightman, A.P. *Radiative processes in astrophysics*. 1979.

Sastry, C.V., Pauliny-Toth, I.I.K. and Kellermann, K.I. Observations of the polarization of discrete radio sources at 6-cm wavelength. AJ, 72:230–234, March 1967. doi: 10.1086/110224.

Scaife, A. et al. Constraints on spinning dust towards Galactic targets with the Very Small Array: a tentative detection of excess microwave emission towards 3C396. MNRAS, 377:L69–L73, May 2007. doi: 10.1111/j.1745-3933.2007.00305.x.

Schultz, G.V. and Wiemer, W. Interstellar reddening and IR-excess of O and B stars. A&A, 43:133–139, September 1975.

Seiffert, M. et al. 1/f noise and other systematic effects in the Planck-LFI radiometers. A&A, 391:1185–1197, September 2002. doi: 10.1051/0004-6361:20020880.

Silsbee, K., Ali-Haïmoud, Y. and Hirata, C.M. Spinning dust emission: the effect of rotation around a non-principal axis. MNRAS, 411:2750–2769, March 2011. doi: 10.1111/j.1365-2966.2010.17882.x.

Smoot, G.F. et al. Structure in the COBE differential microwave radiometer first-year maps. ApJ, 396:L1–L5, September 1992. doi: 10.1086/186504.

Sneden, C. et al. Infrared colors and the diffuse interstellar bands. ApJ, 223:168–179, July 1978. doi: 10.1086/156247.

Story, K.T. et al. A Measurement of the Cosmic Microwave Background Gravitational Lensing Potential from 100 Square Degrees of SPTpol Data. ApJ, 810:50, September 2015. doi: 10.1088/0004-637X/810/1/50.

Stumpff, P. Prozeßsteuerung des 100-Meter-Teleskops - Astronomisches Konzept. *Mitteilungen der Astronomischen Gesellschaft Hamburg*, 31:101, 1972.

Sutton, D. et al. Map making in small field modulated CMB polarization experiments: approximating the maximum likelihood method. MNRAS, 393:894–910, March 2009. doi: 10.1111/j.1365-2966.2008.14195.x.

Sutton, D. et al. Fast and precise map-making for massively multi-detector CMB experiments. MNRAS, 407:1387–1402, September 2010. doi: 10.1111/j.1365-2966.2010.16954.x.

Suyu, S.H. et al. Dissecting the Gravitational lens B1608+656. II. Precision Measurements of the Hubble Constant, Spatial Curvature, and the Dark Energy Equation of State. ApJ, 711:201–221, March 2010. doi: 10.1088/0004-637X/711/1/201.

Thrall, H. et al. High Resolution Observations of a Selection of Faint 1.4GHz Radio Counterparts to Optical Sources in the HDF-N. In Afonso, J. et al, editors, *Deepest Astronomical Surveys*, volume 380 of *Astronomical Society of the Pacific Conference Series*, page 291, December 2007.

Tibbs, C.T. et al. Very Small Array observations of the anomalous microwave emission in the Perseus region. MNRAS, 402:1969–1979, March 2010. doi: 10.1111/j.1365-2966.2009.16023.x.

Tibbs, C.T. et al. A Multi-wavelength Investigation of RCW175: An H II Region Harboring Spinning Dust Emission. ApJ, 754:94, August 2012. doi: 10.1088/0004-637X/754/2/94.

Tibbs, C.T. et al. Constraints on Free-Free Emission from Anomalous Microwave Emission Sources in the Perseus Molecular Cloud. ApJ, 770:122, June 2013a. doi: 10.1088/0004-637X/770/2/122.

Tibbs, C.T. et al. AMI Observations of the Anomalous Microwave Emission in the Perseus Molecular Cloud. ApJ, 768:98, May 2013b. doi: 10.1088/0004-637X/768/2/98.

Tielens, A.G.G.M. Interstellar Polycyclic Aromatic Hydrocarbon Molecules. ARA&A, 46:289–337, September 2008. doi: 10.1146/annurev.astro.46.060407.145211.

Todorović, M. et al. A 33-GHz Very Small Array survey of the Galactic plane from l = 27 to 46. MNRAS, 406:1629–1643, August 2010. doi: 10.1111/j.1365-2966.2010.16809.x.

Ulich, B.L. Millimeter wave radio telescopes - Gain and pointing characteristics. *International Journal of Infrared and Millimeter Waves*, 2:293–310, March 1981. doi: 10.1007/BF01007036.

van der Walt, S., Colbert, S.C. and Varoquaux, G. The numpy array: A structure for efficient numerical computation. *Comput. Sci. Eng.*, 13(2):22–30, 2011.

Vidal, M. et al. Dust-correlated cm wavelength continuum emission from translucent clouds ζ Oph and LDN 1780. MNRAS, 414:2424–2435, July 2011. doi: 10.1111/j.1365-2966.2011.18562.x.

Vidal, M. et al. Polarized radio filaments outside the Galactic plane. MNRAS, 452:656–675, September 2015. doi: 10.1093/mnras/stv1328.

Vinyaikin, E.N. Frequency dependence of the evolution of the radio emission of the supernova remnant Cas A. *Astronomy Reports*, 58:626–639, September 2014. doi: 10.1134/S1063772914090078.

Vrba, F.J. and Rydgren, A.E. The ratio of total-to-selective extinction in the Chamaeleon T1 and R Coronae Australis dark clouds. ApJ, 283:123–128, August 1984. doi: 10.1086/162281.

Vrba, F.J. and Rydgren, A.E. On the ratio of total-to-selective extinction in the Taurus dark cloud complex. AJ, 90:1490–1493, August 1985. doi: 10.1086/113860.

Wallace, P.T. TPOINT – Telescope Pointing Analysis System. *Starlink User Note*, 100, 1994a.

Wallace, P.T. The SLALIB Library. In Crabtree, D.R., Hanisch, R.J. and Barnes, J., editors, *Astronomical Data Analysis Software and Systems III*, volume 61 of *Astronomical Society of the Pacific Conference Series*, page 481, 1994b.

Watson, R. et al. Perseus anomalous emission as seen with VSA. In *CMB and Physics of the Early Universe*, page 66, 2006.

Watson, R.A. et al. Anisotropy measurements of the cosmic microwave background radiation at intermediate angular scales. Nature, 357:660–665, June 1992. doi: 10.1038/357660a0.

Watson, R.A. et al. Detection of Anomalous Microwave Emission in the Perseus Molecular Cloud with the COSMOSOMAS Experiment. ApJ, 624:L89–L92, May 2005. doi: 10.1086/430519.

Weaver, H. et al. Observations of a Strong Unidentified Microwave Line and of Emission from the OH Molecule. Nature, 208:29–31, October 1965. doi: 10.1038/208029a0.

Weiland, J.L. et al. Seven-year Wilkinson Microwave Anisotropy Probe (WMAP) Observations: Planets and Celestial Calibration Sources. ApJS, 192:19, February 2011. doi: 10.1088/0067-0049/192/2/19.

Weingartner, J.C. and Draine, B.T. Dust Grain-Size Distributions and Extinction in the Milky Way, Large Magellanic Cloud, and Small Magellanic Cloud. ApJ, 548: 296–309, February 2001. doi: 10.1086/318651.

Wright, E.L. et al. The Wide-field Infrared Survey Explorer (WISE): Mission Description and Initial On-orbit Performance. AJ, 140:1868, December 2010. doi: 10.1088/0004-6256/140/6/1868.

Wright, M.C.H. Polarization of the Crab nebula at 21.1-cm wavelength. MNRAS, 150: 271–278, 1970.

Wright, M.C.H. and Forster, J.R. An aperture synthesis map of the Crab Nebula at 23 gigahertz. ApJ, 239:873–879, August 1980. doi: 10.1086/158172.

Ysard, N., Miville-Deschênes, M.A. and Verstraete, L. Probing the origin of the microwave anomalous foreground. A&A, 509:L1, January 2010. doi: 10.1051/0004-6361/200912715.

Yu, J.T. and Peebles, P.J.E. Superclusters of Galaxies? ApJ, 158:103, October 1969. doi: 10.1086/150175.

Zacchei, A. et al. Planck early results. V. The Low Frequency Instrument data processing. A&A, 536:A5, December 2011. doi: 10.1051/0004-6361/201116484.

Zaldarriaga, M. and Seljak, U. All-sky analysis of polarization in the microwave background. Phys.Rev.D, 55:1830–1840, February 1997. doi: 10.1103/PhysRevD.55.1830.

Zhang, C.Y. et al. Dust ring around Lambda Orionis. A&A, 218:231–240, July 1989.

Zwart, J.T.L. et al. The Arcminute Microkelvin Imager. MNRAS, 391:1545–1558, December 2008. doi: 10.1111/j.1365-2966.2008.13953.x.

Appendix A

MFI Observing Modes

The QT1 telescope has four principal observing modes that are discussed regularly throughout this thesis: Sky-dips, drift raster scans, sky raster scans and nominal mode. This appendix gives a brief summary and illustration of each observing mode, what the observing mode is used for and any important points. Note all the figures in this appendix are assuming observations are taken from the focal centre of the telescope, which is not true for observations by QT1 and the MFI.

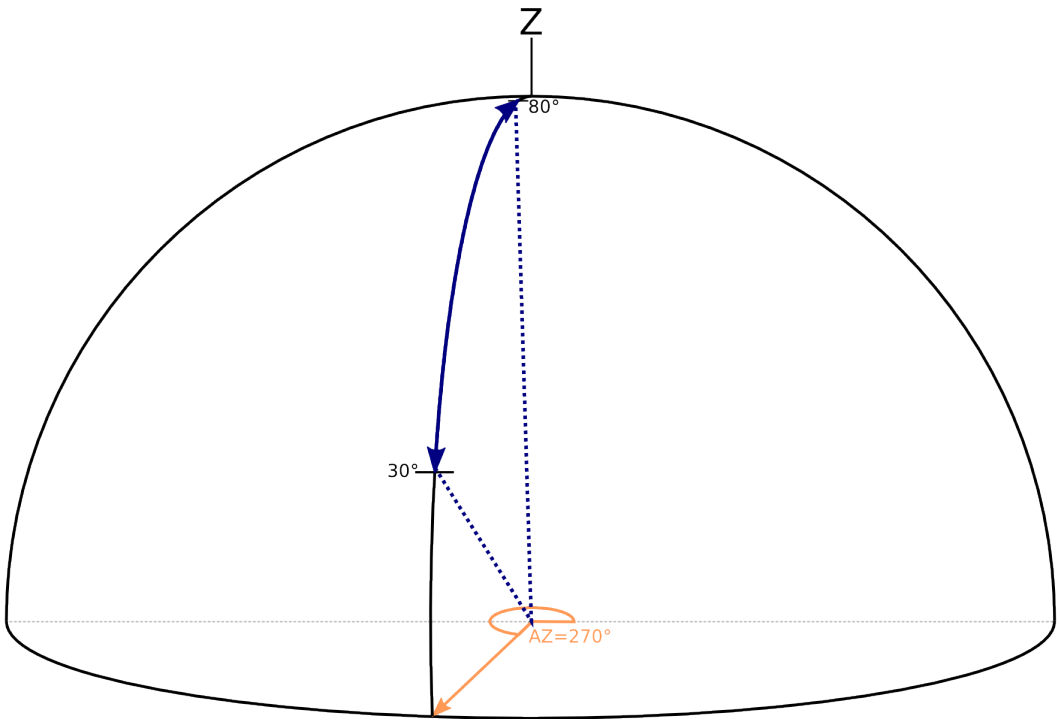

Figure A.1: **Sky-Dip**: The sky-dip observing mode is used for characterising the response of the MFI to the atmosphere. All sky-dip observations were made between 30 degrees, the minimum elevation of QT1, and 80 degrees as illustrated by the dark blue line. Nearly all the MFI sky-dips were performed towards the *West*, which corresponds to 270 degrees azimuth. The choice of direction for the sky-dip was purely motivated by the distribution of local RFI. Ideally a sky-dip measurement over all elevations will contain only the receiver noise and the atmospheric contribution.

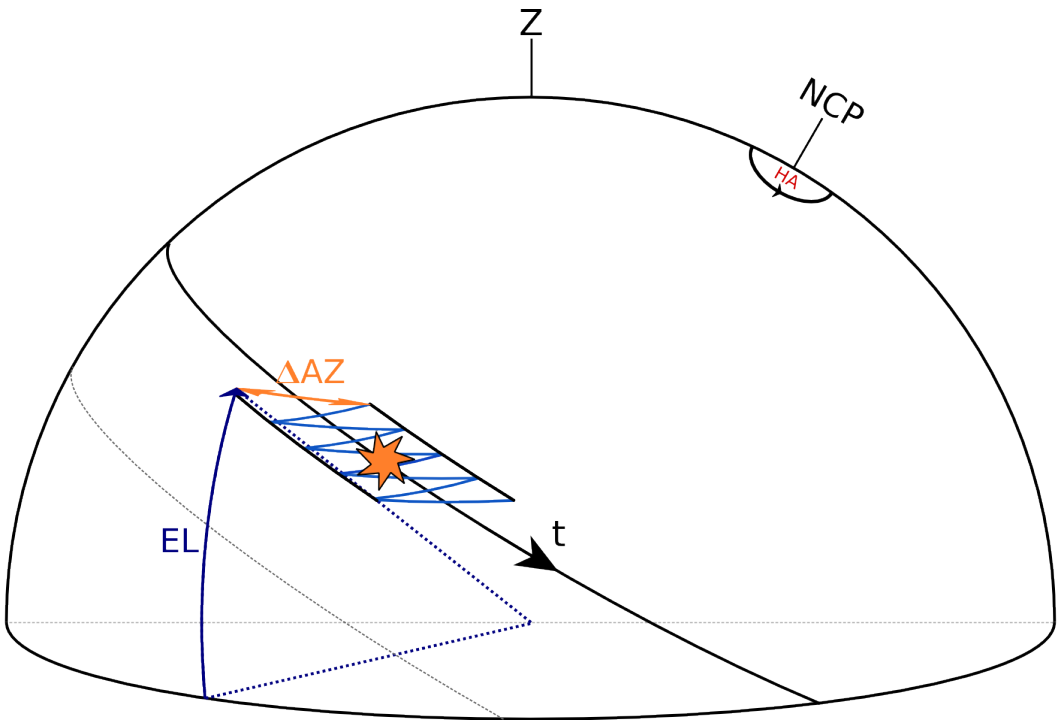

Figure A.2: **Drift Raster**: The drift raster scan method involves slewing the telescope back and forth in azimuth while maintaining a constant elevation. As the sky turns the tracks are smeared across the celestial sphere as indicated by the light-blue lines in the figure. The benefit of this observing mode is that the airmass along the line-of-sight remains constant, this ensures no strong gradients appear in the resulting TOD and absorption from the atmosphere remains constant.

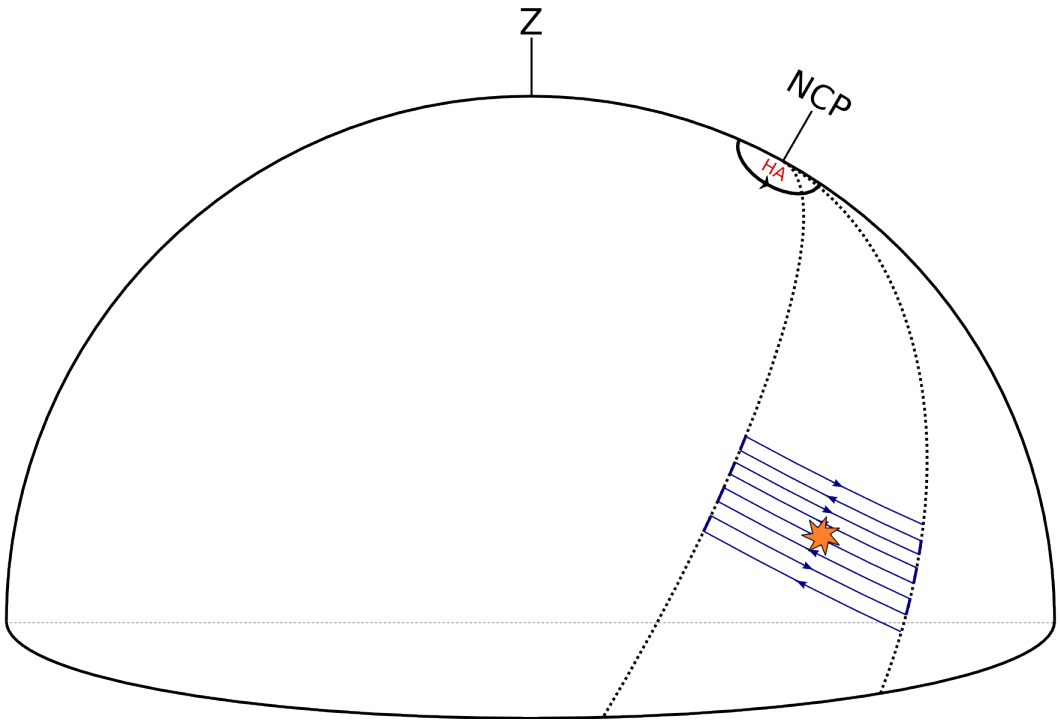

Figure A.3: **Sky Raster**: The sky scan raster method slews the telescope along the right ascension (or hour angle) coordinate direction and after each slew the telescope is moved a step in the declination direction as shown by the blue lines. This observing mode is ideal for making small observations on bright targets in a much shorter space of time than the drift raster scan. Many Cas A calibrator observations were observed using the sky raster scan mode. However, strong gradients due to changing atmospheric emission can make it difficult to recover extended emission when observing in this way.

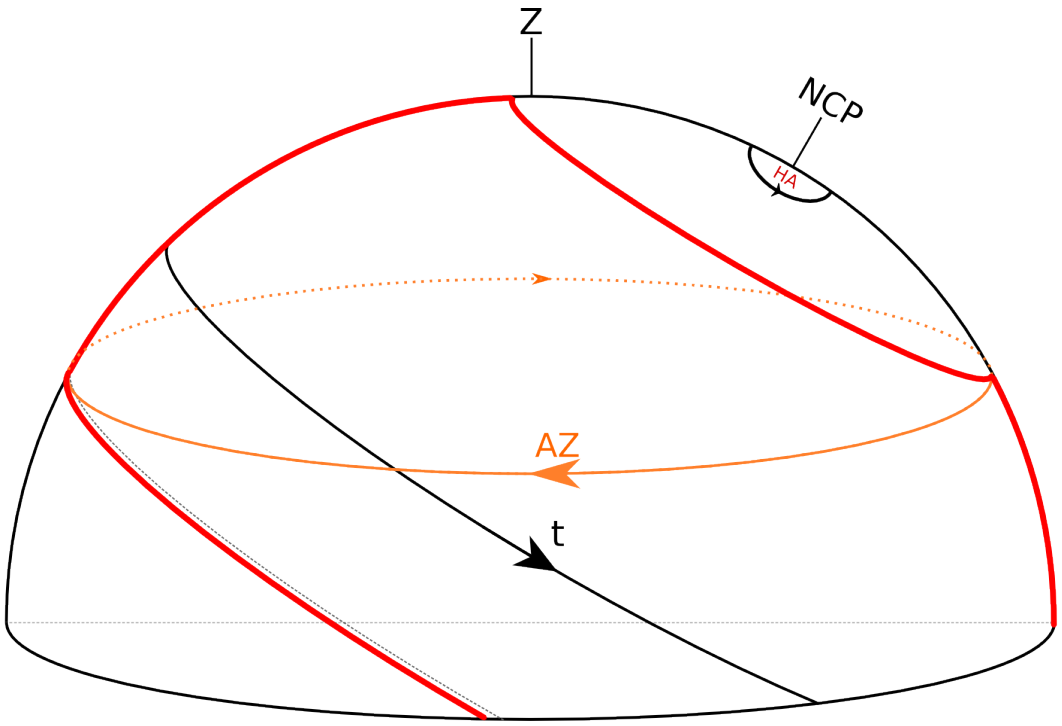

Figure A.4: **Nominal Mode**: Nominal mode (or wide-survey mode) observing involves continually slewing the telescope in a single azimuthal direction. Over the course of 24 hours the azimuthal ring will observe all the sky highlighted in red. This observing mode has all the same advantages as drift raster scan in terms of minimising atmospheric based systematics. However, it is a limited observing mode in that it can only be used for observing large portions of the sky.

Appendix B

Table of Tau A Polarisations

Table B.1: Summary of references and polarisation measurements of Tau A.

	ν (GHz)	$\Pi(\%)$
Wright (1970)	1.42	1.5±0.1
Dmitrenko et al. (1970)	2.0	2.0±0.4
Dmitrenko et al. (1970)	2.1	2.2±0.396
Dmitrenko et al. (1970)	2.3	2.4±0.408
Dmitrenko et al. (1970)	2.5	2.7±0.405
Dmitrenko et al. (1970)	2.7	3.0±0.42
Dmitrenko et al. (1970)	2.9	3.2±0.448
Dmitrenko et al. (1970)	3.0	3.4±0.442
Dmitrenko et al. (1970)	3.0	3.4±0.408
Dmitrenko et al. (1970)	3.1	3.5±0.42
Dmitrenko et al. (1970)	3.4	3.8±0.418
Dmitrenko et al. (1970)	3.7	4.15±0.415
Dmitrenko et al. (1970)	4.0	4.3±0.43
Sastry et al. (1967)	5	5.7±0.5
Dmitrenko et al. (1970)	5.7	5.9±0.885
Hobbs and Haddock (1967)	8	7.2±0.4
Boland et al. (1966)	14.5	8.6±0.3
Green et al. (1975)	15	6.4±0.5
Mayer and Hollinger (1968)	19	6.6±1.2
Page et al. (2003)	22.5	7.0±0.3
Wright and Forster (1980)	23	9±1.0
Johnston and Hobbs (1969)	31	8.1±1.0
Page et al. (2003)	32.8	6.9±0.3
Hafez et al. (2008)	34.0	7.8±0.6
Page et al. (2003)	40.4	6.6±0.9
Page et al. (2003)	60.2	7.0±1.1
Page et al. (2003)	92.9	7.6±2.0